Innovative Structural Materials and Sections with

Strain Hardening Cementitious Composites

by

Vikram Dey

A Dissertation Presented in Partial Fulfillment
of the Requirements for the Degree
Doctor of Philosophy

Approved April 2016 by the
Graduate Supervisory Committee:

Barzin Mobasher, Chair
Benjamin Underwood
Narayanan Neithalath
Subramaniam Rajan
Yongming Liu

ARIZONA STATE UNIVERSITY

May 2016

ABSTRACT

The motivation of this work is based on development of new construction products with strain hardening cementitious composites (SHCC) geared towards sustainable residential applications. The proposed research has three main objectives: automation of existing manufacturing systems for SHCC laminates; multi-level characterization of mechanical properties of fiber, matrix, interface and composites phases using servo-hydraulic and digital image correlation techniques. Structural behavior of these systems were predicted using ductility based design procedures using classical laminate theory and structural mechanics. SHCC sections are made up of thin sections of matrix with Portland cement based binder and fine aggregates impregnating continuous one-dimensional fibers in individual or bundle form or two/three dimensional woven, bonded or knitted textiles. Traditional fiber reinforced concrete (FRC) use random dispersed chopped fibers in the matrix at a low volume fractions, typically 1-2% to avoid to avoid fiber agglomeration and balling. In conventional FRC, fracture localization occurs immediately after the first crack, resulting in only minor improvement in toughness and tensile strength. However in SHCC systems, distribution of cracking throughout the specimen is facilitated by the fiber bridging mechanism. Influence of material properties of yarn, composition, geometry and weave patterns of textile in the behavior of laminated SHCC skin composites were investigated. Contribution of the cementitious matrix in the early age and long-term performance of laminated composites was studied with supplementary cementitious materials such as fly ash, silica fume, and wollastonite. A closed form model with classical laminate theory and ply discount method, coupled with a damage evolution model was utilized to simulate the non-linear tensile response of these composite materials. A

constitutive material model developed earlier in the group was utilized to characterize and correlate the behavior of these structural composites under uniaxial tension and flexural loading responses. Development and use of analytical models enables optimal design for application of these materials in structural applications. Another area of immediate focus is the development of new construction products from SHCC laminates such as angles, channels, hat sections, closed sections with optimized cross sections. Sandwich composites with stress skin-cellular core concept were also developed to utilize strength and ductility of fabric reinforced skin in addition to thickness, ductility, and thermal benefits of cellular core materials. The proposed structurally efficient and durable sections promise to compete with wood and light gage steel based sections for lightweight construction and panel application.

ACKNOWLEDGMENTS

I dedicate this to my grandmother, Late Anita Nag, my parents Radha and Dilip Kumar

Dey, my brother Ankur Dey, my teacher Chitra Bhattacharjee. Without their love,

mentoring and motivation this journey would not have been possible.

TABLE OF CONTENTS

LIST OF TABLES

LIST OF FIGURES

1. INTRODUCTION

Strain Hardening Cement Composites (SHCC) are an exciting class of composite have a significantly higher strength, ductility, and versatility as compared to conventional fiber reinforced concrete (FRC) [1]. These composites are known to exhibit significant increase in flexural strength beyond the formation of first crack due to crack bridging, fiber pullout, and fiber rupture mechanisms. This makes them ideal for structural applications as light-weight thin sections with good energy absorption capacity and high strain capacity with fatigue and impact resistance. Typical stress-strain response and toughening mechanisms observed in SHCC systems are shown in Figure 1-1 [2]. Beyond a critical fiber volume fraction, distributed cracking is observed in such systems once the matrix yields. Since a substantial amount of energy is required to extend existing cracks, secondary parallel cracks form. Single crack localization is therefore shifted to multiple distributed cracking mechanisms, leading to macroscopic pseudo-strain hardening behaviors as shown in Figure 1-1(a,c). Due to this aspect, SHCC systems could be used in seismic regions which requires performance from materials beyond its initial elastic response and into the strain-hardening range. Fiber-matrix delamination and matrix cracking are the distinct modes of failure as evident in Figure 1-1(b,c). Along with continuous fiber systems, micro-reinforcement of the matrix further aids in energy dissipation and toughening through crack bridging mechanisms in the fracture process zone (FPZ) as shown in Figure 1-1(d,e). The approach of this study is to integrate the toughening effects at the micro- and macro-scale by reinforcing brittle cement matrix with mineral micro-fibers, characterize and toughen fiber-matrix interface, and macro-scale fiber/fabric reinforcement with a viewpoint of optimizing

the behavior of SHCC sections for different structural applications as shown in Figure 1-1(f).
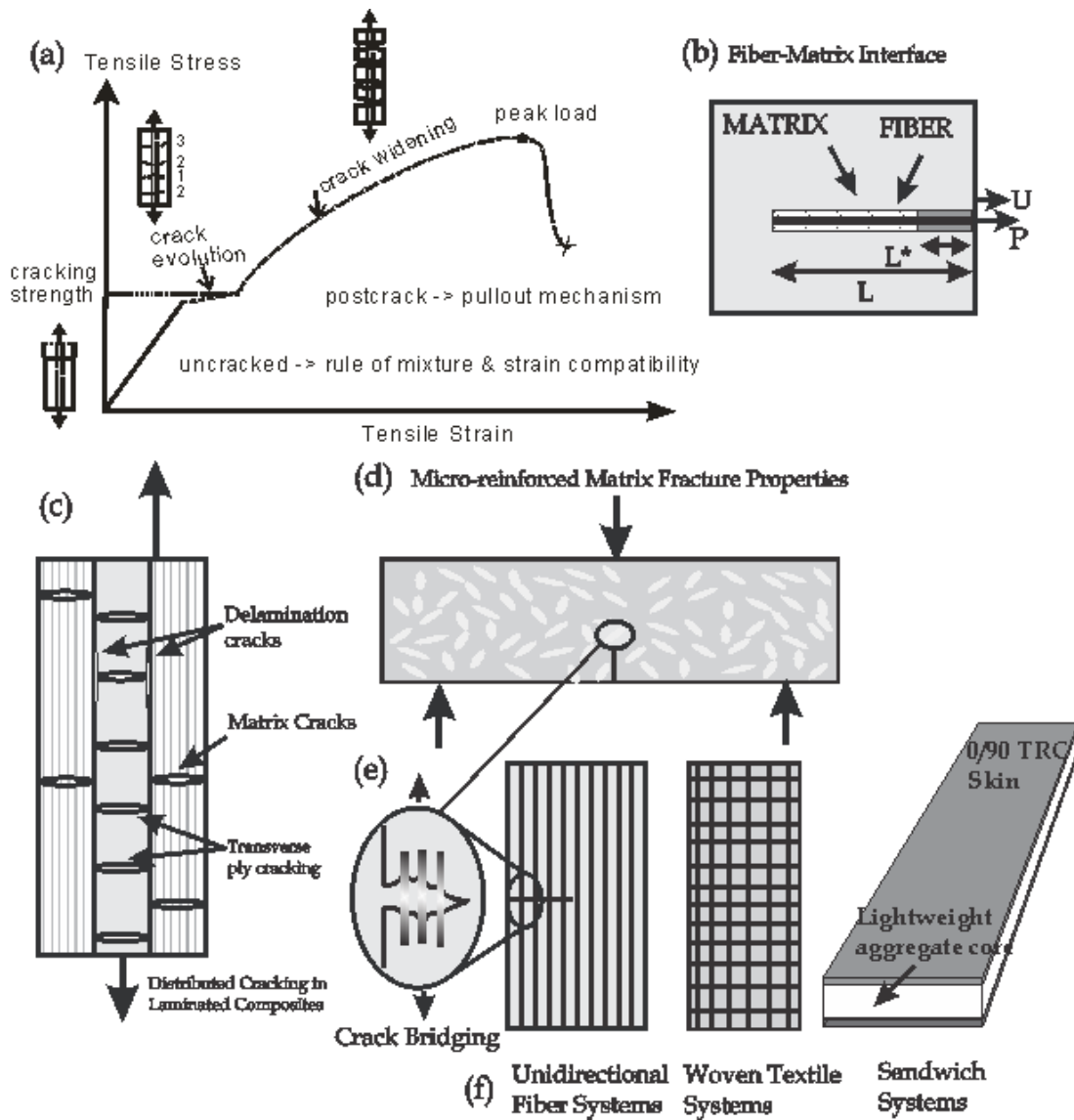
Figure 1-1: (a) Typical tensile response of a strain hardening fiber-cement composite, (b) fiber-matrix interface, (c) modes of failure, (d) matrix strengthening, (d, e) crack bridging, (f) SHCC and sandwich systems [2].

Strain hardening cement composite (SHCC) systems can be broadly classified broadly into two types of composites depending on the structure of the yarn: continuous 1-D fiber

reinforced and 2-D/3-D textile reinforced concrete (TRC) systems. Continuous fiber reinforced cementitious systems have superior load bearing capacity than conventional FRC section and can be used as structural material in diverse loading conditions such as tension, flexure, impact, fatigue, shear and multi-axial loading [3] and fall into the category of High Performance Fiber Reinforced Cementitious Composites (HPRFRCC). This is a promising new class of structural material which comprises of unidirectional, cross-ply and angle ply laminates with Portland cement based matrix for severe loading conditions. The enhanced strength and ductility behavior is primarily governed by interfacial bond characteristics between fabrics and matrix. Filament winding a novel automated composite manufacturing system was developed at ASU for manufacturing economic and versatile HPFRCC thin laminates. The technique provides desired agility, precision and quality control to develop composite materials of desired geometry and lamina stacking scheme; and is an excellent alternative to traditional labor intensive techniques such as hand layup process.

Textile reinforced concrete (TRC) composites is another new class of sustainable construction materials with superior tensile strength and ductility. TRCs are suitable for applications that involve large energy absorption, high strain capacity, and especially for structures in seismic regions where high ductility is desired [2]. Application areas of these composites include structural panels, impact, blast resistance, repair and retrofit, earthquake remediation, strengthening of unreinforced masonry walls, and beam-column connections are being developed. The development of textile reinforced concrete (TRC) field generated tremendous interest in the international scientific community and has been followed by many researchers in the field [4,5,6,7,8]. Dominant toughening mechanisms

3

such as distributed matrix cracking, ply delamination, and crack deflection are observed in TRC composites, resulting in tensile strength and strain capacity in the range of 22 MPa and 4.5% respectively [2].

Different components of this research on development and characterization of innovative structural materials are shown in Figure 1-2. Engineered matrices with short glass fibers, wollastonite micro-fibers, and fly ash was incorporated to strengthen and micro-reinforce the cementitious matrix in SHCC systems. Contribution of wollastonite micro- and sub-micron fibers on the early age and long-term performance of cement-based systems were extensively studied using compression, tension, fracture and plastic shrinkage tests. A series of blended paste and mortar mixtures with silica fume and wollastonite particles of different morphology, size and dosage were developed. Non-linear fracture mechanics concepts used indicate considerable effect of wollastonite reinforcement on the fracture resistance of the cementitious matrix. Morphology of fractured surfaces was studied using scanning electron micrographs to correlate the mechanical properties with internal micro-structure. It was observed that at optimal dosage, wollastonite fibers promote classical toughening mechanisms such as crack bridging and crack path deflection.
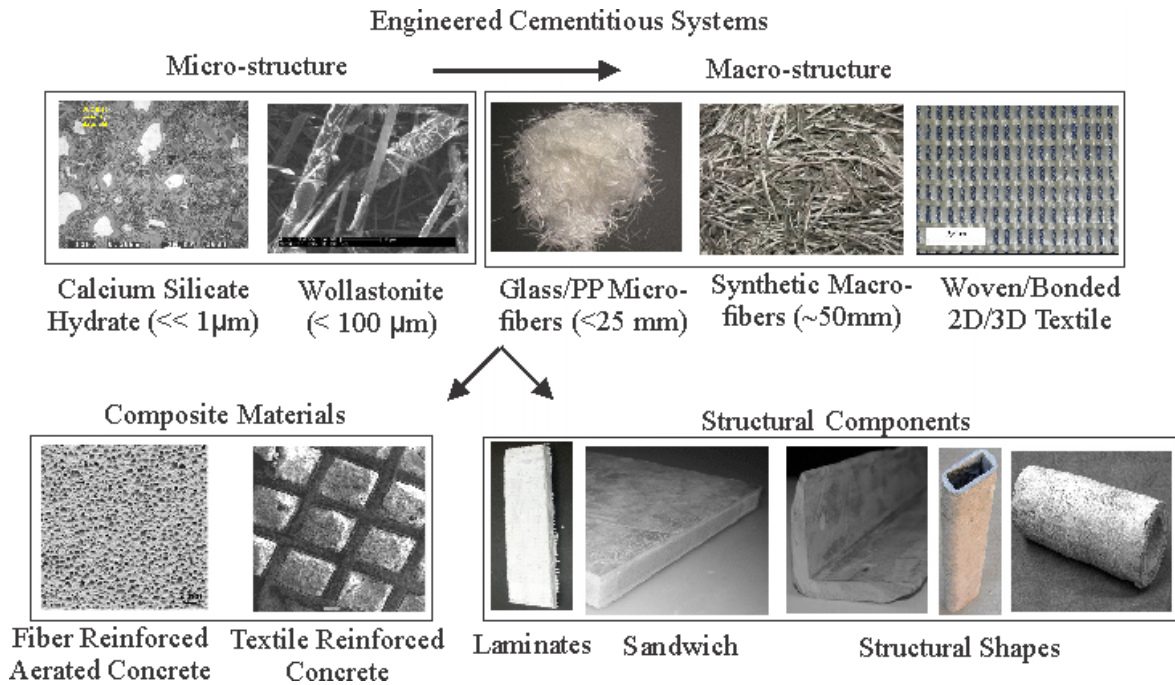
Figure 1-2: Components of proposed research on development on innovative structural sections

Macro-structure reinforcement through continuous yarns were considered and the effect of yarn composition, geometry and weave patterns of the fabric in the behavior of laminated composites were investigated. Two-dimensional woven/bonded fabric systems comprising of aramid, carbon, glass and polypropylene were investigated using mechanical tests to characterize their performance in a cementitious matrix. In addition, innovative hybrid fabric systems with high strength and modulus fabrics (such as aramid and carbon), with low strength and high ductility fabrics (glass) were studied at different relative proportions. Uniaxial tension and three-point bending quasi-static configuration on these pultruded sections to compare the different fiber systems. Influence of weave structures, were studied with polypropylene fabrics made out of proprietary fibrillate multi-filament micro-fibers. Plain and tricot weave knit patterns with 50% open-closed structures were developed at

RWTH Aachen University in Germany. Extensive testing program has been undertaken to measure quasi-static tension, flexural and pullout properties to characterize these TRC systems. The performance of these TRC composites have been compared with unidirectional polypropylene based HPFRCC composites.

The current work is primarily focused on the development of new construction products from SHCC laminates such as angles, channels, hat sections, closed sections and sandwich sections with optimized cross sections as shown in Figure 1-3. By developing methods to utilize, design, and construct cement based composites for structural applications, we pursue sustainable new materials and design approaches. The direction of work addresses a serviceability based design and promises to deliver a robust design methodology for new composite sections that integrates materials ductility with serviceability, strength and long term durability. The proposed structurally efficient and durable sections promise to compete with wood and light gage steel based sections for lightweight construction and panel application.
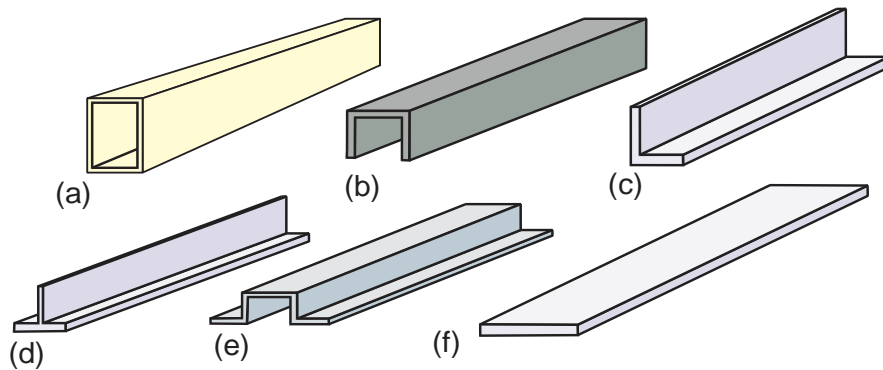
Figure 1-3: Cross-sectional shapes for manufacturing using the ASU cement composite pultrusion equipment: a) closed cell, b) C channel, c) equal leg angle, d) T-section, e) hat section, f) flat board

Automated manufacturing system based on pultrusion process was developed to fabricate full-scale structural shapes and sandwich sections with different thickness, shapes, effective lengths, and multiple layers of core and fabric elements. In this process the fabric layer impregnated with matrix and then stacked on a mold in between alternate layers of cement matrix [9]. The existing pultrusion process at ASU was automated to introduce a pneumatically controlled, automated pull-press-release mechanism system. Transformation into an automated continuous process enables casting of long full-scale sections, and multiple pneumatic pressure points allow improvement in the impregnation process. Geometrical anchorage due to the intersection of longitudinal and transverse yearns result in superior bonding with the matrix in TRC systems. Also pultrusion technique allows for normal and shear stresses to be applied on the specimen to efficiently impregnate the textile, resulting in reduced porosity in the matrix, and better bonding at the interface [10].

Another focus of this study is on the development of sandwich composites with stress skin-cellular core concept to utilize strength and ductility of fabric reinforced skin in addition to thickness, ductility, and thermal benefits of cellular core materials. The proposed sandwich composite system with aerated concrete core and TRC skin layers, are shown in Figure 1-4.
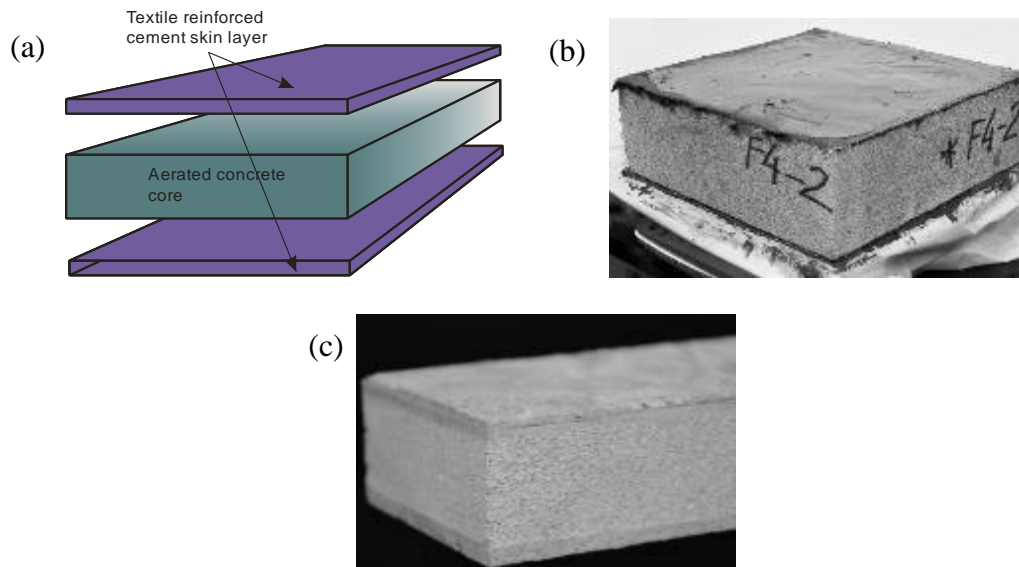
Figure 1-4: (a) Schematics of the proposed textile reinforced-aerated concrete sandwich composite system, (b) finished sandwich panel, (c) beam test coupon harvested from panel.

Potential area of application of sandwich composites is in load bearing precast structural members such as wall, roof and floor panels. Among the various alternatives of fiber types studied earlier, Alkali Resistant Glass (ARG) textiles offer moderate strength, stiffness, and are particularly designed to resist the highly alkaline environments [2]. Aerated Concrete known to be an ideal material for sustainable construction, is manufactured from a mixture of Portland cement, fly ash, quick lime, gypsum, water, and an expansive agent such as aluminum paste was used as the core element. It is characterized by a closed foam pore structure with almost 80% micro-pores and air pores in the ratio of 1:2.5; and remaining as macro-pores [11,12]. Thermal conductivity of aerated concrete typically lies in the range of 0.15-0.22 W/°K-m. The network of disconnected pores improves the thermal insulation with conductivity about 10% of normal-weight concrete, resulting in more energy efficient building systems [13]. Unreinforced and fiber reinforced aerated concrete

were considered and mechanical performance of ductile skin-brittle core with TRC-AAC and ductile skin-ductile core with TRC-FRAC composites were investigated. An extensive experimental study was conducted to understand behavior of plain aerated concrete and sandwich composite systems under quasi-static and medium stain rate impact loading. Impact test setup was modeled on a free fall drop of an instrumented hammer using three point bending configuration. The effect of impact energy on the mechanical properties was investigated for various drop heights, and on different cross-sections.

Finally use of SHCC systems is repair and rehabilitation of existing structures were studied from the viewpoint of ability of these systems for crack mitigation. An experimental study was undertaken to evaluate the bonding abilities of TRC laminates with normal weight concrete and aerated concrete masonry units. Bond assemblies with masonry blocks and TRC laminates with several layers of alkali-resistant glass textile in a cementitious matrix were tested under direct tension, and the strength to cause multiple cracking in TRC layer, failure of the interfacial bond and failure of the masonry units were evaluated under monotonic tension and fatigue loading conditions. Results from these tests showed the ability of TRC laminates to bond effectively with existing structural units, further validating the use and application of the class of SHCC systems.

1.1. Objectives and Expected Significance of the Proposed Research

The objective of this proposal is develop new-age sustainable infrastructure materials. The proposed research is shown as a multi-level approach in Figure 1-5, and has three main objectives: automation of existing manufacturing systems for SHCC laminates; multi-level characterization of mechanical properties of fiber, matrix, composite and interface phases using servo-hydraulic and digital image correlation techniques; and development of

ductility based design procedures using classical laminate theory and structural mechanics to predict structural performance using closed form solutions. The overall objective of such a technology is to develop cement-based composites to be used as structural elements and for repair and retrofitting of existing structures. These cementitious composites in the form of sandwich composites could be used such as beam and roof elements, whereas structural shapes could be used as compression and tension elements. They offer direct competition for wood based commercial sections such as 2x4, and 2x6, structural insulated panels, as well as light gage steel members that are increasingly used in the construction and framing applications. The research path is development of automated manufacturing systems, characterization of different reinforcing systems in terms of geometry and material properties, design of pseudo-ductile blended matrices with low cement-content with early age and long term durability. It is expected that the proposed research will make a substantial contribution to the new product development market in the infrastructure sector. Several specific goals of the proposal are listed below:

1) Characterize and automate existing manufacturing methods for composite materials to fabricate full-scale industry standard pultruded sections. Characterize and optimize components of sandwich construction with available technology from performance, durability and sustainability viewpoints.

2) Conduct fundamental materials test of uniaxial tension, fiber pullout, and flexural tests under quasi-static loadings, and medium-to-high strain rates on fiber and textile reinforced cementitious composites. These tests provide several fundamental information pertaining

to the bonding and reinforcing efficiency of the fibers and textiles in a cement based environment.

3) Experimental stress analysis, micro-structure investigation, and digital image correlation of distributed cracking in textile laminates and sandwich composites to address the role of interface in toughening mechanisms.

4) Develop parametric theoretical models for multi-scale interface, composite lamina, and tension–flexural, and structural applications. Improve the fundamental theoretical understanding of the mechanisms that control performance.

New Product Development

- Energy Efficient Building Systems
- Sustainable Low-Cost Infrastructure
- Impact & Strain Rate Sensitivity

Engineering Components

Automated Production	Light-weight Thermal Efficiency	Strength Ductility	Fiber-Matrix Bonding	Brittle Cement Matrix
Filament Winding Pultrusion	Aerated Concrete	Strain Hardening Cement Composite	Interface Characterization	Micro-Reinforcement

Technology Elements

- Automation
- Impregnation Efficiency
- Mechanical Characterization
- Strain-Rate Sensitivity
- Fabric Alternatives
- Structure Weave Pattern
- Low-Cement Systems
- Micro-structure Refinement
- Shrinkage Control

Fundamental Knowledge

- Material Science Stress Analysis Mechanics of Composites
- Strain rate effects Damage Characterization
- Digital Image Correlation
- Theoretical Modelling

Figure 1-5: Multi-level approach of proposed research

2. UNIDIRECTIONAL CEMENTITIOUS COMPOSITES WITH CONTINUOUS POLYPROPYLENE FIBERS

The influence of engineered hydrophobic polypropylene fibers in the formation of distributed cracking and the associated strengthening and toughening of fabric-cement composites under mechanical loading were studied. Composites were made from low modulus surface modified hydrophobic macro-synthetic continuous polypropylene fibers and compared for their reinforcing ability with fibrillated micro-synthetic fibers. A series of mechanical tests were performed on the individual fibers and fiber-matrix interface, while uniaxial tension and flexural tests on composite sections were conducted to show the applicability of the fiber systems for a variety of civil infrastructure applications. An automated filament winding system was developed to manufacture continuous fiber composites (CFC). The automated manufacturing system comprises of state-of-the-art integrated motion control and data acquisition systems and provides desired agility, precision and quality control to develop economic and versatile composite materials. The influence of fabric geometry, matrix modification and curing were studied using tensile and flexural response. Digital image correlation technique was used for damage characterization using quantitative analysis of crack width and spacing, and correlated with the tensile response and stiffness degradation. Also, the microstructure of the different composites was characterized and correlated with their mechanical properties using optical and scanning electron microscopy. It was observed that the mechanical properties as well as crack spacing and composite stiffness were significantly affected by fiber structure and matrix formulation.

The interfacial bond between the round monofilament macro-synthetic fibers and hydrating cement based matrix is limited and results in a major drawback to their application in concrete materials. Low bond strength does not allow for the effective stress transfer to the fibers and hence their effectiveness is significantly restricted by the lack of organic-inorganic bond. The bond that develops at the fiber-matrix interface plays an important role in controlling the mechanical performance of fiber reinforced composites. The proposed engineered polypropylene fiber systems are expected to address and enhance the bond strength between the polymeric fibers and the cement matrix. The use of macro synthetic fibers with smaller fiber diameter, improved surface texture, and geometrical modifications provides an opportunity to invoke geometrical anchorage and bond development by mechanical interactions [14]. The fibers arrest and bridge across the matrix cracks and through de-bonding and pullout [15]. This results in efficient stress transfer between the fiber and matrix, allowing formation of multiple cracks, thus producing toughening effects and improving energy dissipation capacity of the composite [16].Application areas of these composites include structural panels, impact, blast resistance, repair and retrofit, earthquake remediation, strengthening of unreinforced masonry walls, and beam-column connections are being developed [15].

Filament winding was used as a novel computer–aided composite manufacturing approach to develop unidirectional thin laminates with these continuous polypropylene fiber systems. Significant strength and toughness improvements have been reported with increasing aspect ratio of fibers, which makes continuous fiber composites ideal for materials under severe loading conditions [17]. The automated manufacturing system comprises of state-of-the-art integrated stepper motors, motion control and data acquisition

system. The technique provides desired agility, precision and quality control to develop economic and versatile composite materials. The system also allows full potential of the fibers to be utilized and reduces labor intensive manufacturing cost of manual pre-fabricated construction products [17].

In order to better understand the role of these fibers on the mechanical properties, several factors including the fiber structure, matrix formulation, hydration periods are addressed in the context of tensile stress, the spacing of cracks, and the degradation of stiffness as a function of applied strain. A series of fly ash blended cementitious matrices reinforced with continuous polypropylene fibers were developed and effect of additives such as chopped glass microfibers and sub-micron wollastonite fibers were evaluated as a hybrid matrix design. Three different volume fractions of continuous yarns were studied and performance of the yarns were quantified and compared to identify the key design parameters. Instrumented mechanical tests were performed on continuous fiber composites under uniaxial tension and four-point bending. Image analysis by means of three-dimensional digital image correlation (DIC) method was used to understand the damage mechanism by quantify the non-uniform displacement and strain distributions. Distributed cracking mechanism observed in these systems were quantified by measuring crack width and spacing and further compared to the experimental stress-strain measures.

2.1 Experimental Program

Two types of proprietary polypropylene yarns manufactured by BASF Construction Chemicals, OH, USA were investigated in the current study as shown in Figure 2-1. Master Fiber MAC 2200CB is a commercial chemically enhanced monofilament macro-synthetic polypropylene (PP) based fiber and is known for superior bond with cementitious matrices

due to its architecture (see Fig. 2-1(a)). This macro-fiber is recommended for use as secondary reinforcement in cast-in place and precast concrete, slab-on-ground, pavements, and to control shrinkage and temperature cracking [18]. MF 40 is a recent development of a PP microfiber that is fibrillated with micro-synthetic yarns comprising of 500 thin filaments of 40 microns each (see Fig. 1(b)).

(a)

(b)
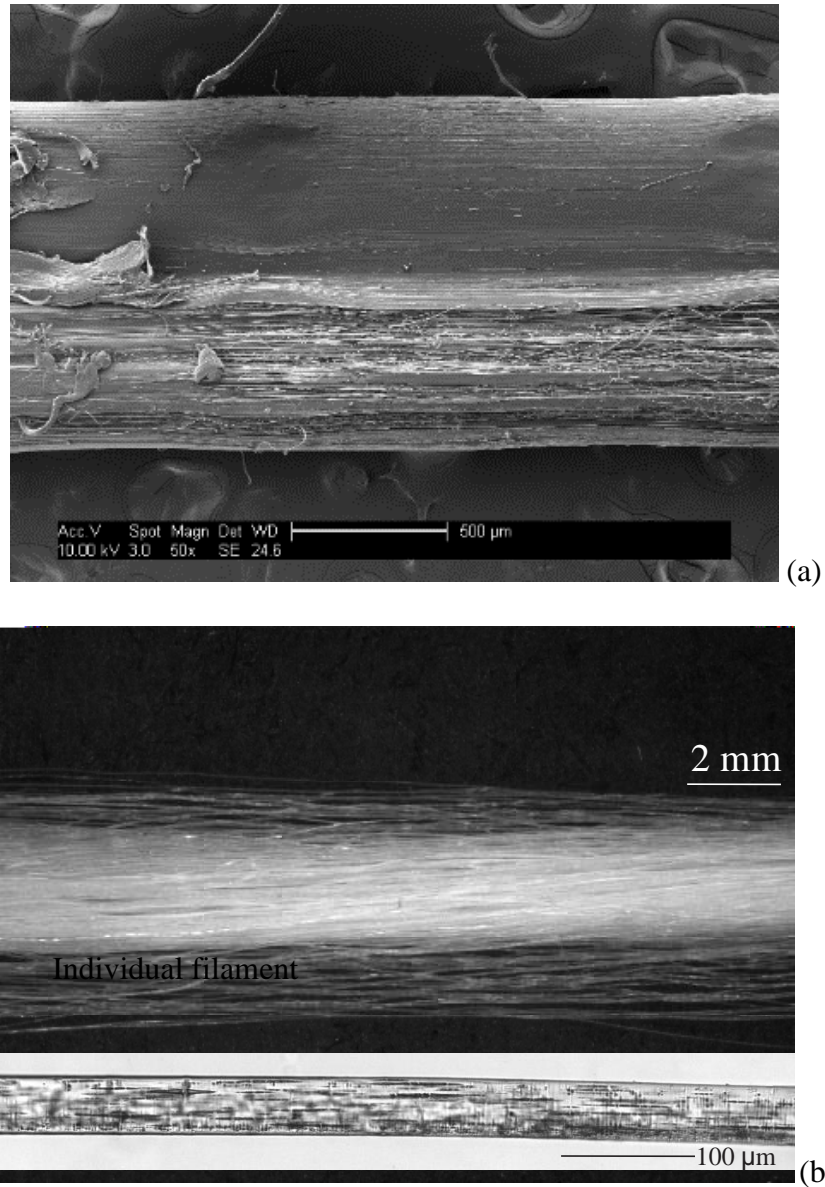
Figure 2-1: (a) Macro-synthetic MAC 2200CB fiber, (b) fibrillated microfiber MF40

15

A series of mechanical tests were performed on the individual fibers, and continuous unidirectional fiber composites (CUFC) manufactured using the filament winding technique. Uniaxial tension and flexural tests on composite sections were conducted to show the applicability of the fiber systems for a variety of civil infrastructure applications. Cement-based composite laminates with continuous fibers allow the full potential of fibers in reinforcing the brittle matrix. The manufacturing technique is fully controlled and the composite laminates can be designed for the specific service loads [17]. This promising new class of structural members utilizes a combination of ductile fiber and brittle matrix and can result in extremely large ductility and strain capacity that leads to high strength and toughness strain hardening cement composites. The testing matrix is summarized in Table 2-1. Effect of the micro-structure of the fiber, matrix modification, and fiber volume fraction were investigated.

Table 2-1: Testing matrix developed in this study

Test Type	Fiber Types		Matrix Types			
Fiber Tension	MAC 2200CB	MF 40	N/A			
Unidirectional Continuous Fiber Composite	MAC 2200 CB	MF 40	Mortar-Control	Mortar w. Wollastonite	Mortar w. Fly Ash	Mortar w. Wollastonite, Fly Ash

Note: MAC 2200 CB - Surface Modified Monofilament Macro-Fiber; MF 40 - Fibrillated Bundle Micro-Fiber; Cofisa - Low strength Monofilament Macro-Fiber; Dramix – Hooked Steel

2.2. Filament Winding Technique

A filament winding system was developed at ASU for manufacturing cementitious composites reinforced with continuous yarns. The system can be easily configured to fabricate continuous fiber composites such as unidirectional laminates, cross-ply and angle

ply laminates. Computer-aided manufacturing provides the computational and control power needed to develop economic and versatile materials, for a wide range of structural applications. The mechanical components of the system consist of the feed, guide, and the take up (mold) sections as shown in Figure 2-2.These components are discussed in detail in the subsequent sections.
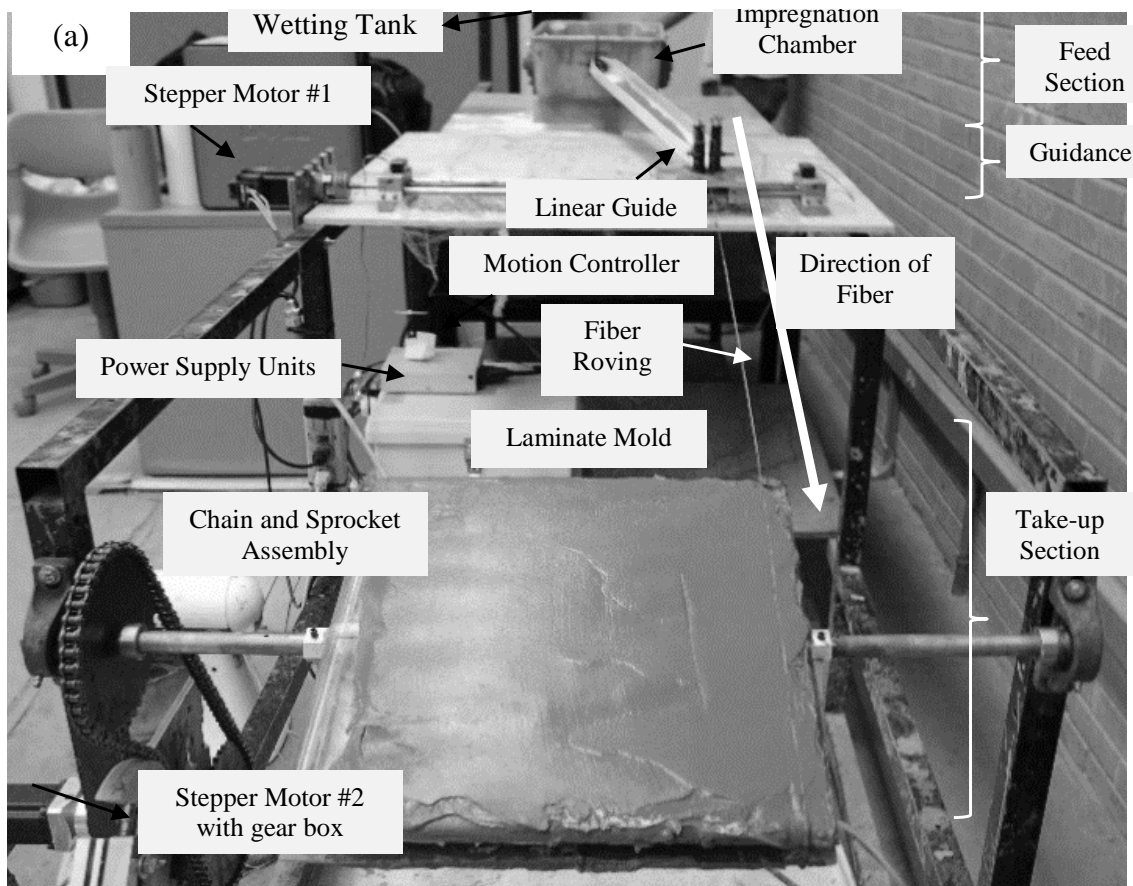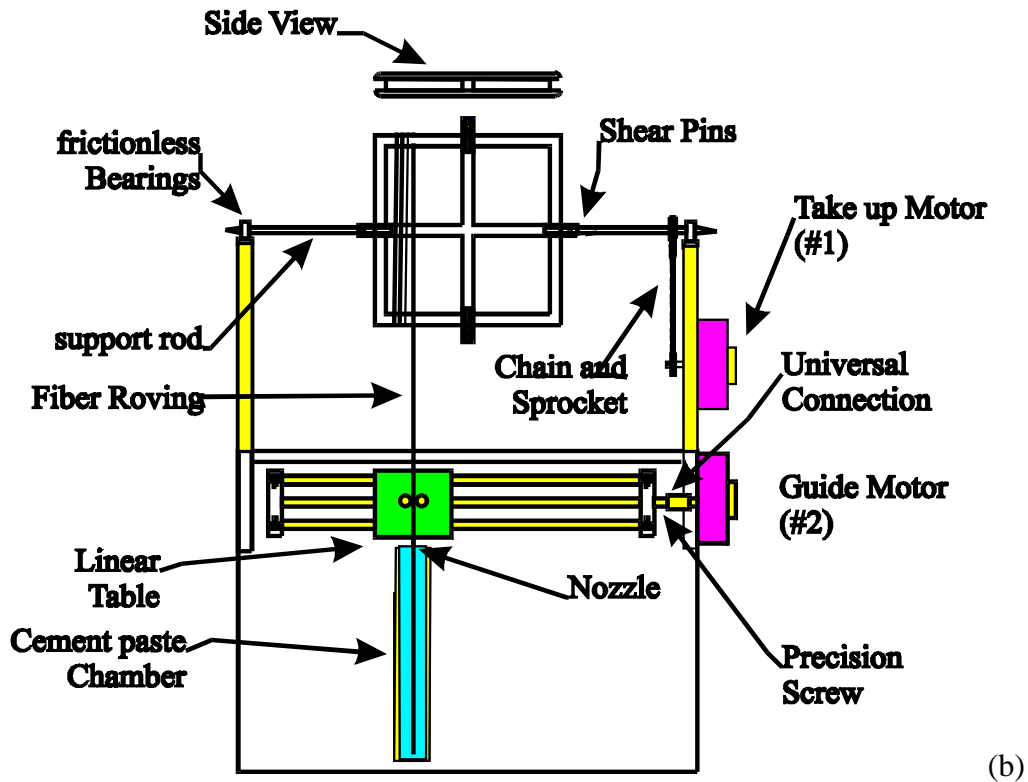
Figure 2-2: (a) Filament winding setup at ASU, (b) schematics of the take-up section [3]

The electrical and electronics components consist of two stepper motors, encoders, limit switches, and a computer system. The computer runs on a Lab View interface to monitor a closed-loop system which controls the rotation and translation of the two stepper motors. The user interface of the program is shown in Figure 2-3. Configuration of the stepper motors determine the winding, pulling, and guidance of the composites, while the take up section controls the fiber (lamina) orientation. The manufacturing system consist of three components: feed, guidance and take up sections. The feed section consists of the spool of fibers, a wetting tank, and an impregnation chamber. As the fiber section unwinds from the spool, it goes through a water tank and passes over several round steel bars. Fresh matrix is placed in the impregnation chamber which coats the fiber as the fiber is pulled from the spool towards the guidance section.
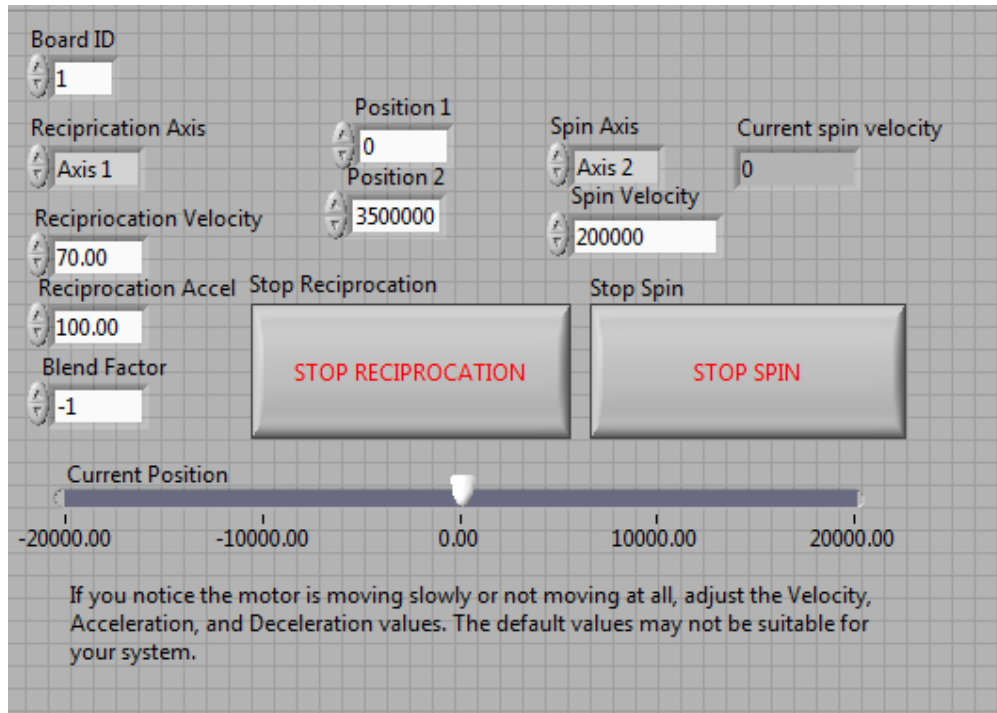
Figure 2-3: Lab view interface (VI) which runs the filament winding setup

An extensive experimental program was undertaken to evaluate the performance of unidirectional composite laminates with the mono filament MAC 2200CB and multi filament MF-40 fibers at three different volume fractions ranging from 1-4%, and four different matrix compositions. The aging effect of these composites was studied for select specimens at 7 and 28 day curing periods. A total of ten different mixes developed in this study are summarized in Table 2-2. Direct tension tests and four point bending tests (marked with asterix) were performed on at least four replicate samples were tested for each mix design. Specimen groups marked with a plus sign (+) were tested also tested after 7 days of curing.

Table 2-2: Groups of specimens with continuous fibers developed in the study

Group ID	Yarn Type	Yarn V_f%	Matrix Composition
I, II*, III	MAC 2200CB	1.0, 2.5, 4.0	Control Mortar
IV+, V*+, VI	MF 40	1.0, 2.5, 4.0	Control Mortar
VII	MAC 2200CB	2.5	Hybrid Mortar 1 (HM 1): AR Glass
VIII*	MAC 2200CB	2.5	HM 2: Wollastonite
IX*, X*	MAC 2200CB, MF 40	2.5	HM3: Wollastonite + AR Glass

A control mortar mix design was adopted with fly ash partial substitution of 15% of cement, sand/cement ratio of 0.45, and a water/binder ratio of 0.35. Hybrid blended mixes, HM:1-3 with wollastonite fibers (NYAD-G) at 5% dosage by weight which is added as a substitution of 10% of cement content in the mix, and alkali-resistant glass (ARG) micro-fibers at 1.5% by volume were also developed. Mix design of hybrid mix, HM-3 is shown in Table 2-3.

Table 2-3: Mix design used for hybrid mix 3 with MAC 2200 CB continuous fibers and glass micro-fibers and wollastonite sub-micro fibers.

Material	Weight Fraction (%)
Portland Cement (Type III/IV), C	45%
Fly Ash (Class F), FA	7%
Fine Silica Sand, S	23%
Water, W	18%
Wollastonite (NYAD-G), Wol.	4.5%
Glass Microfibers (Nippon), ARG	2.2%
HRWR (BASF Melflux)	0.03%

2.2. Testing Procedure

2.2.1. Tensile Properties of Polypropylene Fibers

Direct tension tests were performed on these fibers in Structural and Materials Testing Laboratory in Arizona State University. Displacement controlled tests (0.4-2.5 mm/min) were performed on a minimum of 10 replicate fiber coupons at a gage length of 25 mm, using a setup as shown in Figure 2-4(a), and stress-strain response measured from these tests are summarized in Figure 2-4(b).

The effective yarn diameter of MAC 2200CB and MF 40 was considered to be 0.82 and 0.89 mm, respectively. A 1300 N (300 lb) interface load cell was used to measure the load capacity of the yarns. The strain measures reported here are recorded from the stroke of the servo-hydraulic actuator. Tensile strength, elastic modulus, and total toughness of MAC 2200CB were found to be 311 (+/-38), 4499 (+/-351), and 34 (+/-12) MPa, respectively. Tensile strength, elastic modulus, and total toughness of MF 40 were found to be 492 (+/-65), 1601 (+/-117), and 5058 (+/-1748) MPa, respectively Thus the macro-synthetic fiber, MAC 2200CB has comparatively higher elastic modulus by almost a factor of 3. However the tensile capacity of MF 40 is about 60 % greater than MAC 2200 CB. The main difference however lies in the strain capacity of the microfibers as toughness of MF 40 is greater than MAC 2200 CB by almost a factor of 150.
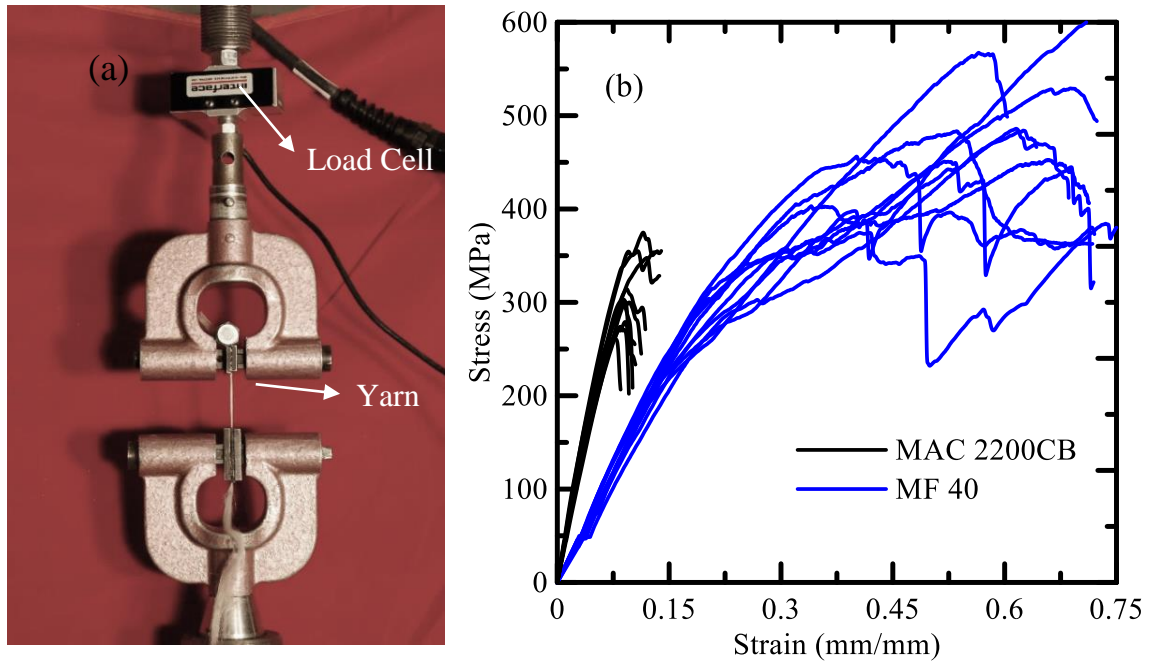
Figure 2-4: (a) Setup used to perform tension tests on yarns, (b) measured stress-strain

response

2.2.2. Characterization of Fiber-Matrix Interface

The bond that develops at the fiber-matrix interface plays an important role in controlling

the mechanical performance of fiber reinforced composites. Bond characteristics of fiber-

cement systems using analytical and experimental techniques have shown to be the most

significant parameter that characterizes the interface parameters and also the toughening

mechanisms [19,20]. Mechanical properties of interface influence the strength, toughness,

and durability of the composite. The fibers bridge across the matrix cracks and through

debonding and pullout, lead to toughening and energy dissipation. The bond of round

monofilament macro-synthetic fibers in cement is limited and results in a major drawback

to their application in concrete materials. The use of macro synthetic fibers with smaller

fiber diameter, improved surface texture, and geometrical modifications provides an

opportunity to invoke geometrical interlock and improve the bond by mechanical

22

interaction. Pullout tests conducted by fiber debonding under slip controlled closed-loop tests have been developed earlier by Sueki et. al and Silva et. al. [21,22]. These tests were adopted in this study to understand the fiber pull-out behavior of several fiber systems under different sample preparation conditions such as length, curing and matrix formulation. Results were used to determine the interfacial shear bonding. In addition to the macro-synthetic fiber, pullout characteristics of hooked Dramix steel fibers were also investigated.

The cementitious matrix was produced using a bench-mounted mechanical mixer of 5 L capacity, water-binder ratio of 0.4. Control paste and mortar matrices were developed along with blended mixes various cement substitutes. Cement-to-sand ratio of 1:1 was used in the mortar mixes. Standard laboratory mixing procedure was followed wherein dry ingredients were first mixed for 1 minute, followed by addition of water and mixed for total of 5 minutes, or until desired consistency is achieved. The matrix is then poured inside the PVC mold was achieved using medical syringes as shown in Figure 2-5a. Fly ash and wollastonite were added up to 15 % substitution of the cement content. Wollastonite sub-micron fibers manufactured by NYCO Minerals and fly ash (class F) were also used to refine the paste and mortar matrices. The PVC mold had a nominal diameter of 12 mm and was 50 mm long. Accuracy of fiber alignment was ensured by using special wooden base plates with small holes drilled at the center, and using straws for alignment of the embedded length. Schematics of the layout of the fiber in the setup are shown in Figure 2-5(b). Each capsule was filled in two layers, and each layer was manually compacted using trowel along the periphery roughly six times. Upon completion of casting, the specimens were

covered with polyethylene sheets for 24 hours at ambient temperature, and then in the

curing chamber at 73 F and 95 % RH until the day of testing
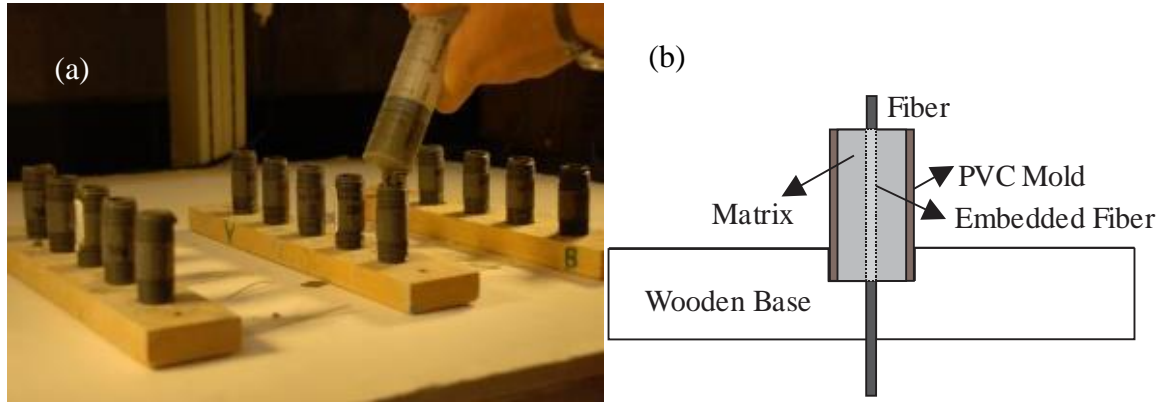
Figure 2-5: (a) Molds for casting pullout specimen, (b) schematic drawing of the fiber

pullout

Displacement controlled tension tests were performed on the pullout specimens at loading

rate of 0.4 mm/min. The experimental parameters included length of embedded fiber inside

matrix, fiber types, and matrix constituents. A load cell with capacity of 1300 N (300 lbf)

was used to measure the load. The test setup is shown in Figure 2-6(a). Figure 2-6(b) shows

the typical load-slip response of replicate MAC 2200CB fiber coupons at embedment

length of 20 mm.
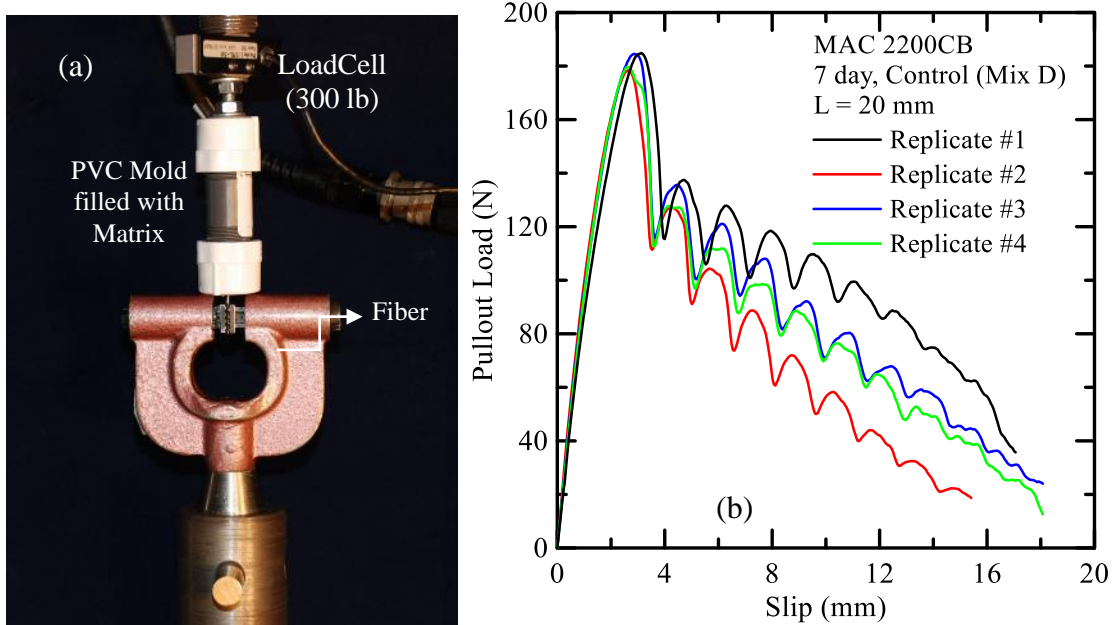
Figure 2-6: (a) Fiber pullout test setup (b) pullout of MAC 2200 CB from control matrix

2.2.3. Tension tests on laminated composites

The test setup used to conduct tension tests on test coupons with nominal dimension of 300x62x13 mm is shown in Figure 2-7(a). Hydraulic grips are used to hold the specimen which is contained within a rectangular metal fixture. Two LVDTs are mounted on the specimen to measure the elongation of the specimen under load. The tension test is conducted using a closed loop servo-hydraulic testing frame operated under stroke control, while the applied stress and specimen elongation is recorded throughout the test. The experimental data is analyzed using a MATLAB program for data reduction, smoothening and calculation of important test parameters.

Schematics of a typical stress strain response is shown in Figure 2-7(b). The elastic region is evident till the first crack point and is used to estimate the elastic modulus of the material. Two points of BOP- and BOP+ are identified representing the start and completion of the first crack across the entire thickness. After the first main crack occurs, and in the second

25

zone, strain hardening behavior is dominant as a series of parallel cracks appear along the gage length of the specimen. The spacing and width of these cracks in this stage depend mainly on the fiber type and volume fraction. The third zone is characterized by the ultimate tensile strength (UTS) and specimen failure. Shaded regions in the curve represent the strain limits at which specific toughness measures are reported. Replicates of continuous fiber composites with MAC 2200CB fibers at dosage of 4% is shown in Figure 2-7(c). As evident the tensile response is very much reproducible in between different replicates.

(a)

(b)

26
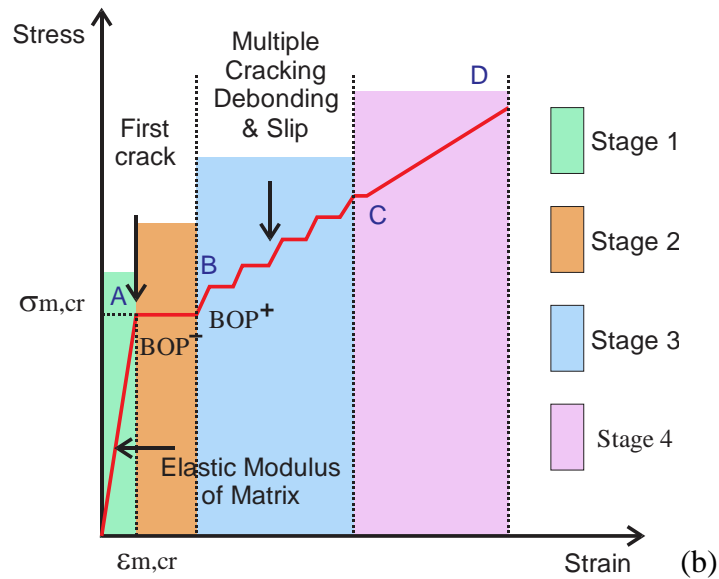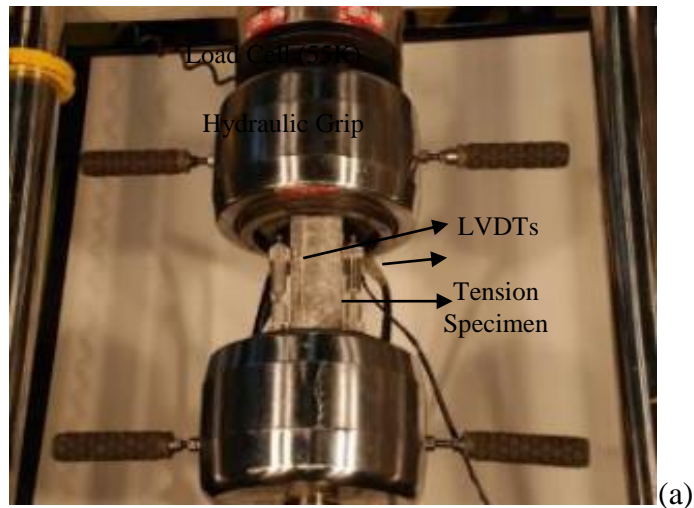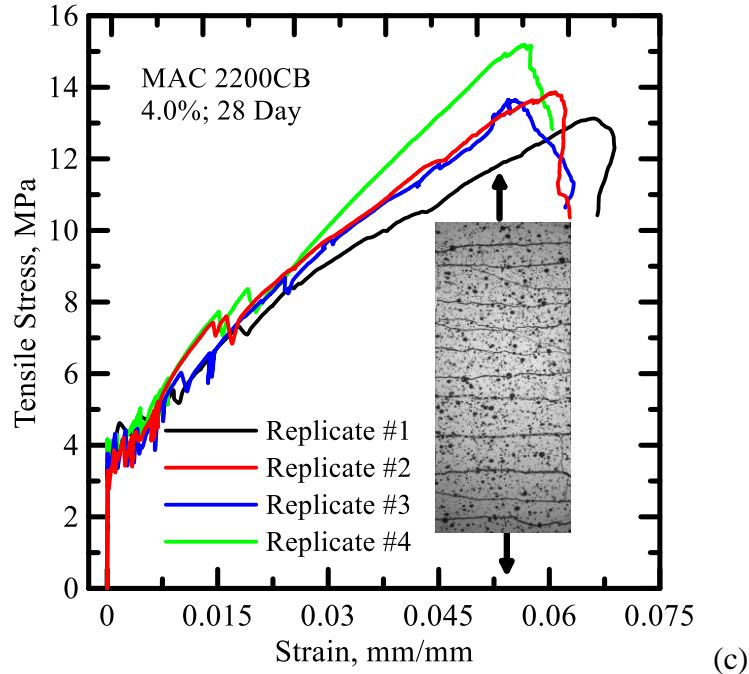
Figure 2-7: (a) Tensile testing setup, (b) typical stress-strain response and damage zones

[23], (c) replicates of continuous fiber cement composites with MAC2200CB fibers

2.2.3. Flexural tests on laminated composites

Four-point bending tests were performed on flexural specimens using a closed-loop servo-controlled testing system,. The experimental setup is shown in Figure 2-8(a). Two clamps for a flexural jig will be attached on the sample at the support locations and a rod connects these points. The rod holds 2 LVDTs used to measure the deflection at the center point of the specimen. The response of the LVDT is used for the measurement of the stiffness of the sample, and deflection at first cracking point. The response of the stroke signal is used to calculate total energy absorption (toughness) and ultimate capacity of the sample under the load. Typical load-deflection response of MAC 2200CB continuous fiber reinforced composites at fiber volume fraction of 2.5% is shown in Figure 2-8(b). The initial elastic domain is evident up to the point of first crack which is also referred as limit of proportionality. Subsequently distributed flexural cracks appear on the tension side of the

27

specimen under the applied loading. The peak loading point is called the Modulus of Rupture (MOR) and is referred as the flexural strength of the composite. As evident these tests are very reproducible.
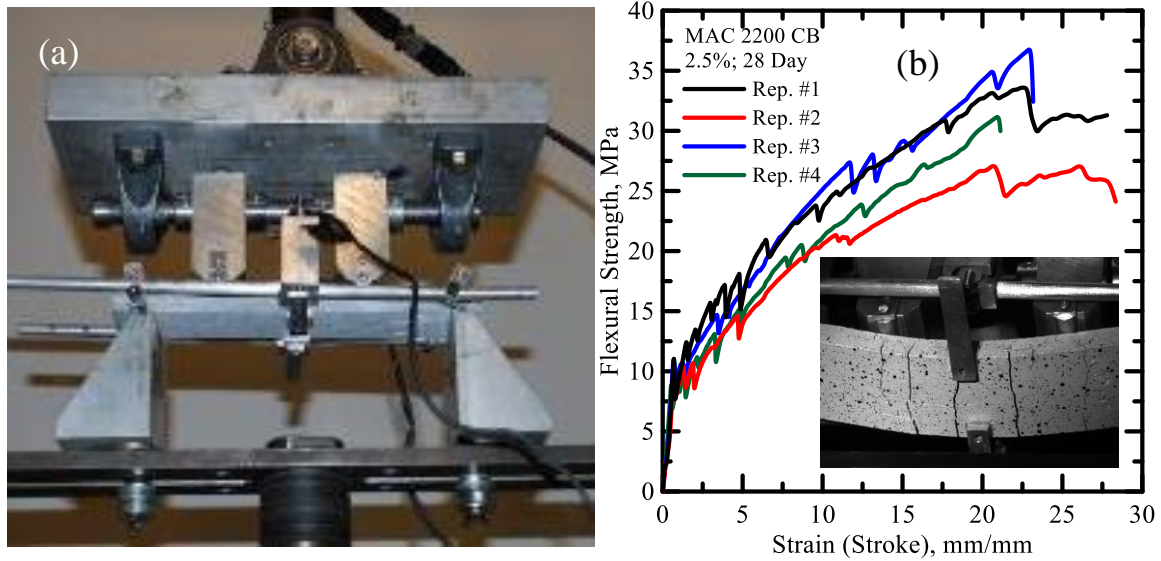
Figure 2-8: (a) Flexural testing setup, (b) typical load deflection response

2.2.4. Digital Image Correlation

Digital Image Correlation (DIC), is a non-contacting optical full field deformation measurement approach that can better address the complex behavior of this class of materials. DIC technique was developed by Sutton et al. [24] and Bruck et al. [25] and has been widely applied for composites, and reinforced concrete sections [26,27,28]. The technique can also be used for automated determination of crack density, crack spacing, and damage evolution. Initially an area of interest (AOI) is manually specified and further divided into an evenly spaced virtual grid as shown in Figure 2-9(a). The displacements are computed at each point of the virtual grids to obtain full-field deformation. Figure 2-9(b) shows the contour of longitudinal displacement of continuous MAC 2200CB (2.5%) fiber reinforced specimen. The sequential formation of seven individual cracks is indicated

in the figure. The distribution of the longitudinal displacement field is shown in Figure 2-9(c) for various stress levels with the cracks identified as the discontinuities in the displacement response. The location and width (w) of a certain crack is represented by the x-coordinate and the vertical amplitude of the discontinuity. Whereas the horizontal distance between the centers of consecutive cracks are used to measure the crack spacing. Figure 2-10(a) shows the time history of the damage evolution, tensile strength obtained from the experiments and the mean crack width versus time up to failure. Depending on the location of the cracks along the gage length, the width of the different cracks vary considerably. Hence the mean crack width are estimated and used to correlate with the experimental stress responses of different samples. The experimental strain response can also be correlated with the evolution of crack spacing as shown in Figure 2-10(b). Since the onset of first crack, a general decrease in crack spacing is observed until they reach a steady state defined as saturation crack spacing. Beyond this stage additional strain results in widening of the existing cracks, and no new crack are formed [14].
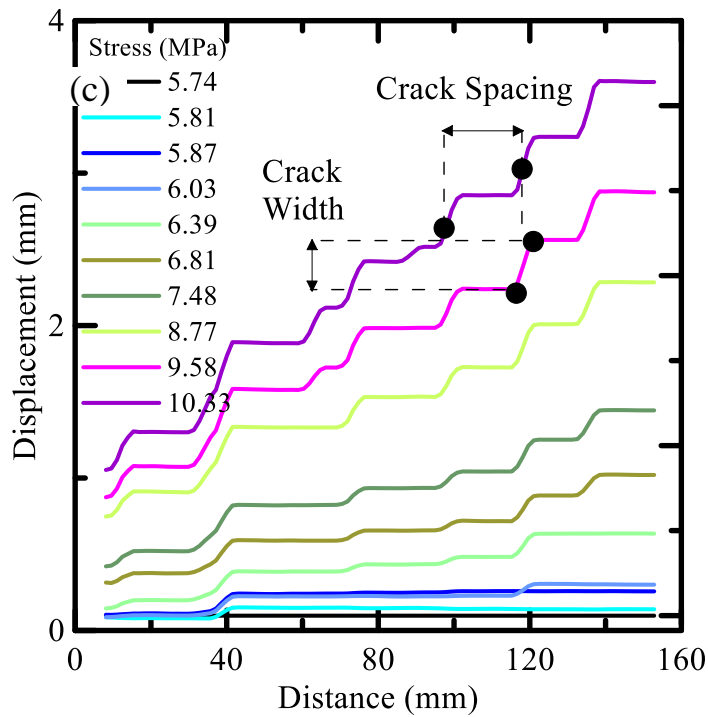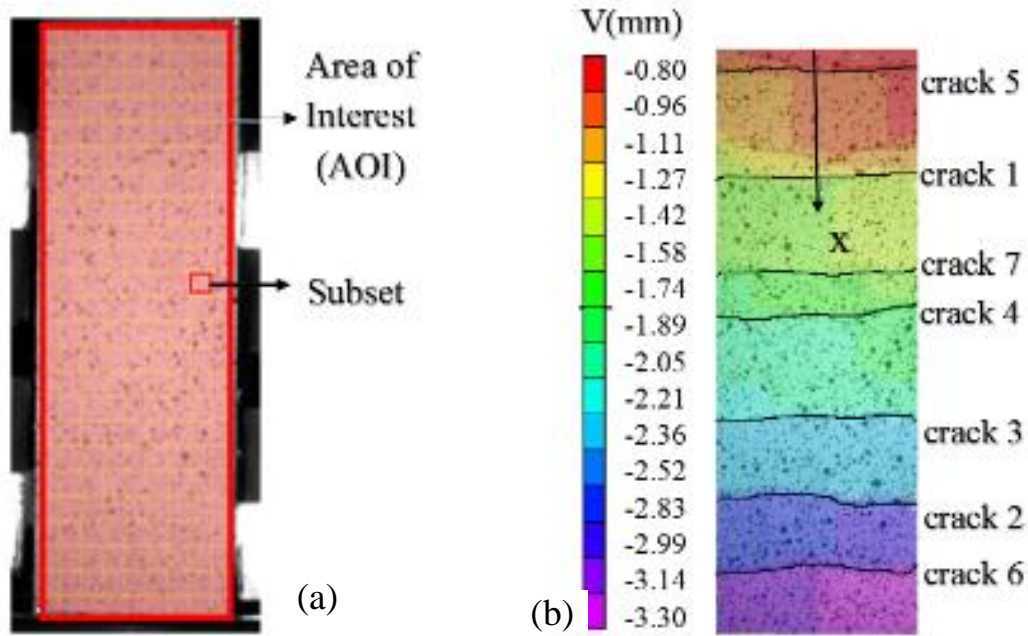
Figure 2-9: (a) Area of interest (AOI) and subset in reference image; (b) displacement contour along the gage length of the tension coupon; (c) displacement distribution across different cracks
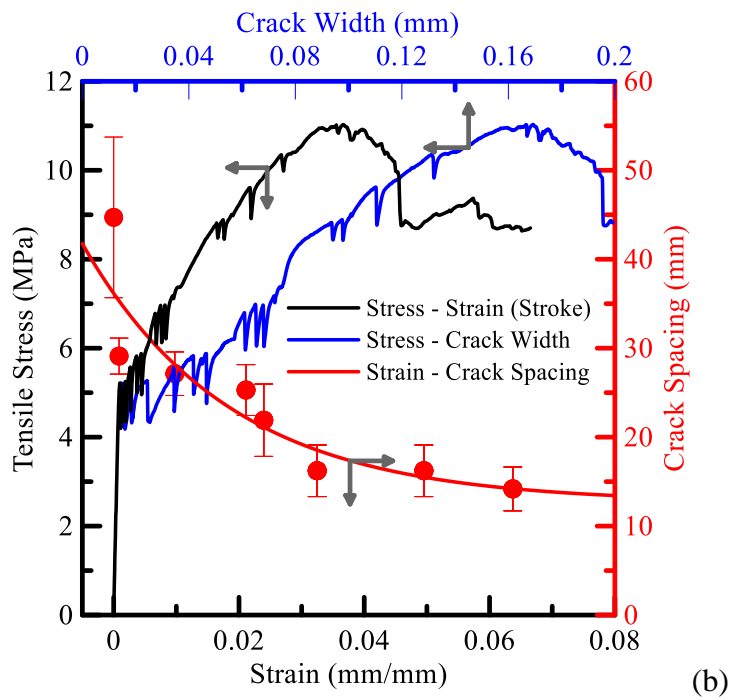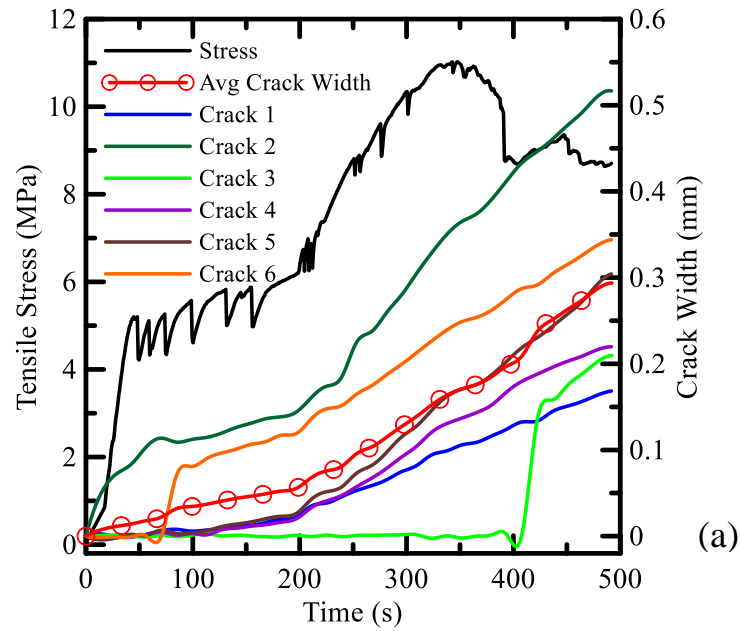
Figure 2-10: (a) Time history of stress and crack width development, (b) tensile stress-strain, crack width and crack spacing response of MAC 2200 CB reinforced specimen at vol. fraction. of 4%

Displacement measure using the DIC technique was compared to the response obtained from the LVDTs mounted directly on the specimen. It is to be noted two LVDT with deformation measurement capacity of up to 8 mm were mounted on the specimen at the middle of the gage length. An average response is reported here in Figure 2-11. Longitudinal deformation of the specimen was also measured using DIC and reported at three different locations, near the top grip (A), middle section (B), and bottom grip (C). As evident the deformation measured using DIC near the middle section of the specimen i.e. point B matches very well the experimental deformation measure using LVDT. It could also be commented that the particular specimen deformed more near the bottom grip, resulting greater deformation at that location.
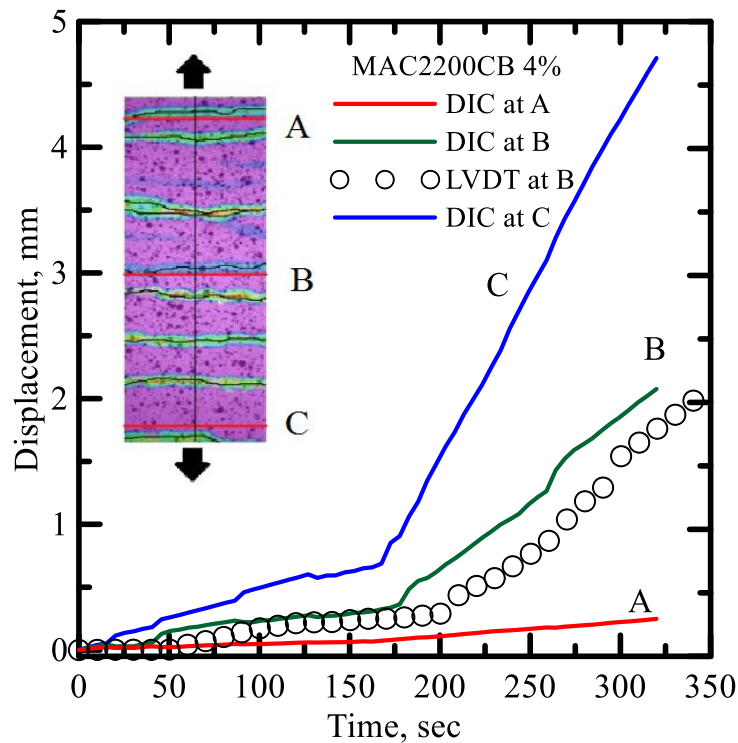
Figure 2-11: Comparsion between displacement measured from LVDT and DIC with time.

Evolution of distributed cracking mechanism and local strain fields can be easily documented as shown in Figure 2-12. As evident the strain contours could also be reported in 3-D, and the post-processing of distribution of damage parameters could be performed in 3-D too. However this step requires extensive computational efforts, and has been excluded in the current approach.
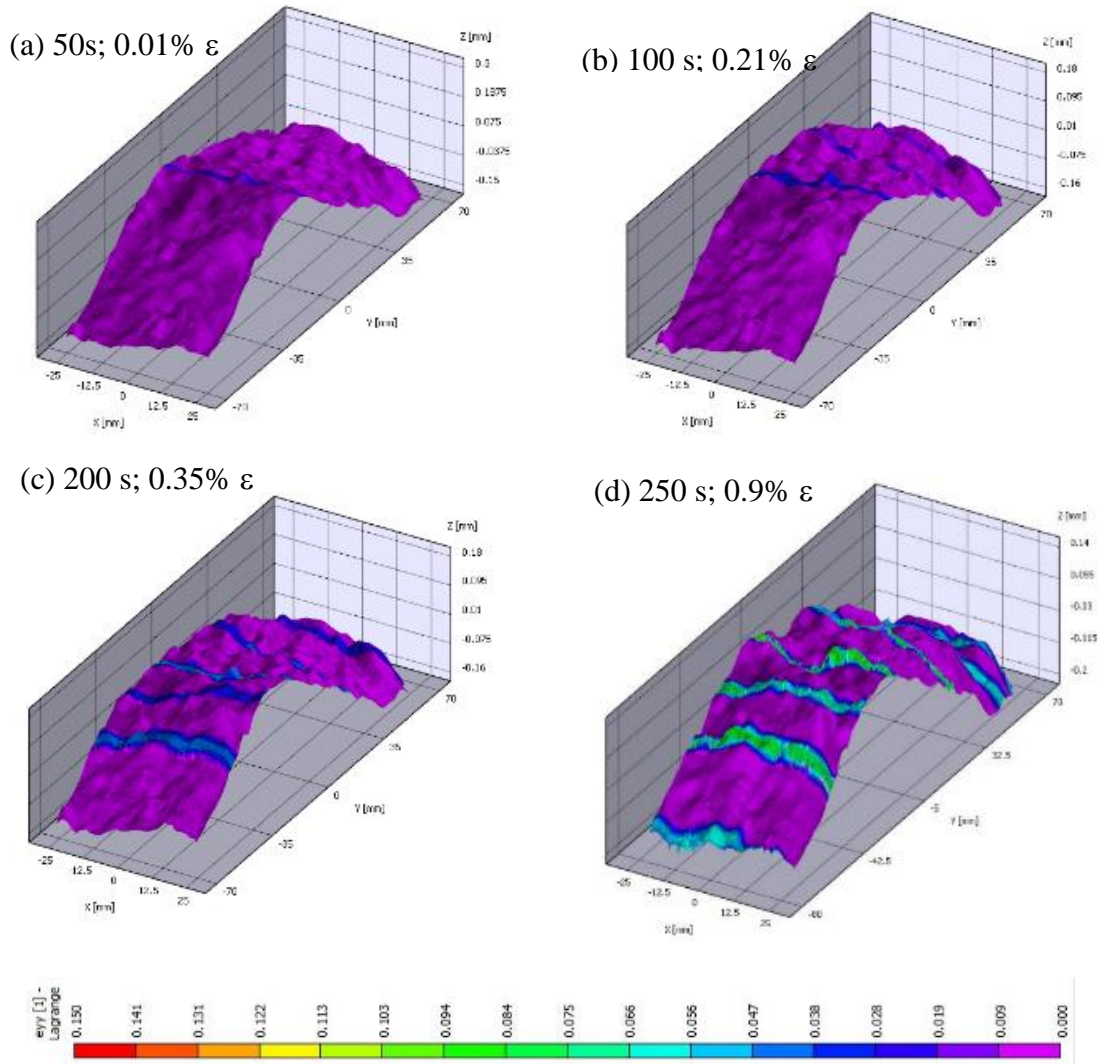
Figure 2-12: 3D strain field of filament wound composite with MAC 2200CB at 4% dosage in tension

2.3. Results and Discussions

2.3.1. Single fiber pullout tests

Figure 2-13(a-b) shows the load-slip response of representative specimens of commercial macro-synthetic polypropylene fiber MAC 2200CB manufactured by BASF Construction Chemicals and Dramix hooked steel fibers manufactured by Bekaert, at different embedment length of 12-25 mm [29, 30]. Effect of embedment length is more prominent for MAC 2200CB fibers, compared to the hooked steel fibers. The work was also extended to study the fiber-matrix interaction with low strength synthetic polypropylene fibers made in Mexico referred to as Cofisa [31], and multifilament polypropylene microfiber MF40 fibers manufactured by BASF Construction Chemicals.
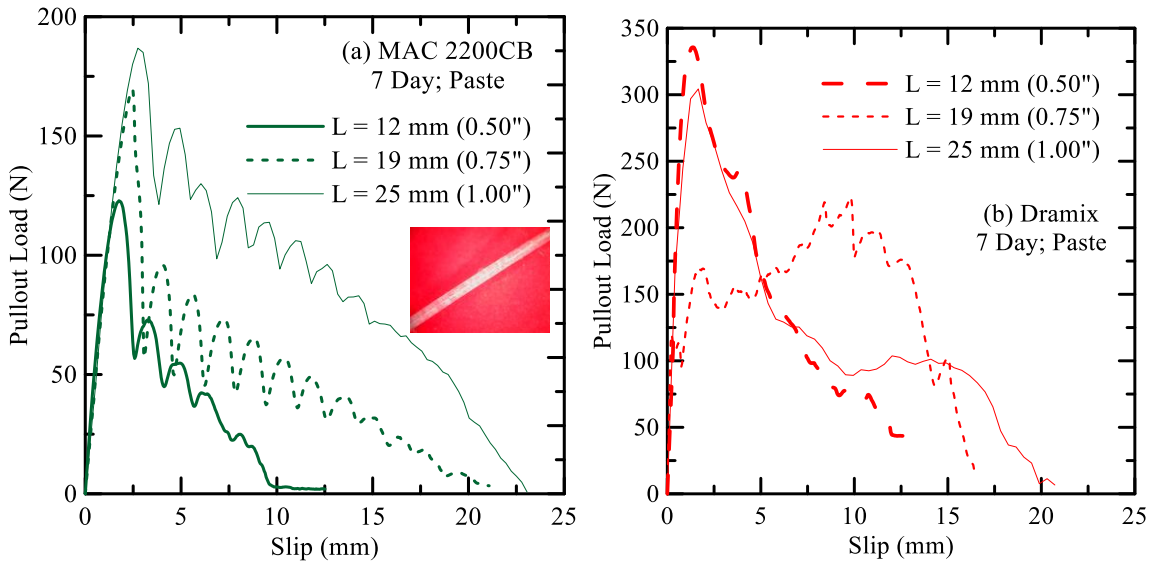
Figure 2-13: (a) Setup used for pullout tests, (b) pullout of MAC 2200 CB from control paste matrix at different embedded lengths

It is clear that the maximum load and energy required to separate the fiber from the matrix phase is highest at embedment length of 25 mm. The pullout results are also summarized

in Figure 2-14, where in the pullout force and pullout energy is presented for different fibers at different embedment length. As evident amongst the 3 different fiber types, reported here the fiber pullout strength is maximum for Dramix steel fibers, followed by MAC 2200CB and Cofisa fibers. The pullout force and energy increases considerably with increasing embedment length, especially for the polypropylene fiber types.
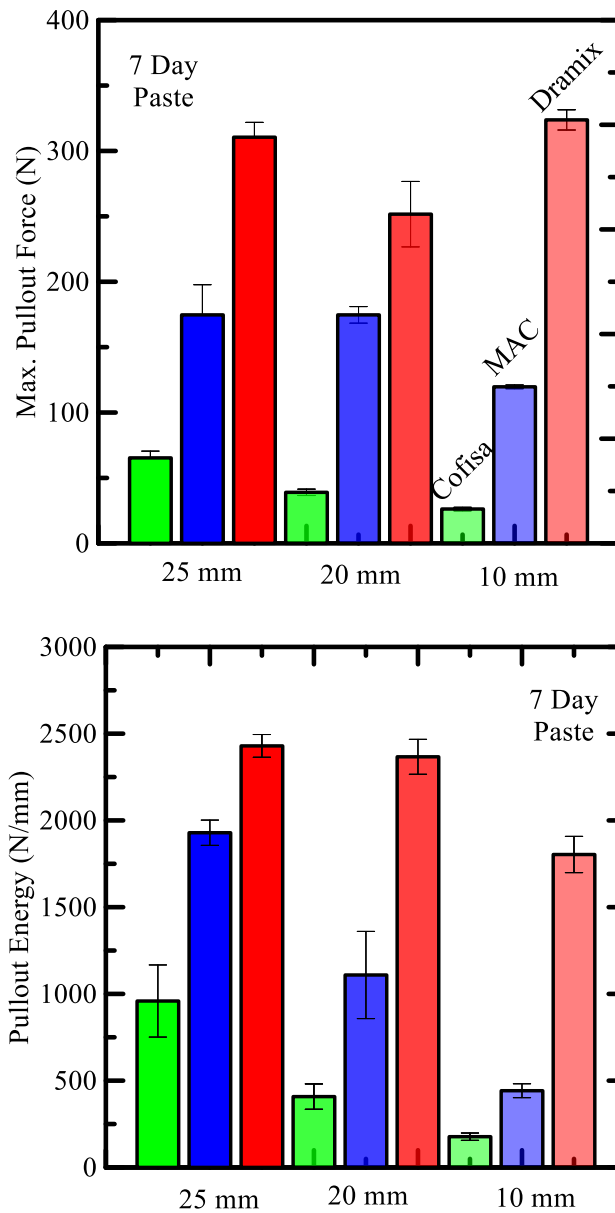
Figure 2-14: Summary of fiber pullout tests at different embedment lengths

Figure 2-15(a) is a summary of the compressive strength of the different matrices considered in the pullout study. Compressive strength tests were performed on each mix design at 7 day strength using 50 mm cubes based on ASTM C109 and reported here. Base mortar matrix as expected has the maximum compressive strength, which almost 15% higher than control paste matrix. Wollastonite blended mix has about 8 % higher strength compared to the control mix. Flyash blended mixes– D and F however showed comparatively lower strength, possibly due to the high cement replacement ratios. Figure2-15(b) repots the tensile strength of different fibers tested in the current study. As expect, the tensile strength of steel fibers obtained from the literature [30], is the highest followed by MAC 220CB, MF40 and Cofisa fibers.

36
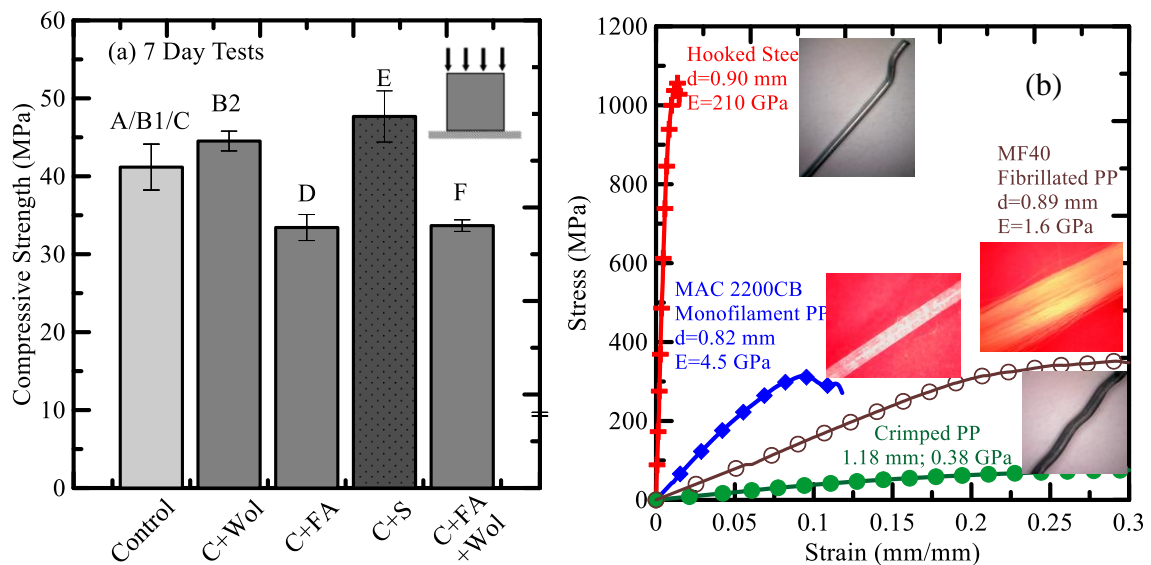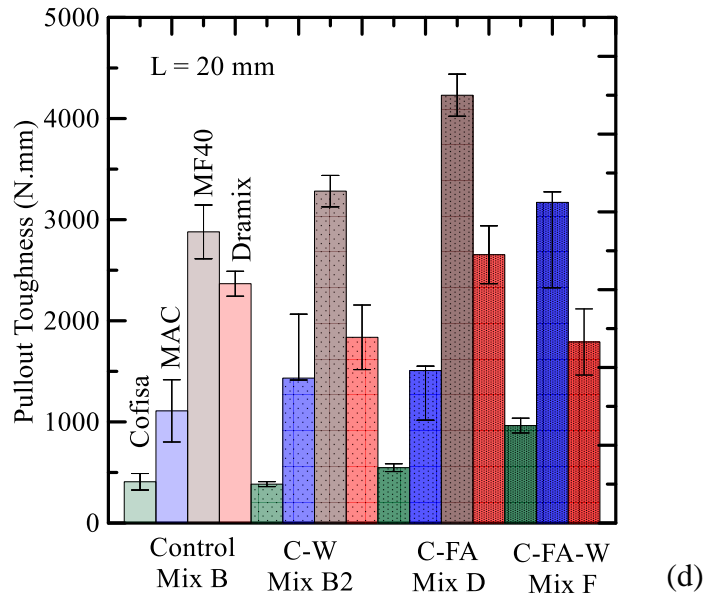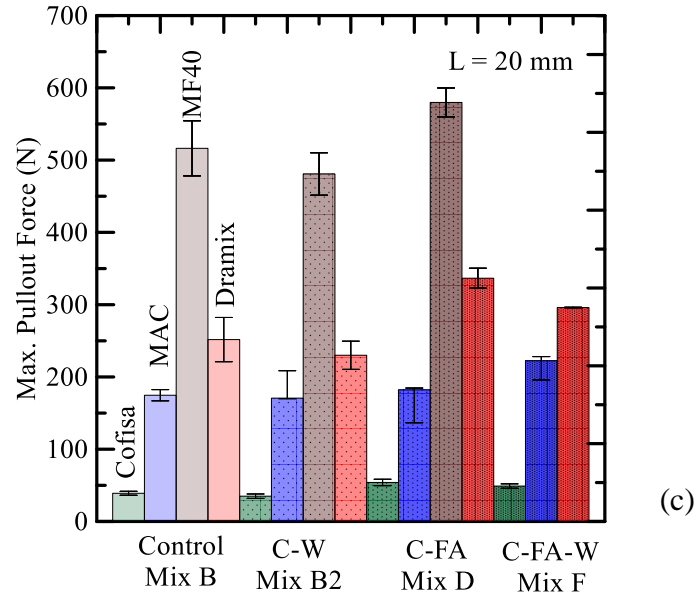
Figure 2-15: (a) Summary of compressive strength of different matrices, (b) summary of tensile response of different fibers studied, (c) and (d) summary of pullout behavior.

Figure 2-15(c-d) presets the effect of matrix composition on the pullout resistance on all the fibers studied in this chapter. Addition of fly ash and wollastonite as partial cement substitutes improves the fiber-matrix interface strength. Matrix with 15% fly ash (D) gives the maximum bond strength, followed by matrix with 15% wollastonite (B2). Mix F with

30 % replacement of cement with fly ash and wollastonite also shows superior bonding with both the fiber types, when compared to the control matrix (B1).

Energy required to pull out the embedded length of the fiber from the matrix is measured from the area enclosed in the load-slip response and can also be used as a measure to characterize fiber-matrix interaction. As shown in Figures 2-15(c) and (d), most blended mixes show superior pullout energy response compared to the control mixes, signifying the densification effect of the matrix due to the smaller sized fly ash and wollastonite particles. The analyzed results from the pullout tests are summarized in Table 2-4.

Amongst the fiber types, clearly multi-filament micro-fiber bundle MF 40 has the best pullout strength and toughness amongst all the fiber types. In fact, MF 40 shows superior performance with all matrices than steel fiber in terms of maximum pullout force by over 100%, and toughness by about 80%. This is really exciting in terms of replacing high cost steel fibers with comparatively cheaper synthetic fibers in discrete and continuous fiber reinforced concrete. The fibrillated structure of micro-fiber bundle MF 40, allows for enhanced penetration of cement paste thus improving the fiber-matrix bond. This clearly has a positive effect in terms of fiber pullout and overall composite behavior (discussed earlier), as opposed to mono-filament individual macro- fiber systems.

2.3.2. Continuous polypropylene fiber cement-mortar composites

The results from the instrumented tensile and flexure tests on the two polypropylene based continuous fiber structures: MF 40 and MAC 2200 CB is shown in Figure 2-16. MF 40 as discussed earlier has fibrillated fiber structure resulting in enhanced bonding with the cementitious matrix. The abundant open spaces in the multiple filaments of MF 40 fibers allow for easier penetration of the cementitious matrix inside the fiber structure, resulting

38

in superior mechanical performance. This results in tensile strength over 10 MPa, and flexural strength of as much as 40 MPa for laminated composites with continuous MF 40 fibers. MAC 2200 CB being a mono-filament macro-fiber however provides limited improvement in the performance of the composite, despite its engineered structure. Tensile strength of about 8 MPa and flexural strength of about 35 MPa is evident in composites with MAC 2200 CB fibers. The flexural and tensile responses of the MAC 2200 CB composites versus those with MF40 are shown below in Figure 2-16. As shown the tensile and flexural response are nearly identical for each composite type while those with MF40 were nearly 3 times stronger than the MAC 2200 CB composites.

\
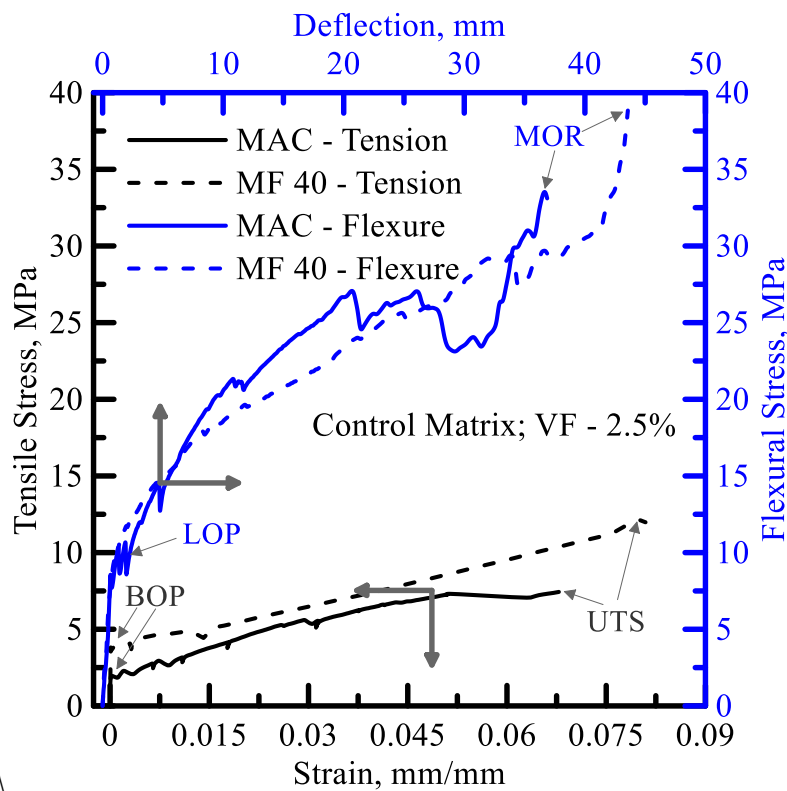
Figure 2-16: Tensile and flexural response of composites with MF40 fiber versus those with MAC2200CB fiber

39

Effect of curing age on tensile properties was studied on composite laminates with MF-40 continuous fibers. Multiple tension coupons were tested after 7 and 28 days of moist curing at 73 F, 90% RH. The tensile stress-strain curves from these tests are shown in Figure 2-17. In these curves, two different volume fractions of 1 and 2.5% are shown. As evident, the first cracking strength and ultimate tensile strength (UTS) increase by about 20% and 30% respectively. Composite toughness however increased considerably by as much as 75% with increase in age of the specimens. This is particularly true for higher volume fraction of 2.5%.
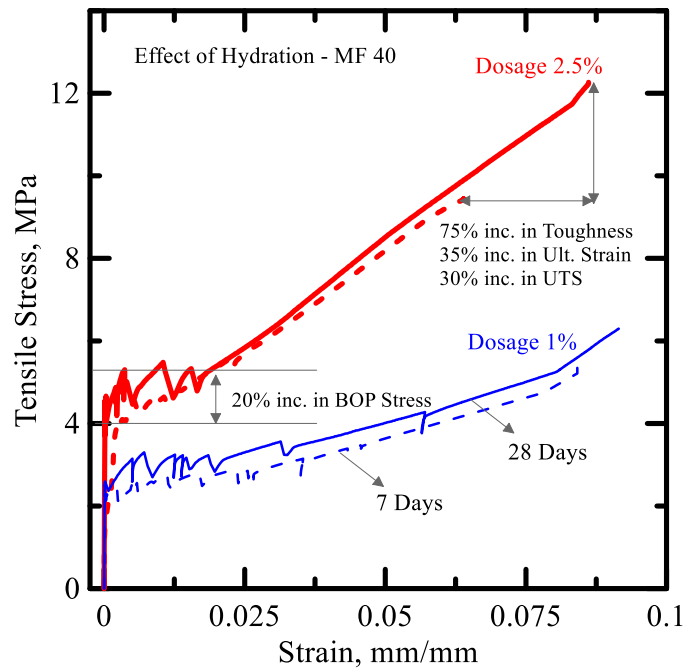
Figure 2-17: Tensile stress-strain response of continuous fiber composites with MF-40

Three levels of fiber volume fractions of 1, 2.5 and 4% were considered in this study. The stress- strain response of these composites at different volume fractions are summarized in Figure 2-18(a). In composites with MAC 2200CB continuous fibers, marginal

40

improvement in strength and toughness can be seen with increase in volume fraction from 1-2.5%. However the ultimate tensile strength (UTS) and toughness measured from the area enclosed within the stress-strain curve increases by a factor of 2 at 4% dosage. Effect of increasing dosage on tensile properties is distinctly evident for MF40 fibers as the UTS and toughness increases by a factor of 4 as the dosages increases from 1-4%.
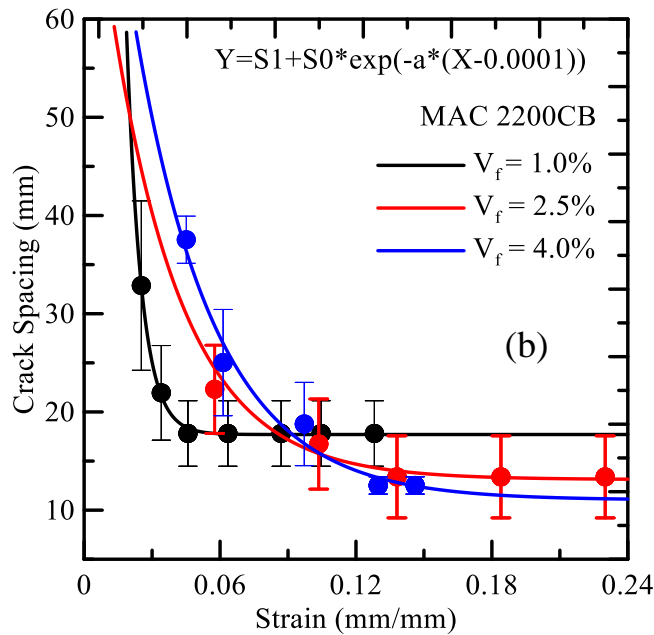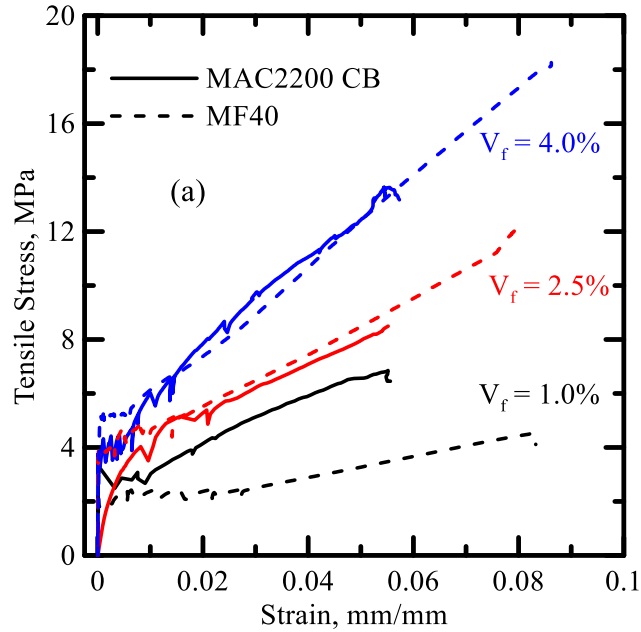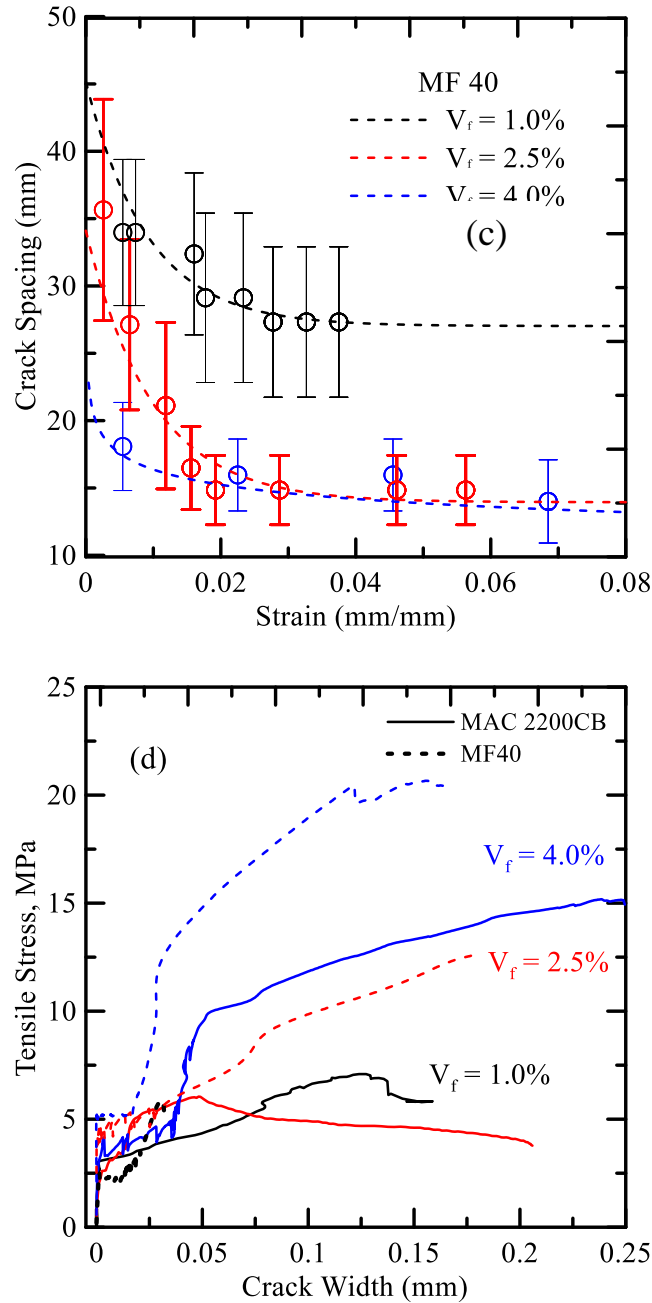
Figure 2-18: Effect of fiber volume fraction on the tensile response of continuous fiber composites with: (a) stress-strain response, (b) strain-crack spacing, and (c) stress-crack width.

Strain-crack spacing response is summarized in Figure 2-18(b, c). A damage function is fitted to the average response of these curves. The intensity of crack growth and extent of

cracking increases significantly at higher dosages. As evident the saturation crack spacing reduces from about 20 to 10 mm, as the fiber dosage increases from 1-4% for MAC 2200CB composite, whereas saturation crack spacing reduces from 30 to 15 mm. This suggests formation of fewer cracks, and more influence of crack widening mechanisms at lower fiber dosages. The MF40 fibrillated fibers owing to their open structure, produces better bond with the cement matrix, as the matrix can easily enter inside the loosely packed fibrillated fiber bundle of MF40. This is evident from the larger extent of cracking in the strain-crack spacing response in Figure 2-18(c). Stress-crack width response is shown in Figure 2-18(d). The linear elastic stage (no crack formed) is represented by an almost vertical line and extends to the bend over point as the first cracking strength, approximately from 2.5 to 5.0 MPa depending on the fiber dosage. For a given fiber dosage, MF40 composites exhibit smaller crack widths at a constant stress magnitude. This follows the trends from the crack-spacing plots as the MF40 composites tend to develop significant multiple cracking at higher strain levels. Pronounced strain hardening effect is observed after cracking as the tensile stresses increased with a reduced stiffness.

In order to summarize the effect of the two fiber types at different volume fraction, select testing properties were plotted as a function of these experimental variables, as shown in Figure 2-19 (a-c). In general, all tensile properties related to strength and toughness increased considerably with increase in dosage of fibers from 1-4%. Upon comparing the two fiber types, MF 40 especially at higher dosage of 2.5 and 4% exhibited a higher first crack strength, ultimate strength, toughness by as much as 65%, 30%, and 80% respectively when compared to MAC 2200CB. At low dosage of 1%, the performance of the macro-fiber MAC 2200 CB is slightly better than MF 40. It can be speculated that the fibrillated

multifilament structure of MF 40 fibers allow plenty of open space for easier matrix penetration between the filaments. This allows for better fiber-matrix interfacial bonding, when compared to the monofilament MAC 2200CB fibers.

44
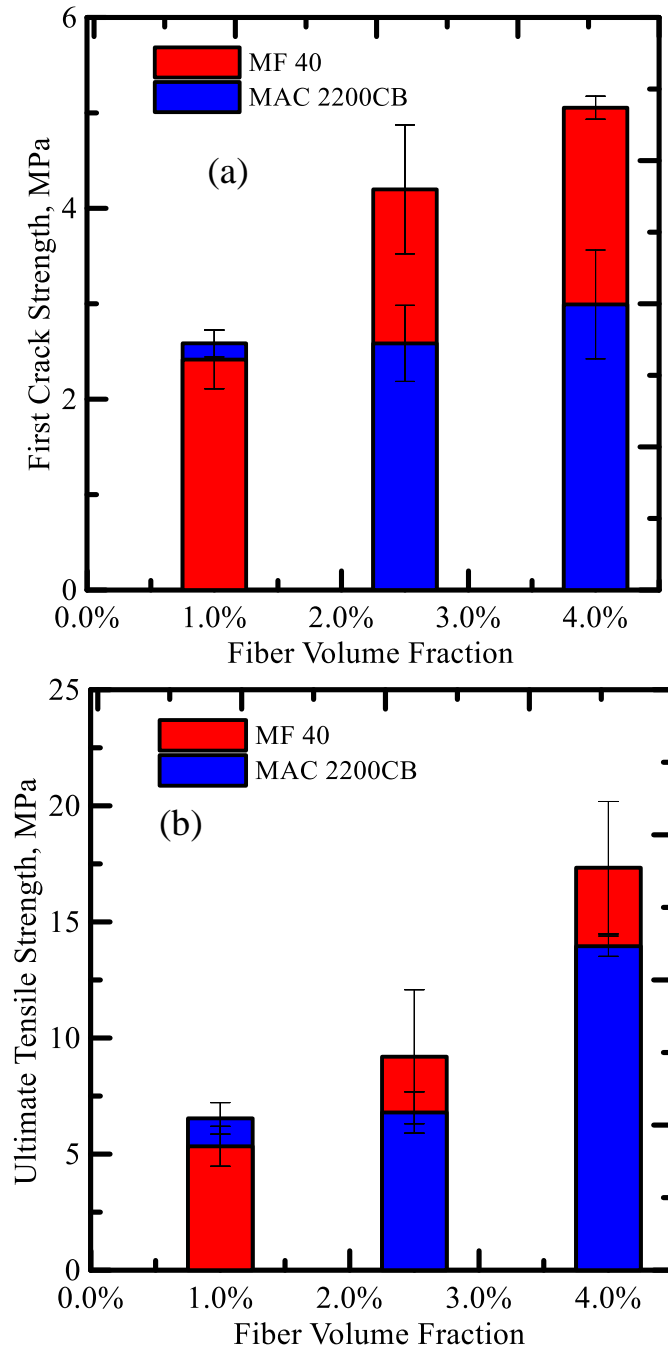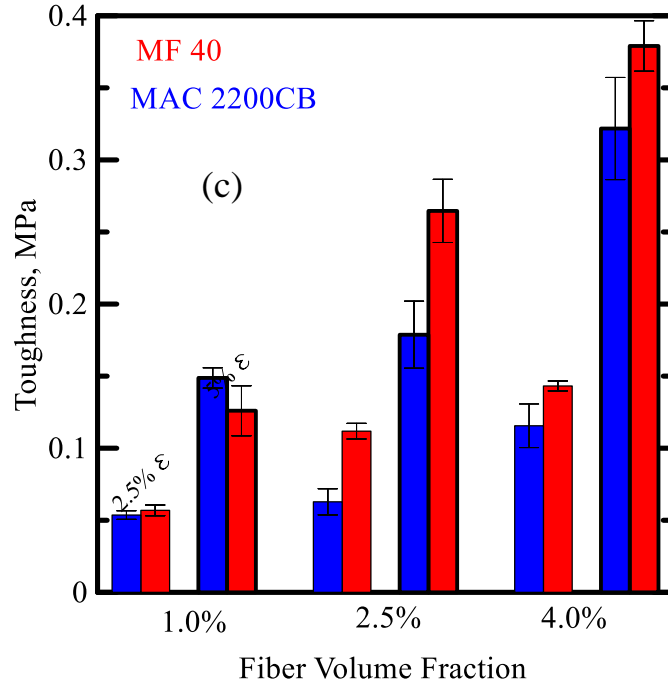
Figure 2-19: Summary of effect of fiber type and dosage on tensile properties.

Short discrete glass fibers are used as secondary reinforcement to bridge micro cracks, enabling finer crack pattern and reduced crack widths. The addition of short fibers causes formation of greater number of disconnected micro-cracks over the length of the specimen and additional stress transfer over the macro-cracks, which results in a less pronounced relaxation of the matrix in the vicinity of the cracks. New cracks can form at a smaller distance from an existing one; resulting in more pronounced multiple cracking [32]. Wollastonite is an acicular shaped naturally occurring calcium meta-silicate mineral, which is considered as cementitious admixture. The acicular shape promotes strengthening of the matrix by impending crack propagation, micro cracking and crack path deflection. Improvement of compressive strength and flexural properties of cementitious systems with mineral wollastonite micron and sub-micron fibers have been reported earlier [33].

45

The fly-ash blended control mortar matrix was compared to three other hybrid mixes with glass micro-fibers and wollastonite fibers labeled as mixes HM-1,2,3, reported earlier in Table 2-2. ARG and wollastonite fibers were added as 1.5% and 5% by weight of the total mix. Wollastonite was however considered as supplementary cementitious material due its cement like characteristics, and was used to partially replace 10 % of cement mass [33]. The effect of hybridization of the matrix phase on the tensile and flexural properties is summarized in Figure 2-20. The addition of short fibers and wollastonite resulted in an appreciable increase of the first cracking strength, ultimate tensile strength, and strain capacity of the composite as evident in Figure 2-20(a). In case of flexural response, addition of wollastonite also improves the flexural strength and toughness as evident in Figure 2-20(b). However addition of AR-glass fibers causes reduction in the flexural strength and toughness.

The effect of hybridization of matrix on the mechanical properties is also summarized in Figure 2-21. As evident, the tensile strength of the matrix increases gradually from 6-11 MPa, and toughness increases from 0.18-0.31 MPa. Residual strength under flexural loading measured at nominal limits of span, L/150 showed increasing trend with the advent of wollastonite in the matrix, but showed a posterior decay in the presence of combination of glass and wollastonite. Residual strength at L/600 however saw a continuous decrease for hybrid matrices under flexure.
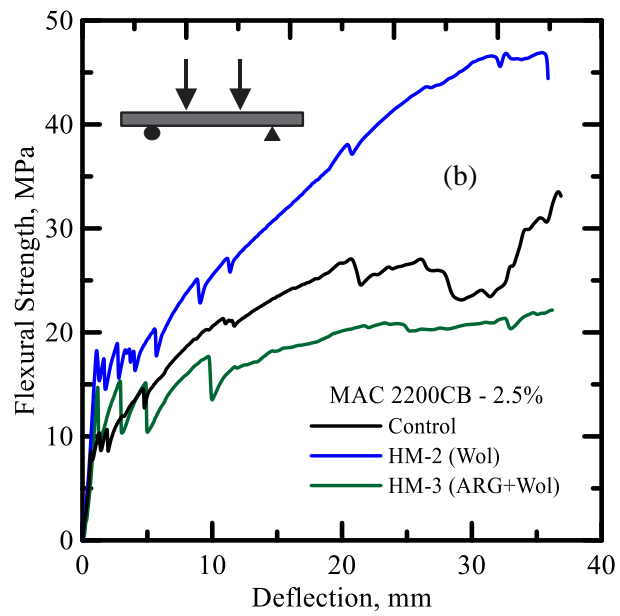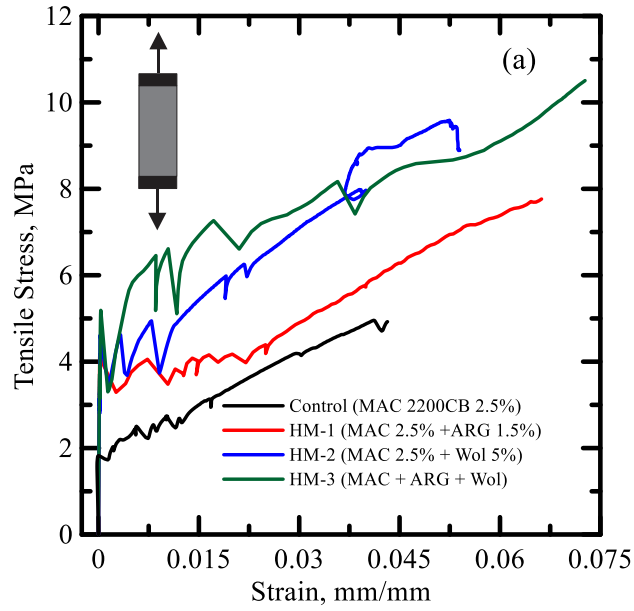
Figure 2-20: (a) Tensile and (b) flexural response of continuous unidirectional fiber composites with different matrix compositions

47
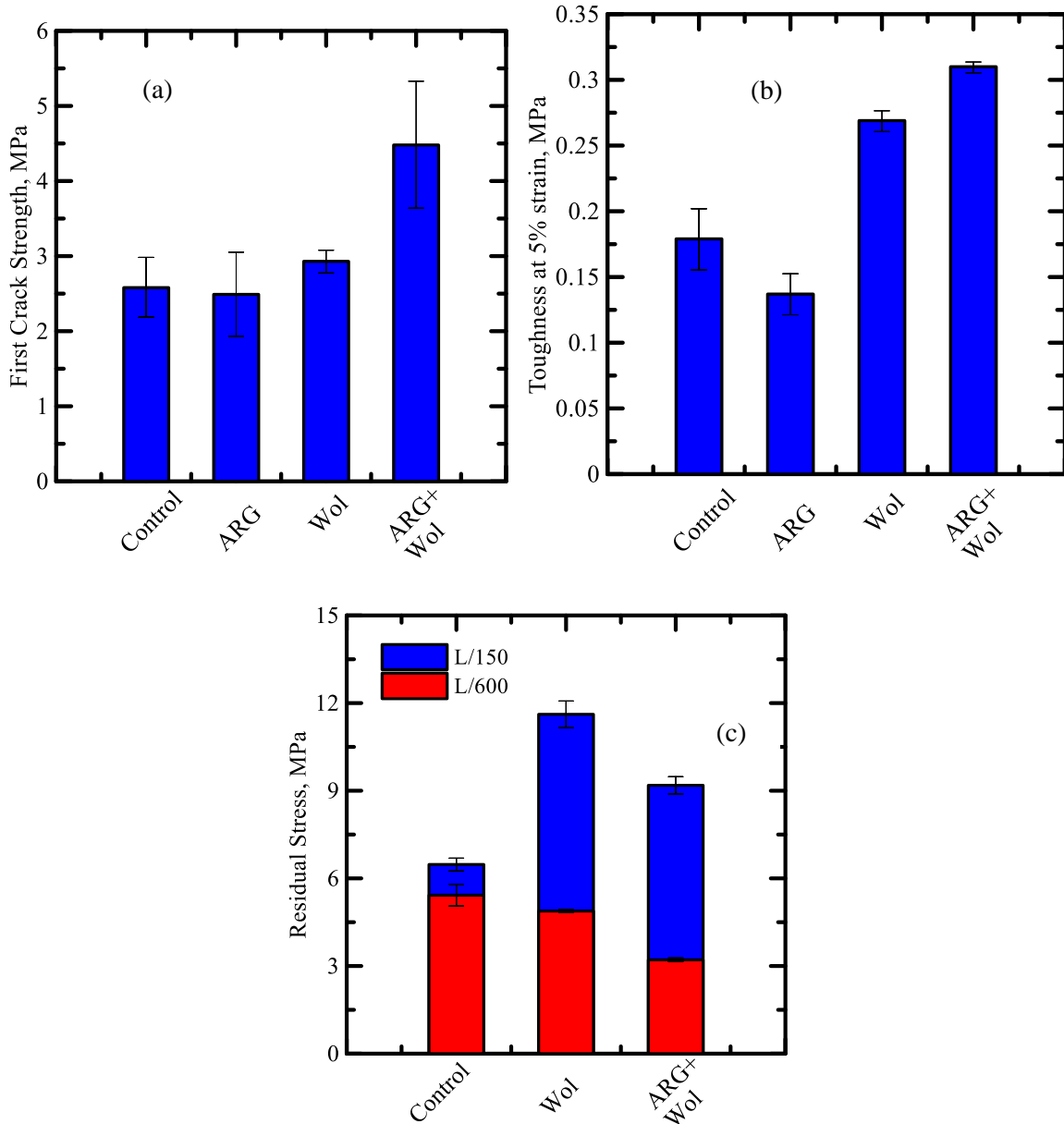
Figure 2-21: Effect of hybridization of matrix on: (a,b) tensile and (c) flexural properties

The surface crack morphology of specimens at discrete time step corresponding to peak stress with different mixes are shown in Figure 2-22. Digital image correlation (DIC) technique was used to document the crack width and spacing of the different matrices as shown in Figure 26(a-b). Obtained stress-crack width responses can be characterized using three parameters: first-cracking strength, post-cracking stiffness and ultimate crack width.

The hybrid mixes tended to show higher first crack strength, post-crack stiffness, and crack width as shown in Figure 2-23(a). Distribution of crack spacing in Figure 2-23(b), clearly demonstrates that the saturated crack spacing increases significantly from 10 mm to about 30 mm in the presence of secondary reinforcement in the form of ARG chopped micro-fibers and wollastonite nano-fibers. The matrix becomes significantly toughened and less evidence of distributed cracking is seen with the hybrid mixes. Thus it could be inferred that for hybrid mixes, tensile response could be characterized by crack widening behavior rather than distributed cracking in the gage length. There is less propagation of cracks and significantly higher crack widths. This is of great significance in design considerations.
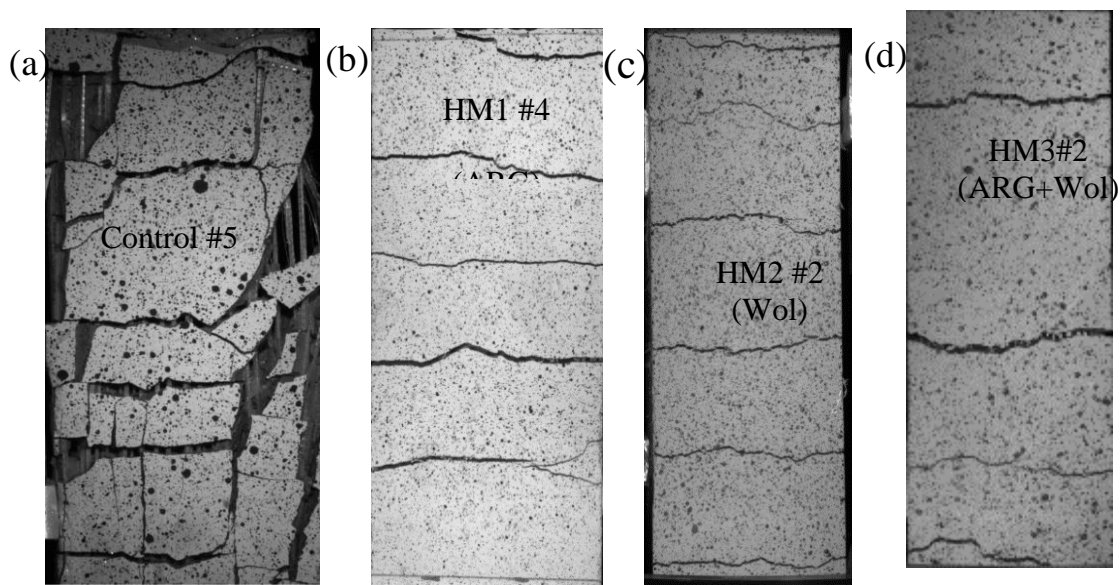
Figure 2-22: Propagation and extent of cracking in tension specimens with MAC 2200CB and: (a) control matrix, (b-d) hybrid matrices
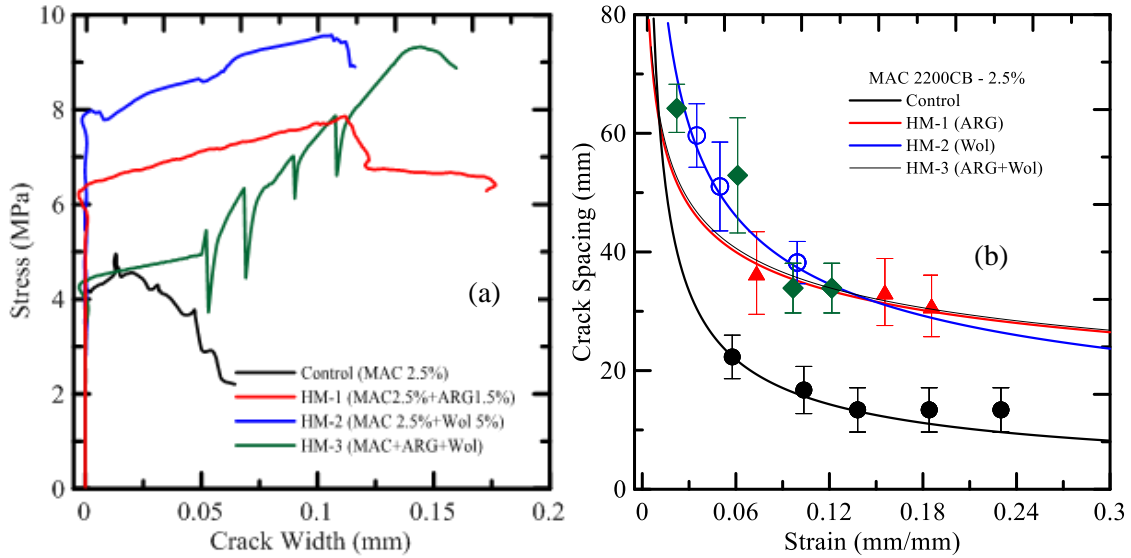
Figure 2-23: Effect of hybridization of matrix on (a) -crack width, (b) crack spacing response.

The test results from the single fiber pullout tests are summarized in Table 2-4. Parameters from the tension and flexure tests on the continuous unidirectional fiber composites with MAC 2200CB and MF 40 fibers are summarized in Tables 2-5 and 2-6. The average parameters are reported in bold, whereas the standard deviation estimates are reported in regular fonts.

2.4. Toughening Mechanisms

The fiber reinforcement within these composites help increase the toughness and ductility of the specimens through several strengthening mechanisms: distributed parallel cracking, crack bridging, fiber pullout and fiber failure. As specimens are pulled in tension, the fiber-matrix interface prevents fracture through a series of distributed cracks transverse to the direction of the load thereby giving the composite higher ductility and toughness capacity. The distributed crack patterns for fiber reinforced specimens pulled in tension can be seen in Figure 2-24(a) for MAC2200CB at a volume fraction of 2.5%.
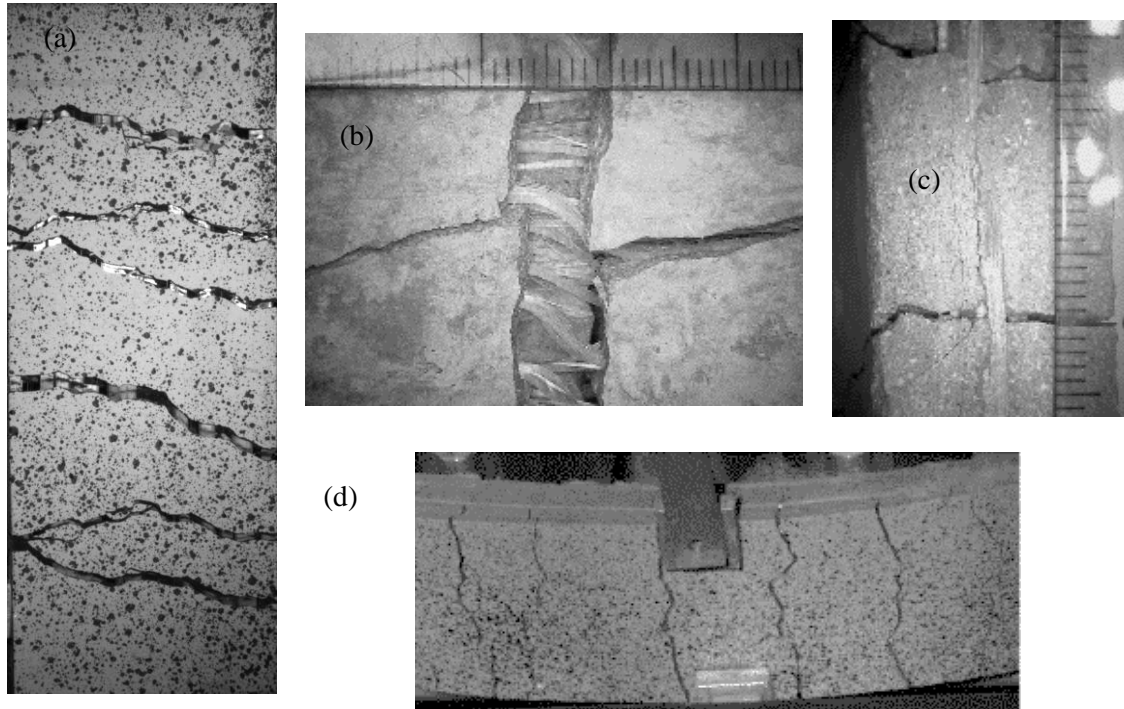
Figure 2-24: Parallel cracking in (a)PP composite laminates under tension, (b) crack bridging across the sample width, (c) crack bridging through thickness; and (d) distributed flexural cracks under four-point bending in MF40 composite

2.5. Conclusions

An extensive experimental program was conducted to characterize the performance of two forms of polypropylene fibers to be used in continuous fiber reinforced cementitious composites. Macro-synthetic fiber, MAC 2200 CB and fibrillated microfiber MF40 were considered in this study. A series of mechanical tests on fiber phase which included tension tests on the fibers, fiber pullout tests, and composite phase which included direct tension and four point bending tests were conducted. A manufacturing setup based on filament winding technique was develop to manufacture the unidirectional composite laminates. Digital image correlation technique was used to quantify the damage parameters: crack width and spacing. It was found out that the microfiber MF40 due to open fibrillated

51

structure offered much better bonding with the cementitious matrix, and resulted in significant improvement in fiber-matrix bond and composite tension and flexure properties compared the macro-synthetic MAC 2200 CB. Effect of the hybridization of the matrix was studied with addition of mineral wollastonite micro-fibers and chopped glass-fibers. It was found out the synergistic effect of multi-scale reinforcement with polymeric macro-fibers, micro-fibers and wollastonite sub-micro fibers offer excellent improvements in mechanical properties under flexure and tension.

Table 2-4: Results from single fiber pullout tests on PP and steel fibers.

Mix ID	Cured	Fiber Type	Mix Spec	L (mm)	Stiffness, K (N/mm)	Max Load, P_{max} (N)	Slip at Max Load, S_{max} (mm)	Toughness (N.mm)
A	3	MAC	C+W	25	121 ± 15.9	211 ± 13.2	3.13 ± 0.15	2395 ± 313
A	3	Dramix	C+W	25	234 ± 31.4	313 ± 24.2	3.47 ± 0.93	3668 ± 512
A	7	MAC	C+W	25	87 ± 1.7	175 ± 56.5	2.56 ± 1.12	1929 ± 178
A	7	Dramix	C+W	25	371 ± 37.1	311 ± 26.1	1.56 ± 0.21	2430 ± 152
B1	7	MAC	C+W	20	95 ± 5.0	175 ± 15.5	2.47 ± 0.34	1109 ± 615
B1	7	Dramix	C+W	20	668 ± 44.6	252 ± 61.3	6.79 ± 4.78	2367 ± 247
B1	7	MF40	C+W	20	134.2 ± 7.8	516.3 ± 76.2	5 ± 0.8	2879.2 ± 531.4
B2	7	MAC	C-Wol+W	20	90.7 ± 5.5	171 ± 13.3	2.77 ± 0.20	1433 ± 270
B2	7	Dramix	C-Wol+W	20	388 ± 159	230 ± 39	4.68 ± 5.1	1837 ± 639
B2	7	MF40	C-Wol+W	20	132.5 ± 29.7	480.8 ± 58.7	4.9 ± 0.6	3282.4 ± 309.9
C	7	MAC	C+W	12	108 ± 9.8	120 ± 3.5	1.83 ± 0.20	442 ± 98
C	7	Dramix	C+W	12	369 ± 106.9	324 ± 17.9	1.46 ± 0.12	1804 ± 241
D	7	MAC	C-FA+W	20	119 ± 174	85 ± 159.1	0.45 ± 0.68	511 ± 869
D	7	Dramix	C-FA+W	20	744 ± 258	337 ± 27.6	1.232 ± 0.36	2654 ± 572
D	7	MF40	C-FA+W	20	147.8 ± 18.4	579.8 ± 40	5.8 ± 0.6	4230.5 ± 416.7
E	3	MAC	C+S+W	25	73 ± 11.7	202 ± 9	3.65 ± 0.21	2358 ± 402
E	3	Dramix	C+S+W	25	530 ± 33	332 ± 42.6	1.29 ± 0.35	2859 ± 1019
E	7	MAC	C+S+W	25	92 ± 5.2	208 ± 21.1	3.33 ± 0.38	2661 ± 273
E	7	Dramix	C+S+W	25	428 ± 42.7	366 ± 51.9	1.97 ± 0.80	3379 ± 967
F	7	MAC	C-FA-Wol+W	25	89 ± 6.1	222 ± 30.4	3.44 ± 0.33	3171 ± 726
F	7	Dramix*	C-FA-Wol+W	25	294 ± 59.4	296 ± 1.4	1.58 ± 0.23	1791 ± 654

Table 2-5: Analyzed tension test results from HPFRCC continuous fiber specimens

(average in bold, std. dev. in regular fonts)

Group ID	Fiber	V_f	BOP σ	BOP ε	First Crack σ	First Crack ε	UTS σ	UTS ε	Ultimate, ε_{tu}	Stiff-ness	E	E'	Toughness 2.5 % ε	Toughness 5 % ε
		%	MPa	mm/mm	MPa	mm/mm	MPa	mm/mm	mm/mm	N.mm	GPa	MPa	MPa	MPa
1	MAC 2200CB	1	**1.48**	**0.00026**	**2.59**	**0.0029**	**6.54**	**0.11**	**0.154**	**35600**	**3.3**	**88**	**0.05**	**0.15**
			0.33	0.00020	0.29	0.0017	1.36	0.03	0.015	18730	1.6	26	0.01	0.01
2	MAC 2200CB	2.5	**1.55**	**0.00021**	**2.58**	**0.0018**	**6.79**	**0.08**	**0.159**	**86143**	**6.9**	**120**	**0.06**	**0.18**
			0.54	0.00021	0.80	0.0027	1.78	0.03	0.051	57586	4.8	80	0.02	0.05
3	MAC 2200CB	4.0	**2.30**	**0.00006**	**2.99**	**0.0001**	**13.95**	**0.10**	**0.141**	**445000**	**39**	**140**	**0.12**	**0.32**
			0.63	0.00003	1.14	0.00002	0.87	0.03	0.052	126886	11	23	0.03	0.07
4	MF 40	1.0	**1.55**	**0.00009**	**2.42**	**0.0002**	**5.33**	**0.18**	**0.198**	**150125**	**14**	**35**	**0.06**	**0.13**
			0.20	0.00004	0.31	0.00005	0.86	0.03	0.028	73178	7.4	9	0.01	0.02
5	MF 40	2.5	**2.91**	**0.00009**	**4.20**	**0.0002**	**9.19**	**0.08**	**0.116**	**333333**	**31**	**66**	**0.11**	**0.26**
			0.43	0.00003	0.68	0.00005	2.89	0.03	0.021	77632	8.3	35	0.01	0.02
6	MF 40	4.0	**3.69**	**0.00015**	**5.05**	**0.0003**	**17.33**	**0.10**	**0.119**	**235714**	**24**	**177**	**0.14**	**0.38**
			0.73	0.00006	0.12	0.00008	2.85	0.02	0.022	140814	13.9	28	0.01	0.02
7	MAC + ARG	2.5	**1.19**	**0.00005**	**2.49**	**0.0002**	**6.84**	**0.14**	**0.215**	**260500**	**19.6**	**61**	**0.05**	**0.14**
			0.42	0.00002	1.12	0.00014	2.01	0.02	0.021	168011	11.6	17	0.01	0.03
8	MAC + Wol	2.5	**2.40**	**0.00007**	**2.93**	**0.0001**	**8.59**	**0.07**	**0.107**	**353333**	**32.7**	**90**	**0.10**	**0.27**
			0.04	0.00003	0.30	0.00004	0.86	0.01	0.014	130512	12.7	28	0.01	0.02
9	MAC + Wol + ARG	2.5	**2.29**	**0.00009**	**4.48**	**0.0002**	**9.78**	**0.08**	**0.123**	**340000**	**27**	**66**	**0.13**	**0.31**
			0.77	0.00004	1.69	0.00004	0.75	0.00	0.006	60828	5.2	30	0.00	0.01
10	MF40 + Wol + ARG	2.5	**3.68**	**0.00010**	**5.09**	**0.0002**	**9.36**	**0.09**	**0.117**	**393333**	**32.7**	**63**	**0.13**	**0.29**
			0.31	0.00004	0.22	0.00002	1.23	0.01	0.006	130128	9.0	16	0.01	0.01

Note: Abbreviations for volume fraction is V_f, stress is σ, strain is ε, elastic modulus is E, and post-crack modulus is E'.

Table 2-6: Analyzed flexural test results from HPFRCC continuous fiber specimens

(average in bold, std. dev. in regular fonts)

Group ID	Fiber	Stiffness	First Crack		Defl. Limit : L/150			L/600			MOR	δmax	T
			δ	P	P	σr	T	P	σr	T			
		N/mm	*mm*	*N*	*N*	*MPa*	*N.mm*	*N*	*MPa*	*N.mm*	*MPa*	*mm*	*N.mm*
1	MAC 2.5%	**2312**	**0.62**	**376**	**335**	**6.48**	**174**	**263**	**5.42**	**65**	**35**	**26.8**	**24885**
		735	0.08	50	38	0.53	27	63	0.90	20	3	8.6	3928
5	MF40 2.5%	**1101**	**1.33**	**494**	**391**	**7.31**	**189**	**211**	**3.99**	**44**	**56**	**43.9**	**50518**
		62	0.71	186	75	1.15	38	13	0.37	2	26	4.6	11965
8	MAC 2.5% + Wol 10%	**1324**	**1.12**	**584**	**548**	**11.62**	**292**	**194**	**4.88**	**52**	**49**	**25.2**	**36314**
		292	0.09	25	41	1.12	41	20	0.12	19	14	9.9	9330
9	MAC 2.5% + ARG 1.5% + Wol 10%	**1337**	**1.04**	**571**	**553**	**9.18**	**265**	**177**	**3.21**	**36**	**22**	**35.0**	**24763**
		456	0.15	112	117	0.72	80	20	0.16	7	2	2.8	5443
10	MF40 2.5% + ARG 1.5% + Wol 10%	**2802**	**2.28**	**1022**	**949**	**10.27**	**684**	**498**	**5.43**	**249**	**34**	**27.5**	**66837**
		1454	0.96	122	165	1.21	215	136	0.80	134	2	7.2	19877

Note: Abbreviations of load is P, deflection measured is δ, deflection at maximum stress is δ$_{max}$, residual stress is σ$_r$, modulus of rupture is MOR and toughness is T.

3. DEVELOPMENT OF POLYPROPYLENE TEXTILE REINFORCED CONCRETE

Textiles are frequently made from single or multifilament yarns and the potential penetrability of the cementitious matrix into the bundle spaces depends on the structure and the density of the weave. Textile reinforced concrete (TRC) composites are a new class of sustainable construction materials with superior tensile strength and ductility [34,35]. The geometric pattern of fabric consisting of a large number of interconnected longitudinal and transverse fill yarns, develops an excellent bond with cement matrix by mechanical interlock and anchorage of yarns [36]. Various research groups have developed a wealth of recent information pertaining to the methodologies, properties, and areas of applications for fabric reinforced cement based materials [37, 38,39]. Very encouraging tensile strength and ductility responses have been observed by various experimental programs with tensile strength of the order of 20-25 MPa and tensile strain capacity of 3-5% [40, 41]. The tightening of the joints that connect the weft and fill yarns induced by the junction points of the fabric strongly hold the filaments of the bundle and prevents them from being opened. Paste penetration into the openings in the fabric structure and inside multifilament yarns leads to improve significant strength and ductility. TRC laminates could be easily adopted and modified to fabricate different structural shapes such as channels, angles, hollow sections and rectangular plates of any desired length and cross-sections. Application areas of these composites include structural panels, impact, blast resistance, repair and retrofit, earthquake remediation, strengthening of unreinforced masonry walls, and beam-column connections are being developed.

A collaborative project was developed with colleagues at Composites Division of Institutfür Textiltechnik (ITA) of RWTH Aachen University where in MF-40 polypropylene microfibers were woven into textiles with plain and tricot weave patterns as shown in Figure 3-1. Open weave is a basic one-face warp in which a knit is worked from one fully threaded warp. In the first row the thread forms a stitch on the first needle; in the second row this occurs on the third needle. Stitches are made alternately, first on one side, then on the other. In tricot weaves one thread forms stitches alternately in two neighboring columns. By the pulling of loops, stitches are made alternately on one side, then on the other [42]. TRC cement-based laminates were developed with pultrusion process and uniaxial tension tests and four-point bending tests were conducted to compare the TRC systems with the continuous fiber reinforced cementitious laminates discussed in the previous chapter.

(a)

(b)

(c)

2,5 cm
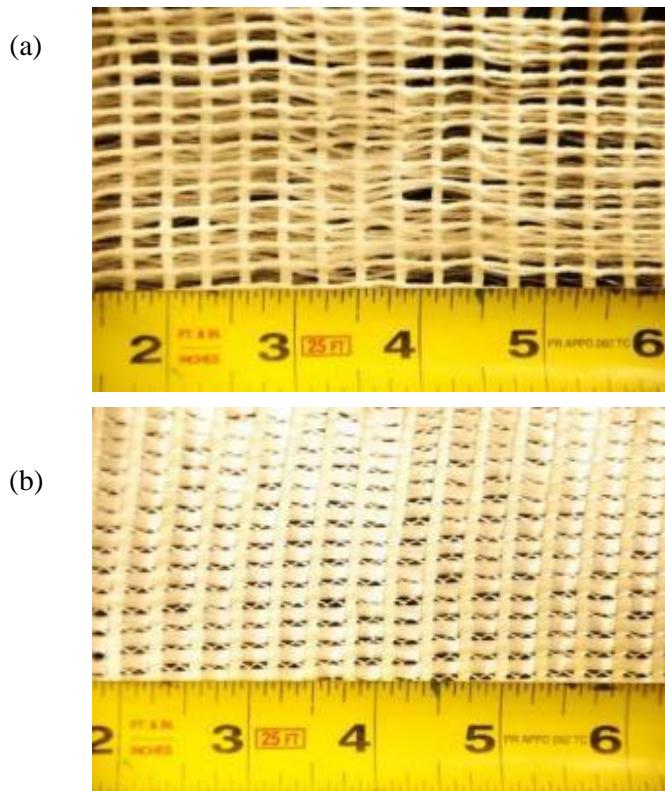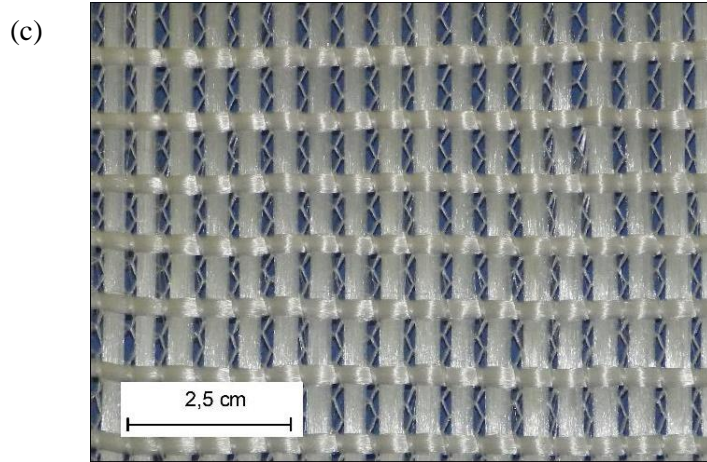
Figure 3-1: (a) Open and (b,c) tricot weave patterns of textiles woven from MF40 microfibers

3.1. Automated Pultrusion Process

An efficient production method for Textile reinforced composites is the pultrusion process as shown in Figure 3-2(a) [43,44,45,46]. Schematics of this setup is shown in Figure 3-2(b), which shows the different components of this setup. During the pultrusion process, fabric passes through a water bath and then a slurry infused impregnation chamber. The coated fabric is then pulled through a set of rollers to squeeze the matrix between the fabric openings while simultaneously removing excess matrix. The set of rollers are powered with a DC motor and operate in opposite directions to apply uniform pressure and distribute the matrix evenly on the surface of the textile. Next the matrix coated fabric is clamped and pulled through continuously by the use of tractor pulling mechanism powered by a set of pneumatic pistons. The pulling mechanism grips and tows the composite as it moves through each station. These pistons are controlled by a set of solenoid valves, which are interfaced with a computer system using a lab view program. Next the pultruded fabric is placed on a mold wherein multiple fabric layers are stacked together and pressed together using an in-situ pneumatic press. The shape of the mold can be easily modified to

manufacture laminates with different cross-sections such as flat rectangular, channel, angle, or hat sections. The fabric layers are held at a constant air pressure of between 10-20 psi for 24 hours, before being demolded and cured in a curing chamber under controlled environment. Being an automated process, sections of infinite length and thickness can be easily manufactured with desired precision and optimized layout.

(b)
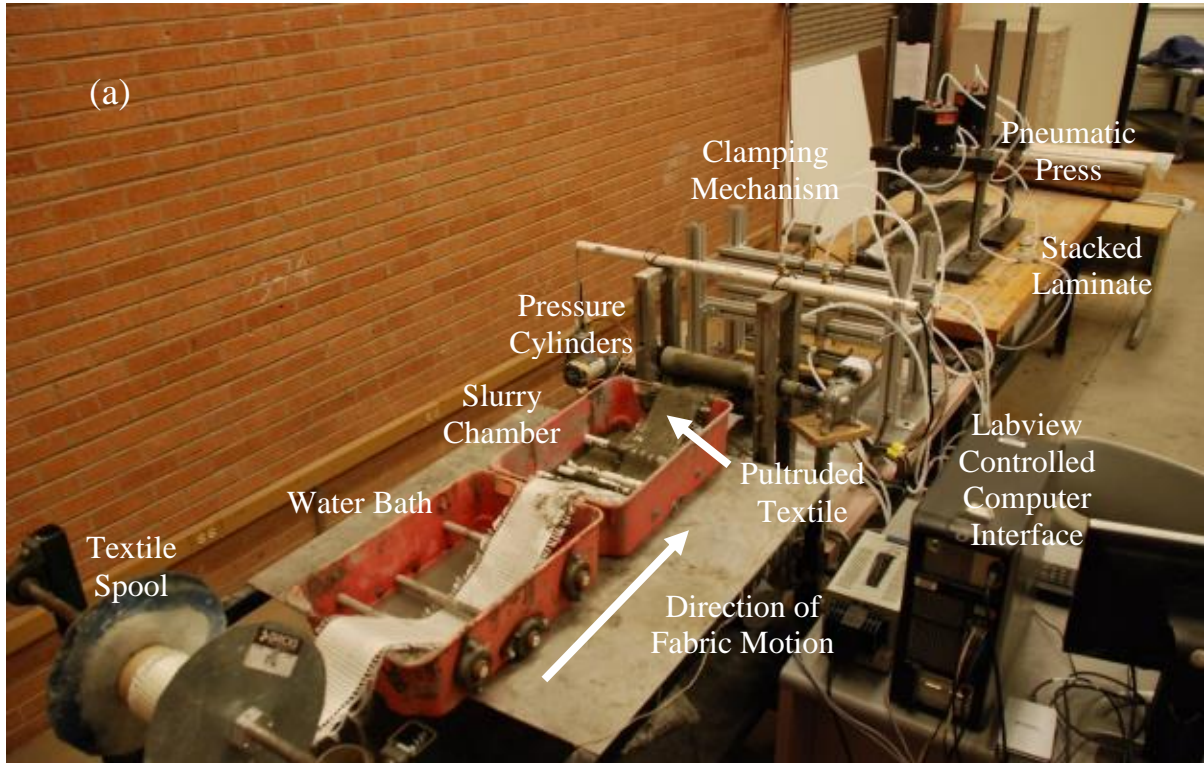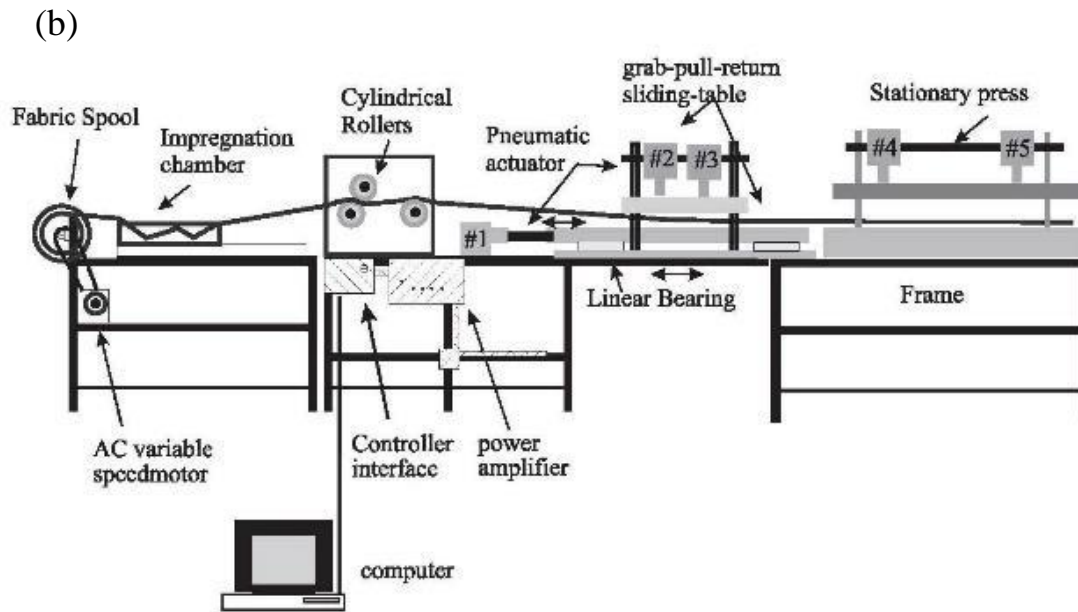
Figure 3-2: (a) Automated pultrusion system for manufacturing TRC, (b): Schematics of

the automated pultrusion system for manufacturing TRC

Impregnation of cement-based matrix into the open cell structure of the textile remains a

concern. In the absence of uniform impregnation, the composite strength can be

compromised due to improper stress transfer between the matrix and reinforcement. The

automated pultrusion system consists of five central stations oriented in succession along

a continuous production line. The pultrusion process consists of feed section which

includes the fiber spool, the water and paste baths; guidance sections which is powered by

the DC powered rollers and the pneumatic pulling mechanism, and ultimately the take up

section which consists of the composite die (mold) and the in-situ pneumatic press.

3.1.1. Feed Section

Textile spool is the first station within the pultrusion process and ensures uniform feed of

the textile on to the subsequent stations. Pulling of the textile from the spool could be either

a manual process or an automated process using a DC/stepper motors. The water and paste

baths are the next two stations in the pultrusion process. The textile after being pulled from the spool is wetted in the water bath to ensure better bonding the cementitious matrix. Along with water, chemical compounds can be added to enhance the fabric-matrix bonding. The water bath is fitted with three rollers which act as contact points oriented in a triangular pattern to enable uniform distribution of water on the fabric and maintain tension in the textile as it moves down the line. After passing through the water bath, the textile is pulled through the paste bath. The textile passing through the paste bath is shown below in Figure 3-3. The paste bath has a set of rollers mounted in a trapezoidal shape to enable additional contact points for the fabric submerged inside the matrix. Flowability of the cement-based matrix can be ensured using chemical admixtures such as high-range water reducers and hydration retarder, or using mechanical needle vibrators.

Figure 3-3: Textile passing through paste bath

3.1.2. Guidance Section

The coated textiles are next passed through a set of rollers, which are powered by two DC motors. Figure 3-4 shows the coated textile entering the rollers from the paste bath. These rollers are mounted on two steel frames that hold them in place but allow them to rotate as the coated textile passes through them. They rollers are each attached to a 24V DC motor through a universal joint and a mechanical couplers. The motors are positioned opposite of each other so that the rollers spin in opposite directions. The motion and spacing of these rollers ensure that the paste is distributed evenly along the width of the textile. With uniform coating, the textile get efficiently impregnated as all cells of the textile get filled with the matrix and the textile will remain plane within the composite.

(a)

Figure 3-4: (a) Textile being pulled through the treatment baths, (b) pultruded textile squeezed in between the rollers powered by DC motors

The next station in the pultrusion production line is the tractor pulling mechanism. This pneumatically controlled mechanism is the driving force behind the pultrusion process. In this technique the coated fabric is gripped using a set of compression pads and pulled it down the line before being released and pushed forward in the production line. Next the compression pads are pulled back to the starting position to grab a new section of the fabric and the process cycle is repeated henceforth. Tractor pull mechanism is shown in Figure 3.5(a), and the schematics of the setup is shown in Figure 3.5(b).

(a)

(b)
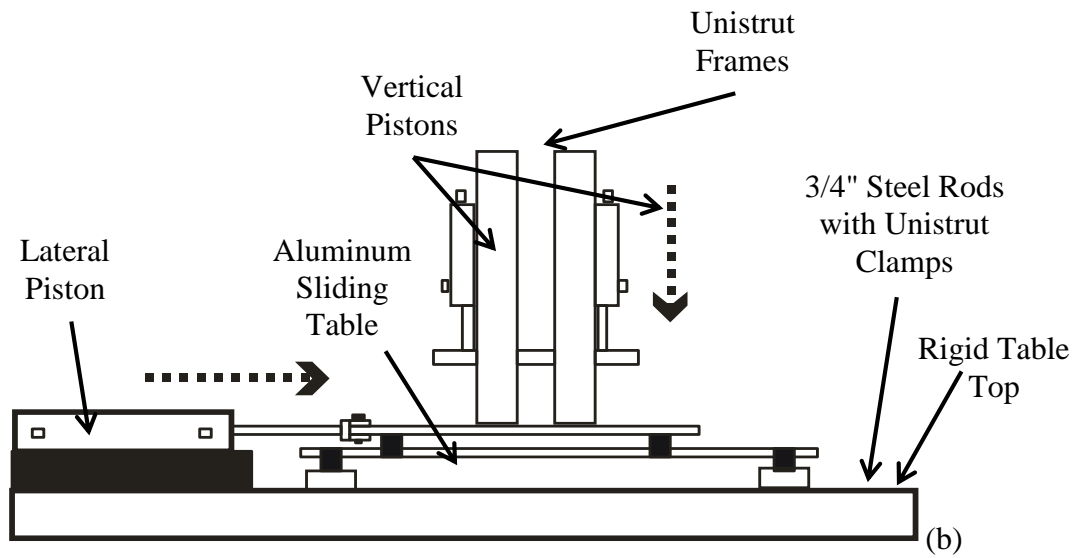
Figure 3-5: (a) Pulling mechanism used in automated pultrusion system, (b) schematic of

pulling mechanism

The pulling mechanism for this system is composed of rigid aluminum table top and a sliding aluminum sliding table and couple of vertical frames built with several unistrut sections. A pneumatic piston with a stroke of 150 mm is used to laterally translate the sliding table. Four pneumatic pistons with stroke of 100 mm were used to apply pressure on to the pultruded specimen with two compression pads. A combination of these two axis of motions drives the pultruded specimen forward in a continuous process. The pneumatic pistons are powered by the building air pressure, and are turned into active state through several solenoid valves. The flow lines are connected between the five pistons with plastic hosing, tee connectors, and adapters. The air flow pressure is controlled through a pressure regulator that maintains a uniform pressure of about 3 psi. This allows for smooth motion of the pistons and adequate gripping pressure in the clamp. The air flow diagram of the pulling mechanism is shown below in Figure 3-6.
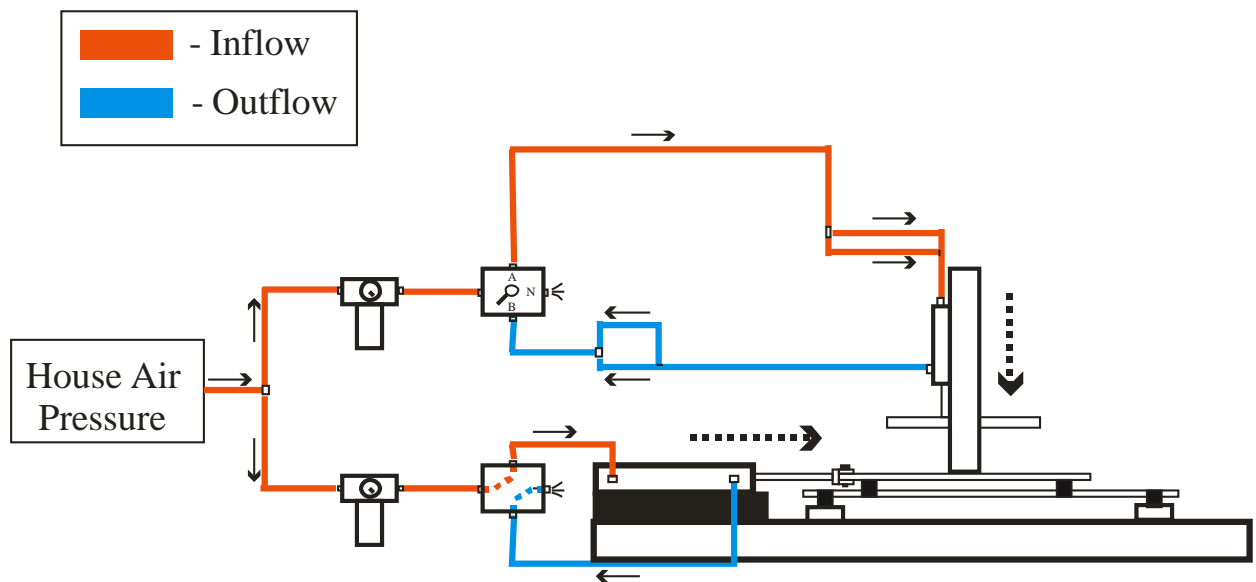
Figure 3-6: Air flow diagram of pulling mechanism [47]

The air solenoids act as the driving controllers for the automated pultrusion system and are turned off and on through their connection to a 24V DC power supply. A National

Instruments chassis acts as an interface and connects DC power supply and solenoid valves s to the computer in order to run the system. The wiring diagram for a single solenoid is shown in Figure 3-7.

The automation aspect of the pultrusion system was controlled through the use of a Lab View virtual instruments (VI) program that was developed specifically for the system. Lab View VI's are computer controlled interfaces with a series of variables and switch controls that are connected to the driving components of a system. Continuity loops, safety stops, and output functions are coded through the construction of the block diagram as shown in Figure 3-8. To control the air solenoids in the proper sequence, a true\false matrix was used to turn the proper solenoids on (true) and off (false) as the program runs continuously.
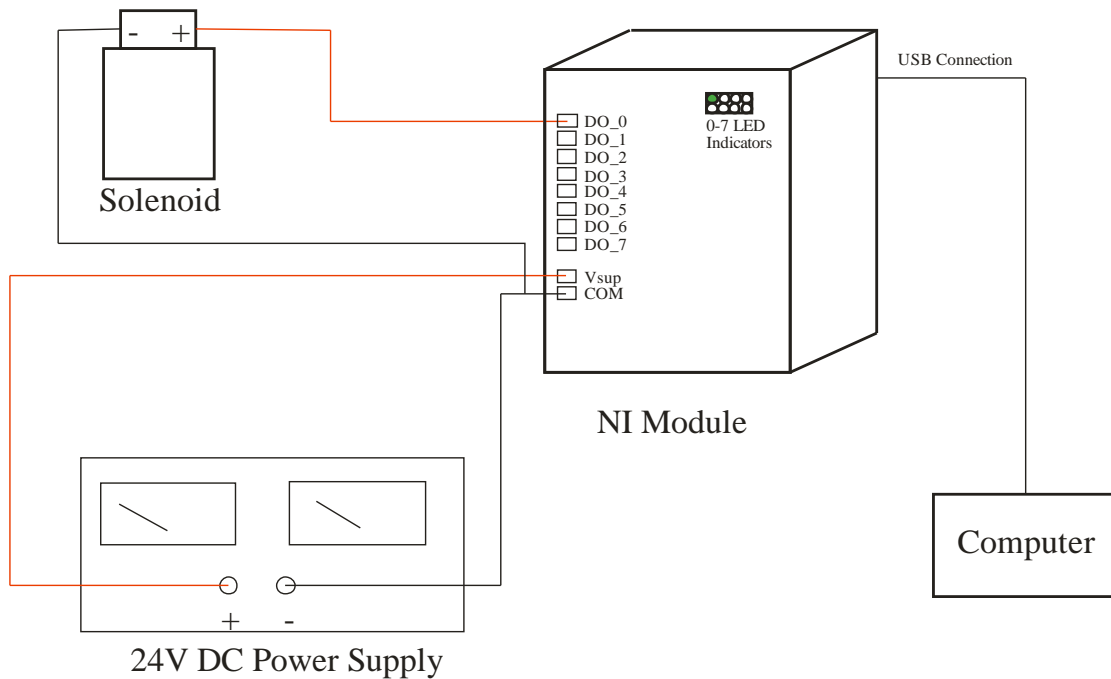
Figure 3-7: Wiring diagram of air solenoid connection to NI module [47]
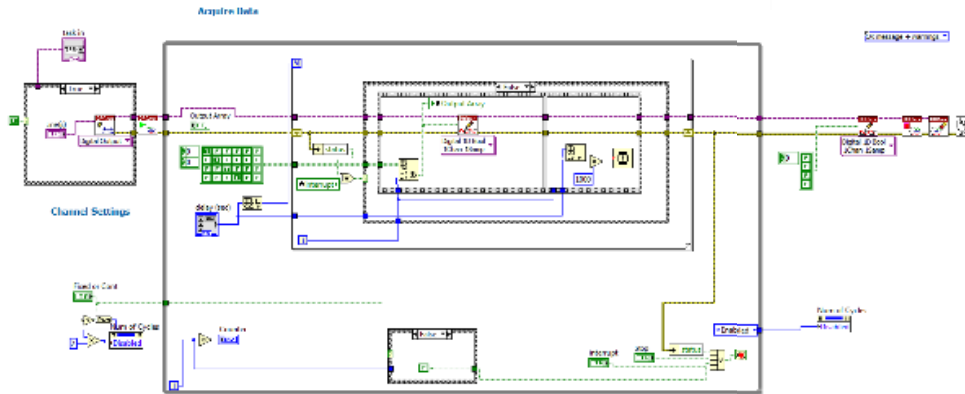
Figure 3-8: Block diagram of pultrusion VI

When creating a VI in Lab View, the system is built with a block diagram that is represented in the operating interface as buttons on the front panel display as shown in Figure 3-9. The sequence consisted of five segments correlate to the complete pulling mechanism: clamping, pulling, releasing, return to origin, and rest. Speed of each segment could be varied through user input on the front panel.
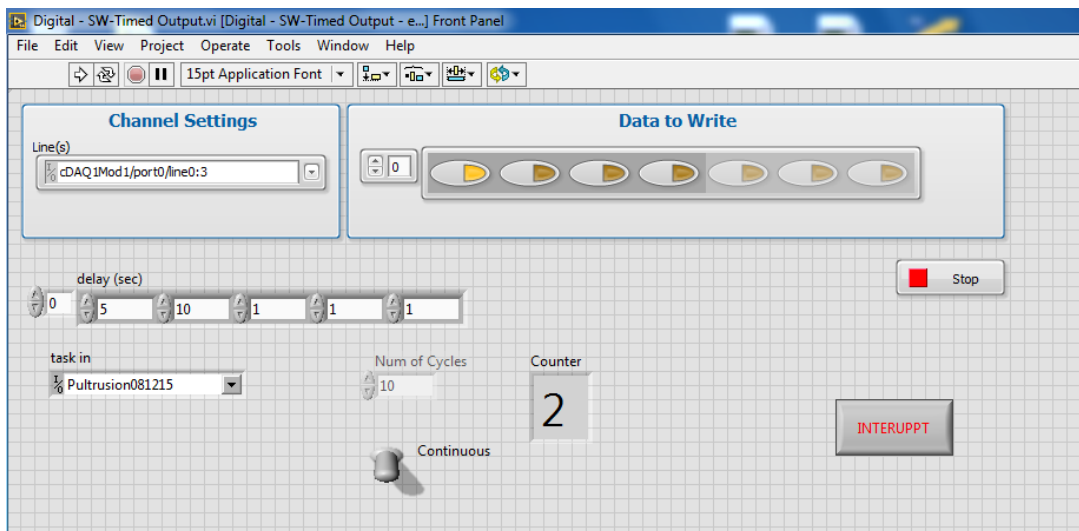
Figure 3-9: Front panel of LabView VI

3.1.3. Pneumatic Press

The final step in the pultrusion system is the in-situ pneumatic press. The press is intended to work along with a set of dies to transform the flat pultruded into cross-sections of different shapes and geometries, and also provide a uniform surface finish to the specimen before it hardens. The press consists of two pneumatic actuators mounted on a steel loading frame. The actuators have a 50 mm displacement capacity and are fitted with heat treated aluminum plates to apply pressure onto the specimen. The press is connected to the building air pressure and is controlled through a pressure regulator that maintains a constant pressure of 10-20 psi. Figure 3-10 shows the pneumatic press as it is about to press a sample.
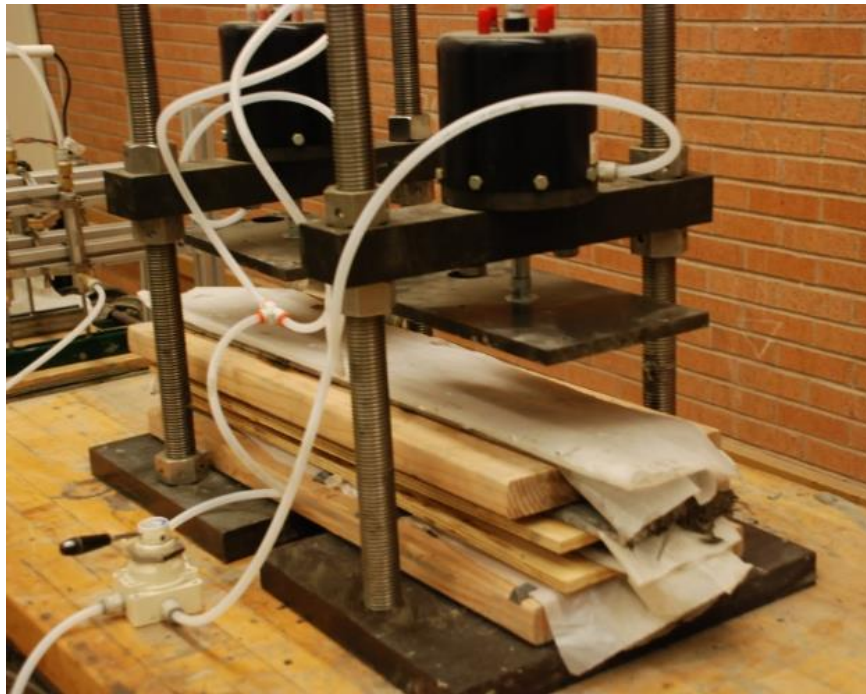
Figure 3-10: Pneumatic press before pressing a plate sample

3.2. Specimen Production

The use of automated pultrusion system enables casting of textile reinforced concrete laminates of desired geometry and layout with desired consistency, accuracy, and speed.

The main input variables in this system are the specimen geometry, mix design of the cementitious matrix, type and dosage of fabric, and amount and duration of the applied pressure while casting. While the pultrusion process is automated, certain manual efforts are necessary during the manufacturing process. This includes handling of the pultruded section and surface finishing of intermediate and final layers of laminate, to ensure a uniform and smooth composite surface. For production of TRC sections, a general mix design from the previous chapter was used. A water to cement ratio of 0.32 and cement to sand ratio of 2:1 were used for all samples. 5% of the cement was substituted with silica fume and 10% was replaced with wollastonite for a total cement substitution of 15%. Superplasticizer was used to increase the workability of the mix, specifically for the paste bath to allow for better coating of the textile. Standard laboratory mixing procedures were followed as a fixed, 5L Hobart mixer was used to dry mix materials for one minute, followed by four minutes of wet mixing. A high range water reducer and a retarder were used to ensure Flowability of the fresh cementitious matrix. The basic mix design used in this study is summarized in Table 3-1.

Table 3-1: Mix Design of TRC Samples

Material	Weight Percentage
Portland Cement (Type III/IV)	46.75%
Silica Fume	2.75%
Fine Silica Sand	27.5%
Water	17.5%
Wollastonite	5.5%
Superplasticizer	0.01%

Before casting a TRC sample, the necessary number of textile layers which amounts to the fabric volume fraction must be calculated. The number of layers required is dependent upon the desired specimen cross-section and length; along with the textile properties such as weave and diameter of fiber. Flat rectangular sections are the simplest cross-sections to produce using the pultrusion system. After deciding on the desired textile volume fraction and matrix proportioning, the system was prepared by filling the water and paste baths, greasing the pulling mechanism and rollers, and turning on the building air pressure. In the feed section, an initial layer of matrix was laid on a buffer board to act as the bottom laminate of the composite. The VI inputs were then entered to control the speed of production. The system was then activated and the textile was pulled through the production line. As the coated textiles reached the press, they were laid upon the initial matrix layer. Textiles were continuously placed until the desired volume fraction was reached. Matrix was continuously added between the textile layers to ensure proper impregnation and thickness to the composite. Once the desired number of layers were laid, the specimen was wrapped in polyethylene sheets and then pressed for about 4 hours at a pressure of 15 psi. The samples were then demolded and moist cured for 28 days. Multiple laminate sections can be cast and pressed simultaneously as shown in Figure 3-11(a-b).

Figure 3-11: (a) Multiple plate samples cast in one session; (b) Pressing of multiple plates

3.3. Mechanical Properties of PP-TRC Laminates

Pultruded TRC composites were tested under direct tension and flexure under static loading to characterize the strength, strain capacity, stiffness, and distributed cracking mechanisms. Mechanical properties of the newly developed textile reinforced composites (TRC) were compared to the filament wound continuous fiber composites studied earlier as identical

dosages and mixture composition The three different TRC specimen groups studied are shown in Table 3-2.

Table 3-2: Groups of specimens of TRC developed in the study

Group ID	Yarn Type	Textile Weave	Yarn V_f%	Matrix Composition
I	MF40	Open	4.0	Control
II	MF 40	Tricot	4.0	Control
III	MF 40	Open	8.0	Control

Three sets of TRC laminate sections (30x6x0.5 in) were cast in the preliminary study of the textile materials with the two different weave patterns mentioned above. Direct tension tests were conducted on TRC coupons (12x2.25x0.5) after 7 and 28 days of curing. These trends are shown in Figure 3-12, wherein stress-strain responses of the TRC composites were compared to the HPFRCC composites with continuous yarns of MF 40 after 28 days of curing. The composites were made with volume fractions of 4% and 8%. As evident the 28 day tensile strength of continuous fiber reinforced composites (HPFRCC) with MF 40 fibers at 4% are considerable higher by 50 %, when compared to trends from the TRC composites with 4% textile dosage. It is to be noted that due to the two-dimensional structure of the woven textiles, effective volume fraction of TRC composites along the loading direction is only 2%.Hence when the results from TRC with 8% of textiles is compared to the continuous MF 40 fibers at 4%, the tensile response is quite similar. Interestingly, the total strain capacity of the TRC composites is much higher compared to

the HPFRCC composites. This could be attributed to the tightening and interlocking effect of the woven filaments contributing to better ductility as opposed to continuous fiber reinforced composites.
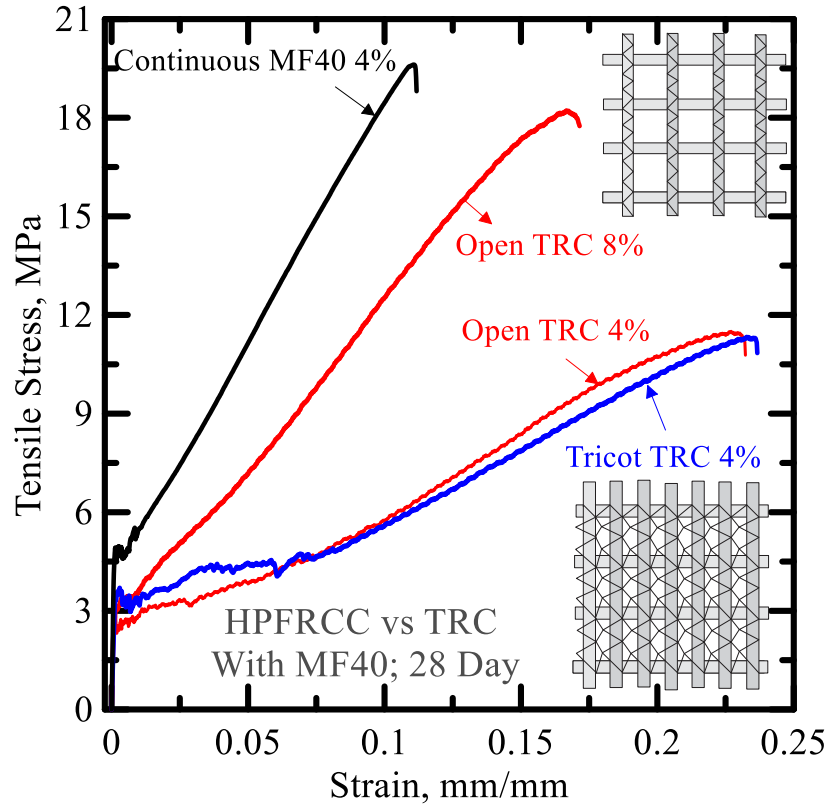
Figure 3-12: Stress-strain response of TRC with MF 40 textiles after 28 days of curing in tension

The flexure responses of the three TRC composite types versus a representative continuous MF40 specimen are shown in Figure 3-13(a). The tricot weave TRC composite showed a slightly better response than that of the open weave. This is likely due to additional stitching within the tricot textile which provides for a slight increase in ductility. The high volume fraction open weave TRC composite showed a response greater than that of the continuous MF40 specimen. This was likely due to the higher effective volume fraction in the

73

continuous direction as well as toughening from the lateral fibers within the TRC composite. Figure 3-13(b) shows that the high volume TRC has a tensile strength lower than that of a continuous fiber composite with the same effective fiber volume fraction as well as a higher flexural response than that of a continuous fiber composite with a lower effective volume fraction.
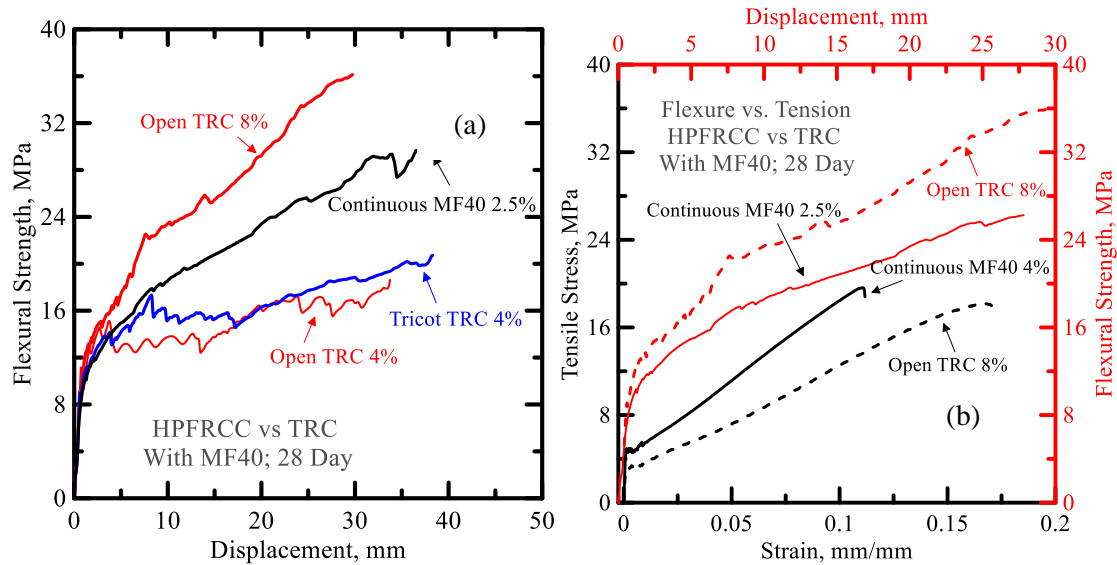
Figure 3-13: (a) Flexural response of MF40 TRC composites; (b) tensile versus flexural response

Results from the tensile and flexural tests are summarized in Tables 3-2 and 3-3. The material property in tension which includes elastic modulus, BOP stress and strain, first crack stress and strain, post crack modulus, ultimate strength capacity, and toughness are reported. Distributed cracking mechanism observed in these TRC specimens can be observed using the DIC technique discussed earlier. Strain contours along the loading direction of TRC specimens made with MF 40- open weave fabrics at dosage of 4% and 8% are shown in Figure 3-14 and 3-15.
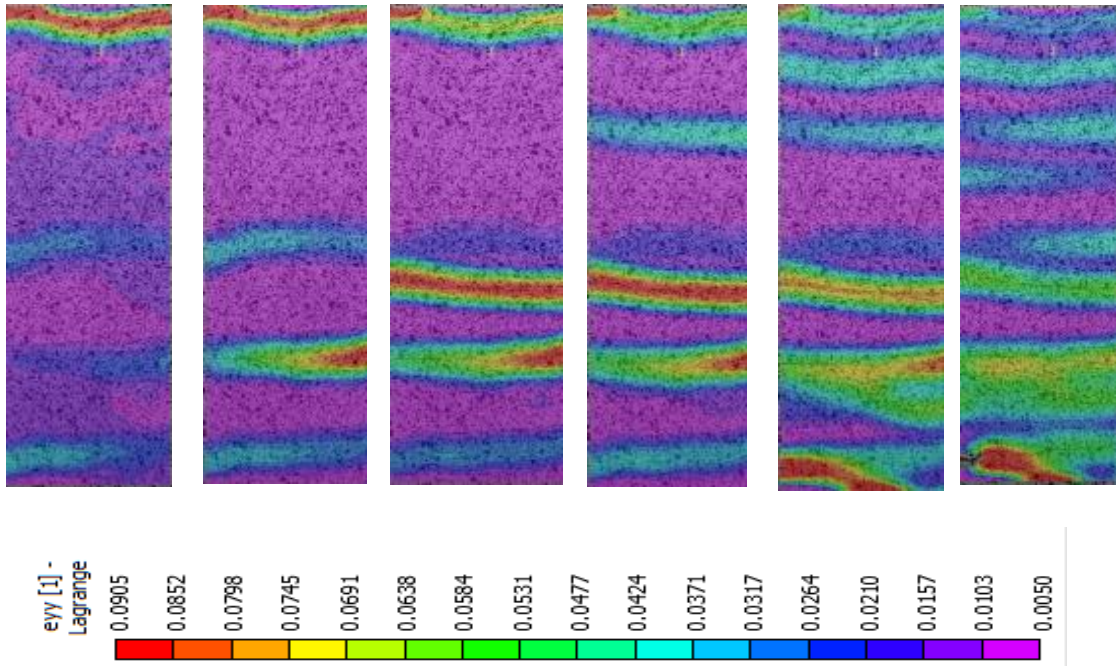
Figure 3-14: Distributed crack and DIC strain contour observed in representative MF 40

Open weave TRC Specimen at 4% dosage
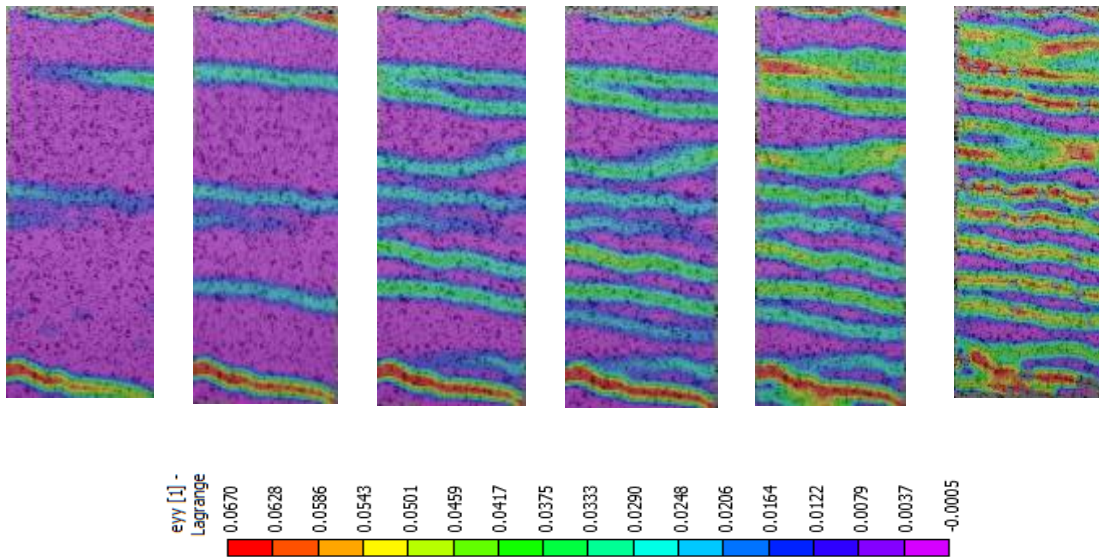
Figure 3-15: Distributed crack and DIC strain contour observed in representative MF 40

Open weave TRC Specimen at 8% dosage

3.4. Analytical Simulation of Tensile Response of Fabric Reinforced Cement Composites

The knitting structure of fabric consists of a large number of interconnected longitudinal and transverse fill yarns, which develops an excellent bond with cement matrix by mechanical interlock and anchorage of yarns [48]. This enhancement can be evaluated in the context of bond stiffness, which maintains the newly formed cracks at a minimal width while transferring the loads back into matrix. A model based on the ply discount method of classical laminate theory [49] and evolution of distributed cracking was used for simulating the tensile behavior of fabric-cement composites. The model correlates the properties of the matrix, fabric, interface and the damage parameters to predict the overall mechanical response of the composites. An incremental approach which updates the stiffness of the nonlinear matrix phase at each loading increment is used and various aspects of stress strain relationship, stiffness degradation, and distributed crack formation are combined. An anisotropic scalar damage parameter is also used to relate the axial strain to the reduction in crack spacing [50,51], while other critical parameters include the stiffness of the cement-fabric system during de-bonding and pullout.

The formulation was applied to simulate the tensile response of continuous polypropylene fiber and textile reinforced concrete composites. Figure 3-16 represents a typical tensile stress strain and distributed cracking response measured using DIC technique discussed earlier, of reinforced cement composite with polypropylene fabric made ofMF40 multifilament fibrillated yarns are presented. The tensile response shows a linear behavior up to about 3.5-4 MPa, beyond this level the stress-strain response becomes nonlinear, while a major change in the stiffness of the sample occurs at Bend Over Point (BOP) around

3-4 MPa and is characterized by a knee in the stress-strain curve. The specimen continues to carry load at a significantly lower stiffness up to an ultimate strain level of close to 20%. In the region between the BOP and ultimate strength, there is evidence of significant distributed cracking, and later on as widening of existing cracks.
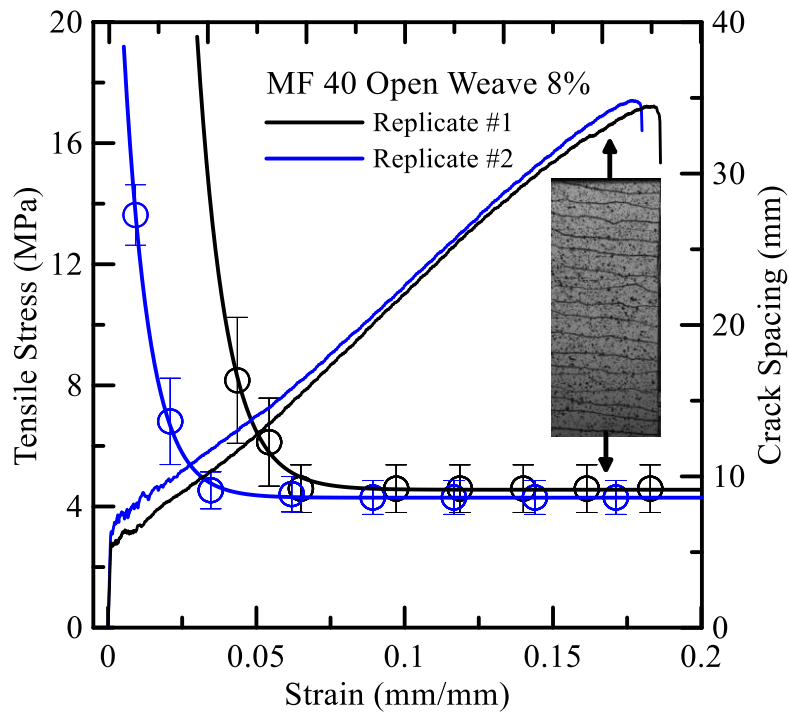
Figure 3-16: The crack spacing and stress as a function of applied strain for the polypropylene textilc reinforced cement based composite

3.4.1. Lamina Stresses and Deformations Prior to Distributed Cracking

A general 2D plane stress approach for the treatment of cross ply laminate composites made with various fiber and matrix materials has been proposed earlier [2]. The cross-section of the specimen throughout its depth can be divided into several layers referred to as lamina and the stresses and strain within each lamina are assumed to remain uniform. Each lamina is modeled as an orthotropic sheet in plane stress with directions "1" and "2"

representing the longitudinal and transverse direction of yarns as shown in Figure 3-17. θ is an angle measured from the axis of loading to the longitudinal direction of yarn "1". The tests reported in the current study represented here are concentric loading i.e. $\theta = 0$, as the loading direction is the same as the longitudinal direction of yarn. Parameters h_k and h_{k+1} refer to the coordinates at the top and bottom of lamina number "k" in a stack of "n" laminates. The property of a layer is specified using the material properties and volume fraction of matrix and fabric components. An incremental approach is used to impose a constant tensile strain field across the cross section for a uniaxial tension case. At each iteration level the strains at the top and bottom of each lamina are increased linearly and applied to the orthotropic model to compute ply stress and identify the state of cracking [52]. The equivalent elastic stiffness assumes the fabric remains elastic and sums their contributions from each layer to the overall value.
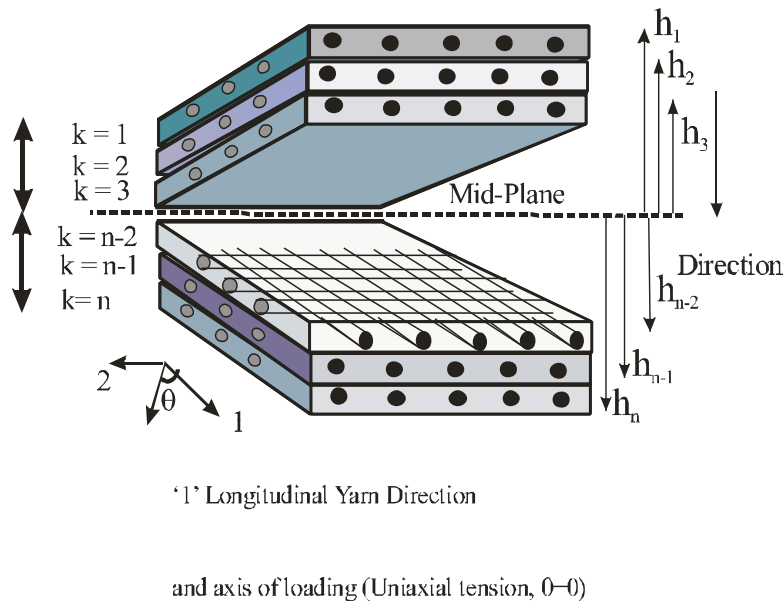
Figure 3-17: Definition of lamina and coordinates used in generating stiffness coefficients [21].

The model proposed for the stress-strain response of the matrix, fabric, and the composite is shown in Figure 3-18. Four distinct zones are identified using roman numerals with two zones prior to BOP and two zones after the BOP range. Zone I corresponds to the elastic-linear range where both matrix and the fabric behave linearly. This zone is modeled using composite laminate theory with an iso-strain model to relate the properties of fabric and matrix to the composite response using rule of mixtures for longitudinal modulus. Due to low volume fraction of fibers (usually less than 10%) the stiffness of the lamina is controlled by matrix properties. This zone is terminated by initial crack formation in the matrix phase at a point labeled "A" and designated as $\sigma_{\tau1}, \varepsilon_{\tau1}$ [53], reported as of BOP-point in the tensile tests. BOP- is the instance of first crack formation resulting in stiffness reduction. The second range (Zone II) is defined as the formation of first complete crack across the cross section between points "A" and "B", defined by the stress levels of σ_{BOP}^- and σ_{BOP}^+. At BOP+ point, the matrix cracks further and propagates across the width of the specimen. The stiffness degradation is assumed to follow a self-consistent approach and degrade up to the BOP$^+$ level according to a single scalar damage parameter 'ω' as proposed by Karihaloo [54] in the form of a power law:

$$\omega(\varepsilon_i) = \omega_1 + \alpha(\varepsilon_i - \varepsilon_{t1})^\beta \qquad \varepsilon_{t1} < \varepsilon_i < \varepsilon_{mu} \qquad \text{Equation 3-1}$$

Where, ε_i is strain at which the damage parameter is computed; ε_{t1} is strain at first crack; $\omega1$, α, and β are constant terms in the power law model. The values of these constants, α and β, are used as fitting parameters and $\omega1 = \varepsilon_{t1}H$ where H is the gage length of the specimen used. Parameter $\sigma t1$ is the tensile strength of the unreinforced matrix past, and

$\varepsilon_{t1} = \sigma_{t1}/E_{m0}$ was defined as the strain at failure under uniaxial tension of the matrix in the absence of fibers as shown in Figure 3.
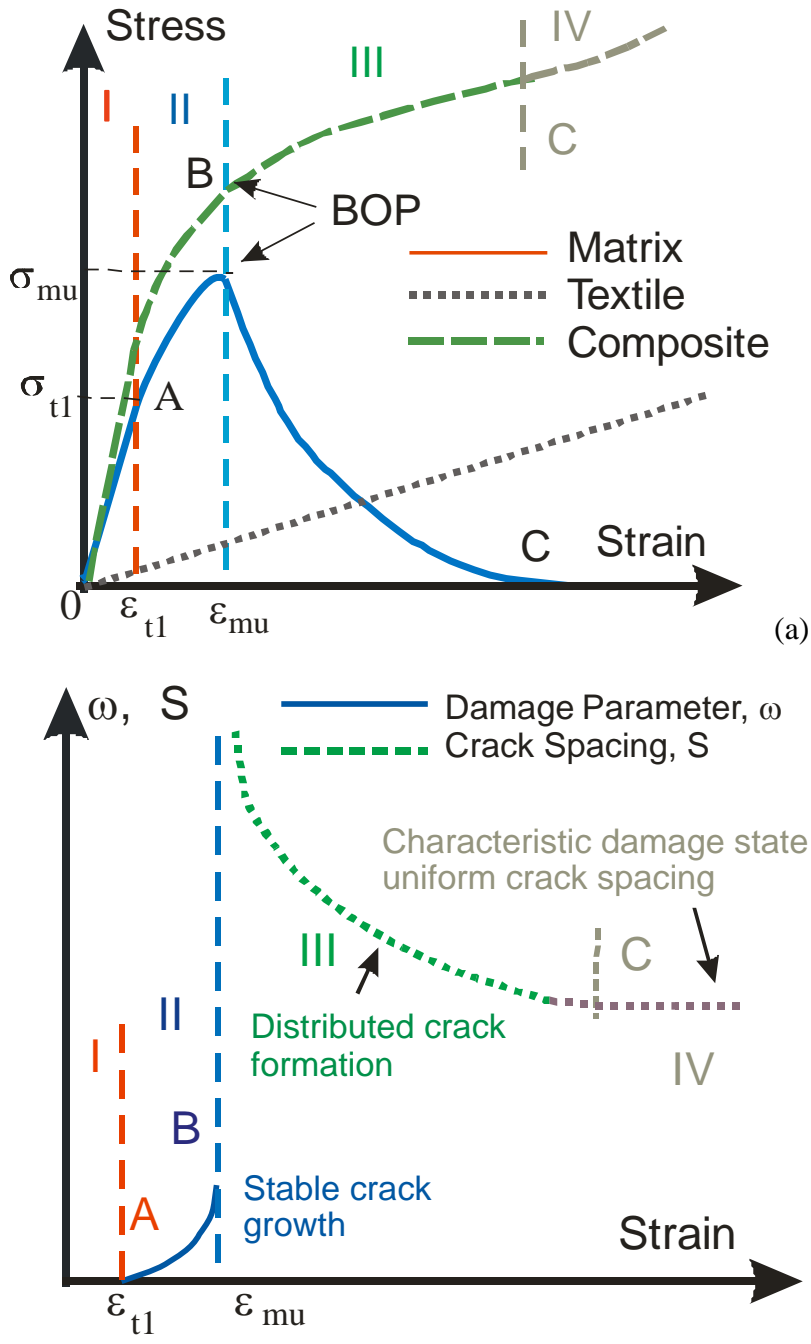
Figure 3-18: Idealized stress-strain response and different damage zones for SHCC systems [55]

The damage parameter, 'ω' was used in a model proposed by Horii [56] and Nemat Nasser and Hori [57]to simulate the decrease in the stiffness in the cracked matrix as the strain increases. Stiffness parameter $E_m(\omega)$, as a function of damage and initial matrix elastic modulus E_{m0} in Zone II was defined:

$$E_m(\omega) = \frac{E_{m0}}{1 + \frac{16}{3}\omega(1 - \upsilon_m^2)} \qquad \text{Equation 3-2}$$

Where ν_m is the Poisson ratio of the matrix. This value of matrix stiffness is used in the rule of mixtures to obtain the longitudinal stiffness of the lamina $E_1(\omega)$. A modified rule of mixture is used in modeling the stiffness computation of a lamina according to Equation 3-3:

$$E_1(\omega) = E_f V_f + E_m(\omega)(1 - V_f) \qquad \text{Equation 3-3}$$

Where, E_f and V_f are the stiffness and volume fraction of the fiber. The stress is computed using an incremental approach by adding the products of strain increments by the effective stiffness at that level. The stress in the matrix phase beyond the elastic range is calculated incrementally as:

$$\sigma_1^i(\omega) = \sigma^{i-1} + \Delta\sigma^i_{\ t} = \sigma_{t1} + \sum_{n=1}^{i} E_m(\omega)(\varepsilon_n - \varepsilon_{n-1}) \quad < \sigma_{mu} \qquad \varepsilon_{t1} < \varepsilon_i < \varepsilon_{mu} \qquad \text{Equation 3-4}$$

The max stress in the matrix phase is achieved at a strain level of ε_{mu} described in the next section using equation 5 and is referred to as σ_{mu}.

3.4.2. Lamina Stresses and Deformations in the Distributed Cracking Zone

Zone II terminates at a damage level corresponding to the stress at the BOP level (σ_{BOP}^+) which is also ultimate strength of matrix in the presence of fibers σ_{mu}. The degraded stiffness at each strain value from ε_{t1} up to the BOP strain level (ε_{mu}) is computed and used

81

to calculate the stress. The parameter ε_{mu} may be theoretically obtained using the ACK approach [58], which predicts the strain capacity of the matrix phase in the presence of fibers as shown in Equation 6.

$$\varepsilon_{mu} = \left[\frac{12\tau\gamma_{\mathrm{m}}E_fV_f^2}{\mathrm{E_c}E_m^2rV_m}\right]^{\frac{1}{3}}$$

Equation 3-5

Where, τ is the shear strength of the matrix; γ_m is the fracture toughness of the matrix; E_c is the composite modulus; r is the fiber radius and V_m is the volume fraction of the matrix. This equation has been verified to be applicable for the cement based materials by showing that the strength of the matrix is increased in the presence of fibers [59].

In this zone, stiffness of the fabric cement system is sufficiently high which prevents widening of existing cracks and promotes additional cracking. Initiation of distributed cracking can be quantified using the distribution of crack spacing measured using the Digital Image Correlation technique discussed in the previous chapter. This approach results in a statistically viable sampled set of data collected at each strain level as shown in Figure 3-16. An empirically based damage evolution law based on an exponentially decaying function representing the crack spacing versus stain was assumed and represented as:

$$S(\varepsilon_i) = S_1 + S_0 e^{-\alpha(\varepsilon_i - \varepsilon_{mu})} \qquad \varepsilon_i > \varepsilon_{mu}$$

Equation 3-6

Where, S is average crack spacing; S_1 is a parameter describing saturation crack spacing; S_0 and α are parameters describing the decay rate; ε_i is strain at which the spacing is computed; ε_{mu} is strain at the BOP(+) level. At sufficiently high strain levels a saturation

level is reached as indicated by the flattening of the crack spacing curve at about 9 mm as shown in Figure 3-16. Beyond this point, reduction in crack spacing is not observed, as further increase in the strain causes widening of existing cracks by fabric pullout. Typical values of S_1, S_0, ε_{mu} and α for different testing combinations based on equation 3-6, are given in Table 3-3. In addition, parameters w_1, α and β for the damage function presented in Equation 3-1, are also provided in the same table.

The gradual reduction of matrix stress levels in the vicinity of the cracked matrix is referred to as the softening zone. In this zone the matrix cracks widen and while there may be no localization in the strain softening zone, the response is modeled by contributions from a softening matrix and the fabric pullout force. The stress strain response of matrix in the post peak region is assumed to be an exponentially decaying function of the maximum stress and asymptotically approach zero.

$$\sigma_1^i(\varepsilon_i) = \sigma_{mu} e^{-q(\varepsilon_i - \varepsilon_{mu})} \qquad \varepsilon_i > \varepsilon_{mu} \qquad \text{Equation 3-7}$$

Where, q represents the exponential coefficient affecting the rate of decay in stress from the peak composite stress. The definition of strain in this region is gage length dependent and the present approach uses the mean strain over the length of several cracks in the matrix. As the specimen undergoes strain softening, an exponential decaying stiffness similar to Equation 8 utilizing the stiffness at peak was used. The modulus $E_m(\varepsilon_i)$, computed for each strain level ε_i, was proportional to the reduction of the stress from the peak value.

Zone IV is dominated by progressive damage and characterized by a crack widening stage ultimately leading to failure by fabric pullout, failure, or delamination. This zone is

asymptotically terminated at the saturation crack spacing represented by parameter S_l. The behavior of both the matrix and the fabric in addition to their interaction is studied in each of these four ranges, and the formulations are compiled together to present a comprehensive material simulation model. In this zone of loading, the cross sections containing matrix cracks are held in equilibrium due to the fabrics which carry the load by bond and eventually fabric pullout mechanism. As fabrics bridge across an existing matrix crack, the stress is transferred back into the matrix through the interfacial zone. A theoretical basis was developed earlier in the group to analyze the experimental results of fabric pullout from a cementitious matrix. The load transfer across a matrix crack can be calculated using a closed form fabric cement bond model [60]. The magnitude of the shear stress is a function of the contact bond stiffness and the frictional properties between the two surfaces. The experimental stiffness values, K, were obtained from single fiber pullout tests conducted earlier. Assuming constant stiffness approach, a linear spring model can be assumed across the crack and the experimental pullout stiffness values can be used. The theoretical method to obtain the entire de-bonding and pullout slip model is presented in an earlier work [61]. The displacement of the specimen is obtained by integrating the strain components in the un-cracked segments and adding it to the slip parameters obtained from

the cracked regions. A representative volume element of the sample in Figure 3-19 shows a single crack across a representative specimen with length equal to average crack spacing.
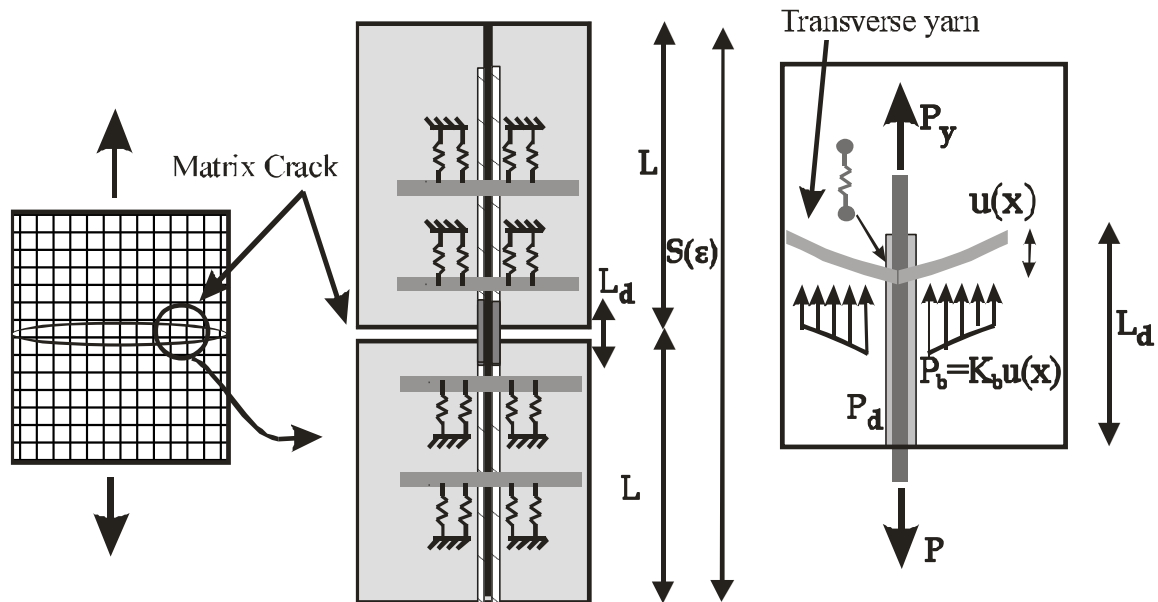
Figure 3-19: Schematic of the distributed cracking and the debonding model, a) composite segment with the length of average crack spacing, b) beam on elastic foundation model, c) load contributions by the debonded region, P_d, bonded region, P_y, and junction P_b

According to the model for Fabric pullout, as shown in Figure 3-19, load on the fabric can be divided in three portions: load carried by the debonded region, P_d, load carried by the bonded region, P_y, and load transferred at the junctions points to the transverse yarns P_b. In the de-bonded region two parameters are important, the debonded length, L_d, and the constant frictional shear stress acting along this length τ_f [62]. In the bonded region, a shear lag mechanism is operating with a decaying shear stress due to parameter β_2 which models the stiffness of the interface. This theoretical procedure was used in order to characterize the pullout slip response of a fabric according to the de-bonded length, and the number of active junctions in redistributing the load. The general load slip relationship for a de-bonding fabric is expressed as:

$$P = P_d + P_y + P_b = \tau_f (2\pi r) L_d + \frac{-2\pi r \tau_{max}}{\beta_2 \coth(\beta_2 (L - L_d))} + \sum_{i=1}^{n} K_b u(x_i)$$

Equation

$$3\text{-}8 \quad U(L) = \frac{P - \tau_f L_d}{E_f \pi r^2 \beta_2} \coth\left(\beta_2 (L - L_d)\right) + \frac{P - \frac{1}{2}\tau_f L_d}{E_f \pi r^2} L_d$$

Equation

3-9

Where, $K_b = \dfrac{2k}{\lambda} \dfrac{\sinh(\lambda l) + \sin(\lambda l)}{\cosh(\lambda l) + \cos(\lambda l) - 2}$ $\qquad \beta_2 = \sqrt{\dfrac{G_i}{E_f \pi r^2}} \qquad \lambda = \sqrt[4]{\dfrac{k}{4EI}}$ Equation 3-10

In these equations, $k = b k_0$. k_0 is the modulus of foundation in N/m^3, b is the constant

width of the beam in contact with the foundation and EI is the flexural rigidity of the yarn

treated as a beam. In the present approach, b is considered as thickness of yarn and I is

calculated from fill-yarn geometry [63]. k_0 and E are considered as the values related to

matrix and fiber interface.

Function $C(P)$ represents the compliance of the de-bonded fabric as a function of applied

load and is obtained from the pullout load slip response defined using Equations 3-8 and

3-9.

$$C(P) = \frac{U(L)}{P} = \frac{\dfrac{-2\pi r \tau_{max}}{\beta_2 \coth(\beta_2 (L - L_d))} + \tau_f (2\pi r) L_d + \sum_{i=1}^{n} K_b u(x_i)}{\dfrac{P - \tau_f L_d}{E_f \pi r^2 \beta_2} \coth\ \beta_2\ L - L_d \ + \dfrac{P - \frac{1}{2}\tau_f L_d}{E_f \pi r^2} L_d}$$

Equation 3-11

Where, $U(L)$ is the slip for embedded length L; P is the pullout load; τ_{max} and τ_f are the

maximum and residual shear strength of the interface; r is the fiber radius, L_d is the

debonded length; K_b is the equivalent spring stiffness obtained from beam on elastic

foundation system; $u(x_i)$ is the deformation in direction of the pullout load; parameter

$\beta_2 = \sqrt{\dfrac{G_i}{E_f \pi r^2}}$, where G_i is the shear modulus of the interface. Assuming constant bond

stiffness measure, K which would require assumption of zero debonded length (i.e. $L_d = 0$); the average displacement $\Delta(\varepsilon_i)$ of the specimen, can be expressed as:

$$\Delta(\varepsilon_i) = \bar{\varepsilon} H = \left[\varepsilon_{mu} + 2P(\varepsilon_i) \frac{1}{KS(\varepsilon_i)} \right] H \qquad \varepsilon_i > \varepsilon_{mu} \qquad \text{Equation 3-}$$

12

Where, H is the gage length. This approach states that the average strain is primarily related

to the magnitude of crack spacing, the force applied, and the stiffness (or compliance) of

the bond between the fabrics and the cement matrix. Using the updated crack spacing, the

quasi-elastic stiffness parameters are obtained and used to calculate the stress and load for

that increment.

3.4.3. Formulation for a Laminate in Tension

Depending on the state of normal strain in each lamina, the stiffness is calculated

incrementally and applied to the orthotropic model to calculate lamina stress. The

constitutive relations for a general orthotropic material include the stiffness matrix which

relates the stress and strain within a lamina loaded in its principal directions. The stiffness

of the matrix phase due to cracking is updated with each increment of applied strain. An

elastically equivalent compliance matrix is calculated with the updated elastic properties.

$$\begin{aligned} \Delta \sigma^i &= E_1(\omega) \Delta \varepsilon^i \\ \sigma^i &= \Delta \sigma^i + \sigma^{i-1} = E_1(\omega) \Delta \varepsilon^i + \sigma^{i-1} \end{aligned} \qquad \text{Equation 3-13}$$

By inverting the compliance matrix, S, the stiffness matrix $\bar{A}$ is obtained [64] which relates the strains into stresses for each lamina loaded in principal material direction:

$$\bar{A} = \sum_{m=1}^{n} E_1(\omega)(h_m - h_{m-1}) \qquad \text{Equation 3-14}$$

$\bar{A}$ is the extensional stiffness of the material, it is used to compute P the force per unit length of cross section and takes into account the layers which have cracked, softened, or fractured. With knowledge of incremental strain the lamina stress is computed for each loading step and the results are added to the loads and strains from previous iteration, i.e. the applied load at the step i[th] (P_i) was represented as:

$$P_i = P_{i-1} + \Delta P_i = P_{i-1} + \bar{A}\Delta\varepsilon_i \qquad \text{Equation}$$

3-15

The ultimate strength of fabric material F_{fu}, was used as the point of termination of computation and used to define the failure of composite at a stress defined as σ_{cu}. The ultimate strength F_{fu}, is dependant on the fabric type and geometry. These values were obtained by multiplying the number of yarns per unit thickness (n/t) by the experimentally obtained strength of plain fabrics.

$$\sigma_{cu} = V_f \sigma_{fu} = nF_{fu}/t \qquad \text{Equation 3-16}$$

The algorithm for calculation of load-deformation in the axial response is as follows:

1) Geometrical dimensions of the lamina and the stacking sequence have to first define.

2) The strain distribution is imposed incrementally, and the stiffness coefficients of matrix $\bar{A}$, are calculated and used to obtain the stress.

3) If the stresses meet the maximum stress criterion, the stress and stiffness are adjusted according to the constitutive response and the material properties are updated for subsequent analysis.

3.5. Prediction of experimental results

The parameters used in the analytical model were calibrated with the experimental results of stress -strain and crack spacing- strain response of continuous polypropylene unidirectional fiber cement composites and polypropylene textile reinforced concrete at different dosages. Elastic modulus and poisons ratio of matrix was assumed to be about 25-30 GPa, and 0.17, where tensile and compressive strength of matrix was assumed to be about 2.5 and 50 MPa. These numbers were observed from previous studies. Fiber properties were obtained from the experiments performed in the previous chapter. Table 3-3 presents the summary of stiffness degradation and crack spacing parameters of these composite specimens. Crack spacing distribution as a function of applied strain is shown in Figure 3-20(a). Figure 3-20(b) presents the experimental and simulated response of continuous fiber composites with macro-synthetic MAC 2200CB fibers under tension at a volume fraction of 1%. As evident the model can successfully predict the tensile responses based on the crack spacing distributions.

The model was also extended to predict the tensile response of MAC 2200CB fiber composites at higher dosages of 2.5% and 4%. These results are shown in Figure 3-21(a-b). As evident, the predicted responses correlate well with the experimental observations.
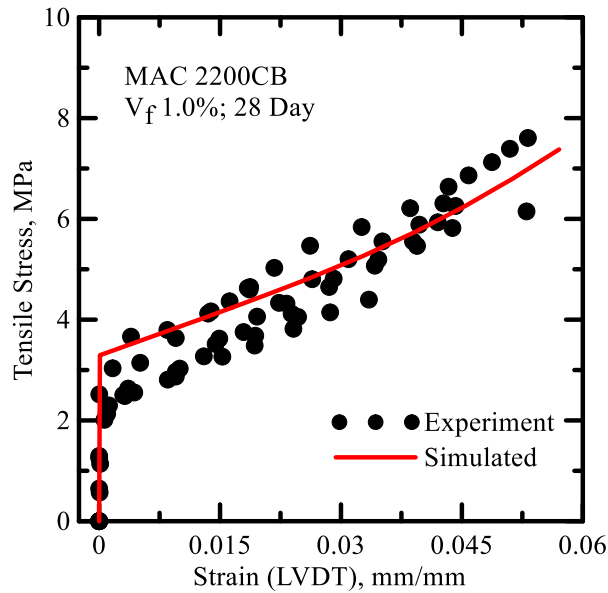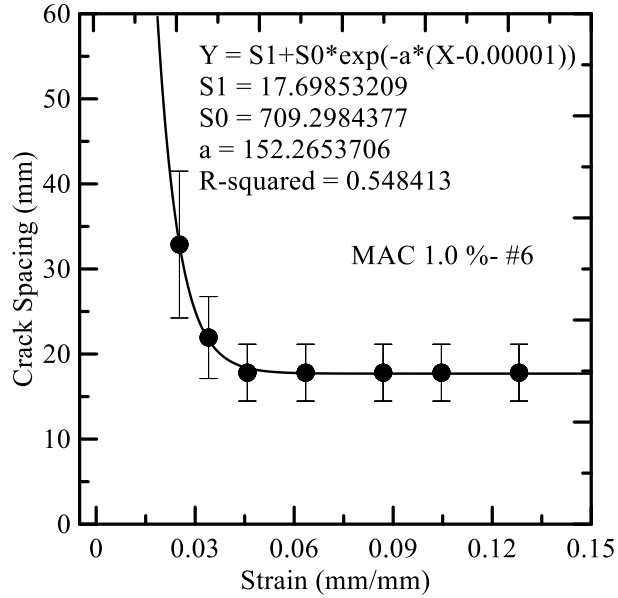
Figure 3-20: (a) Distribution of crack-spacing, (b) predicted tensile response of

MAC2200 CB composites at a dosage of 1%

Effect of dosage of continuous fibers on the overall tensile response of composites is

presented in Figure 3-22. The initial cracking stress, the post crack stiffness, the ultimate

strength, and also the mean crack density are all dependent on the fiber volume fraction.

An increase in the fiber content from 1-4% increases the tensile strength of the composite

by as much as 150%, and the saturation crack density decreases from 18 mm to 10 mm suggesting better bonding with the matrix. Figure 3-22(a) also shows that crack widening is the control mechanism at the low fiber dosage, as the crack spacing function beyond strain of 5% is not significantly changed. This value of strain is significantly less than the strains of about 14% obtained for the higher dosages suggesting higher extent of distributed cracking. The above discussion suggests relatively poor bond of the low-dosage systems whereas, enhanced interaction between the fabric and the cement matrix is indicated for the high fiber dosage composites as most of the tensile response is controlled by multiple cracking mechanisms due to stress transfer between the fabric and the matrix. One can clearly see the effect of the fiber dosage on the model predictions of tangent stiffness of the composite. This change is integrated in the model by means of the crack spacing parameters and stiffness degradation parameters used. Low dosage results in low post-crack stiffness, whereas the composite with the high dosage is much stiffer through the whole range of loading.
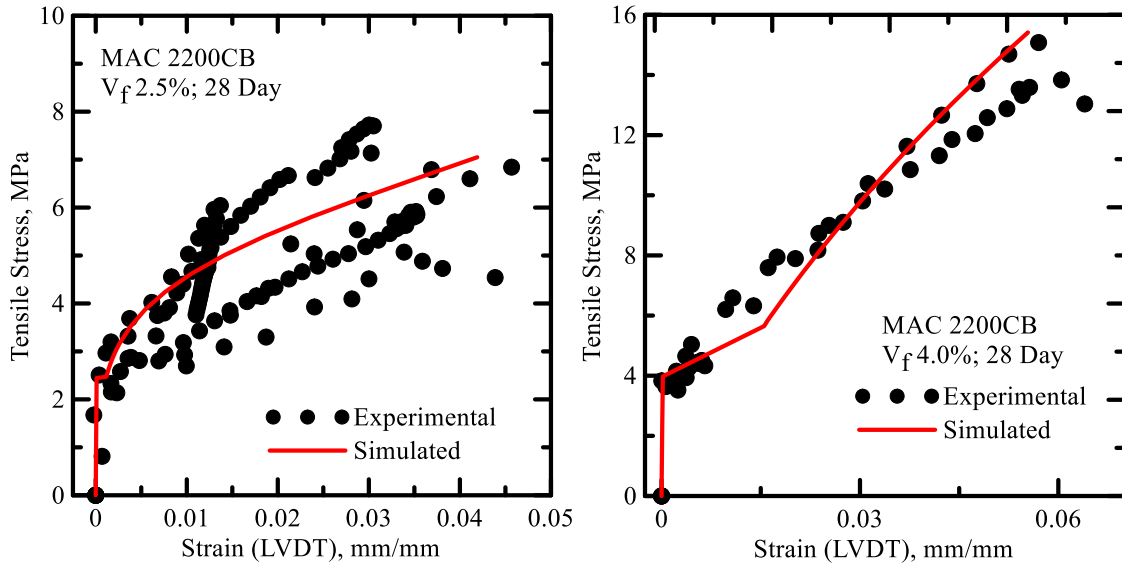
Figure 3-21: Predicted tensile response of MAC 2200CB composites at dosage of a)

2.5%, b) 4%

The same model was extended to simulate the tension response of TRC composites with polypropylene micro-fibers MF40. The effect of volume fraction and weave pattern on the overall tension response of TRC composites are shown in Figure 3-23. Similar to the previous discussion, high dosage results in better stress transfer between the matrix and fibers systems and causes higher extent of distributed cracking in open weave TRC composites with 8 % fiber volume compared to 4%. This results in as much as 200% increase in tensile strength, and reduction in saturated crack spacing from 15 to 10 mm. Effect of weave studied through open and tricot weave is not very distinct in the tension response of these composites.
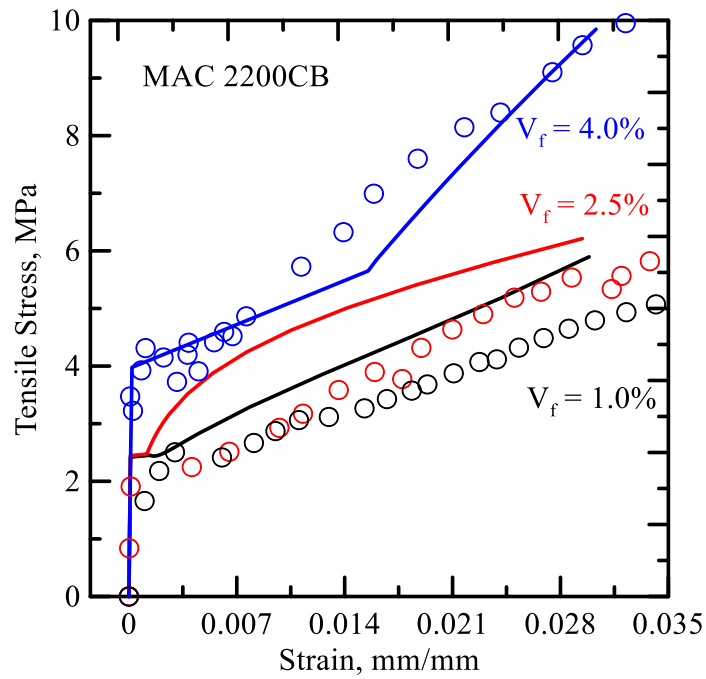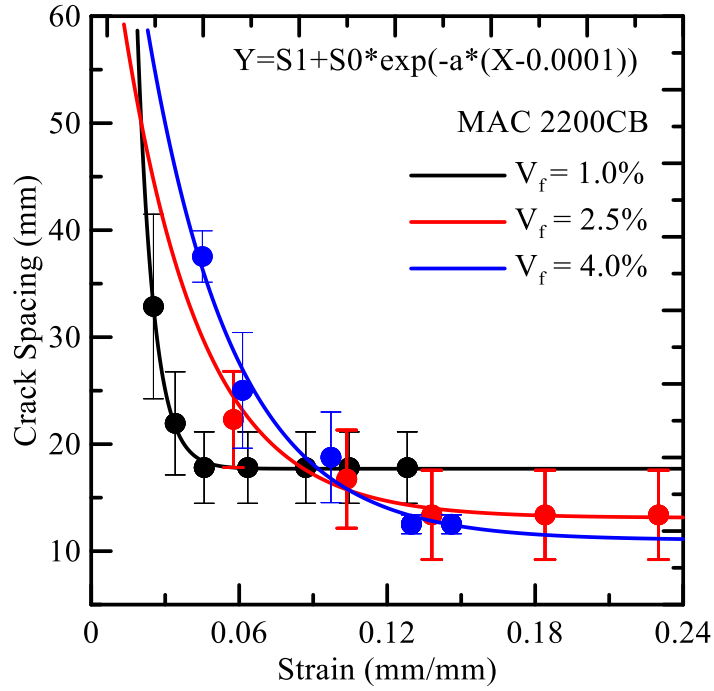
Figure 3-22: Effect of dosage on crack spacing and tensile response of MAC 2200CB composites
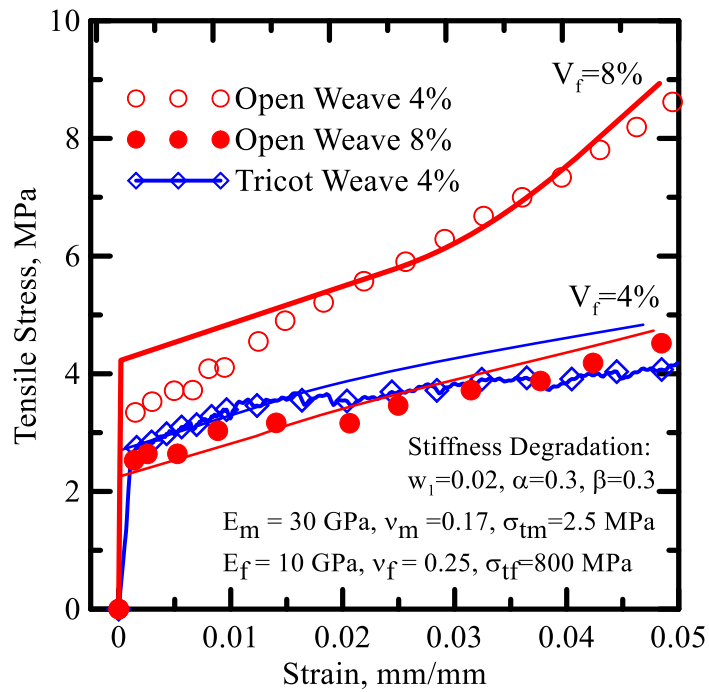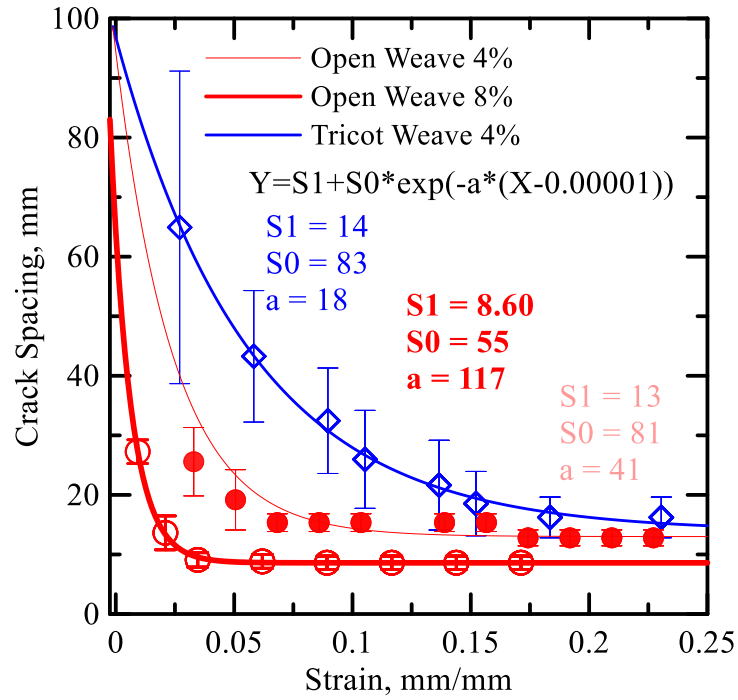
Figure 3-23: Effect of dosage on strain-crack spacing and stress-strain response of TRC composites with MF40 microfibers

Table 3-3: Stiffness and crack spacing parameters obtained from the experimental data and used in the theoretical model.

Specimen Group	Vol. Frac (%)	Stiffness Degradation before peak $\omega_1 + \alpha\,(\varepsilon_t - \varepsilon_{t1})^\beta$			Stiffness Degradation before peak q	Fracture Tough-ness γ_m	Crack spacing $S_1 + S_0*\exp(-\alpha*(\varepsilon_t - \varepsilon_{mu}))$			
		w_1	α	β			S_1	S_0	α	ε_{mu}
MAC220CB - Unidirectional	1.0	0.01	0.2	0.2	50	0.15	7	10	200	1.0E-4
	2.5	0.01	0.25	0.1	30	0.10	8	150	125	1.0E-4
	4.0	0.02	0.4	0.2	0.1	0.5	3.25	18	11	1.0E-4
MF40 – TRC - Open Weave	4.0	0.02	0.2	0.8	0.01	0.05	2	5	500	1.0E-4
	8.0	0.02	0.3	0.3	100	0.1	2.5	5	500	1.0E-4
MF40 – TRC – Tricot Weave	4.0	0.02	0.3	0.3	0.01	0.1	7	2	500	1.0E-4

Table 3-4: Analyzed tension test results from TRC specimens (average in bold, std. dev. in regular fonts)

ID	TRC Type	V_f	Age	Stress at BOP	Strain at BOP	Stress at First Crack	Strain at First Crack	UTS	Strain at UTS	Ult. Strain	E. Modulus	Post-FC Mod.	Tough-ness at 5 % strain
		%	Days	MPa	mm/mm	MPa	mm/mm	MPa	mm/mm	mm/mm	MPa	MPa	MPa
1	MF40-Open	4	7	**1.769**	**0.00005**	**2.706**	**0.00010**	**11.22**	**0.181**	**0.203**	**14233**	**96**	**0.16**
				0.146	0.00007	0.094	0.00007	0.96	0.005	0.015	5654	7	0.01
1a	MF40-Open	4	28	**1.587**	**0.00006**	**2.443**	**0.00035**	**13.06**	**0.201**	**0.217**	**13500**	**130**	**0.16**
				0.655	0.00001	0.983	0.00030	4.59	0.031	0.025	12946	35	0.08
3	MF40-Open	8	30	**2.449**	**0.00011**	**3.020**	**0.00048**	**17.62**	**0.176**	**0.182**	**25233**	**197**	**0.24**
				0.158	0.00004	0.197	0.00013	0.53	0.009	0.013	16651	6	0.02
4	MF40-Tricot Weave	4	8	**1.994**	**0.00007**	**2.599**	**0.00021**	**10.46**	**0.235**	**0.240**	**20667**	**100**	**0.16**
				0.218	0.00005	0.092	0.00009	0.57	0.013	0.010	9713	20	0.01
4a	MF40-Tricot Weave	4	30	**2.203**	**0.00006**	**3.439**	**0.00072**	**10.88**	**0.235**	**0.240**	**23000**	**90**	**0.18**
				1.003	0.00003	0.376	0.00095	0.64	0.003	0.000	16971	15	0.01

Table 3-5: Analyzed flexural test results from TRC specimens

(Average in bold, std. dev. in regular fonts)

ID	TRC Type	Stiffness	Cracking Load	Cracking Defl.	L/150		L/600		Flex. Strength	Defl. at Max Stress	Total Tough-ness
					Load	Residual Stress	Load	Residual Stress			
		N/mm	*N*	*mm*	*N*	*MPa*	*N*	*MPa*	*MPa*	*mm*	*N.mm*
1	MF40 - 4.0% - Open	**458**	**150**	**0.85**	**146**	**6.75**	**49**	**2.35**	**20**	**32.9**	**6772**
		157	6	0.21	21	0.32	13	0.24	4	2.2	350
2	MF40 - 4.0% - Tricot	**948**	**282**	**1.87**	**218**	**5.95**	**111**	**3.03**	**20**	**34.7**	**13653**
		758	62	1.42	105	0.49	82	0.80	2	3.5	8467
3	MF40 - 8.0% - Open	**1247**	**294**	**1.01**	**256**	**6.14**	**153**	**3.75**	**34**	**31.6**	**21081**
		918	71	0.36	109	2.06	99	2.33	4	1.8	4806

4. CORRELATION OF CONSTITUTIVE RESPONSE OF TEXTILE REINFORCED CONCRETE FROM TENSILE AND FLEXURAL TESTS

Textile Reinforced Concrete (TRC) composites utilize innovative fabrics, matrices, and manufacturing processes and have as much as one order of magnitude higher strength, and as much as two orders of magnitude higher in ductility than fiber reinforced concrete [65,66]. Uniaxial tensile strength as high as 25 MPa, and strain capacity of 1-8% are routinely obtained [67,68]. A variety of fiber and fabric systems such as alkali resistant glass fibers (G), polypropylene (P), PVA, aramid (A), and carbon (C) have been utilized [65,69,70]. In order to fully utilize these materials. Material properties and design guidelines are needed to determine the size and dimensions, and expected load carrying capacity of structural members constructed with them.

An analytical constitutive model for back-calculation and design of TRC materials is presented in this paper. Several models have been proposed for correlation of tensile stress-strain response of fiber reinforced concrete to its flexural response. These models can be classified into different groups including cracked hinge formulations by Sousa and Gettu [71], Olesen [72], fictitious crack models by Zhang and Stang [73], Kitsutaka [74], and fracture based models [75,76]. A closed-form formulation presented by Soranakom and Mobasher [77] which has recently been used by Taheri et al. [78, 79], Varma and Barros [80] and Ferrara et al. [81] compares quite favorably with the inverse analysis method of Olesen [82]. This generalized approach for back-calculation of constitutive relationship from experimental data uses closed form moment-curvature equations to obtain the load deflection response of fiber reinforced concrete material [68,83]. Implementation of the inverse analysis algorithm helps in implementation of closed form moment-curvature

models in non-linear finite element analysis for simulation and design of TRC composites [69,83].

This paper extends the back-calculation approach to correlate the tensile and flexural properties of thin sections of cementitious composites, measured from static mechanical tests. Warp knitted fabric alternatives considered in this study are: alkali-resistant glass (AR), polypropylene, carbon and aramid as the reinforcing yarns. In addition, a hybrid composition of aramid and polypropylene textile with yarn ratios of 25:75, 50:50, and 75:25 was also investigated. High-strength, high-modulus fibers primarily tends to increase composite strength, whereas low-modulus fibers are expected to improve toughness and ductility. The motivation was to combine yarns with different properties in one fabric to obtain synergistic effects of high strength and ductility, low cost and improved durability, as compared to traditional single type fiber composite.

4.1. Simplified Strain-Hardening Fiber Reinforced Concrete Model

The tensile behavior of TRC systems has been simplified by a constitutive model of a tri-linear strain-hardening tensile, and an elastic-perfectly-plastic compression model as derived by Soranakom and Mobasher [84, 85]. By normalizing all parameters with respect to minimum number of variables, closed form derivations are obtained. Material parameters as shown in Figure 4-1 are summarized as tensile stiffness E, first crack tensile strain ε_{cr}, cracking tensile strength $\sigma_{cr} = E\varepsilon_{cr}$, and post cracking modulus E_{cr} which is assigned a negative or positive value in order to simulate either strain softening or hardening materials. Constant tensile strength at the end of tension model $\sigma_{cst} = \mu E\varepsilon_c$ and an ultimate tensile capacity ε_{tu}, are defined in the postcrack region.
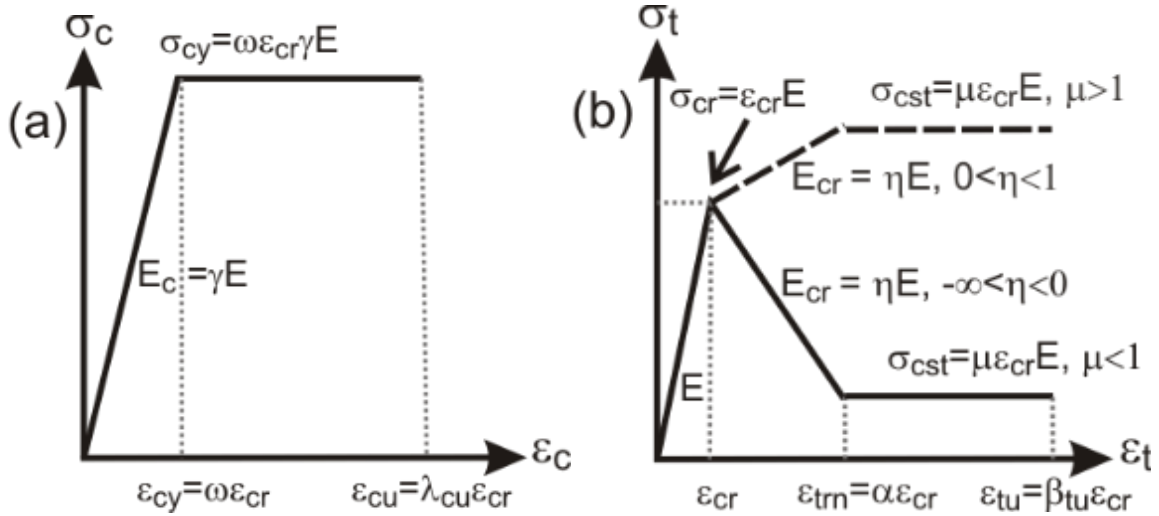
Figure 4-1: Full option material models for both strain-hardening and strain-softening FRC: (a) compression model; and (b) Tension model [23, 24].

The elastic-perfectly-plastic compressive stress-strain is characterized by a linear response which is terminates at yield point (ε_{cy}, σ_{cy}). This is followed by a plateau phase in the stress-strain response at constant compressive yield stress $\sigma_{cy}=\omega\varepsilon_{cr}\gamma E$ until reaching the ultimate compressive strain ε_{cu} as shown in Fig. 1a. Applied tensile and compressive strains at bottom and top fibers, β and λ are also defined as model variables. Using the first crack tensile strain and modulus as intrinsic material parameters, ε_{cr} and E, seven normalized variables are defined as listed in Table 1(a) for different fiber reinforced materials. Parameter γ represents the ratio of modulus of elasticity tension to compression [86]. For a rectangular cross section with a width "b" and depth "d", the Kirchhoff hypothesis is applied. The normalized maximum tensile strain, β and maximum compressive strain λ are linearly related through the neutral axis parameter, k as in Equation 4-1.

$$\beta = \frac{\varepsilon_{tbot}}{\varepsilon_{cr}}; \quad \lambda = \frac{\varepsilon_{ctop}}{\varepsilon_{cr}}; \quad \frac{\lambda\varepsilon_{cr}}{kd} = \frac{\beta\varepsilon_{cr}}{d-kd} \quad \text{or} \quad \lambda = \frac{k}{1-k}\beta \qquad \text{Equation 4-1}$$

Using the parameters defined in Table 4-1 and Equation 4-1, normalized stress strain responses and toughness G_f are expressed as:

$$\frac{\sigma_c(\lambda)}{E\varepsilon_{cr}} = \begin{cases} \gamma\lambda & 0 \le \lambda \le \omega \\ \gamma\omega & \omega < \lambda \le \lambda_{cu} \\ 0 & \lambda_{cu} < \lambda \end{cases} \qquad \frac{\sigma_t(\beta)}{E\varepsilon_{cr}} = \begin{cases} \beta & 0 \le \beta \le 1 \\ 1+\eta(\beta-1) & 1 < \beta \le \alpha \\ \mu & \alpha < \beta \le \beta_{tu} \\ 0 & \beta_{tu} \le \beta \end{cases}$$

Equation 4-2

$$G_f = E\varepsilon_{cr}^2 \left[\left(\frac{\alpha - \mu - \mu\alpha}{2} \right) + \mu\beta_{tu} \right]$$

Equation 4-3

Table 4-1: Back calculation model parameters

Normalized tensile strain	$\alpha = \dfrac{\varepsilon_{trn}}{\varepsilon_{cr}}$
Constant post peak stress level	$\mu = \dfrac{\sigma_{cst}}{E\varepsilon_{cr}}$
Post-crack modulus	$\eta = \dfrac{E_{cr}}{E}$
Compressive yield strain	$\omega = \dfrac{\varepsilon_{cy}}{\varepsilon_{cr}}$
Tensile strain at bottom fiber	$\beta = \dfrac{\varepsilon_t}{\varepsilon_{cr}}$
Compressive strain at top fiber	$\lambda = \dfrac{\varepsilon_c}{\varepsilon_{cr}}$

Parameter α represents the strain capacity normalized with respect to the first crack strain, ε_{cr}. Parameter η represents the post crack stiffness normalized with respect to the initial stiffness, E, and parameter μ represents the post tensile strength strain softening parameter which is normalized with respect to the first crack strain ε_{cr}. By assuming linear strain distribution across the depth and ignoring shear deformations, stress distribution across the

cross section at three stages of imposed tensile strain: $0 \leq \beta \leq 1$, $1 < \beta \leq \alpha$ and $\alpha < \beta \leq \beta_{tu}$ is obtained in closed form [84].

Moment capacity of a beam section according to the imposed tensile strain at the bottom fiber ($\varepsilon_t = \beta\varepsilon_{cr}$) is derived based on the force components and the centroidal distance to the neutr al axis. The location of neutral axis, k, moment, $M^{'}$ and curvature $\phi^{'}$, for a given tensile strain level β are provided in Table 4-2 and represents all potential combinations of interaction of tensile and compressive material models. The moment M_i and curvature ϕ_i at each stage i (corresponding to input β) are normalized with respect to the values at cracking M_{cr} and ϕ_{cr}.

$$M(\lambda,k,\omega,\mu) = M_{cr} M^{'}(\lambda,k,\omega,\mu); M_{cr} = \frac{1}{6}bd^2 E\varepsilon_{cr}$$
<div align="right">Equation 4-4</div>

$$\phi(\lambda,k,\omega,\mu) = \phi_{cr}\varphi^{'}(\lambda,k,\omega,\mu); \varphi_{cr} = \frac{2\varepsilon_{cr}}{d}$$
<div align="right">Equation 4-5</div>

During stage 1, the tensile and compressive zones are both elastic and are represented as a straight line on a moment-curvature plot. As the elastic stage 1 ends by the initiation of tensile cracking, the neutral axis moves toward the compression zone. The compression zone is in elastic behavior as Stage 2.1 (tension cracking-elastic compression) or plastic range, Stage 2.2 (tension cracking -plastic compression). As the tension response dominates, the condition in Stage 2.1 ends under two potential alternatives of entering either of region 3.1 or region 2.2, depending on the compression zone in elastic or plastic range. If the compression zone has already entered the plastic range (2.2) then the next step would be tension softening-plastic compression or Stage 3.2. Depending on the relationship among material parameters, any of the stages 2.1 and 2.2, or 3.1 and 3.2 are potentially possible in succession, however in typical strain-hardening FRC, with compressive

strength higher than tensile strength, the flexural capacity is controlled by the tension component.

Table 4-2: Neutral axis parameter k, normalized moment M' and normalized curvature ϕ' for each stage of normalized tensile strain at bottom fiber (β) [23, 24].

Stage	k	M_i' and ϕ_i'
1 $0<\beta\leq1$	$k_1 = \begin{cases} \dfrac{1}{2} & \text{for } \gamma=1 \\[2mm] \dfrac{-1+\sqrt{\gamma}}{-1+\gamma} & \text{for } \gamma<1 \text{ or } \gamma>1 \end{cases}$	$M'_1 = \dfrac{2\beta\left[(\gamma-1)k_1^3 + 3k_1^2 - 3k_1 + 1\right]}{1-k_1}$ $\phi'_1 = \dfrac{\beta}{2(1-k_1)}$
2.1 $1<\beta\leq\alpha$ $0<\lambda\leq\omega$	$k_{21} = \dfrac{\beta^2\gamma + D_{21} - \sqrt{\gamma^2\beta^4 + D_{21}\gamma\beta^2}}{D_{21}}$ $D_{21} = \eta\left(\beta^2 - 2\beta + 1\right)$ $+2\beta - \beta^2\gamma - 1$	$M'_{21} = \dfrac{(2\beta\gamma + C_{21})k_{21}^3 - 3C_{21}k_{21}^2 + 3C_{21}k_{21} - C_{21}}{1-k_{21}}$ $C_{21} = \dfrac{-2\eta\beta^3 + 3\eta\beta^2 - 3\beta^2 - \eta + 1}{\beta^2}$ $\phi'_{21} = \dfrac{\beta}{2(1-k_{21})}$
2.2 $1<\beta\leq\alpha$ $\omega<\lambda\leq\lambda_{\chi\upsilon}$	$k_{22} = \dfrac{D_{22}}{D_{22} + 2\omega\gamma\beta}$ $D_{22} = \eta\left(\beta^2 - 2\beta + 1\right)$ $+2\beta + \omega^2\gamma - 1$	$M'_{22} = (3\omega\gamma + C_{22})k_{22}^2 - 2C_{22}k_{22} + C_{22}$ $C_{22} = \dfrac{2\eta\beta^3 - 3\eta\beta^2 + 3\beta^2 - \omega^3\gamma + \eta - 1}{\beta^2}$ $\phi'_{22} = \dfrac{\beta}{2(1-k_{22})}$
3.1 $\alpha<\beta\leq\beta_{\tau\upsilon}$ $0<\lambda\leq\omega$	$k_{31} = \dfrac{D_{31} - \sqrt{\gamma\beta^2 D_{31}}}{D_{31} - \beta^2\gamma}$ $D_{31} = \eta\left(\alpha^2 - 2\alpha + 1\right)$ $+2\mu(\beta - \alpha) + 2\alpha - 1$	$M'_{31} = \dfrac{(C_{31} - 2\beta\gamma)k_{31}^3 - 3C_{31}k_{31}^2 + 3C_{31}k_{31} - C_{31}}{k_{31} - 1}$ $C_{31} = \dfrac{3\left(\mu\beta^2 - \mu\alpha^2 - \eta\alpha^2 + \alpha^2\right) + 2\eta\alpha^3 + \eta - 1}{\beta^2}$ $\phi'_{31} = \dfrac{\beta}{2(1-k_{31})}$
3.2 $\alpha<\beta\leq\beta_{\tau\upsilon}$ $\omega<\lambda\leq\lambda_{\chi\upsilon}$	$k_{32} = \dfrac{D_{32}}{D_{32} + 2\omega\gamma\beta}$ $D_{32} = \omega^2\gamma + \eta\alpha^2$ $+2\left(\mu\beta - \eta\alpha - \mu\alpha + \alpha\right) + \eta - 1$	$M'_{32} = (C_{32} + 3\omega\gamma)k_{32}^2 - 2C_{32}k_{32} + C_{32}$ $C_{32} = \dfrac{3\left(\mu\beta^2 - \mu\alpha^2 - \eta\alpha^2 + \alpha^2\right) + 2\eta\alpha^3 - \omega^3\gamma + \eta - 1}{\beta^2}$ $\phi'_{32} = \dfrac{\beta}{2(1-k_{32})}$

Steps in calculation of load-deflection response from the moment-curvature have been discussed in detail in recent publications dealing with strain hardening [87] and softening type composites [88].The load–deflection response of a beam can be obtained by moment distribution and moment–curvature relationship using crack localization rules. The mid-span deflection is obtained directly using the double integration of curvature distribution, or by closed form solution of bilinear moment curvature response. A set of equations for calculating the mid-span deflection δ of four-point and three-point bending at the first cracking (δ_{cr}) and at ultimate (δ_u) under the condition of $\mu > \mu_{crit}$ are presented in Table 4-3.

Table 4-3: Equations for calculating deflection at mid-span

Deflection	Four-point bending	Three-point bending
Elastic region	$\delta_{cr} = \dfrac{23}{216} L^2 \varphi_{cr}$	$\delta_{cr} = \dfrac{1}{12} L^2 \varphi_{cr}$
$\mu > \mu_{crit}$ Deflection hardening	$\delta_u = \dfrac{L^2}{216}\left[a_1 \varphi_u + a_2 \varphi_{cr}\right]$ $b = \dfrac{M_{cr}}{M_u},$ $a_1 = 23 - 4b - 4b^2, \quad a_2 = 4 + 4b$	$\delta_u = \dfrac{L^2}{24}\left[a_1 \varphi_u + a_2 \varphi_{cr}\right]$ $b = \dfrac{M_{cr}}{M_u},$ $a_1 = 2 - b - b^2, \quad a_2 = 4 + b$
$\mu < \mu_{crit}$ Deflection hardening or softening	$\delta_u = \dfrac{5L^2 \varphi_u}{72} + \dfrac{M_u L^2 \varphi_{cr}}{27 M_{cr}}$	$\delta_u = \dfrac{\varphi_u L_p}{8}\left(2L - L_p\right) + \dfrac{M_u \varphi_{cr} L}{12 M_{cr}}\left(L - 2L_p\right)$

Applicability of this model on TRC composites was verified by analyzing a series of available data. Tensile response of polyethylene (PE) textile reinforced composite [70,89], glass and carbon fiber cementitious laminates [90] along with steel fiber-reinforced concrete (SFRC) [91] were studied. The simulation of the experimental data are shown in Figure 4-2.
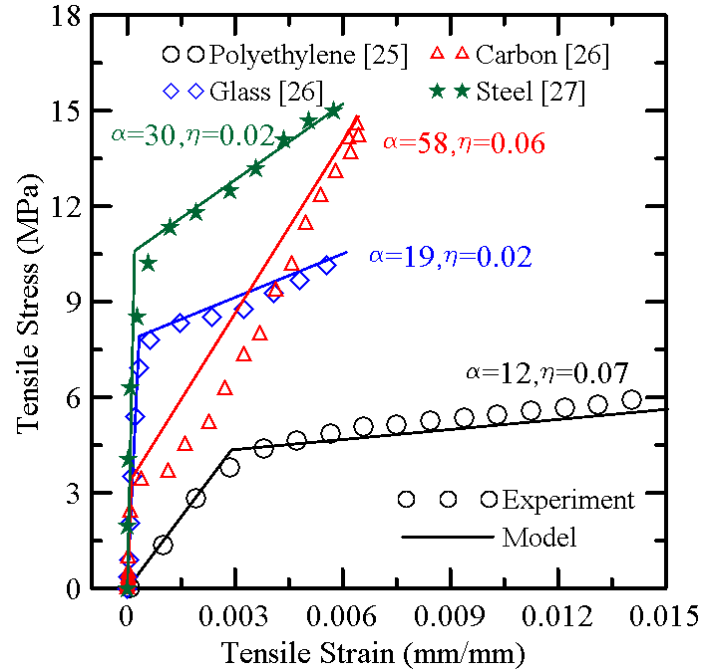
Figure 4-2: Simulation of reference tensile response of textile reinforced concrete (TRC)

[25, 26], steel fiber reinforced concrete [27].

Modelling parameters introduced in Table 4-4 which were used to calibrate the model for the experimental tensile responses and reported in Table 4-4. As evident the analytical approach is able to predict the tensile properties of the different cementitious composites with a reasonable degree of accuracy. However availability of flexural properties of these composites from experiments assists in essentially verifying the predictions in a more realistic manner. As in that case, tensile properties can be back-calculated from more convenient flexural tests using an inverse analysis algorithm. The design-oriented model based on the inverse analysis has been adopted in the current study, to explicitly study the behavior of TRC composites with mono and hybrid fabric systems.

Table 4-4: Model parameters used to simulate tensile response of reference data

Ref. Data	E (MPa)	ε_{cr} (μstr)	α	η	μ	β_{tu}
Polyethylene TRC [46]	1500	2900	12	0.070	0.80	14
Glass TRC [47]	24000	330	19	0.019	0.16	20
Carbon TRC [47]	31000	111	58	0.058	0.90	58
Steel FRC [48]	53000	200	30	0.015	0.65	75

4.2. Experimental Plan

The mechanical performance of four different warp knitted textiles were examined. Two types of composites were studied: (i) plain single fiber type composites made with both high and low modulus textiles, and (ii) hybrid composites. This was in order to evaluate whether a combination of low stiffness fibers in the presence of high stiffness fibers can provide a level of reinforcement that is comparable to 100% systems, i.e., fabrics with only one yarn type. Hybrid composites were made with a combination of different yarns of low and high modulus within a single fabric. Aramid (A), carbon (C), and AR glass yarns (G) were used as the high strength/high stiffness systems and polypropylene (P) yarns were selected as low strength systems as shown in Table 4-5.

Note that the bundle diameter was calculated based on tex number. The aramid yarns were prepared with 322 tex and the polypropylene with 444 tex. In all fabrics the weft yarns (perpendicular to the loading direction) were AR glass with 1200 tex. The stitches connected the yarns together to a fabric form were of polypropylene with 16.7 tex. The reinforcing (warp) yarns were inserted in a two in - two out formation, e.g., two yarns are

as a pair and then two as empty spaces, alternately. The weft yarns were inserted in a one in one out formation. Both warp and weft yarns were made from multifilament bundle. All cement board specimens were prepared by the pultrusion process [3, 14] with 4 layers of fabrics. The matrix in all cases was a plain cement paste with water cement ratio of 0.4, compressive strength of 51 MPa and flexural strength of 5 MPa (83N) with brittle behavior. Two sets of laminated cement boards were prepared: (i) single (mono) fabric board of one yarn type; and (ii) hybrid fabric board using combination of aramid and polypropylene yarns at each fabric layer. The general fabric structure of mono-fabrics and hybrid-fabrics are shown in Figure 4-4.

Table 4-5: Properties and geometry of yarns made up the fabrics (under static condition)

Yarn type	Yarn nature	Tensile strength, MPa	Modulus of elasticity, MPa	Filament size, mm	*Bundle diameter, mm
PE	Monofilament	240	1760	0.250	0.25
Aramid	Bundle	2370	55000	0.012	0.38
Carbon	Bundle	2200	240000	0.008	1.15
AR Glass	Bundle	1372	72000	0.014	0.30
PP	Bundle	500	6900	0.040	0.40

Table 4-6: Experimental data used for back-calculation

	Details of System	Nomenclature
100 % TRC Systems	Aramid	100A
	Carbon	100C
	Glass	100G
	Polypropylene	100P
Hybrid TRC Systems	75% Aramid – 25% Polypropylene	75A25P
	50% Aramid – 50% Polypropylene	50A50P
	25% Aramid – 75% Polypropylene	25A75P

The results of 100% systems. i.e., individual aramid, carbon, glass, and polypropylene fabrics, and the aramid-polypropylene hybrid system are discussed. Aramid-polypropylene yarns were combined in a single fabric, located along the longitudinal direction of the fabric (warp direction) and reinforcing direction of the composite. Different hybrid fabric combinations were investigated with ratios of: 100:0, 75:25, 50:50, 25:75, 0:100%, aramid (A) -polypropylene (P) respectively, providing five different combinations referred to as follows: 100A, 75A25P, 50A50P, 25A75P and 100P (see Figure 4-4 for yarns arrangement within the fabrics). The volume fractions of reinforcements at each composite of both mono and hybrid types are presented in Table 4-7.

Table 4-7: Volume fraction (V_f) of reinforcement

Specimen Code		V_f(%)		
		Composite	Polypropylene	Aramid
100A	**Average**	**1.29**		**1.29**
	Std.	0.06		0.06
100C	**Average**	**5.16**		
	Std.	0.04		
100G	**Average**	**2.29**		
	Std.	0.24		
100P	**Average**	**3.02**	**3.02**	
	Std.	0.09	0.09	
75A25P	**Average**	**1.75**	**1.01**	**0.74**
	Std.	0.07	0.04	0.03
50A50P	**Average**	**2.11**	**0.66**	**1.45**
	Std.	0.10	0.03	0.07
25A75P	**Average**	**2.58**	**0.34**	**2.24**
	Std.	0.07	0.01	0.06

For the hybrid composites the average value of both yarns is presented as well as the volume fraction of each yarn within the fabric. For the hybrid composites with 75/25 ratios at each fabric layer, three yarns were of one material (P or A) and one from the second

material (P or A). For the bending tests three specimens were prepared where the single yarns were in the middle of the specimen and three specimens were prepared where the single yarns were at the side of the specimen for each composite type. No difference was observed in behavior during the bending tests between the two specimen sets, thus the average values are included in the results of both yarn locations.

The effect of various fabric types in suppressing the localization and crack bridging mechanisms as well as the microstructure were studied using tensile stress-strain results. Uniaxial tension tests were conducted on a closed loop control MTS testing machine with a capacity of 89KN. The rate of cross head displacement was set at 0.008 mm/sec. Metal plates with dimension of 25 x 50 mm and 1 mm thick were glued on the gripping edges of the specimen to minimize localized damage and allow better load transfer from the grips. Samples were held using hydraulic grips operated at low pressure to avoid localized crushing. Another identical sets of samples were tested in flexure. The flexural specimens were tested under a three point bending configuration with a clear span of 220 mm, with 15 mm of overhang on each side of the supports. Six replicate samples of each category were tested under flexure and tension. Results in Tables 4-8, 4-9 reflect the average and standard deviation values obtained from these tests. All the specimens were of dimensions 250 (L) x 30 (B) x 9 (D) mm. For tension experiments, free length between the grips of the specimen (gage length) was maintained as 150 mm. Stress-strain response of several replicate coupons of four different mono-TRC composites tested as shown in Figure 4-4. Typical stress-strain curves representing the tensile behavior and typical load-deflection curves representing the flexure behavior of individual composites of mono and hybrid type were chosen for comparison.
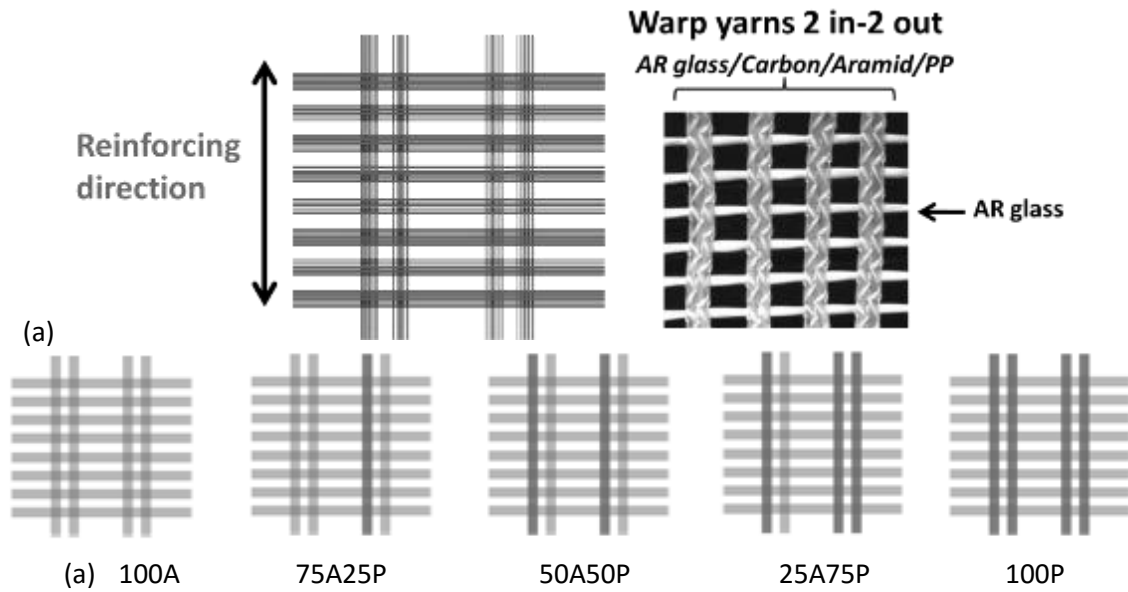
Figure 4-3: General fabric structure of (a) mono and, (b) hybrid fabrics
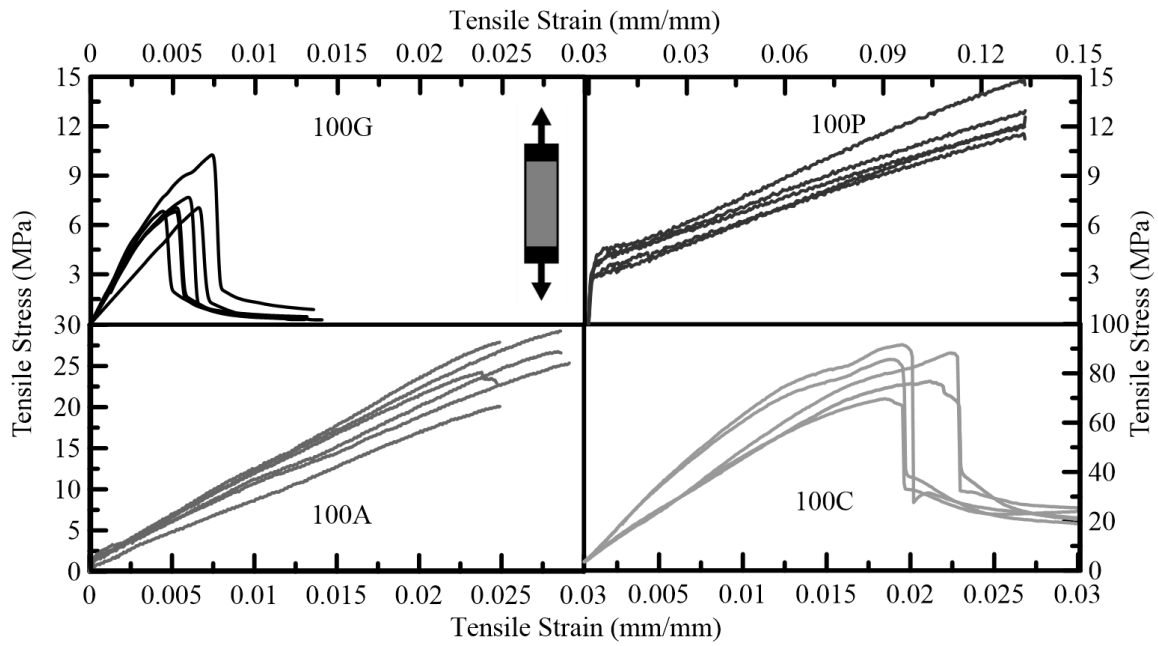
Figure 4-4: Experimental tensile stress-strain response of TRC laminates

Table 4-8: Average experimental flexural data of representative TRC samples.

Specimen Code		Stress at 1st Crack	Max Flex Load	Defl at Max Flex Load	Defl Capacity	Flexural Toughness	Flexural Stiffness	Flex. Strngth, MOR
		MPa	N	mm	mm	N-mm	N/mm	MPa
100A	Average	5.9	338	18.8	23.0	4035	47	46.9
	SD	1.8	82	2.4	4.0	832	24	14.3
100C	Average	8.3	509	9.1	21.7	5061	63	64.3
	SD.	1.6	76	1.5	0.3	1349	19	6.3
100G	Average	2.3	180	2.3	14.0	495	139	17.0
	SD v.	0.6	30	0.5	1.3	41	46	3.6
100P	Average	3.0	89	32.7	32.9	2026	97	12.2
	SD.	0.8	8	8.3	8.2	789	17	1.7
75A25P	Average	9.1	405	21.5	29.4	5673	48	60.7
	SD.	3.3	119	3.8	0.2	1593	18	20.4
50A50P	Average	5.1	316	21.9	29.6	5495	88	44.3
	SD	1.3	60	2.9	0.0	1537	38	8.1
25A75P	Average	4.5	214	22.9	29.6	3778	66	31.2
	SD	1.8	52	3.7	0.1	567	19	7.0

Table 4-9: Average experimental tension data of representative TRC samples.

Specimen code		Cracking Load	Stress at 1st Crack	Maximum Load	Displacement at Max Load	Stiffness	Tensile Strength
		N	Mpa	N	mm	N/mm	Mpa
100A	Average	286	1.0	7086	4.1	16642	25.9
	Std. Dev.	90	0.5	589	0.4	7149	3.1
100C	Average	361	1.3	22207	2.9	35947	79.5
	Std. Dev.	153	0.8	2097	0.4	16887	10.7
100G	Average	399	1.3	2077	0.9	2521	6.6
	Std. Dev.	161	0.5	362	0.2	466	1.1
100P	Average	405	1.5	3047	18.3	8340	11.7
	Std. Dev.	213	0.8	834	4.1	2712	3.1
75A25P	Average	176	0.6	5595	3.9	15900	20.5
	Std. Dev.	96	0.4	1460	0.5	10909	6.5
50A50P	Average	200	0.7	3986	3.9	23171	14.8
	Std. Dev.	68	0.2	813	0.3	5691	2.8
25A75P	Average	304	1.2	2883	8.3	10231	11.0
	Std. Dev.	97	0.3	507	10.1	6682	1.7

Load-deflection response of fabric cement composites was used to back-calculate the mechanical properties of different TRC composites including the upper and lower bound curves [68, 70]. In order to correlate the responses, experimental data for each set of specimens under uniaxial tension and three point bending tests were used. It is to be noted that no attempt was made to obtain best fit models to the flexural or tensile responses. The material parameters were determined by fitting the hardening model to both the uniaxial tension and flexural tests result. The result is shown by the simulated upper and lower bounds encompassing all the selected composites. A summary of results in each category are presented next.

4.3. 100% Systems

There are two ways to accomplish the curve fitting, forward calculation using tension data and back-calculation of the flexural data. Only the back-calculation approach is used since it uses multiple attempts of the forward calculation procedure. Curve fitting of flexural results by varying the input tensile data was accomplished for the composites with the 100% mono fabrics, i.e., aramid (100A) carbon (100C), glass (100G) and polypropylene (100P) and the resulting final tensile model was compared with the experimental tension data. The key parameters α, η, and μ were changed to fit the experimental load-deflection and predict tensile stress-strain curves and the results are shown in Table 4-9. Figures 4-5, 4-6, 4-8, and 4-9 present the comparison of the simulated curves with the experimental responses of mono fabric samples. Solid lines represent the simulated response for both flexural and tensile response, obtained from the constitutive model. Experimental flexural data is represented by symbols only, whereas experimental tensile responses are presented as shaded bands. Table 4-9 summarizes the results of prediction of tension model based on

111

flexural load-deflection responses. Material parameters, α and β_{tu} are scalar multipliers that apply to the first crack strain, ε_{cr}. Parameters γ and η are multipliers that apply to the modulus E. Parameter, μ is a scalar multiplier that applies to the first crack tensile strength, σ_{cr}. Simulated flexural response is therefore generated by changing these tri-linear tensile model parameters using an approach to fit the elastic modulus, E, followed by cracking strain parameter, ε_{cr} which determines the start of elastic-plastic phase. Post-cracking modulus, η is obtained from the post-cracking slope, and the transition phase is terminated by strain capacity, α. Finally, the residual strength parameter, μ is used to simulate the constant stress region.

Figure 4-5 shows the experimental and predicted responses of mono aramid fabric composites (100 A). Figure 4-5a shows the flexural load-deflection and Figure 4-5b shows the tensile stress-strain responses of the aramid composites. The load versus deflection response based on the simulated fit of the data matches the experimental response as shown in Figure 6a. The overall predictions are well established and the discrepancies could be attributed to the variation between the individual test results. Representative properties for the simulation of upper and lower bound values obtained from the 100 % Aramid specimens were: E = 2.9 – 5.9 GPa , α = 18 – 36, μ =8–14, η = 0.29 – 0.76, ε_{cr} = 680 – 970 μstr. In all these fits the parameters for the ratio of compressive to tensile stiffness and strength were held constants at γ = 1, and ω = 11. The strain limits were set at β_{tu} = 23– 42 and λ_{cu} = 71. As evident, direct correlation between samples shows lower flexural strength associated with lower values for the fit parameters.

Tensile stress-strain responses are shown in Figure 4-5b and exhibit the comparison between the back-calculated response from the flexural data and the experimentally

112

obtained values. Note that the initial linear portion of the curve is not well captured since the experimental data did not record the first crack strain accurately. Also additional instrumentation for deflection measurement such as LVDT transducers or strain gages were not used during the conduct of the experiments. Strain measurements reported in this paper are measured using the deformations reported by the hydraulic actuator, which overestimates the real deformation in the test coupon. This affects estimation of the real deflection/strain in the specimen under the imposed loading. While the model is quite accurate in fitting the flexural data, the tensile fit parameters obtained do not correlate very well in terms of the overall post crack stiffness, stress capacity, strain capacity, and ductility.
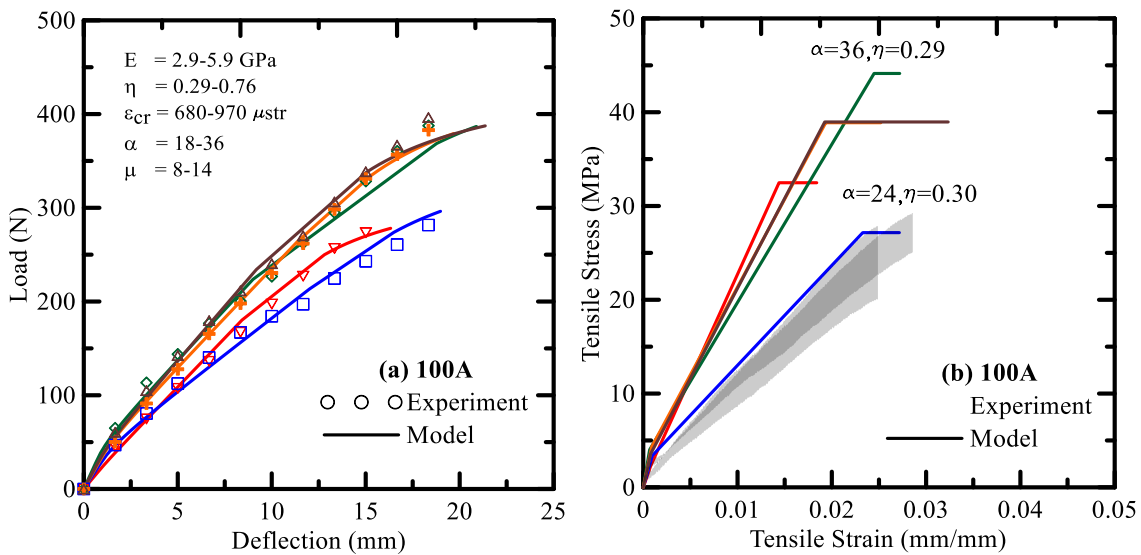
Figure 4-5:100 % aramid; (a) flexural, (b) tension responses

Majority of the back-calculated tensile results over-predicts the experimental tension data. This is attributed to the definition of axial strain based on the cross-head displacement which leads to inclusion of spurious and excessive deformations. The size effect is apparent as the tensile results are generally lower than the values predicted from the flexural tests

and that is well accepted as the specimen under tension is much larger in a tension test than the high stress region of tensile stress in a flexural test.

The flexural load vs. deflection results of composites with carbon textiles are shown in Figure 4-6a for both experimental and simulated. Figure 4-6b shows the back-calculated tension results compared with the experimentally obtained data. While it is clearly possible to fit the flexural test results with a good degree of accuracy, back-calculated results point to underestimation of the experimental tension data. This is also attributed to the difficulty in maintaining proper bond between the carbon yarns and the cement paste matrix which causes the shear stresses to cause premature de-bonding in flexure.
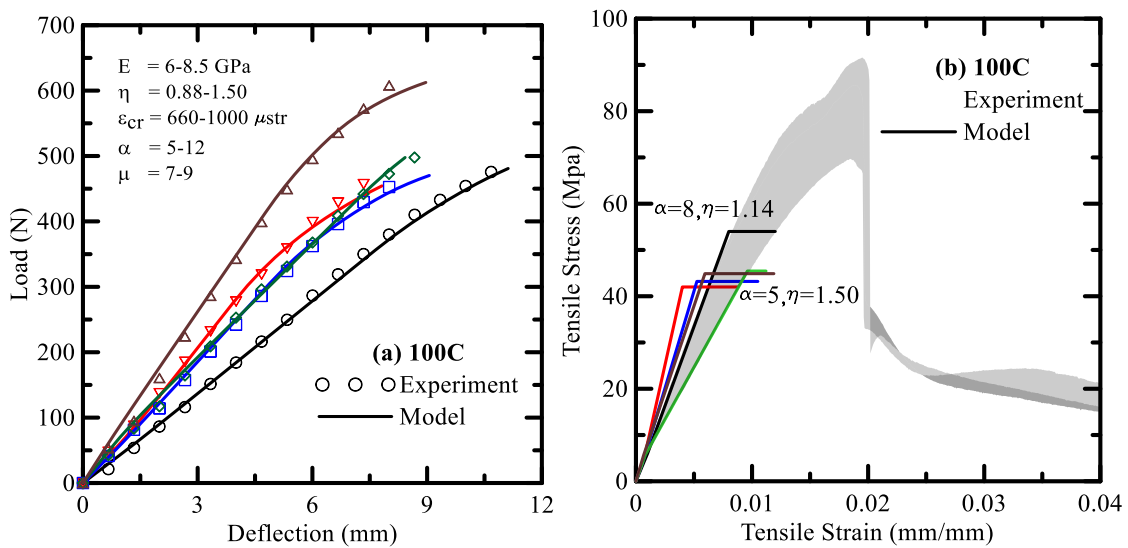
Figure 4-6: 100 % carbon; (a) flexural, (b) tension responses

In the flexural tests, the load transfers to the filaments of the carbon yarn through the interfacial zones. The weak bond properties of carbon-cement systems is generated by low penetrability of the relatively large cement grains into the tiny filament spaces [92]. This lack of penetrability is shown in Figure 4-7 with the individual un-bonded internal carbon filaments. The only force that can be transferred among the fibers is through sliding

114

friction; therefore the overall composite capacity is rather low (see Table 4-7). In tension tests the carbon filaments are more effectively clamped, causing an efficient load transfer mechanism to the filaments. This may explain the superior tension results of carbon composites as compared to the other textile systems (Table 4-8), as the tensile response follows the yarn properties, and the carbon fibers have the strongest and stiffest yarns. The loading of the yarns in flexure is mainly controlled by bonding and under low filament to filament bond strength, the flexural response is adversely affected. The simulated tensile strength is about 40 MPa whereas the experimental tensile strength is as high as 90 MPa which is purely a fibber response. The tensile results are characteristic of the carbon yarn response and the overall composite behavior is dominated by the high strength/stiffness yarns. Loading conditions with perfect gripping of the carbon yarns is not attainable in a flexural test.

(a)   (b)
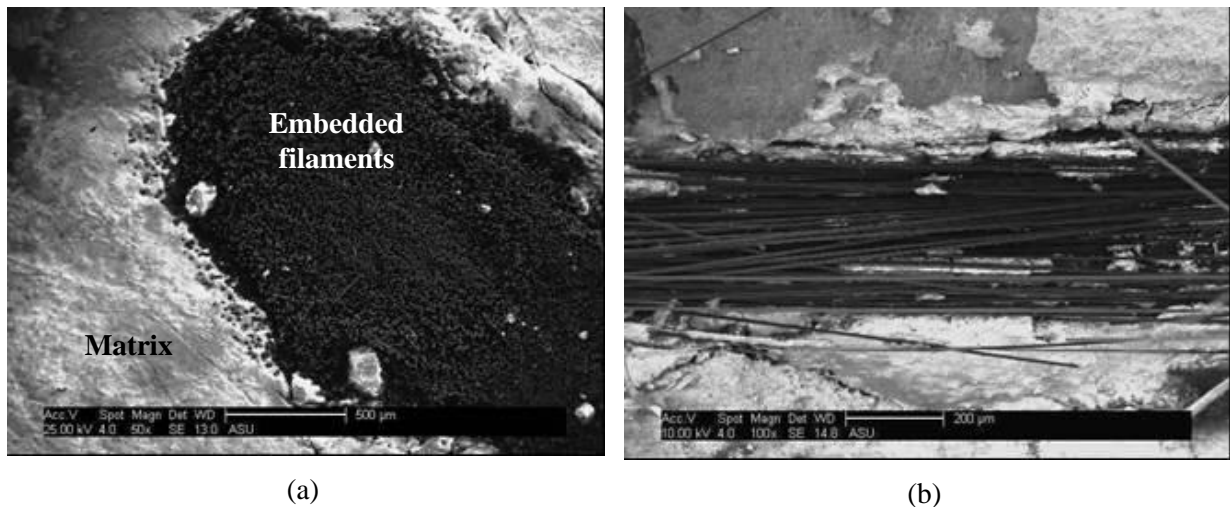
Figure 4-7: SEM micrographs of carbon fiber bundle embedded in cement matrix: (a) view of cross section and (b) side view

The lower and upper bound values of the representative material properties for the 100 % carbon specimens were: E = 6–9 GPa, α=5–12, μ=7–9, η=0.88–1.50, ε_{cr} = 660–1000 μstr.

115

The normalized strength parameters are $\gamma=1$, and $\omega=11$. The limits of the modeling were $\beta_{tu} = 11$–18 and $\lambda_{cu}=71$. Values shown do not represent a model optimization where upper and lower bound values for each variable are required.

The flexural load- deflection for both experimental and simulated response results of AR-glass fibers are shown in Figure 4-8a. Back-calculated tension response and experimental stress-strains curves are shown in Figure 4-8b. The back calculated tension response in this case is much stiffer than the experimentally obtained values, although the ultimate strength results are comparable. The back-calculated strain capacity is between 0.1-0.3% as compared to experimental results in the range of 0.5-0.8%. Clearly the slip effects due to clamping of the tension filaments is important since few filaments are loaded due to the multifilament nature of the yarns. In addition, yarn curvature or misalignment reduces the initial stiffness of the tension samples whereas due to the imposed curvature in the flexural test, more filament to filament interaction is expected. The representative material properties and their range for 100 % AR Glass specimens were: E = 7.2–11.0 GPa, $\alpha = 10$–20, $\mu = 5$–8, $\eta = 0.21$–0.44, and $\varepsilon_{cr} = 115$–180 $\square$str. The constants were: $\gamma=1$, and $\omega=11$. The limits of the modeling were $\beta_{tu} = 5$–8 and $\lambda_{cu} = 71$.
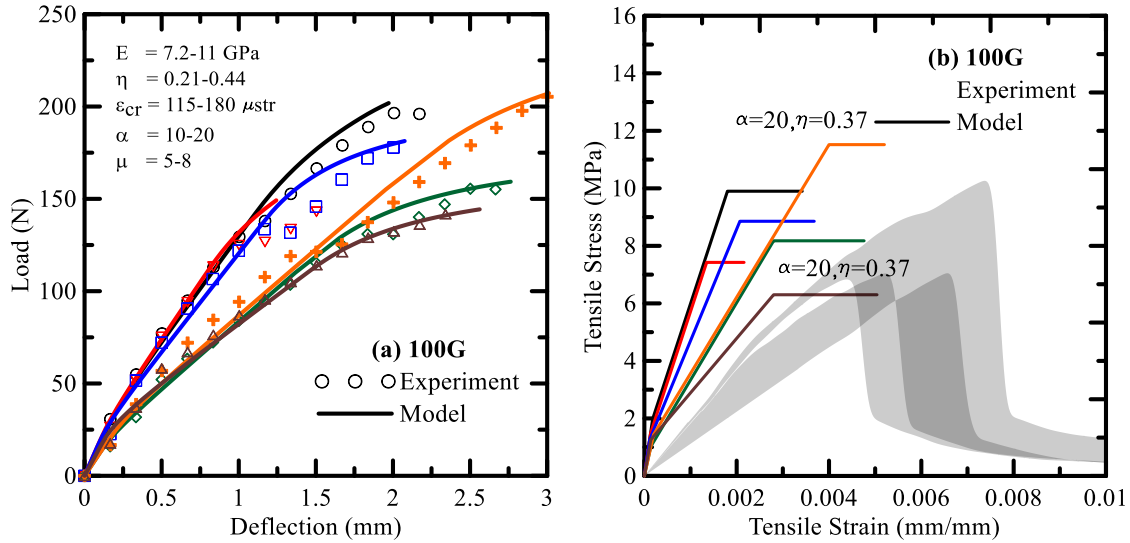
Figure 4-8: 100 % glass; (a) flexural, (b) tension responses

In the case of the glass composites the dominant mechanism is the low durability of the glass yarns within the hydrated cement paste and strength reduction due to accelerated ageing process used [69]. The properties of the yarn are affected by the curing process and the tensile behavior mainly shows this reduction as compared with the carbon, PP, and Aramid systems. The degradation is not as pronounced in the flexural results as the response in flexure is dominated by bonding while yarn properties is the dominant mechanism in tension.

Results of 100% polypropylene textiles are shown in Figures 4-9(a-b). Once again, the model underpredicts the tension response for these fabrics. The simulated tensile strength is within 4–6 MPa, whereas the experimental tensile response is in the range of 10–15 MPa. The range of material properties for 100% polypropylene specimens obtained from the simulations were: E=5.8–8.2 GPa, α = 165–275, μ = 8–9, η = 0.007–0.012, ε_{cr} = 190–335 μstr (constant values of γ=1, and ω=11). The limits of the modeling were β_{tu} = 200 – 400 and λ_{cu} = 71.

117
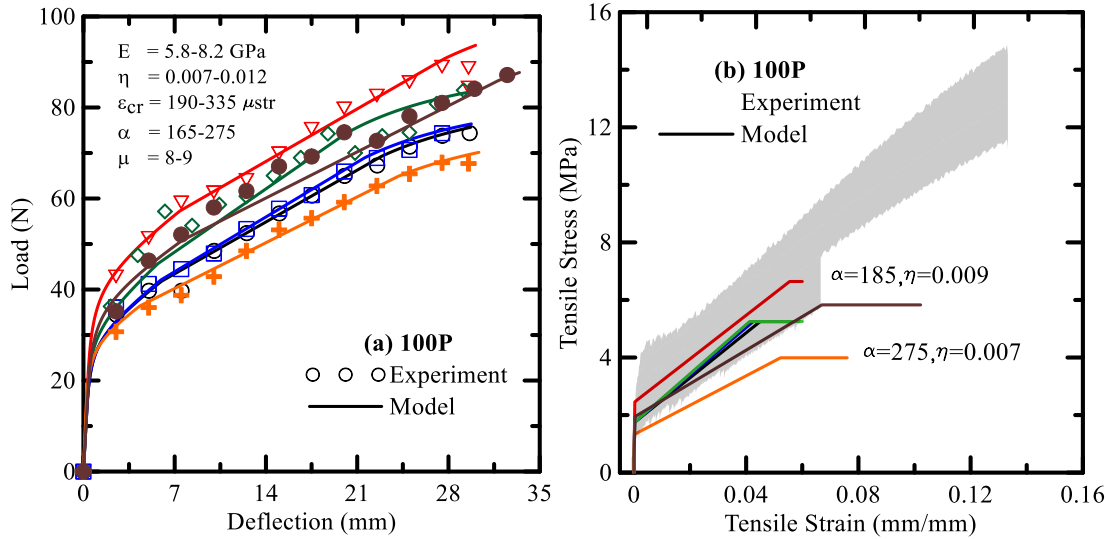
Figure 4-9: 100 % polypropylene; (a) flexural, (b) tension responses

Response of different 100% fabric systems studied here are shown in Figure 4-10(a-b). As evident carbon system shows an exceedingly high tensile strength and post-peak modulus which can be evaluated using model parameter, η. However its flexural stiffness and deflection capacity is comparable to the glass composites. Transitional strain capacity which can be characterized by model parameter, α is moderately higher for glass composites compared to carbon systems. Aramid system shows intermediate tensile/flexural strength and post-crack modulus, and has transitional strain capacity similar to glass system. The polypropylene system exhibits the lowest load carrying but highest deflection capacity. Transitional strain capacity of polypropylene composites is about an order of magnitude higher than the other textile systems studied here. First-cracking strain capacity of glass and polypropylene systems are similar and much smaller compared to carbon and aramid composites. The comparison of the tension simulated and experimental results in Figure 4-10b indicates that while the backcalculation approach manages to simulate the tensile strength of aramid and glass systems reasonably well,

however the post cracking stiffness in these systems is over predicted. On the contrary, while the simulated tensile strength of carbon and polypropylene composites are over predicted, the initial and post cracking stiffness values are similar to the experimental responses. Potential reasons for the differences between the experimental and simulated trends are explicitly discussed in the following section.
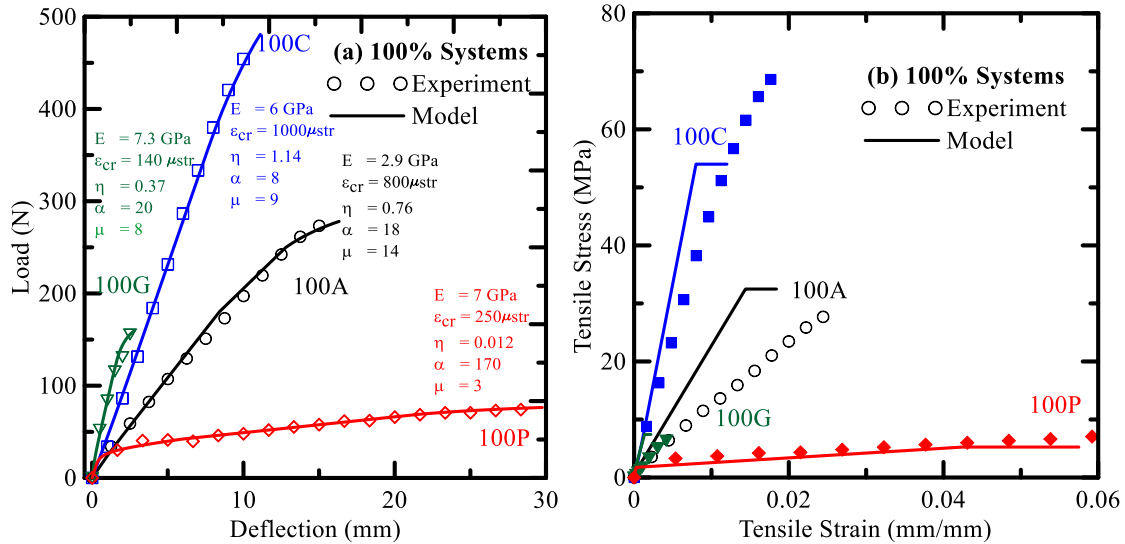
Figure 4-10: Comparison between 100 % systems; (a) Flexural, (b) Tension responses

4.4. Polypropylene – Aramid Hybrid Systems

Hybrid fabrics made of aramid and polypropylene yarns were used to produce the hybrid composites. During the manufacturing of these fabrics, aramid yarns are replaced sequentially with polypropylene yarns proportions of 25%, 50% and 75% (75A25P, 50A50P and 25A75P). In order to achieve such yarn ratios, four warp yarns were alternated within the fabric. Experimental and simulated responses of hybridization of TRC composites with 25% aramid and 75 % polypropylene are shown in Figures 4-11.

119
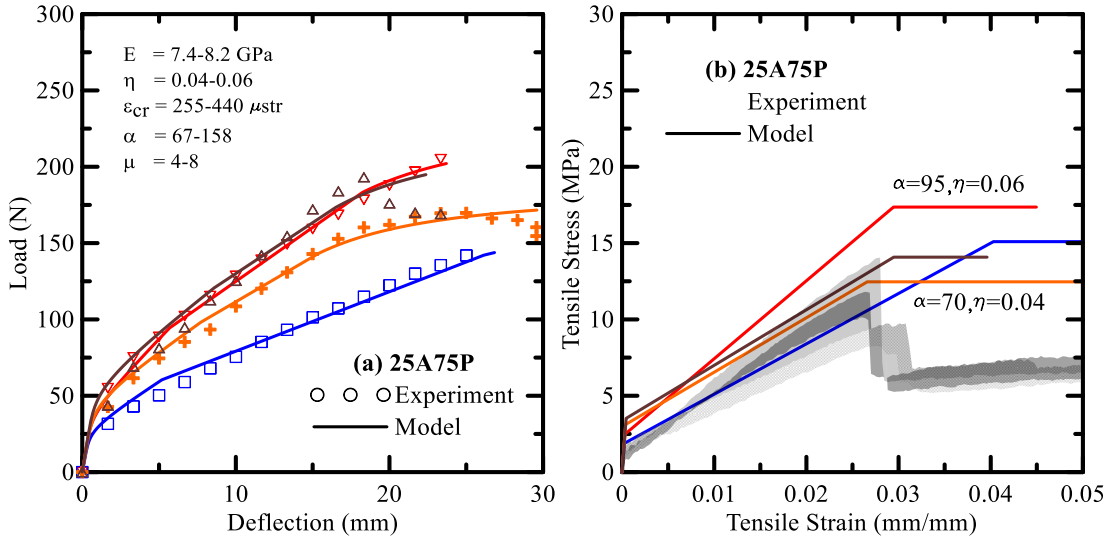
Figure 4-11: Hybrid of 25 % Aramid + 75 % Polypropylene; (a) flexural, (b) tension

responses

Figures 4-11(a) shows the flexural load vs. deflection for both experimental and simulated response of 25A75P samples. Results of the tension back-calculated and experimentally obtained tension responses are shown in Figure 4-11(b). There is a good correlation between the experimental and predicted flexural responses. The back calculated tension curves demonstrating a stiffer response than the experimentally obtained values, and a higher strength values. The back-calculated strain capacity is about 0.4 - 0.5%, which is similar to the experimental measurements. However simulated tensile strength is about 13 – 17 MPa, whereas experimental results vary from 10-14 MPa.

Comparison between polypropylene – aramid hybrid systems is further shown in Figures 4-12(a-b). As evident, hybridization of yarns helps with the general behavior of the composite and overall stiffness reduction is due to replacing a stiff fiber with a more compliant fiber system. It is to be noted that the gradual change in the stiffness which

120

allows one to design for a desired stiffness by properly aligning the yarns and optimizing

the response in accordance to the required stiffness of the sample.
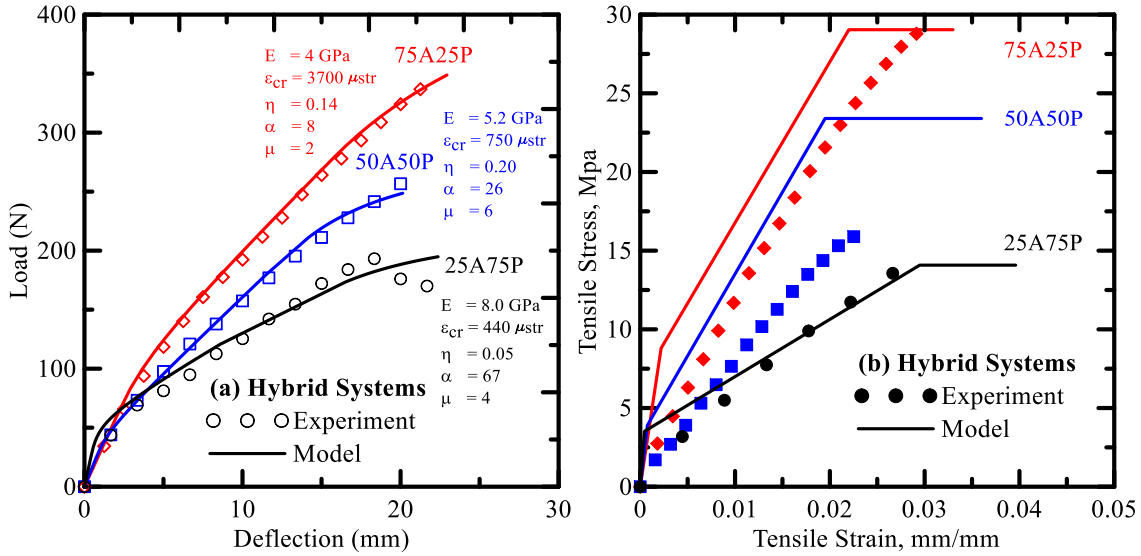
Figure 4-12: Comparison between hybrid systems of aramid and polypropylene; (a)

flexural, (b) tension responses

4.5. Discussion of Results

The differences between experimental and back--calculated tensile results can be studied

using the independently conducted tension and flexural tests. This allows for comparison

of the characteristic tension stress-strain response from opposing perspectives. Back-

calculation models can be verified in consideration to the observed differences and

limitations of each test method. The differences in behavior may be attributed to several

factors including: size effect, uniformity in tension loading vs. the linear strain distribution

in flexure, diagonal tension shear failure, and variation in lamina orientation and placement

which may lead to a wider range of variation among the flexural samples.

The proposed approach fits the experimental data under flexure using realistic tensile

properties reasonably well. The tensile response predicted from flexure is mainly affected

most by the microstructural features in cases of carbon and AR glass composites. The main parameters that influence these differences include: griping, delamination, interfacial bond and matrix penetrability which results in more dominant behavior in flexure, whereas yarn strength is more dominant in tension. In general, flexure is more dependent on bonding and stress transfer, while tension is more dependent on yarn properties due to gripping and tensioning all filaments together.

It is noted that simulations that use flexural response data in calculate direct tension properties tend to both underestimate, and overestimate the magnitudes measured by the tensile experimental data. The former case is observed in several sets of carbon and polypropylene non-fabric textiles. The latter are observed in glass and aramid samples.

An important parameter attributed to the underestimation of actual tension data from flexural tests is the primary mode of failure. During tension tests, almost all specimens experience matrix failure and distributed cracking over a large strain range. The ultimate strength is dominated by either fiber pullout from the grips, or fiber fracture. If the tensile strength or the strain capacity of the fiber is excessively high as is the case of carbon and polypropylene fibers, the shear failure mode may become the dominant failure mode in flexure. In this case, the effect of diagonal shear cracking in the flexural samples affects the final cracking and misinterpreted as flexural strength. This mechanism is responsible for lower estimations for the tensile stress-strain response computed from the flexural samples.

In consideration to matrix shear failure, phenomenological effects such as fiber-matrix debonding leads to inefficient fiber performance and the differences between the tensile and flexural response. In a tension test, the textile phase is often held quite tightly in the

122

grips, whereas in a flexural test, due to the high transverse shear loads, end of the specimen experiences transverse shear effects that lead to delamination, thus resulting in inefficient load transfer. This causes low apparent flexural values since a majority of the loading is primarily through the interfacial load transfer.

In specific cases where the simulated tension data from flexural tests significantly exceeds the experimentally obtained data one must consider the difference between the two specimens in terms of size. In a tension test the entire body is loaded, but there are no shear stresses, whereas in a flexural sample only a small volume of the specimen is subjected to tensile stress, while shear stresses are dominant in the mid-section layers. This indicates that for brittle specimens the flexural strength is much larger than the tensile strength due to the size effect, however in brittle specimens that exhibit distributed cracking, shear stresses may dominate the response and cause failure under very large deformations prior to the fiber phase being loaded fully. The difference between the testing methods may be the contributing factor to the observed differences.

In the case of carbon fabric composites, the method of testing in tension under gripping of the specimens resulted in direct transfer of the load to the yarns whereas in the case of flexure, the load transfer can only take place by means of shear lag. The high stiffness fiber systems with a very high tensile strength may not be good candidates for flexural based applications as the method of load transfer to the stiff fibers may limit the average load applied on them.

The discrepancies in the magnitude of nominal strength obtained from the experiments could be characterized by comparing the cumulative probability distributions of the different fabric systems as shown in Figure 4-13. The main parameters reported here are

the limit of proportionality (LOP) and bend over point (BOP) corresponding to first cracking strength under flexural and tensile loading. Also reported are the modulus of rupture (MOR) and ultimate tensile strength (UTS) values. Flexural strength parameters as reported in Figure 4-13(a) suggests that for glass and polypropylene specimens have similar strength magnitudes. Carbon systems as discussed earlier exhibit the maximum strength amongst all composites, followed by aramid. However when the tensile properties are compared in Figure 4-13(b), while the strength at BOP is mostly similar for all composites, the ultimate strength of carbon systems are about a magnitude 3-6 times higher than the other composite systems. Thus when flexural response is used in an inverse analysis algorithm, the predicted tensile response is under-predicts the experimentally measured strength. The underestimation of the tensile capacity can also be addressed by increasing the apparent tensile capacity using scaling parameters applied to equivalent stressed sections [87].
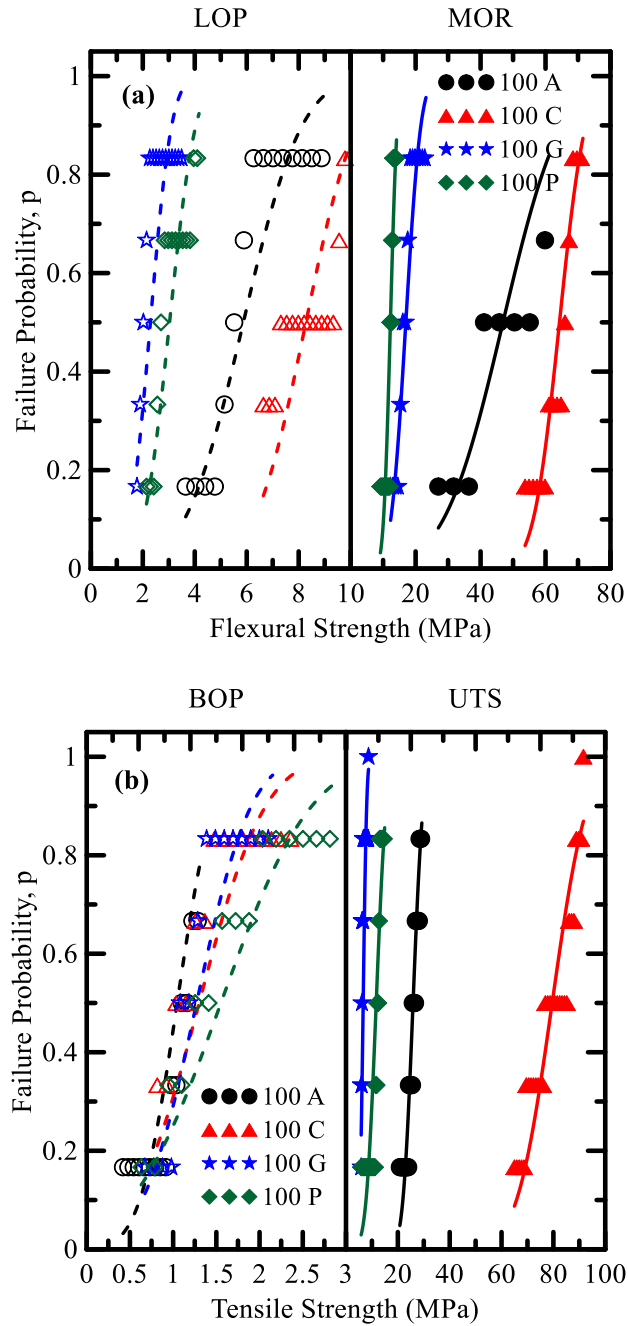
Figure 4-13: Cumulative probability distributions of flexural and tensile strength

Assuming that the strength follows a Weibull distribution function as defined by m the shape parameter or the Weibull modulus, the mean $\bar{\sigma}$ and coefficient of variation of the strength, CV, are given by:

125

$$\bar{\sigma} = \sigma_0 V^{-1/m}\Gamma\left(1+\frac{1}{m}\right) \qquad CV = \left[\frac{\Gamma\left(1+\dfrac{2}{m}\right)}{\Gamma^2\left(1+\dfrac{1}{m}\right)}-1\right]^{1/2} x100 \qquad \text{Equation 4-6}$$

Where σ_0 the scale parameter, V the effective volume, of the tested specimen volume. In the case of the bend test, a stress gradient exists in the specimen reduces the effective volume, V, for the three-point bend and four point bend (with a load span of one-third of a support span) strength is given by [93]:

$$V_{3PB} = \frac{1}{2(m+1)^2 V_0} \quad \text{and} \quad V_{4PB} = \frac{m+3}{6(m+1)}V_0 \qquad \text{Equation}$$

4-7

Where V_0 is the volume of the specimen between two supports. Assuming that the strength data follow weakest-link scaling and that the stress-state is elastic in the flexure specimens, the σ_b/σ_t ratio can be estimated using the following equation derived from the comparison of the failure probabilities of the tensile and the 3-pt bending test specimens:

$$\frac{\sigma_b}{\sigma_t} = \left[2(m+1)2\left(\frac{V_t}{V_b}\right)\right]^m \qquad \text{Equation 4-8}$$

Where V_t is the volume of the tensile and V_b the volume of the 3-pt bending specimens [94]. This correlation approach was adopted for the 100 % composite systems evaluated in this study, as shown in Figure 4-14. Ratio of volume of the specimens between the supports, $V_t/V_b = 1.47$; along with different Weibull modulus parameter ranging from 0.01-0.62 were used to correlate the strength values. As evident for carbon and polypropylene the tensile and flexural strength are quite similar and could be potentially expresses as a ratio of 1:1. Whereas for aramid and glass systems, the ratio of tensile/flexural strength,

σ_β/σ_t is almost a factor of 2 and 3, which correlates well with the overestimation of the flexural results. Characterization of the observed differences between test methods points out the differences that are not captured using simplified data reduction techniques. The procedure for the use of the flexural response to develop a moment-curvature response based on back-calculation however provides a potential way where the flexural results can be applied to the design of flexural load cases.
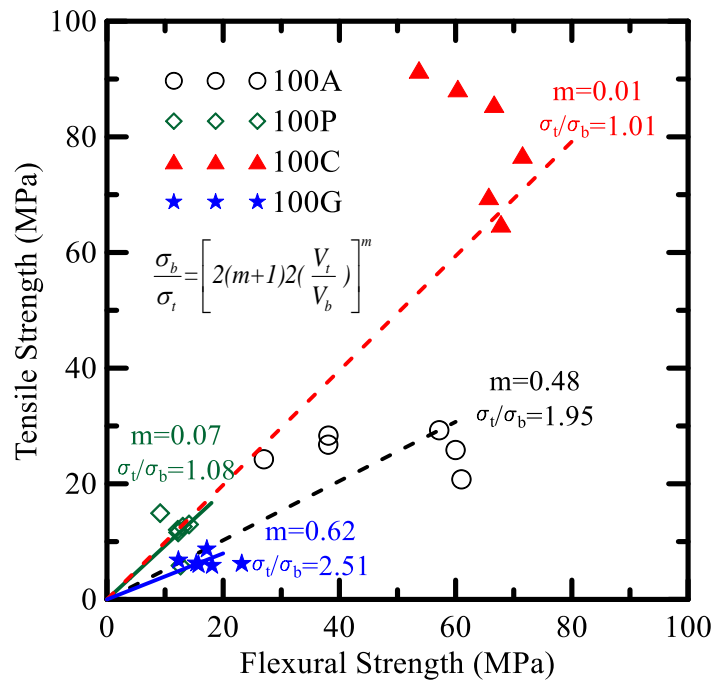
Figure 4-14: Correlation of tensile and flexural strength based on Weibull distribution

Comparison between model parameters is shown in a series of Figures 4-15(a-d). Effect of yarn proportion on the back calculated tension responses in terms of elastic modulus, post crack stiffness, the first cracking strain, and ultimate strain of hybrid aramid-polypropylene yarn combinations are shown. As the proportion of aramid is replaced by the polypropylene yarns, it is shown that the elastic modulus decreases by almost 50%, while the first cracking strain increases. In the post initial cracking range, the stiffness increases where as the

ultimate strain capacity decreases. Note that using these relationships; one can develop proper design tools to customize the material properties for a given design. With the ability to weave three dimensional and also hybrid textiles, it is possible to use a specific fiber and textile configuration for a given loading criteria.
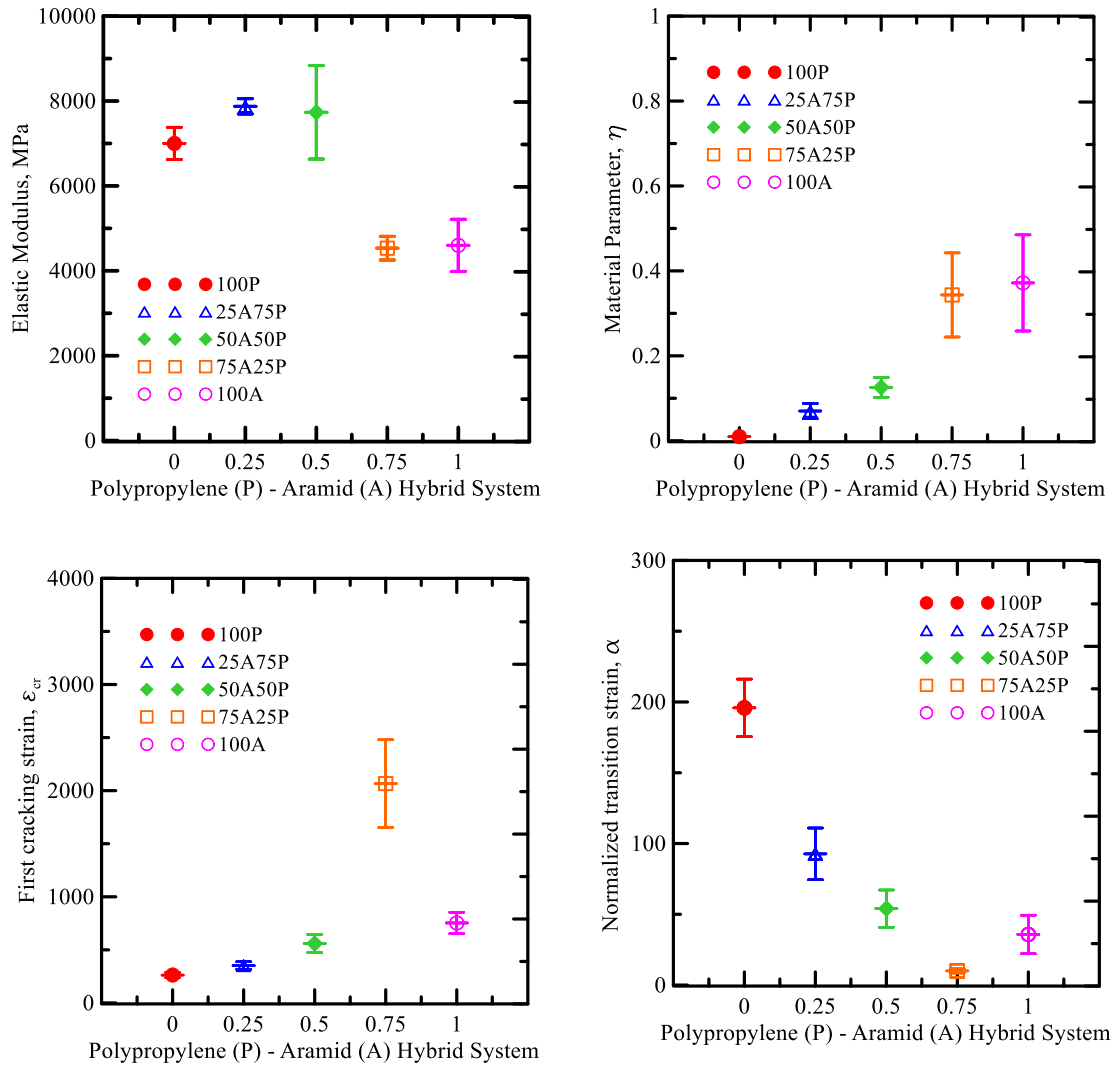
Figure 4-15: (a) Elastic modulus, (b) post-crack stiffness parameter, η; (c) first cracking strain, ε_{cr}; (d) normalized transition strain, α

4.6.   Conclusions

Mechanical properties of different TRC composites were correlated by comparing the experimental tension and flexural results. Experimental data from a single batch of specimens under uniaxial tension and three point bending tests were used to develop fit models to the flexural and tensile responses. The material parameters were determined by fitting the hardening model to the experimental data. Independent tension experimental data were compared with the simulated data from flexural samples. It is noted that simulations that use the flexural response may overestimate and underestimate the tension response under different conditions. Using the relationships studied, one can use the model prediction tools as a design tool and customize the material properties of the composite for any structural application.

Table 4-10: Table of results from the back-calculation analysis (numbers reported in bold are the average estimates, whereas standard deviation are reported with regular fonts)

ID	Model Input						Model Output										
							Back calculated Tensile properties						Back calculated Tensile properties				
	E	δ_{cr}	α	η	μ	β_{tu}	S	δ_{cr}	σ_{cr}	MOR	δ_{max}	T	σ_{cr}	ε_{trn}	ε_{tu}	$\mu\sigma_{cr}$	T
	MPa	μstr	Normalized Units				N/mm	mm	MPa	MPa	mm	MPa	MPa	MPa	μstr	MPa	MPa
100A	4.3	824	25	0.43	11	32	34	0.75	3.52	49	20.37	5053	3.52	20152	26060	36.32	0.61
	1.1	113	7	0.19	2	8	8	0.10	0.76	10	3.55	1924	0.76	3970	5034	6.58	0.21
100C	7.3	802	8	1.07	8	14	65.83	44.78	0.71	64.50	5.74	2692	5.74	6558	10876	45.90	0.35
	0.9	125	3	0.32	1	3	17.51	4.41	0.14	5.08	0.27	511	0.26	2234	1306	4.73	0.06
100G	9.4	152	16	0.36	6	27	161	0.11	1.41	14	2.27	253	1.41	2470	4043	8.7	0.03
	1.8	32	5	0.08	2	8	30	0.02	0.32	2	0.64	87	0.32	940	1176	1.8	0.01
100P	7	263	196	0.01	3	268	57	0.24	1.83	11	33.27	2629	1.83	50583	68863	5.4	0.28
	0.8	50	41	0.002	0	74	7	0.05	0.37	2	8.11	941	0.37	9799	17754	0.9	0.09
75A25P	4.5	2067	10	0.34	4	17	33	1.93	9.18	58	21.79	17854	9.18	19567	31100	33.9	0.74
	0.6	826	3	0.20	1	7	4	0.77	2.98	17	3.89	32086	2.98	5659	8193	12.7	0.23
50A50P	7.7	560	54	0.13	7	69	61	0.52	4.04	44	22.65	5485	4.11	26833	34767	26.9	0.62
	2.2	169	26	0.05	2	28	20	0.17	0.87	8	3.36	1390	0.98	5755	5266	4.4	0.11
25A75P	7.9	346	98	0.05	6	142	59	0.32	2.75	26	27.01	4260	2.75	31455	46428	14.75	0.49
	0.8	81	42	0.01	2	45	5	0.07	0.72	3	3.33	849	0.72	6043	5280	2.05	0.07

Note: Abbreviations for parameters reported in this table: stiffness is S, Deflection at first crack is δ_{cr}, stress at first crack is σ_{cr}, Deflection at max stress is δ_{max}, toughness is represented as T, transitional tensile strain is ε_{trn}, ultimate tensile strain is ε_{tu}, residual strength is $\mu\sigma_{cr}$.

5. QUANTITATIVE CHARACTERIZATION OF ACCELERATED AGING IN CEMENT COMPOSITES USING FLEXURAL INVERSE ANALYSIS

Cement composites use fibers in chopped, continuous, or woven textile form in order to increase damage tolerance, strength, and ductility through the bridging of cracks and controlling crack width [2]. The strength and toughness enhancement is due to the ability of bridging fibers to de-bond and pullout thereby transferring the load across the crack faces [95]. Commonly used fiber types include steel, glass, polymeric, synthetic, and natural fiber forms. While glass and natural fibers are economic alternatives to steel fibers, the long term performance of various composite systems depends on the physical and mechanical nature of fiber, interface, and chemistry of the pore solution.

Alkali-resistant glass fibers have been used in various cement composite products for more than forty years. Glass fiber reinforced concrete (GFRC) is manufactured by the spray up production using blended Portland cement, polymers, and 3-5% high strength alkali resistant glass fiber (AR-Glass). Natural fibers have been gaining attention in the last decade for production of cost-effective sustainable structural materials [96,97,98]. Sisal, for example, is a commonly used natural fiber on account of its low cost, low density, high strength and modulus, availability and sustainability [99].

The durability and long term performance of cement composites with glass and natural fibers remain a concern since reduction in strength, ductility, toughness, and impact resistance has been observed over time [100]. Composites exposed to humid environments exhibit embitterment and loss of flexural strength over time [101,102,103]. The deterioration is primarily caused by the chemical and physical processes as both glass and

natural fibers which chemically degrade due to the alkaline environment of hydrated cement paste and lose strength with time. The chemical cause of strength reduction is attributed to break-up of the Si-O-Si bond in glass due to chemical attack by hydroxyl ions and fiber corrosion, whereas the physical attack is due to densification of fiber-cement interface and formation of hydration products such as calcium hydroxide which fill the spaces between the fiber filaments and reduce the compliance of the fiber yarn. [101,104,105,106]. This loss of flexibility causes stress concentration at the fiber-matrix junction especially in cases that fibers oriented to the plane of matrix crack bend during pullout. However as the bonding at the fiber-matrix interface increases, the interfacial stiffness increases which directly changes the mode of fiber pullout to fracture under tensile loading. Embrittlement in the meantime results in changes in the micro-mechanical bonding, causing the fibers to lose their flexibility and become brittle [107]. In an assembly of filaments or bundle, the cement hydration products penetrate from the periphery of the sleeve filaments towards the core filaments. Additional impregnation by deposition of hydration products over time may have a different nature if some of these are nucleated in the spaces between the filaments. Interfacial changes in the fiber-matrix interface zone and within the fiber bundle due to aging and matrix modification were studied using in-situ push-in and push-through tests on individual fibers [139]. It was observed that in unaged composites, very low push-in resistance was observed for the inner core filaments; whereas the sleeve filaments offered high resistance as they were well bonded with the matrix. The internal core filaments with weaker bond, can engage in slip which provides the desired toughness and ductility to the composite. However upon aging, the bonding of core

132

filaments with the hydration products, result in adhesive cross-link connections which causes embrittlement [108]. The microstructure of the fiber bundle was also studied using an in-situ pull-out test coupled with the FILT method of transmitting light through the individual filaments. This test method enables quantification of bonded fibers at each stage of pull-out loading and identifies the location and number of individual filaments which fail and pullout from the matrix [109]. Difference in bond characteristic of sleeve and core glass filaments with the matrix results in a telescopic failure mechanism as successive layers from the external sleeve to the internal core filaments breakdown.

The adverse effects of reduction in strain capacity, increase in the bond stiffness, and decrease in the total ductility has been experimentally documented in literature, however an analytical model to capture and correlate these interactions is not available [101,110,111]. Controlling the degradation of glass and natural fibers in cementitious matrix is the central aspect of development of blended cements, sizing and interfacial modifications, and innovative fiber formulations in order to promote a widespread application of natural and glass fibers. Common methods of improving the durability of fibers include addition of use of polymer emulsions and pozzolanic materials such as ground granulated blast furnace slag, silica fume, fly ash, and metakaolin to react with calcium hydroxide [98,112,113,114]. Alternate cement types such as sulpho-aluminate cement (SAC) [115,116,117], inorganic phosphate cement (IPC) [118,119,120, 121] and calcium aluminate cement (CAC) [122,123] improve durability of Alkali-resistant glass fibers (ARG) [124]. Cuypers et al. [118,119] reported that using an inorganic based polymer composite GFRC property retention is better for both E and AR-glass compared

with AR-glass OPC GFRC. In case of natural fiber composites, special curing treatment for the composites such as autoclaving, and accelerated carbonation contributed to increase durability [98,125,126]. Pretreatment of natural fiber through silane coating, hornification, sodium silicate, potassium silicate have been also known to improve the mechanical properties and durability of natural fiber in cement based materials effectively [98,127,128].

In order to evaluate the improvement of glass and natural fibers for various treatments, accelerated aging procedures are conducted primarily on flexural samples and the test results are correlated with samples undergoing natural weathering in the field [129,130,131,132]. Assuming that fiber corrosion was the main degradation mechanism, accelerated aging tests such as the "strand in cement" (SIC) were used to predict long term strength [98,129] and compared with weathering data. Empirical relationships for acceleration factors for a range of climatic temperatures between 4 to 80°C were obtained [133,134,135]. A relationship between time in accelerated aging and exposure to weathering was proposed as a basis for testing and design.

Recent developments in new matrix and microstructural formulations for improving the durability of cement composites necessitates a need to model and compare degradation rates using mechanical property test data.

The objective of this paper is use the available flexural test data to back-calculate long term tensile behavior of strain softening and hardening cement composites and develop a rational modeling approach for simulation of time-temperature environmental aging for direct implementation in life cycle modeling [136,137, 138]. The constitutive law for

homogenized fiber reinforced concrete is presented earlier was used to predict the mechanical response of materials subjected to aging [136,137].

In the absence of full mechanical response and when only the flexural strength is available as a measure of degradation, additional assumptions regarding the rate of change of model parameters are needed. This paper addresses both cases of data in terms of flexural strength as well as flexural load-deflection history. Available flexural test responses of fiber reinforced cementitious composites were back-calculated to obtain material parameters and establish their relationship with aging. The material behavior is described by tensile stress-strain parameters including elastic modulus, first cracking strain, post cracking stiffness, ultimate strain, and a residual strength parameter. The model is calibrated using the flexural and tensile data of GFRC composites reported by Litherland et.al. [129], Marikunte et.al [113], Bartos and Zhu [139], and sisal fiber composites reported by Toledo-Filho et al. [98]. This model can be easily applied to different classes of materials to assess their long term durability when subject to accelerated aging under different environmental conditions.

Derivations of the closed form solution for the moment curvature based on a trilinear tensile stress-strain diagrams as a function of the normalized tensile strain have been explicitly reported in previous work [140, 141]. The moment capacity is calculated from internal forces and the neutral axis location, while the curvature is obtained by dividing the top compressive strain with the neutral axis depth. In the elastic stage 1 ($0 < \beta \leq 1$), the stress is directly proportional to the strain,while stage 2 ($1 < \beta \leq \alpha$) and 3 ($\alpha < \beta \leq \beta_{tu}$) have two possible scenarios: the compressive strain at the top fiber is either elastic ($0 < \lambda \leq \omega$) or

plastic ($\omega < \lambda \leq \lambda_{cu}$). The operating mode at any applied tensile strain (β) is determined by the interaction of the three loading stages. The lowest magnitude of the moment among the operating cases for each strain level is selected as the governing mode and the intersection of any two modes represents a transition from one stage to the other. For most fiber reinforced composite materials, the behavior of the material is governed by load stages 2.1 and 3.1 wherein the tension fibers are in residual strength zone, while compression fibers are in elastic/plastic zone [136]. The solutions for depth of neutral axis, moment, and curvature response in closed form for the different stages were summarized earlier in Table 4-2.

A mechanical representation of durability can be simulated either by the loss of flexural strength (modulus of rupture, MOR), or by the load-deflection envelope. The constitutive law for homogenized fiber reinforced concrete is presented earlier was used to model the degradation in flexural capacity of materials with aging. For deflection-hardening or softening type materials (case 1 or 2), loss is flexural strength can be simulated by combination of model parameters related to post-cracking modulus, ultimate strain capacity and residual strength. Aging case 1 is applicable for materials exhibiting deflection-hardening behavior; wherein the flexural strength of the material may even increase after first cracking due to strain hardening and crack bridging mechanisms. In such cases, post-cracking parameter, η might show an increase in magnitude, especially in the early period of accelerated aging. The rise or fall in parameter, η is dependent on the mix-design, type and dosage of fibers, and aging conditions.
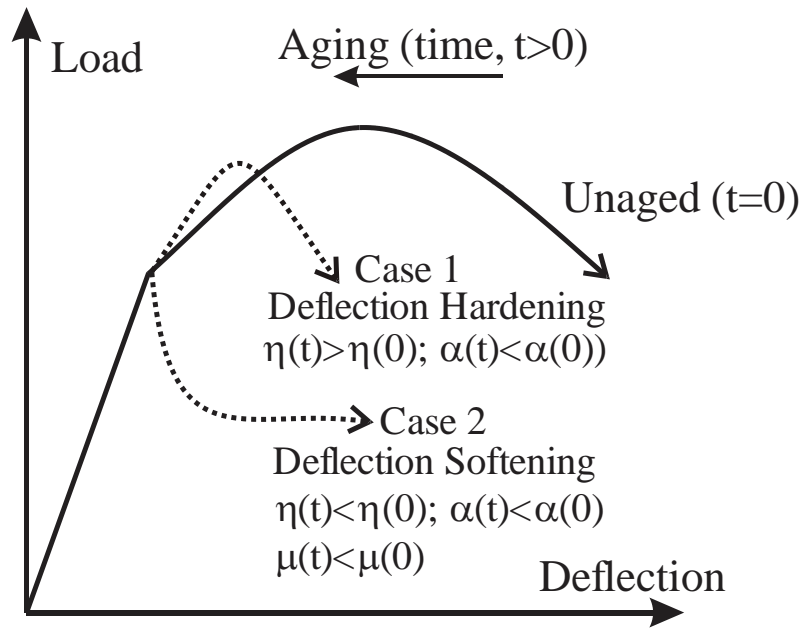
Figure 5-1: Schematic representation of degradation of flexural strength with time [142]

Aging case 2 is associated with deflection-softening materials as they undergo reduction in load capacity beyond first flexural cracking. In such cases, materials are vulnerable to severe loss in strain capacity and ultimate strength with aging. This behavior could be modelled with reduction in post-cracking modulus, η; strain capacity, α and residual strength parameter, μ. Aging is further assumed to have a limited effect on the elastic response of the material, and associated with the reduction of flexural capacity and residual strength. The only variable affecting Zone 2.1 is the post crack stiffness, η. The parametric effect of increase in the post crack stiffness η on the normalized moment response is shown in Figure 5-2(a) as a series of increasing curves. In zone 3.1, an additional parameter, α which represents the transitional strain capacity affects the moment capacity of the material for each variable η. Effect of the parameters in zone 3.1 are as shown by family

of curves in Figure 5-2a. Moment response in both the zones, as a function of normalized tensile strain capacity, β is shown in Figure 5-2(a) for a set of discrete values of normalized post-crack stiffness, η and normalized transitional strain capacity, α. The intersection of a given Zone 2.1 with a curve for Zone 3.1, establishes the moment curvature curve for both zones combined and the point of intersection of these curves is the ultimate moment capacity. Note that the family of curves in Figure 5-2 are universal and represent the normalized moment vs. curvature. Applied moment and curvature can be easily computed by scaling the scaler value with the cracking moment and curvature as shown in equations 5-6. The extent and rate of degradation in moment capacity can be easily modelled with reduction in combination of post-crack stiffness, η and strain capacity, α as shown in Figure 5-2(b). The reduced ultimate moment capacity, M'ult at any temperature (T) and age (t) can also be defined using equation 5-1. Herein, parameter K is the rate of degradation of flexural strength as function of exposure time, and aging conditions.

$$M_{ult}^{'}\left(T,t\right) = M_{ult}^{'}\left(T, t=0\right) - K(\eta(T,t))\left\{\alpha(T,t) - \alpha(T, t=0)\right\}$$

Equation 5-1

Load-deflection response is obtained using closed form equations for a bilinear moment-curvature representation [140]. The solutions for mid-span deflection at first crack and ultimate stress, under three-point and four-point bending were presented in the previous chapter.
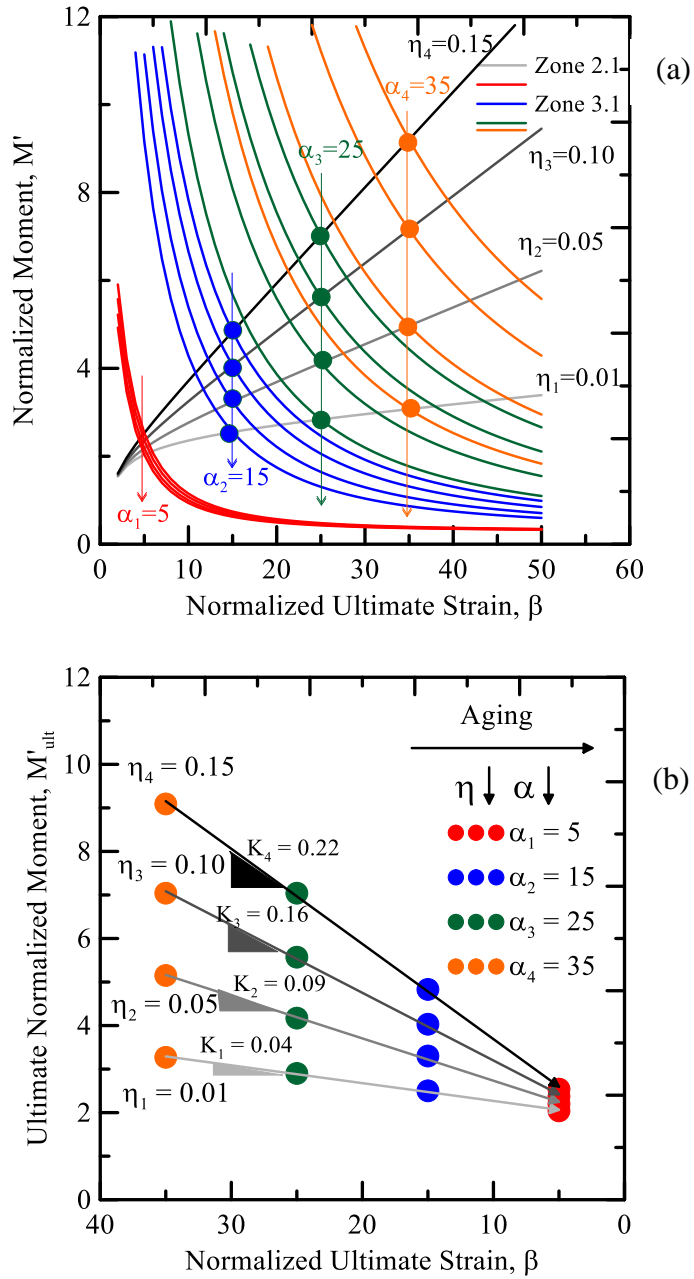
Figure 5-2: (a) Family of moment capacity curves with normalized ultimate strain at different transitional strain and post-crack modulus values, (b) degradation of normalized ultimate moment due to aging effects [142]

139

5.1. Effect of accelerated aging on long term performance of GFRC Composites

The methodology for simulation of accelerated aging of GFRC was applied to a study conducted by Litherland et al [129]. Composites with dimension of 150 mm x 50 mm and 6–8 mm in thickness were subjected to accelerated aging at various temperatures. The strength of composites was a function of fiber content, orientation, distribution, bond strength, and matrix strength. Degradation of average flexural strength (modulus of rupture, MOR) of GFRC specimens corresponding to various temperatures and aging periods were reported.

The inverse analysis procedure was applied to the experimental data of time history of degradation of MOR to reproduce the accelerated aging temperature curves. Since the strength loss is predominantly characterized by the ductility loss, post cracking modulus, η and strain capacity, α were the primary simulation variables. Strength-time curves are characterized by a rapidly degrading initial region followed by a rather constant portion [129]. An exponential decay function was assumed to represent the decrease in the transitional strain capacity α with time and represented by four variables as shown in Equation 5-2. It was also assumed that the aging effect on post-cracking modulus η is presented as a logarithmic function in Equation 5-3. The coefficients for the model parameters, α and η were represented in Table 5-1 as functions of time, t, and temperature, T:

$$\alpha(T,t) = \alpha_o(T) + \alpha_1(T)e^{-\kappa(T)t + \xi(T)}$$
<div align="right">Equation 5-2</div>

$$\eta(T,t) = \eta_o(T)\ln(t) + \eta_1(T) \hspace{4cm} \text{Equation 5-3}$$

In Equation 5, coefficient α_0 represents the ultimate limit of strain capacity, while α_1, ξ, and κ are related to the amplitude and rate of the decay. Coefficients α_1 and κ are the most influential parameters as they are related to the slope of the curve as a function of time, which in turn dictates the rate of degradation of the flexural strength of these composites. Coefficient η_0 in equation 10 represents the increase of post-cracking modulus with aging time until the cut off level. Substitution of coefficients: α_0, α_1, ξ and κ in equation (2), and coefficients: η_0, η_1 in equation (3), provides normalized transitional strain, α; post-cracking modulus, η as shown in Figure 5-3 representing the decay of the strain capacity as function of temperature as presented in Table 5-1. Note that reduction of strain capacity, α is more drastic at elevated temperatures and the parameters, α and η can be used to model loss of flexural strength of composites with time.
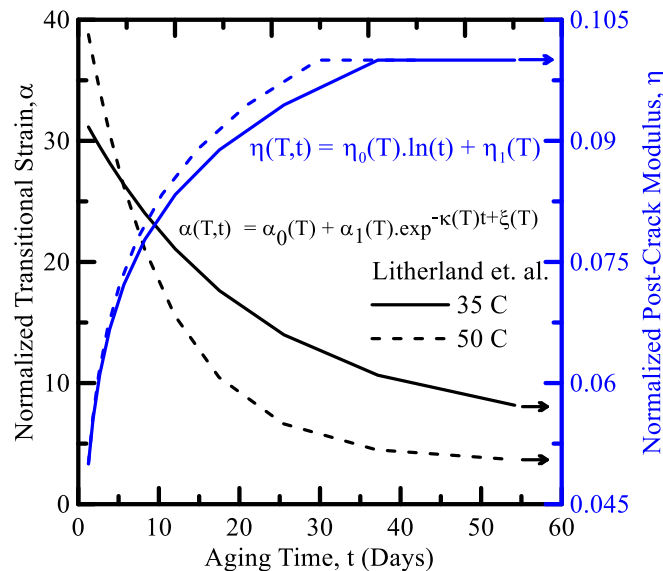
Figure 5-3: Response of transitional strain and post-crack modulus with aging time.

141

Table 5-1: Coefficients of fitting expressions used to model strain capacity, α and post-crack modulus for modelling flexural behavior of GFRC Composites reported by Litherland et al. [129]

Temp., T (°C)	Normalized Transitional Strain, α (Using Eq. 2)				Normalized Post-crack modulus, η (Using Eq. 3)	
	α_0	α_1	κ	ξ	η_0	η_1
19	4.0	20	0.004	8	0.013	0.047
35	6.2	26.5	0.048	0	0.015	0.047
50	3.5	40	0.1	0	0.016	0.047
60	2.3	310	0.15	10	0.012	0.027

It is noted that other fitting expressions of model parameters could be used to simulate the flexural strength reduction with aging. Figure 5-4 compares the simulation of aging with experimental results from flexural tests on GFRC composites reported by Litherland et. al. [129]. Note that in the original work presented by Litherland et. al. the aging period was represented in a logarithmic scale as shown in Figure 5-4(a), whereas a linear scale was used in the current study as shown in Figure 5-4(b).Additional model parameters: elastic modulus, E= 28 GPa; first cracking strain parameter $\varepsilon_{cr} = 250$ μstr; ultimate tensile strain, $\beta_{tu} = 160$; and normalized residual tensile strain, $\mu = 0.1$ were assumed to be constant. This simplification allows fewer parameters to be varied as the final fit was accomplished using only the post cracking modulus and ultimate strain capacity.

The degradation of MOR with aging time and temperature were successfully predicted with the applied model. A rapid decrease in initial strength at accelerated aging temperatures of 60°C and 80°C followed by a constant strength range that refers to the long term strength

retention is observed. For lower aging temperatures of 4°C, 19°C and 35°C the initial strength loss is much slower than the similar results at higher temperatures. For aging at 50°C, the transition between the initial and long term strength is smoother than the abrupt changes observed at the higher temperatures. This approach is attractive since it allows for various degradation rates to be measured from experimentally conducted tests and thus comparison between different material formulations can be achieved.
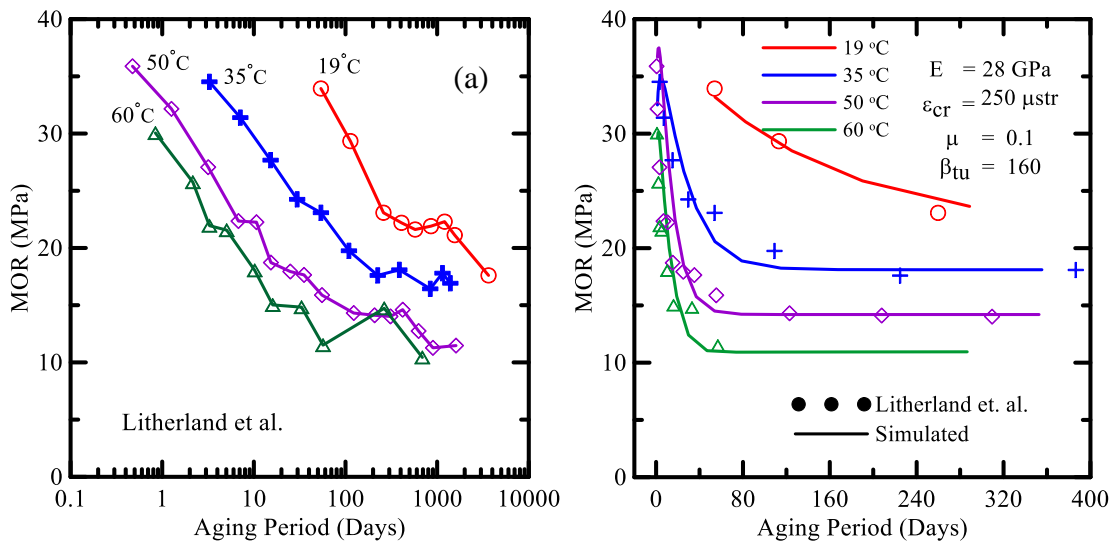
Figure 5-4: (a) Digitized experimental Litherland et al. data [129], (b) simulated response of GFRC composites at different temperatures compared with experimental data

5.2. Effect of matrix modification on aging of GFRC composites

Marikunte et al. [113] studied the flexural and tensile durability of GFRC consisting of control and blended matrices with metakaolin (b) and silica fume. GFRC mixes with silica fume (SF - with and without polymers) are referred as GFRC A and B, respectively were investigated in this. Mixture formulations consisted of white Portland cement, densified silica fume (25% by weight of cement), acrylic polymer (12% by weight of cement) in

143

addition to superplasticizer (3% weight of cement) and AR-glass fibers by 5% by weight of total mix. After normal curing for 28 days, long term aging was conducted using saturated calcium hydroxide solution at 50 ℃ for 28 and 84 days. Tension tests were conducted on notched prismatic specimens of 25 x 10 x 225 mm in size, and crack mouth opening displacement (CMOD) was measured. Four point flexural tests were conducted on specimens of 50 x 10 x 225 mm in size while mid-point deflection was measured.

Tensile and flexural strength of GFRC mix blended with silica fume undergo considerable reduction in ductility and strength with aging. The tensile properties are back-calculated from the flexural response by means of the inverse analysis procedure discussed earlier and compared against the experimentally obtained tension data. A majority of the composites exhibit both strain and deflection hardening followed by brittle failure in the post peak region, it is therefore sufficient to describe the material behavior with four parameters: Young's elastic modulus E, first cracking strain ε_{cr}, post crack stiffness η, and strain at peak stress ε_{trn} (or ultimate strain parameter α). The constant stress in the post-crack region, σ_{cst} for all test series was assumed sufficiently low in accordance to the experimental post peak responses. Since the compressive strength is much higher than the first crack tensile strength, constant parameters $\gamma=1.0$, and $\omega=12$ were used, with γ representing the ratio of tensile to compressive stiffness and ω representing the ratio of compressive strength to first cracking tensile strength.

The inverse analysis was performed by first adjusting Young's modulus until the initial slope of the predicted and experimental flexural stress deflection responses matched. As

144

an initial estimate, equivalent elastic modulus from flexural tests was calculated using the recommendations from ASTM C947[143] (reported in Table 4b). Next, the first cracking strain was matched to the post crack response up to the experimental proportional limit (LOP). Finally, the strain at maximum stress was adjusted until both predicted and experimental maximum stresses were coincident. A relatively low value of post crack stiffness η, in the range of 0.01 - 0.04 was used indicating that the stiffness after cracking is in the range of 1-5% of the elastic stiffness. Figures 5-5 and 5-6 show the results of inverse analysis conducted on the specimens with silica fume with and without polymers exposed to three levels of aging.

Figure 5-5(a) shows the experimental and fitted flexural response of GFRC mix with silica fume without any polymer (GFRC A). The initial post cracking flexural stiffness slightly increases or stays constant between unaged and 28 days of aging. This is attributed to increase in the interfacial bond strength and efficient load transfer. The degradation however affects the response and the stiffness decreases as the specimen ages up to 84 days. Relative reduction of flexural strength from the unaged to the age of 84 days is not significant. Ductility, as defined by an area under the stress-strain curve also decreases slightly with aging. Figure 5-5(b) shows the tensile back-calculation results from flexural data compared with the experimental tension results, which resembles the equivalent tension stress-strain but underestimates the strain capacity by as much as 50%.

GFRC mix with silica fume and acrylic polymer (GFRC B) shows similar trend as the previous case (mix A). Use of polymers show marginal improvement in terms of the overall flexural and tensile behavior across all ages. Figures 5-6(a,b) show that the 28 day samples

145

show higher flexural and tensile strength, followed by the unaged samples and 84 day

samples, showing similar results as the samples from the GFRC A mix. The 28 day aging

samples show higher flexural and back calculated tensile strength which is due to the

enhanced bond development of the inner sleeve yarns due to reaction of silica fume

particles [113]. With additional aging up to the 84 day samples, the enhanced bond

however is increased to the point of composite becoming brittle.
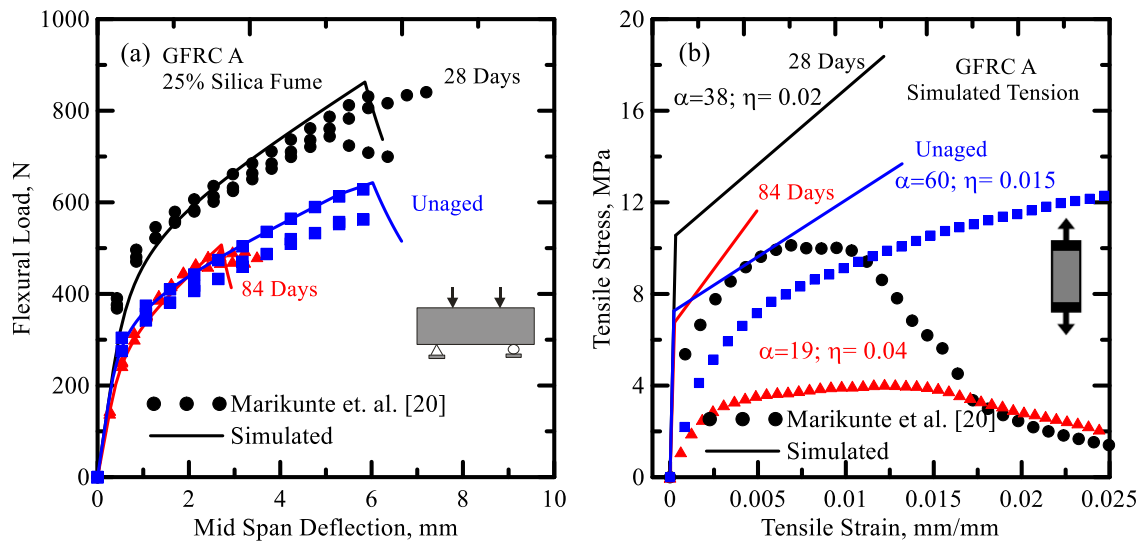
Figure 5-5 (a) : Inverse Analysis of GFRC mix with silica fume, (b): Backcalculated

Tension Models

It is noted that simulations that use flexural response data to calculate direct tension

properties tend to overestimate the experimental tensile data significantly for various

reasons discussed in other publications [**Error! Bookmark not defined.**,136,141]. The

strain values in the experiments were obtained by monitoring the widening of a single crack

on a notched tensile sample. This results in significantly higher than an average strain

obtained as compared to a prismatic sample where the strain is averaged over several

micro-cracks. Due to size effect, the tension notched sample concentrates the stresses at a much more localized region as opposed to a flexural sample. The differences in predicted and experimental tensile response may also be attributed to several factors including: localized failure due to gripping in tension, size effect, uniformity in tension loading vs. the linear strain distribution in flexure, delamination and diagonal tension shear failure that is common in flexure, and variation in lamina orientation and placement which may lead to a wider range of variation among the flexural samples [141]. In general, flexure is more dependent on bonding and stress transfer, while tension is more dependent on yarn properties due to gripping and tensioning all filaments together. Model parameters used in this study are reported in Table 5-2 and corresponding back-calculated material properties have been summarized in Table 5-3. Back-calculated properties from GFRC B are within range of the experimental parameters reported by Marikunte et. al. [113].
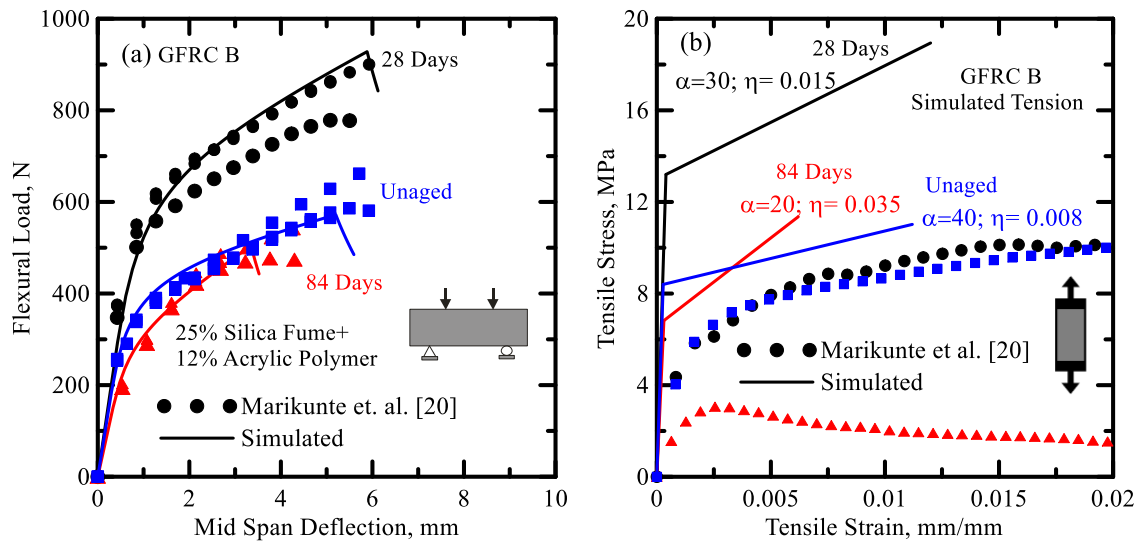
Figure 5-6 (a) : Inverse Analysis of GFRC mix with polymers, (b): Backcalculated

Tension Models

The elastic modulus increases moderately after 28 days of accelerated aging compared to the unaged samples about 33 GPa, followed by a significant drop in magnitude for the 84 days aged samples between 22-26 GPa. It is evident that the elastic modulus is similar between the different mixes, while first cracking strain increases initially after 28 days of accelerated aging and decreases after 84 days of aging. First cracking strain values are also less dependent on the mix constituents and vary between 220-400 microstrains for all GFRC mixes. Residual strength parameter, μ is assumed to be less influential in modelling these mixes, and value range between 0.02-0.1.

Table 5-2: Material parameters used as input to model GFRC composites for inverse analysis

GFRC Mixes and Aging Conditions		Material Parameters		Fixed Parameters: Tension ($\gamma=1$); Compression ($\omega=12$, $\lambda=26$)			
		E	ε_{cr}	α	η	μ	β_{tu}
		GPa	μstr	mm/mm	MPa/MPa	MPa/MPa	mm/mm
GFRC A	A0	33	220	60	0.015	0.05	126
	A28	33	320	38	0.020	0.02	80
	A84	26	260	19	0.040	0.08	110
GFRC B	A0	30	280	40	0.008	0.05	100
	A28	33	400	30	0.015	0.02	70
	A84	22	310	20	0.035	0.1	33

Figure 5-7 plots the response of effective post tensile cracking stiffness, η with aging showing a gradual increase with aging time from 0.02-0.04, suggesting improved fiber-matrix bond with aging. Normalized transitional strain, α shows a continuous decreasing trend with aging across all mixes from 60 to 20 after exposure to 84 days of aging. Normalized ultimate tensile strain, β_{tu} also tends to decrease with aging time, suggesting a significant decrease in strain capacity and loss of ductility upon aging. This is in agreement

with discussions pertaining to Figure 5-3. The loss in ductility could be related to the embrittlement of the fiber bundles due to the penetration of hydration products and chemical degradation of Si-O-Si bond in the glass fibers.

Table 5-3: Predicted mechanical properties by the inverse analysis on GFRC composites (Experimental parameters reported by Marikunte et al. are reported in parenthesis)

GFRC Mixes and Aging Conditions		Flexural Stiffness	Equivalent E. Modulus (ASTM C947)	At first crack		At max. flexural load		Flexural Toughness
				Defl.	Stress	Defl.	MOR	
		N/mm	GPa	mm	MPa	mm	MPa	N.m
GFRC A	A0	628	28.7	0.24	7.26	6.02	28.9	4.57
	A28	680	41.7	0.35	10.56	5.85	38.8	5.70
	A84	535	26.7	0.28	6.76	2.71	22.8	2.02
GFRC B	A0	618	26.1	0.30 (0.99)	8.4 (10.6)	5.20 (8.40)	25.7 (28.0)	3.88 (7.56)
	A28	680	28.7	0.43 (1.07)	13.2 (12.0)	5.88 (4.24)	41.8 (38.2)	6.59 (3.30)
	A84	454	19.1	0.33 (0.76)	6.82 (9.85)	3.35 (1.87)	22.7 (22.1)	1.62 (1.58)
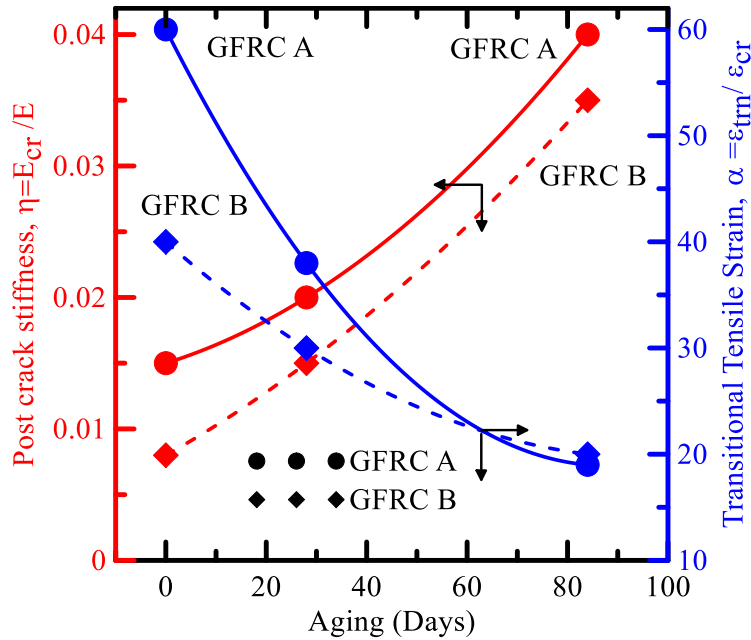
Figure 5-7: Response of normalized post-cracking stiffness, η and normalized transitional

strain, α

5.3. Effect of accelerated aging on residual strength and toughness of GFRC composites

Cementitious matrix and Alkali-resistant glass (ARG) fibers treated with microsilica and acrylic polymer dispersions were studied by Bartos & Zhu [139]. After 7 days of regular curing, specimens were subjected to severe to moderate accelerated aging for 7–42 days in 60 °C water. Flexural behavior was measured using a four point bending configuration on beams with nominal dimensions of 110 x 20 x 9 mm and flexural strength and energy absorption (toughness) were reported. Only the effect of microsilica treatment on the fiber and matrix compositions is investigated as a case study to show the modeling of loss in post-crack flexural strength and toughness. Three mix design were considered which

included plain GFRC mix with OPC and untreated ARG fiber denoted as Ref mix; OPC with 10% microsilica referred as Mmsi mix; and plain OPC with microsilica treated ARG fiber strands referred as Fmsi mix.

Several parameters of the model were assumed to be constant including elastic modulus, E= 20 GPa; first cracking strain parameter ε_{cr}=125 μstr; ultimate tensile strain, β_{tu} =50; and normalized residual tensile strain, $\mu = 0.01$. The parameters for the curve fit were obtained by first developing a range for parameter η, followed by a curve fit of the parameter α in accordance to the method proposed earlier. Three different values of normalized post-crack modulus, η were selected and normalized transitional strain capacity, α were varied to match the experimental flexural strength (MOR) reported in the literature. Toughness was simulated by the integration of the load-deformation response obtained from the material model and compared with the experimental post-crack energy absorbed. Several trend lines of simulated responses can be created based on the combination of parameters, α and η as shown in Figure 5-8(a). Closeness of the fit represents the ability to predict the experimental toughness. Several such series of (α, η) were selected and used for further analysis. Figure 5-8(b) shows the ability of the model to match the experimental MOR and toughness. Using proper parameters, one can effectively predict the experimental strength data, however the predicted toughness trend does not closely match the experimental response especially in the early days of accelerated aging.
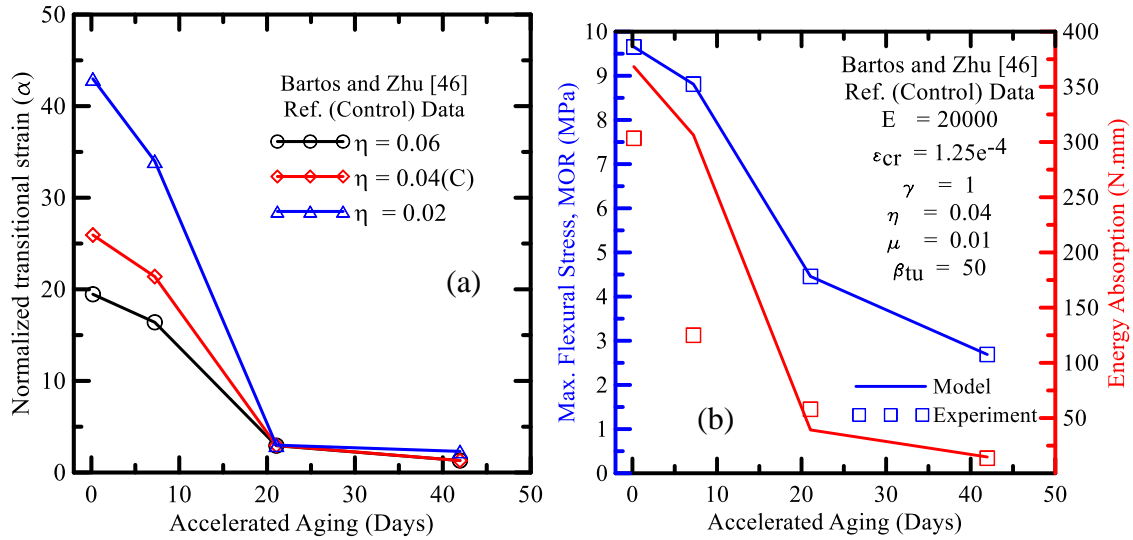
Figure 5-8: Representative simulation of specimens with plain OPC and untreated ARG fibers

The same trends can also be seen in Figure 5-9, wherein data sets – control (Ref), matrix modified with microsilica (Mmsi), and fiber treated with microsilica (Fmsi) have been summarized. Similar to the observations made earlier, modification of the matrix or the fiber with micro-silica use reduces the rate of degradation of mechanical properties significantly.

In order to predict the experimental toughness data, model parameters α and η can be adjusted using several other combinations in order to match the experimental trends. Furthermore these parameters can be optimized to predict both the experimental parameters – flexural strength and toughness. However this is beyond the scope of the current work.

152
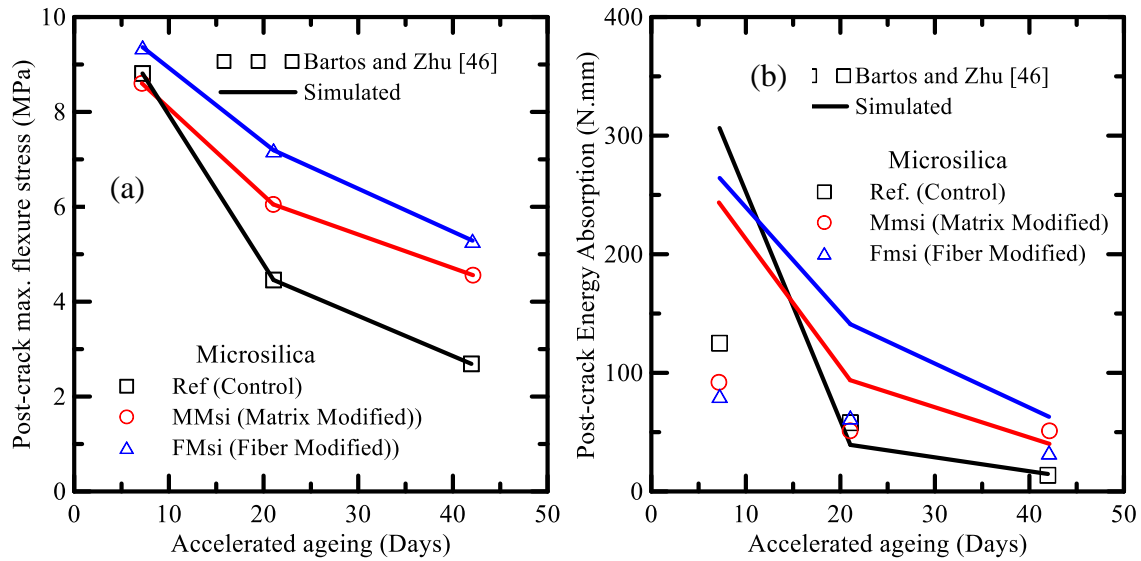
Figure 5-9: Comparison between experimental and simulated aging responses based on:

(a) post-crack flexural strength, (b) post-crack energy absorption

5.4. Long-term performance of vegetable fiber-reinforced mortar composites (VFRMC)

Filho et al. [98] studied the durability of sisal and coconut fiber-reinforced cement mortar composites by testing degradation of the flexural properties of the specimens subjected to aging conditions for up to 10-12 months. Several mortar mixes were developed with short random and long aligned sisal and coconut fibers. Four different aging conditions were evaluated which included control specimens which were tested after 28 days of regular curing, and aged specimens which were tested after aging in water at about 18 °C, exposure to open air and several wetting-drying cycles. Each cycle comprised of 24 hours of exposure in water at 18 °C and six days in a conditioned room at 23 °C and 40% relative humidity. In the current study, durability of these vegetable fiber composites with short random coconut fibers, referred as M1C325 ($V_f = 3\%$) and mix of random (2%), and long

153

aligned (1%) sisal fibers, referred as M1S2S1 were studied. Three-point bending tests were conducted on beam coupons in unaged (control) conditions, and after exposure to 25 and 46 wetting-drying cycles. These beams were tested with a span of 300 mm, and their width and height were maintained as 400 and 100 mm, respectively. The inverse analysis procedure was extended to simulate the degradation of flexural response with aging cycles. Figures 5-10 and 5-11 illustrate experimental and simulated three-point load–deflection curves, and back-calculated tensile response of representative sisal and coconut fiber-reinforced cement mortars treated under the wetting-drying aging conditions.

The behavior of these natural fiber composites could be characterized as deflection/strain softening and hence residual strain parameter, μ plays a significant role in simulating the post-peak response of these composites. Other model parameters such as elastic modulus, E was maintained at about 32 GPa, first cracking strain, ε_{cr} was varied between 120 – 130 μstr, and normalized transitional strain, α was varied between 3-14. Normalized post-cracking modulus, η was set as a negative value to model strain softening behavior and varied between -0.035 and - 0.04. Normalized ultimate tensile strain, β_{tu} was varied between 58- 75 to simulate the deflection capacity of these composites. The effect of aging cycles were more significant on the residual strength parameter, which decreased from 0.8 to only 0.21 after 46 wetting-drying cycles for sisal composites.
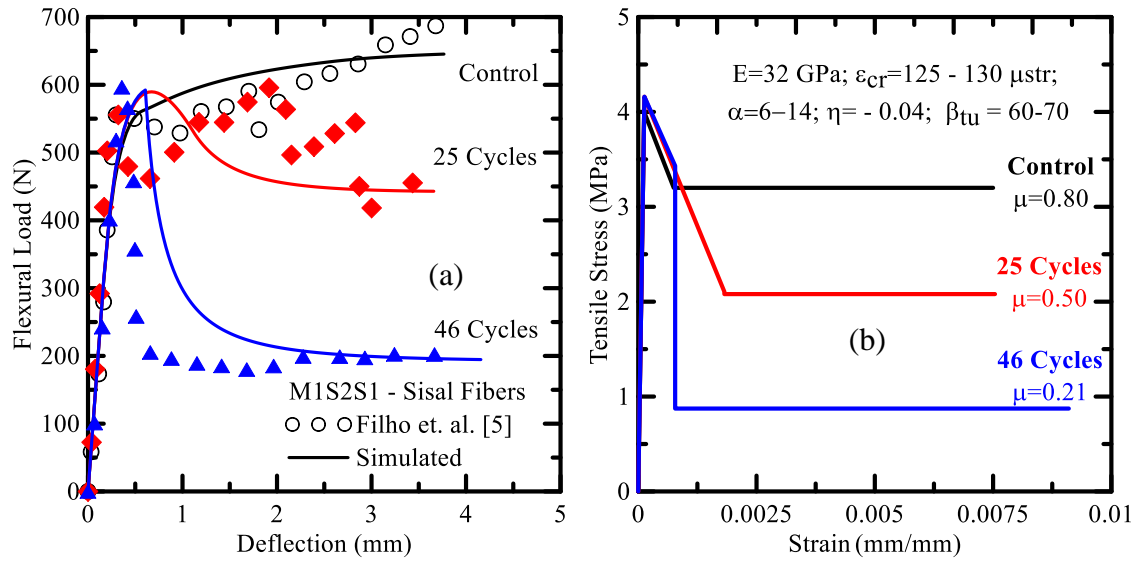
Figure 5-10: (a) Simulated load-deformation and (b) back-calculated stress strain curves

of composite mortar specimens with short and aligned sisal fiber (M1S2S1)

As evident the degradation in the elastic response and bending strength of these natural

fiber composites is comparatively minimal compared to the reduction of the residual

strength with aging cycles. The decline of post-cracking behavior is due to the increasing

brittleness of natural fiber composites, due to the loss of strength of sisal and coconut fibers

with aging and microbiological action when exposed to water [98]. Embrittlement of

natural fibers is also attributed to fiber cell wall mineralization in cement matrix that leads

to the declination of its reinforcing effect [98,144]. When these composites are exposed to

alternating wetting-drying conditions, hydration products such as Ca^{2+} and OH^- ions are

transported from the matrix and get deposited in the lumen and voids of fibers [145,146].

This process of mineralization evident in low modulus, ductile natural fibers, results in

stiffening and brittleness of these fibers upon aging [147]. It was also reported that mixes

reinforced with long fibers showed comparatively less embrittlement when compared to short fibers. Short fibers get mineralized easily as their relatively smaller aspect ratio facilitates easier access for penetration of hydration products, resulting in accelerated loss in ductility of these natural fibers [98]. This results in degradation of the post-cracking tensile strength of natural fiber composites with increasing number of wetting-drying cycles. Estimation of tensile capacity through inverse analysis provides an efficient way of modelling durability of natural fiber composites.
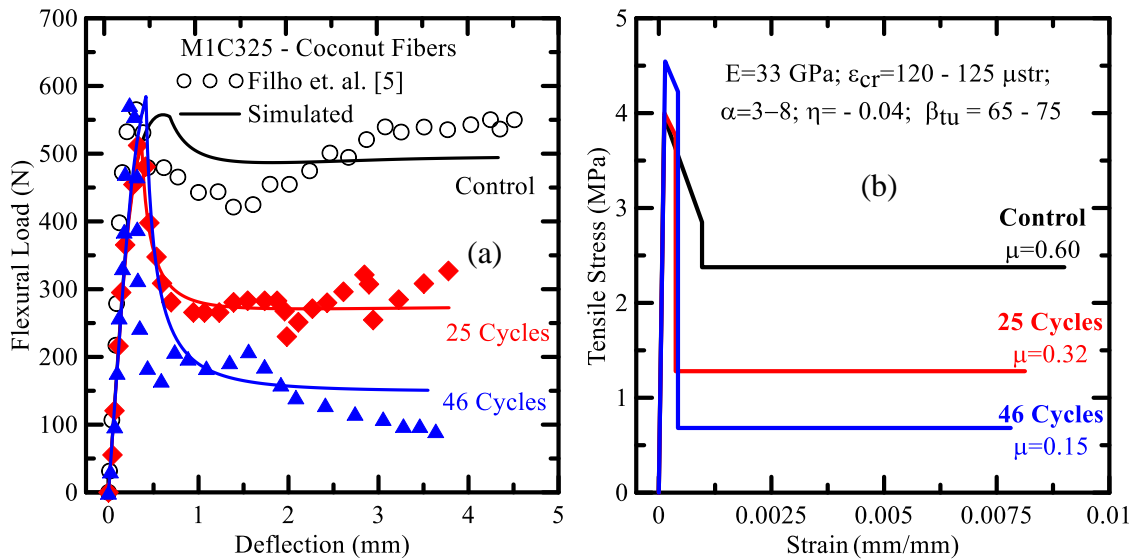
Figure 5-11: (a) Simulated load-deformation and (b) back-calculated stress strain curves of composite mortar specimens with random coconut fibers (M1C325)

5.5. Conclusions

A model is proposed to utilize flexural load deflection data in simulating the aging effect in cement composites containing glass and natural fibers. In the absence of experimental tensile response, the inverse analysis approach can be used to back calculate the tensile response of a material which could then be used as fundamental material property. This

allows for the material properties to be determined from flexural quality control tests and applied in various analysis and design procedure to assess degradation of strength and toughness due to aging. Effect of aging can be described by two main tensile parameters that best characterize aging response are post-cracking tensile stiffness and strain at ultimate stress. Using these two parameters an exponential decay function was proposed to obtain the rate of degradation in ultimate strain capacity and compute the reduction in flexural strength as a function aging and temperature. The model is applicable in comparing different matrix and interface treatment options and to differentiate in between the aging characteristics of different fibers, and matrix constituents. Results further confirm that the effect of aging through loss of flexural strength and ductility can be reduced by matrix modification through addition of pozzolanic materials and treatment of fiber through chemical modification.

6. TOUGHENING EFFECTS IN CEMENT COMPOSITES DUE TO WOLLASTONITE PLATELETS

Large surface areas of freshly-placed concrete such as slabs on grade, thin surface repairs or patching materials are exposed to drying conditions and are often susceptible to early plastic shrinkage cracks[148]. The limited strain capacity of cementitious materials make them weak in tension, brittle, and considerably notch sensitive. Factors such as differential settlement, thermal dilation, and autogenous deformation [149] are also responsible for the formation of plastic shrinkage cracks, but the process is primarily initiated by a high rate of water evaporation from the surface [150,151,152]. The inherent heterogeneity in the microstructure, fracture process with cement-based materials is associated with discontinuous micro-cracking around strong phases that bridge the unbroken ligaments. The inelastic energy dissipation results in marginal toughening of the matrix phase in the fracture process zone (FPZ).

Repercussions of plastic shrinkage cracks include reduction in long-term load carrying capacity, and accelerated deterioration through freezing and thawing and ingress of aggressive agents such as chlorides and sulfates. Such conditions increase maintenance costs, reduce service life, and contribute to long-term durability concerns [153,154,155].Although, effective prevention techniques rely mostly on prevention of water loss, controlling plastic shrinkage cracks can be done effectively by fiber reinforcement [156,157,158]. Use of short distributed wood pulp [159], synthetic [160] and cellulose [161] fibers in reducing shrinkage cracking supports the hypothesis that short

fibers are an effective form of reinforcement against potential plastic shrinkage cracking. [162].

Micro fiber reinforcement increases the tensile strength and ductility of concrete since the energy dissipation in the FPZ increases the load carrying capacity [163]. Propagating micro-cracks intersect the randomly distributed fibers and cause de-bonding and pullout; resulting in energy absorption and toughening [164]. This effect can be measured by evaluating the toughening in the post-peak region of the load-deformation response, often defined in the context of Resistance Curves (R-Curves) [2].

Wollastonite is an acicular shaped - naturally occurring calcium meta-silicate (β-CaSiO$_3$) mineral, formed due to interaction of limestone with silica in hot magmas [165]. It primarily belongs to the group of pyroxenoids which are silicates with a chain structure consisting of silicon and oxygen anions [166]. Chemical composition of wollastonite fibers in general include about 90% of calcium oxide (CaO) and silicon dioxide (SiO$_2$); and less than 1 % of magnesium oxide (MgO), ferric oxide (Fe$_2$O$_3$), aluminum oxide (Al$_2$O$_3$), and potassium oxide (K$_2$O). It also consists of traces of manganese oxide (MnO) and titanium dioxide (TiO$_2$). Natural wollastonite micro-fibers are characterized by loose acicular particles of non-uniform sizes with diameter typically in the same range of the ordinary Portland cement (OPC) particles (about 25-150 µm); and their length is about 40 - 60 microns, have been earlier considered as cementitious admixture [165,167]. Modulus of elasticity of wollastonite fibers vary from about 300 – 530 GPa, and tensile strength ranges between 2700-4100 MPa and are typically used in paint, ceramic products, cement products, pottery and dental care [165,168,169]. Due to its acicular shape, it is commonly used as a reinforcing filler in

159

composite materials. Needle shaped phase increases destruction viscosity, resistance to thermal shocks, and matrix strengthening by impending crack propagation at the matrix boundary, micro-cracking in the crack apex zone and crack path alteration. Since wollastonite is also non-carcinogenic, it can be considered as a substitute to asbestos [166]. High purity wollastonite is compatible with a hydrating cementitious system as it is temperature and chemically resistant. Unlike wood fibers which alter the hydration process of cement and necessitate costly processes to remove lignin, wollastonite being a relatively inert material has little/no effect on the heat of hydration liberated during the hydration process [170,174].

In combination with microsilica, wollastonite offers improvement in packing density [165]. Beaudoin and Low [167,168,170,171] reported that addition of wollastonite micro-fibers to cement-silica fume matrices improved the peak and post-peak deflection responses, and resulted in an increase in flexural strength and toughness by a factor of two. Mathur et.al. [172] also reported improvements in compressive (28-35%) and flexural (36-42%) strengths, with modifications in pre-peak and post-peak load behavior. Reduction of water absorption, drying-shrinkage, abrasion loss, coupled with enhanced durability against freeze-thaw and sulfate attacks were also reported. Kalla et.al. [173] conducted a mechanical and durability study of wollastonite-fly ash concrete systems. Cement replacement by wollastonite (0-25%), fly ash (40%) with water-binder ratio of 0.45-0.55 resulted in reduction in permeability, diffusivity, and improvement in carbonation and corrosion resistance in OPC-wollastonite-fly ash system. Ransinchung et.al. [165,175] studied the use of wollastonite with microsilica in pavement concrete and demonstrated

promotion of water tightness due to refinement of microstructure resulting in higher compressive strength. Optimum dosage of cement, wollastonite and silica fume was 77.5%, 15% and 7.5%, respectively in their study. Deposition of cement reaction products at interface transition zone (ITZ) and resulting matrix densification in the vicinity of boundary of wollastonite fibers can influence calcium hydrate (CH) crystallization sites and reduce matrix permeability [175]. The presence of wollastonite sub-micron fibers therefore promotes refinement of microstructure and provides an efficient micro-reinforcing mechanism that improves early-age mechanical properties [165,172,175,174] and resistance to adverse chemical and physical attacks [172,173]. A key justification for strength and fracture improvement is attributed to the packing factor and matrix densification due to the distribution of a discontinuous phase of sub-micron fibers that interact through the ITZ to introduce a tortuous path ahead of the micro-cracks that initiate and propagate. The changes are related to strength and durability of wollastonite-silica fume-OPC systems [165,172,175,176]. Due to their low cost and limited processing requirements, they can be considered as a viable alternative to commercial microfibers in reinforcing of cementitious systems [170].

Test methodology similar to the recommendations of RILEM 89-FMT [177], was adopted to conduct cyclic three-point bend test on notched beams. Due to the inherent brittleness of cement based materials, the behavior is controlled by crack initiation, damage localization at the notch tip, and subsequent crack propagation [**Error! Bookmark not efined.**,178]. This test is appropriate for characterizing the role of wollastonite fibers in bridging the micro-cracks. Change in the compliance and inelastic deformation at each

loading–unloading cycle are indicators of crack growth and used to calculate fracture energy. The contribution of sub-micron platelets to the toughening potential was studied by means of fracture resistance curves (R-Curves) which measure the increase in energy dissipation due to closing pressure distribution on the crack face and simulate the crack initiation and growth in the matrix [179,180]. The effective crack length was correlated with the apparent compliance of specimens exposed to loading and unloading cycles. The stress intensity factor (K_R) and strain energy release rate (G_R) are computed using non-linear elastic fracture mechanics procedures [181]. The analytical methods were applied extensively to study the effects of material composition, curing duration, and fiber dosage on the fracture behavior of mortar mixes [182].

Majority of recent publications have focused on one-dimensional shrinkage cracking of the cementitious systems by utilizing special restraints [183,184,185], implementing fans [186, 187], fans and heaters [188, 189], heat lamps [190], wind tunnel [191] and vacuum drying [192] to simulate severe evaporation conditions and expedite the drying process causing plastic shrinkage cracks. Such tests provide little information on the principal driving force of plastic shrinkage, lack accurate measurement of moisture evaporation data and characterization of fibers that enable the distribution of cracks throughout the matrix. In this study an experimental setup which monitors growth of shrinkage cracks of cementitious mixtures in fresh state was used and moisture loss in the composite was analyzed by means of a two-stage diffusion simulation approach [198,197]. Fiber-matrix interaction and its influence on transport properties based on the cumulative moisture loss, evaporation rates, and diffusivity were studied. Morphology of the cracked surface in terms

of length, width, area and density was investigated by means of image analysis, and the correlation between moisture loss and crack morphology was established.

6.1. Experimental Program

A series of blended cement paste and mortar mixes were developed using a composition of Portland cement (Type II/V), silica fume, and wollastonite fibers. Micrographs of wollastonite fibers manufactured by NYCO Minerals, Inc. are shown in Figure 6-1.
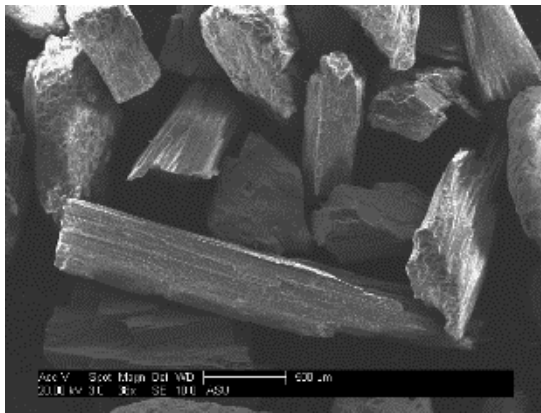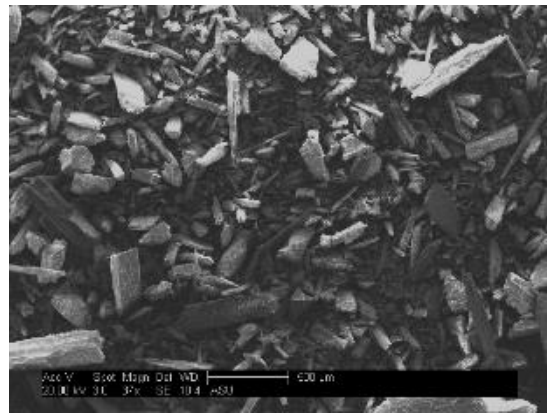
(a) C2000; 38X   (b) C850; 37X
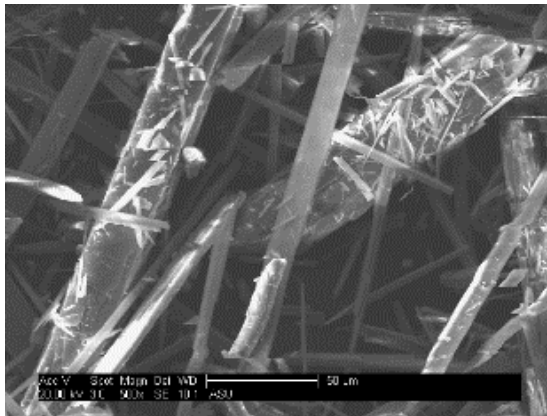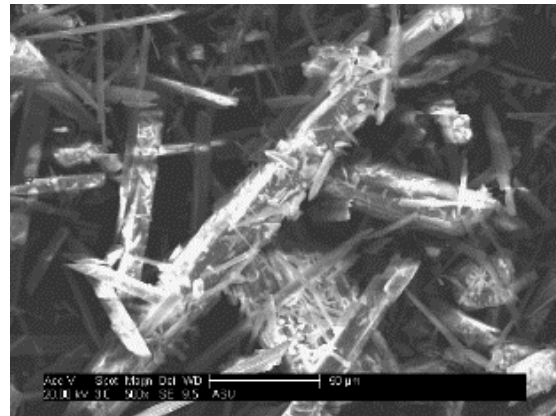
(c) F55; 500X   (d) F33; 500X

Figure 6-1: Microstructure of wollastonite platelets used [193]

The fiber types are designated based on their apparent texture, fineness and average particle size. The fibers were classified as micro or coarse (C) fibers which have higher particle sizes and more angular in shape; and sub-micron or fine (F) fiber types which are relatively more acicular and possess fiber type features. The average particle size of the two coarse grades are 2000 and 850 µm, designated as C2000 and C850; and the fine grades are 55 and 33 µm, which are referred as F55 and F33. Since the mean diameter of the small particles is about only few micron, the fibers in this category are considered as a sub-micron grade. Mortar mixtures were developed with fine silica sand (grit #60), and different sand/cement replacement levels to compare with the paste mixtures.

6.1. Testing Procedure

6.1.1. Cyclic Fracture Tests

Fracture tests were conducted using a closed loop servo hydraulic MTS frame and cyclic three point bending procedure. The beams were loaded along the notch to monitor crack growth, as shown in Figure 6-2. An Instron extensometer was used to measure the crack mouth opening displacement (CMOD). A Linear Variable Differential Transformer (LVDT) with a range of ± 4 mm was used to measure the deflection of the mid span.

(a)

(b)
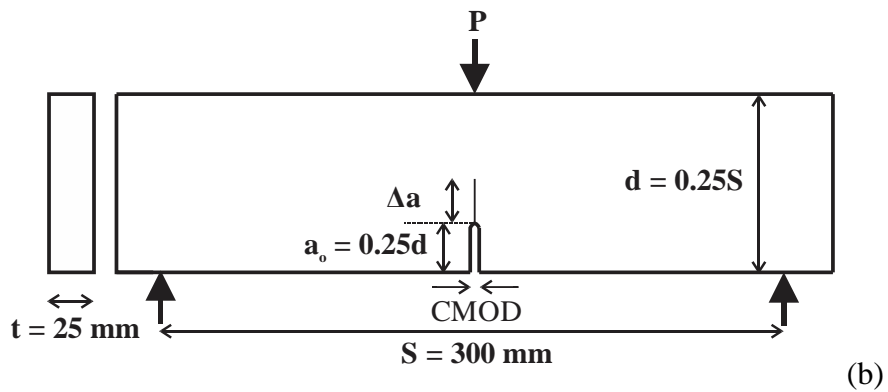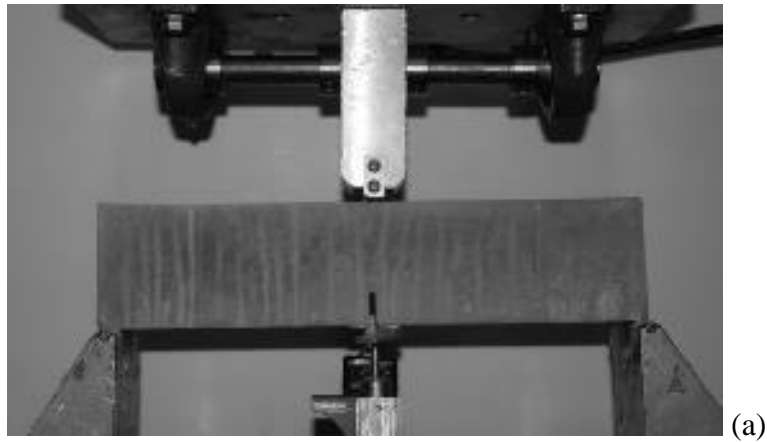
Figure 6-2: Test set up and schematics of fracture testing with mid-point loading

Initially, the testing procedure was controlled monotonically under load control to apply

seating load on the specimen equivalent to about 10 % of the peak load. The feedback was

then switched to CMOD control at a constant rate up to beyond the peak load. First

unloading cycle started at about 80 % of the peak load and the specimen is unloaded to

about 10 % of the peak load, under load control. Cycles of loading-unloading were then

applied under CMOD and load control until five such loading-unloading cycles are

completed at 0.2 mm of crack opening. Compressive strength of the specimens were also

evaluated in accordance with ASTM C109 by testing 50 mm cubes under load control at a constant loading rate of 45 N/sec.

Data reduction procedures included smoothening, interpolation, and estimation of critical testing parameters [182]. Apparent Modulus of rupture (MOR) was obtained by correcting for the notch length using Equation 6-1, based on conventional elastic analysis and represented as:

$$MOR = \frac{3P_{max}S}{2t(d-a_0)^2}$$

Equation 6-1

Where, P_{max} is the maximum flexural load, S is the beam span, $(d\text{-}a_0)$ is the un-cracked depth and t is the thickness of specimen. Numerical differentiation procedure was used to measure loading and unloading compliances based on Linear Elastic Fracture Mechanics (LEFM). Elastic modulus, E, was obtained using Equations 6-2 and 6-3 [181].

$$E = \frac{6Sa_o V(\alpha_o)}{C_i b^2 t}$$

Equation 6-2

Where, $V(\alpha) = 0.76 - 2.28\alpha + 3.87\alpha^2 - 2.04\alpha^3 + \frac{0.66}{(1-\alpha)^2}$

Equation 6-3

Herein, S is the beam span, a_0 is the notch length, α_0 is the normalized notch length defined as a_0/b, C_i is the initial compliance of specimen, b and t are the depth and thickness of specimen. Critical crack length, a_c and also an effective crack length at any compliance was calculated using a numerical solution of Equations (2) and (4).

$$a_c = \frac{EC_u b^2 t}{6SV(\alpha_c)}$$

Equation 6-4

As an intermediate step, the Jenq-Shah two-parameter model was used [178] to calculate: critical stress intensity factor (SIF), K_{Ic}, critical crack tip opening displacement, $CTOD_c$ and G_{IC}, critical intrinsic fracture toughness using Equations (5-8).

$$K_{IC} = 3P_{max} \frac{S\sqrt{(\pi a_c)}F(\alpha_c)}{2b^2 t}$$

Equation 6-5

$$F(\alpha_c) = \frac{1.99 - \alpha_c(1-\alpha_c)(2.15 - 3.93\alpha_c + 2.7\alpha_c^2)}{\sqrt{\pi}(1+2\alpha_c)(1-\alpha_c)^{3/2}}$$

Equation 6-6

$$CTOD_C = \frac{6P_{max}Sa_c V(\alpha_c)}{Eb^2 t}\left[(1-\beta_0)^2 + (1.081 - 1.149\alpha_c)(\beta_0 - \beta_0^2)\right]^{1/2}$$

Equation 6-7

$$G_{IC} = \frac{K_{IC}^2}{E}$$

Equation 6-8

Using the compliance calibration technique the effective crack length and incremental fracture energy in every loading cycle were obtained similar to the linear asymptotic superposition assumption proposed by Xu and Reinhardt [194]. The energy release rate was calculated from the change of stored elastic energy in the specimen [195] and the inelastic absorbed energy component due to the effect of aggregate interlock and bridging zone. The resistance to crack growth expressed in terms of the strain energy release rate, G_R using Equation (9), by using the derivatives of fitted compliance and inelastic CMOD curves [180].

167

$$G_R = \frac{P^2}{2t}\frac{dC_U}{da} + \frac{P}{2t}\frac{d\delta_{in}}{da}$$

Equation 6-9

Where, P is the flexural load, t is the thickness of specimen, C_U is unloading compliance of beam, and a is the effective crack length, δ_{in} is the inelastic deformation, which is equal to inelastic CMOD in this test method. Fracture toughness, G_R can also be related to stress intensity factor, K_R during crack propagation using Equation (10) [180,196].

$$K_R = \sqrt{EG_R}$$

Equation 6-10

Addition of finer inclusions such as wollastonite and silica fume increases surface area of the solids, thus water reducing admixtures were used to compensate for the loss in workability [167,168,170]. Combination of wollastonite and silica fume were used as partial replacement of up to 20% of total cement content. Several control specimens were also prepared with 5% cement replaced with silica fume only. The relative proportions in percentages are presented in Table 6-1 with a cementitious solids-sand ratio of 1:1 and water/cementitious solids of 0.4. Mix designs were classified based on the cement replacement levels by wollastonite alone. The fresh slurry was poured in three layers into polycarbonate 25x75x325 mm beam and 50x50x50 mm cube molds. The specimens were cured under room temperature for 24 hours, and then at 73°F and 100% RH until the day of testing at 7 and 28 days. A circular saw with water cooled diamond blade was used to cut a 19 mm notch at the mid-span of test coupons for a fixed notch/ depth ratio of 0.25. A minimum four replicates beams and three replicate cubes were tested for each mixture set.

Table 6-1: Mix design for fracture tests - proportions by 1000 g of cement

Cement replacement Constituents	0% (Control)	5%	10%	15%
Portland Cement, g	950	900	850	800
Fine Aggregates, g	1000	1000	1000	1000
Silica Fume, g	50	50	50	50
Wollastonite, g	0	50	100	150
Water, g	400	400	400	400
Super Plasticizer	0.5 % - 2.5 % of cementitious solids			

6.1.2. Restrained Plastic Shrinkage

A low-pressure drying apparatus, adopted from corresponding author's previous work, was used to measure the rate of evaporation and quantify the extent of surface cracking of wollastonite fiber reinforced cement pastes. [197,198]. A schematic of this setup is shown in Figure 6-3, wherein fresh paste is filled in a polycarbonate mold with restraint anchors which is then placed in a glass desiccator under imposed drying conditions. The anchor hooks installed in the mold provide restraint in two directions. Inside the glass desiccator, the specimen is placed on a plate resting on a load cell which measures the weight loss during the test.
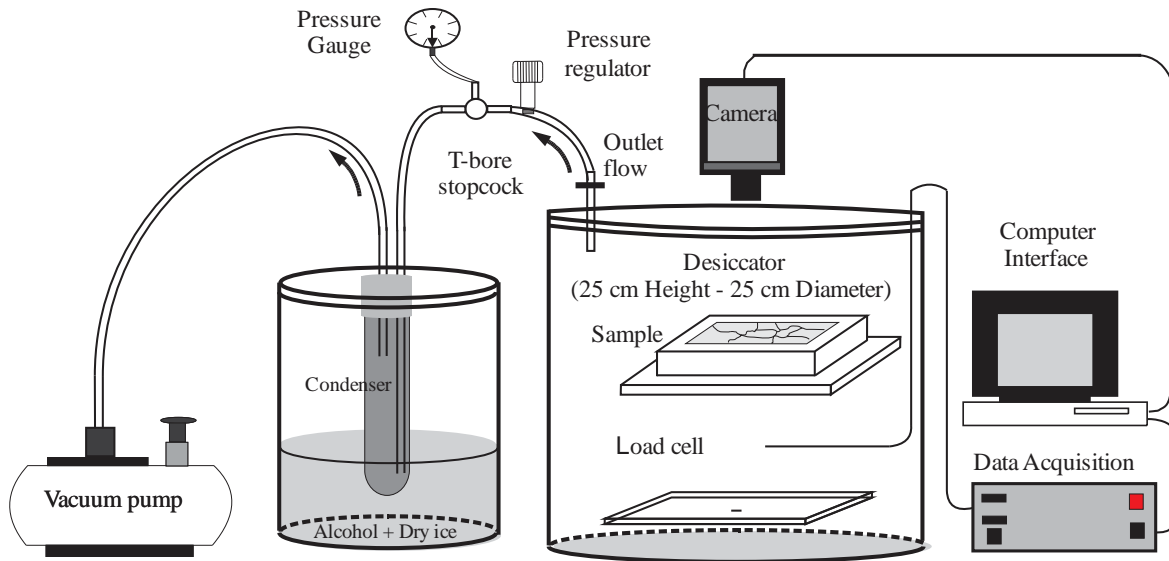
Figure 6-3: Schematics of vacuum drying test setup [199,197]

The vacuum pressure was maintained at 1700 Pa (0.5 in Hg) throughout the test. A D-Drying condensing system was used to remove the water vapor from the desiccator [200]. A digital camera mounted above the specimen captured the surface images of the drying specimen at 15 min intervals. Typical time lapse images analyzed using the Digital Image Correlation technique on a representative alkali activated slag sample are shown in Figure 6-4 [201]. The propagation of 2-D cracks with time for the alkali activated slag. It can be clearly seen that the strain localization is initiated in the first 10 minutes with the major cracks branching and the crack pattern being fully developed by the end of 30 minutes. Beyond this point, there is a predominant crack widening which is reflected in the increase of crack area.
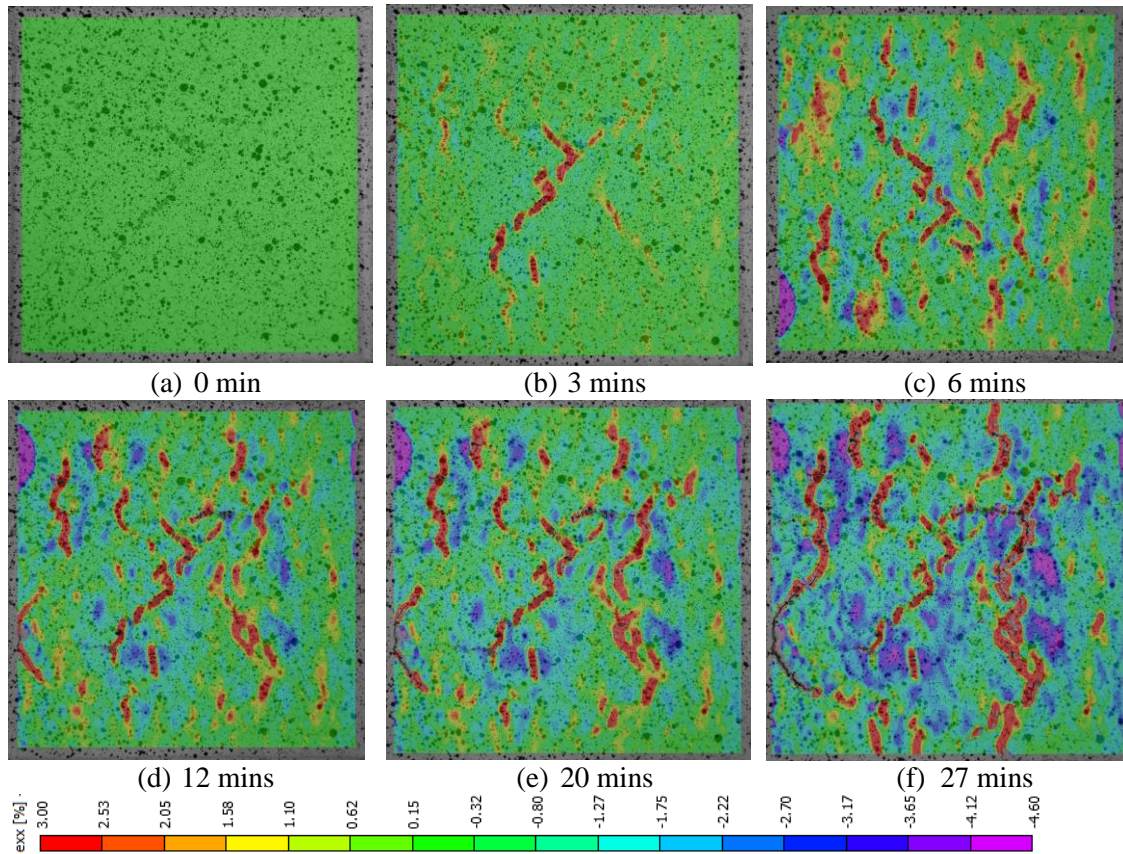
Figure 6-4: Sequential growth of shrinkage cracks observed in an alkali activated slag

specimen wthin the first hour of the test [201].

The loss of moisture from paste samples under vacuum conditions was monitored for a

period of 24 hours. The cumulative moisture loss data was numerically differentiated to

calculate instantaneous evaporation flux expressed in terms of exposed surface area as

shown in Equation 6-11 [197,198].

$$J = \frac{\Delta M}{A \, \Delta t} = \frac{1}{A} \frac{dM}{dt}$$ Equation 6-11

where J is the evaporation flux (kg/m^{2}s), dM is the mass change at specified time steps

(kg), dt is the time step (s) and A is the surface area of the original sample (m^2).

171

Previous studies have represented the moisture evaporation rate in cement pastes using a dual-stage drying model with two-parameter moisture diffusivity constants that represent drying based on both liquid and vapor phases [197,198,203]. Stage I represents the condition where the liquid phase is continuous within the pore structure and drying occurs under external mass transfer. In this regime, water moves to the surface and evaporates at constant rate, producing a continuous moisture loss. Stage I is in effect until the moisture concentration at the surface reaches a value below which external evaporative flux cannot be supported. This is denoted as the transition time, wherein the Stage II mechanism takes over. Stage II describes a discontinuous liquid phase, but a continuous vapor phase within the pore structure. Here, drying occurs under internal mass transfer, where evaporation takes place within capillary pores. The process of moisture removal in Stage II is dominated by diffusion, wherein the evaporation rate reduces and the moisture content decreases until saturation. In summary, the model can be described as a boundary value problem with a specified constant flux at the surface for the first stage and a constant moisture concentration for the second stage. The boundary conditions are given as the following [197,198]:

$$
\begin{aligned}
&\text{Stage I drying:} \quad \text{at } x = L, \quad J = F_0 \\
&\text{Stage II drying:} \quad \text{at } x = L, \quad C_s = C_* = C_{w,low\ pressure}
\end{aligned}
\qquad \text{Equation 6-12}
$$

Wherein x is the pass length of diffusion measured from the bottom face (m), L is the thickness of sample (m), rate of diffusion of water vapor per unit area of the surface kg.m^{-2}.s^{-1}), F_0 is the constant flux in stage I drying (kg/(m^2.s)), C_* is the ambient moisture concentration (kg/m^3), and C_w is the concentration of water vapor present in the low

172

vacuum conditions measured to be constant at about 0.0127 kg of water/kg of air [103].

Assuming a constant diffusivity [202], the analytical solution to the boundary conditions of stage I drying can be expressed as the following:

$$C(x,t) = C_i + \frac{F_0 L}{D_I}\left\{\frac{D_I t}{L^2} + \frac{3x^2 - L^2}{6L^2} - \frac{2}{\pi^2}\sum_{n=1}^{\infty}\frac{(-1)^n}{n^2}\exp(\frac{-D_I n^2 \pi^2 t}{L^2})\cos\frac{n\pi x}{L}\right\}$$ Equation 6-13

where D_I is the diffusivity in Stage I drying. Providing constant F_0 and D_I values, moisture concentration at the top surface can be calculated. Assuming constant concentration at the surface, the analytical solution for the boundary conditions of stage II can be expressed as the following:

$$\frac{C - C_i}{C_* - C_i} = 1 - \frac{4}{\pi}\sum_{n=0}^{\infty}\frac{(-1)^n}{2n+1}\exp\{-D_{II}(2n+1)^2\pi^2 t/4l^2\}\cos\frac{(2n+1)\pi x}{2L}$$ Equation 6-14

Where D_{II} is the average Stage II diffusivity. By integrating both Equation 6-14 over the thickness of sample, total amount of diffusing moisture in Stage I and II drying, which has left the sample at time t, M_t (kg), can be obtained. Using the diffusivity values from Stages I and II, total amount of moisture loss at any time can be measured [203].

6.1.3. Crack Morphology using image analysis

Shrinkage crack morphology was quantified in 2D using a procedure developed earlier in the research group and compared for each type of wollastonite fiber replacement with respect to the control matrix [203]. After the completion of the test, the specimen was scanned using a high resolution (1200 dpi) scanner and the high resolution images were used for the morphological analysis. The scanned images were subjected to filtering and

173

feature recognition algorithms where the unwanted features were removed using Image J$^{©}$, an image analysis software. The image was then cropped to the region of interest which excludes the peripheral cracks around the boundary of the mold and includes the visible two-dimensional shrinkage cracks. The images were then converted to binary form and further extended by a skeletonization process. Figure 6-5 shows the image analysis procedure. Skeletonization allows for the detection of the intersection points by using a single kernel and the convolution function [203]. Sort classes function [204], was employed to reduce the islands of the intersection points down to a single pixel. This function uses specified distance of neighboring pixels to check for non-repetitiveness.

The detected intersection were dilated and filtered with the original image. Such an image was labeled as the final image and used for quantification of crack features. The area was calculated as the summation of the pixels within the region of interest, and the length was measured as length of the major axis of an ellipse that has the same normalized second central moment as the region of interest. All of the subsequent analyses are based on crack lengths and area.
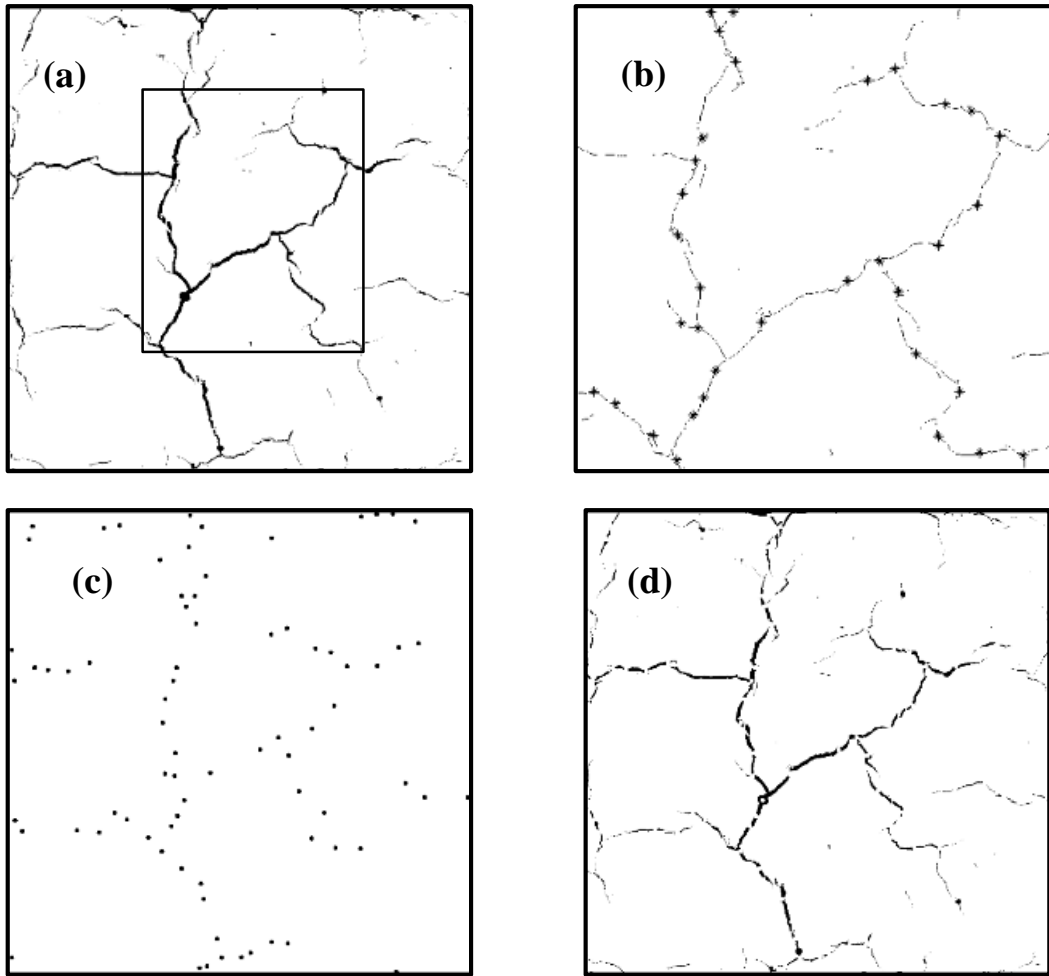
Figure 6-5: Image analysis methodology: a) Binary image of crack pattern, b) Detection of intersection points of cracks from skeletonized image of crack, c) Dilation of the intersection points, d) Subtraction of dilated intersection points from the initial binary image [203]

6.2. Results and Discussion

6.2.1. Compressive Strength

Compressive strength tests on three replicates of 50 mm paste and mortar cubes for each type of wollastonite mixture were performed after 7 and 28 days of moist curing. Average

compressive strength with standard deviations are presented in Figure 6-6. As evident from the trends, marginal improvement due to wollastonite fibers in the early age properties of mortar mixtures is observed. However these fibers are far more effective after 28 days of curing. Compressive strength of control cubes increased by about 10 % after 28 days of curing, with the highest increase in compressive strength for C2000 fibers is about 50%. Compressive strength of specimens with other wollastonite grades increased by about 30 % after 28 days.
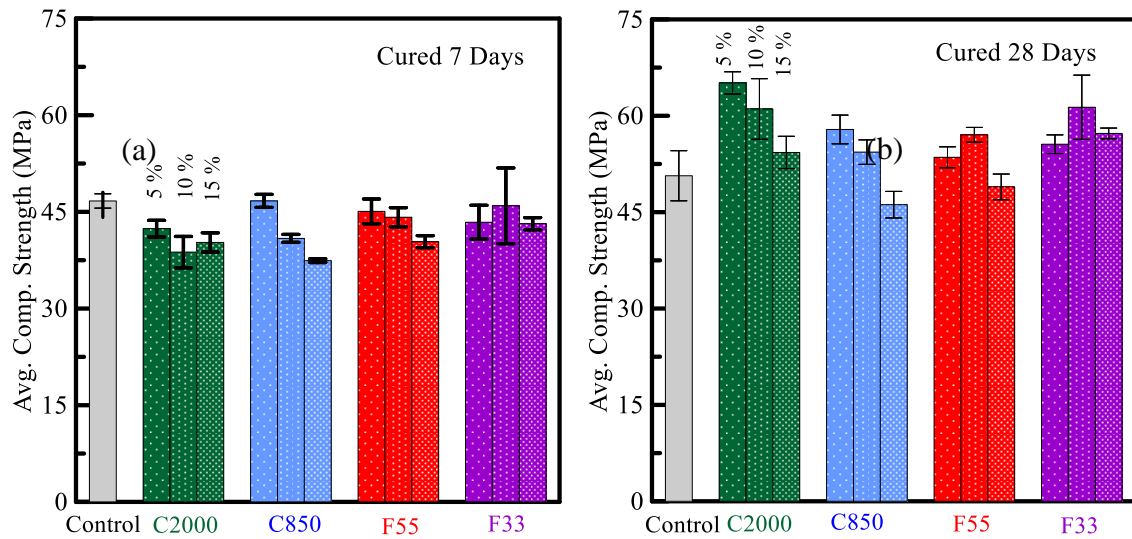
Figure 6-6: Compression test results obtained after (a) 7 days and (b) 28 days of moist curing

Average compressive strength of all grades of wollastonite are significantly higher by as much as 30% at 5% replacement dosage of C2000. This can be attributed to the role of wollastonite fibers in bridging the micro-cracks leading to a delay in micro-crack coalescence. Moderate difference in compressive strength at different dosage levels is observed for the coarser micro fibers. With an optimum dosage of about 5%, a higher

compressive strength is observed for all hydration periods. Finer sub-micron fiber types on the other hand, are more effective at 10 % replacement levels of cement content.

6.2.2. Fracture Properties

A preliminary study with different grades of wollastonite and their contribution in improving the mechanical properties, were measured using paste mixture formulations with 5% and 10% replacement of cement with silica fume and wollastonite, respectively. Similar mix design as reported in Table 6-1 was used, except that contribution of fine aggregates was not considered. Tests were performed after 28 days of moist curing and results of different wollastonite types are compared with plain cement paste and reported in Figure 6-7. Load-CMOD of representative samples and crack growth resistance responses of all the replicates tested are presented.
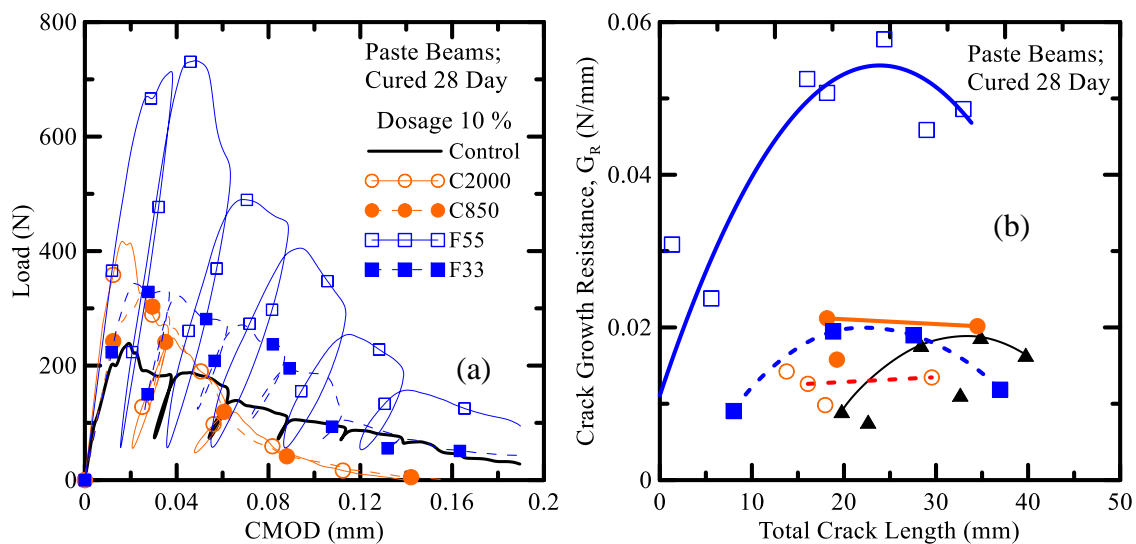
Figure 6-7: Trends of paste mixes: (a) Load vs. CMOD, (b) R-Curve after 28 days [193]

As clearly evident F55 at 10 % dosage is far more effective as a reinforcing medium. MOR and fracture toughness increases by as much as three times for F55 reinforced composites

when compared to control specimens with no fibers. Summary of the analysis conducted on these experimental responses are presented in Table 6-2, which closely match the experimental trends reported in Figure 4.

Table 6-2: Summary of cyclic fracture tests on paste beam Specimens tested at 28 days

Specimen Type / Parameters	Control	C2000	C850	F55	F33
Cycles	4.0 ± 1	2.0 ± 1.0	1.0 ± 0.0	5.0 ± 1.0	4
Apparent MOR (MPa)	1.3 ± 0.0	2.1 ± 0.2	1.8 ± 0.1	4.1 ± 0.6	1.9
Elastic Modulus (GPa)	10.1 ± 0.5	10.3 ± 0.8	9.0 ± 1.1	12.1 ± 0.6	6.7
Critical crack length (mm)	29.4 ± 0.3	30.8 ± 0.4	25.3 ± 2.5	23.5 ± 2.9	19.10
Critical SIF (MPa.mm$^{0.5}$)	8.2 ± 0.2	13.8 ± 1.6	9.8 ± 1.3	21.3 ± 4.7	8.3
Critical CTOD (µm)	9 ± 1	17 ± 1	9 ± 2	12 ± 7	0.85
Critical Strain energy release rate (N/m)	7 ± 1	18 ± 3	11 ± 2	39 ± 17	10
Toughness at 0.20 mm (N.mm)	24.1 ± 2.8	14.8 ± 4.3	17.9 ± 3.0	70.1 ± 10.3	33.2

6.2.2.1. Effect of fiber dosage

Low and Beaudoin [167,168] studied 2-15% by volume of wollastonite fibers incorporated in cement-silica fume matrix and reported a considerable increase in flexural strength and ductility with increasing dosage. Optimum dosage of wollastonite fibers was reported to be about 11.5% beyond which flexural strength decreased. The efficiency of fiber reinforcement is dependent on the ratio of the crystal length to its diameter (aspect ratio), volume fraction of fibers and their bond strength with the matrix. Increasing aspect ratio and volume fraction generally, weakening the bond between the fiber and the brittle matrix, generally improves the mechanical properties of fiber reinforced composites [166]. In the current study, mortar mixtures with three mass fractions of 5%, 10% and 15%, as partial replacement of the total cement content were used. The fracture tests were conducted after

178

7 and 28 days of moist curing. Comparison of flexural load-CMOD and crack growth resistance curves was on the basis of percentage cement replacement by wollastonite fibers. Only C2000 and F55 fibers are presented in Figure 6-8(a) which shows representative trends of load-CMOD response, while Figure 6-8(b) shows crack growth resistance curve for all the replicates tested. It is apparent that the optimum dosage for wollastonite replacement in a cementitious matrix lies between 10 and 15 percent [167]. However as evident from Figure 6-8, optimum dosage is also dependent on the fiber type. For C2000 micro-fibers used at 10% PC replacement, MOR is slightly higher than the remaining dosages by about 6%. However overall toughness of these composites measured up to 0.2 mm of crack opening, is about 40% higher at 15% dosage of C2000 fibers.
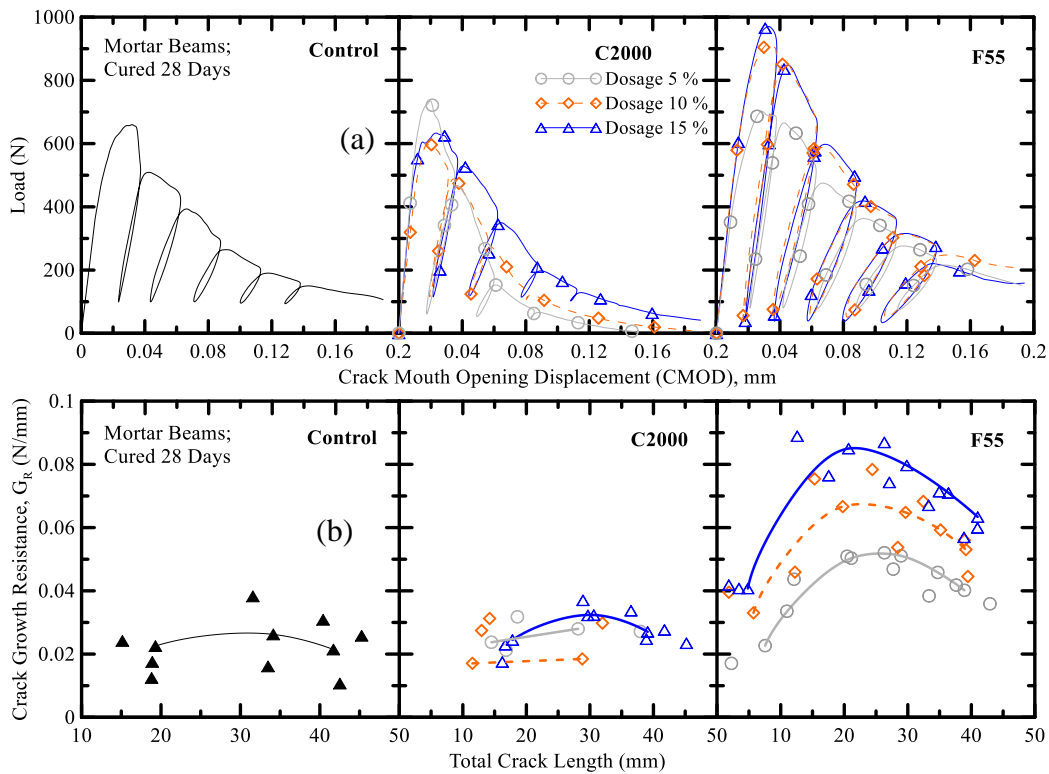
Figure 6-8: Effect of fiber dosage on: (a) Load vs. CMOD, (b) R-Curve [199]

179

Similarly crack growth resistance, G_R is moderately higher at 15% OPC replacement with C2000 fibers. F55 sub-micron particles on the other hand, have higher MOR and flexural toughness at 15% dosage by about 26% and 6% respectively. It is postulated that larger wollastonite particles (C2000/C850) have attributes similar to macro-fibers, wherein higher dosages contribute to enhancement of the overall toughness whereas finer fibers acts as sub-micron reinforcement and enhance matrix packing, thus improving MOR at higher dosages.

6.2.2.2. Effect of Fiber Size

Low and Beaudoin [171] reported that aspect ratio of wollastonite fibers mainly affects the volume and distribution of pore sizes in the microstructure and ductility characteristics of cement-silica fume binder systems. Total porosity and flexural strength of these systems are essentially independent of the aspect ratio. However the characteristics of the pore structure such as volume and pore size distribution are marginally dependent on the aspect ratio of wollastonite fibers with larger aspect ratios being tougher and promoting the formation of large pores in the matrix. It was also reported that cement binders reinforced with wollastonite micro-fibers with larger aspect ratio have larger post-peak deflection and toughness compared to fibers with smaller aspect ratio.

Four wollastonite types, namely: C2000, C850, F55, and F33 were studied with average particle sizes varying from 33 - 2000 μm, as presented in Table 6-2. The aspect ratio of these fibers are not explicitly reported here, however several micrographs with measurements of the lateral and longitudinal dimensions of these fibers have been recorded by the authors. Still it is evident from micrographs in Figure 6-1, the finer fibers (F55 and

F33) are more acicular and have larger aspect ratio than the coarser fibers which are more rounded (C2000, C850). The fracture tests were conducted after 7 and 28 days of curing, however only test data from 28 day tests are presented in this section.

Figure 6-9(a) presents a summary of load-deformation and resistance curves of different wollastonite fibers at a dosage of 15%. It is evident that mechanical properties such as flexural strength, post-peak ductility, and toughness and fracture properties improved significantly with the addition of wollastonite fibers. Unreinforced control cement-silica fume matrix experienced brittle fracture with considerable drop in the residual load-carrying capacity whereas the wollastonite impeded crack propagation in fiber-reinforced coupons. This is observed through enhanced strength, ductility and gradual loss in load-carrying capacity. R-Curves obtained analytically from the loading-unloading cycles are presented in Figure 6-9(b). General results indicate that the toughening effects from the fibers were increased with the longer curing periods. For mortar specimens with C850 fibers, longer curing duration affects the fiber-matrix interaction positively by increasing the energy demand for crack propagation. However for finer fibers such as F55 and F33, improvements in mechanical properties with increase in hydration period were less drastic as they gain high strength at early age. At the end of 28 days of curing, F55 exhibits the best performance among all other grades of wollastonite.

Analyzed fracture parameters are summarized in Table 6-3 and 6-4. Incorporation of fibers increases the fracture resistance. In line with the flexural parameters, wollastonite sub-micron fibers (F55/F33) with higher aspect ratio are more effective in improving the

181

fracture resistance of the composite. Critical crack length, defined as the total length of crack extension beyond which unstable crack growth occurs is increased by as much as 40% for the F55 fibers. Similarly critical fracture toughness increased by almost a factor of 3 for F55 fibers. This can attributed to an improvement in the fracture resistance of the composite due to the fiber bridging action.
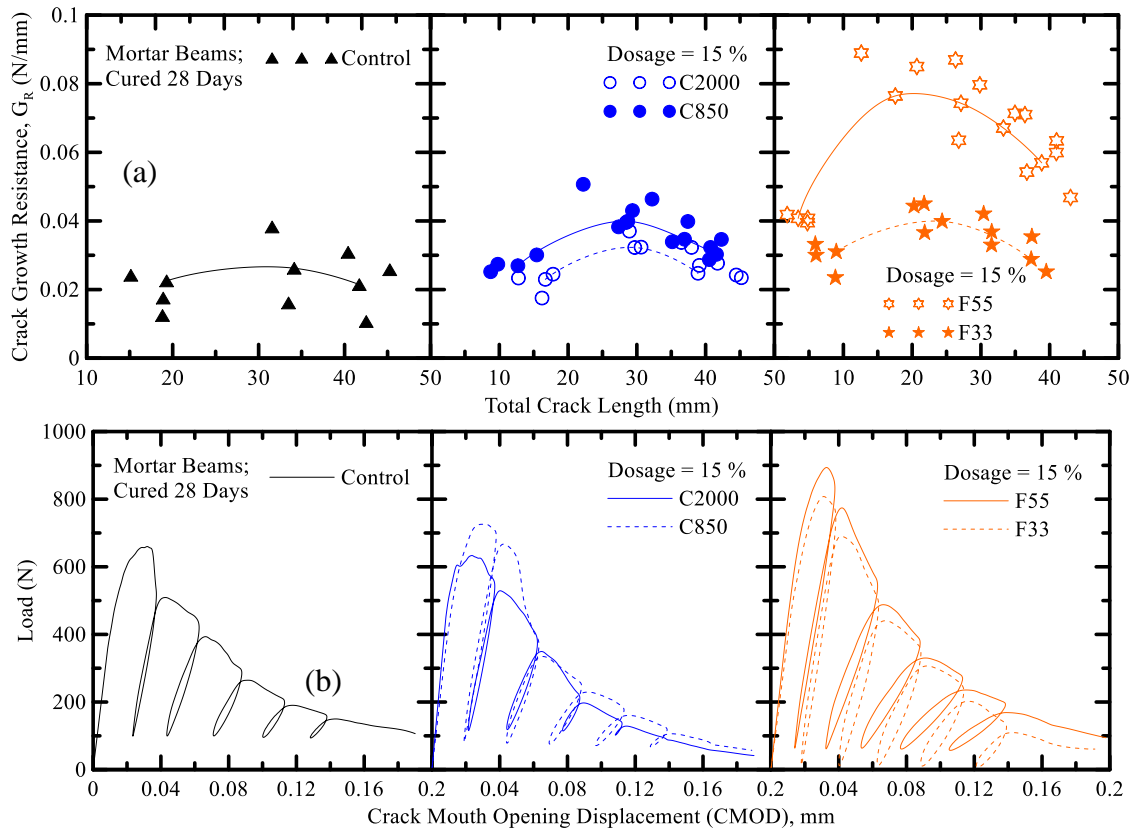
Figure 6-9: Comparison between different grades of wollastonite fibers at 15% dosage:

Table 6-3: Summary of cyclic fracture tests on mortar beams tested after 7 days

	Dosage (cement repl.)	MOR (MPa)	Elastic Modulus (GPa)	Critical crack length (mm)	Critical SIF (MPa.mm$^{0.5}$)	Critical CTOD (µm)	Critical strain energy release rate (N/m)	Toughness at 0.20 mm (N.mm)
Control	0%	3.0 ± 0.3	11.9 ± 1.0	22.3 ± 1.4	14.6 ± 1.9	7 ± 1	18 ± 3	46.9 ± 6.2
C2000	5%	2.6 ± 0.5	14.7 ± 3.2	22.2 ± 2.6	12.8 ± 2.7	5 ± 2	12 ± 4	45.2 ± 7.9
	10%	3.6 ± 0.0	17.4 ± 0.6	27.5 ± 1.2	20.8 ± 0.7	12 ± 1	25 ± 1	54.1 ± 2.7
	15%	2.9 ± 0.1	11.9 ± 1.1	25.5 ± 2.2	15.7 ± 1.1	11 ± 2	21 ± 1	39.7 ± 3.6
C850	5%	3.3 ± 0.1	16.8 ± 1.0	27.2 ± 0.4	18.9 ± 0.7	11 ± 1	21 ± 2	45.3 ± 6.0
	10%	2.8 ± 0.3	12.1 ± 1.2	22.7 ± 2.8	13.7 ± 2.7	7 ± 4	16 ± 5	43.2 ± 10.5
	15%	3.0 ± 0.3	15.1 ± 1.1	25.9 ± 3.5	16.5 ± 3.1	10 ± 5	18 ± 6	39.4 ± 11.2
F55	5%	4 ± 0.3	12.5 ± 2.8	22.7 ± 3.2	20 ± 1.4	9 ± 7	22 ± 6	81.2 ± 15.1
	10%	4.1 ± 0.6	17.0 ± 2.9	24.6 ± 5.6	21.9 ± 3.2	9 ± 6	28 ± 5	70.8 ± 14.3
	15%	4.1 ± 0.2	16.7 ± 1.8	24.8 ± 2.8	21.6 ± 2.1	10 ± 2	28 ± 1	76.7 ± 14.9
F33	5%	3.3 ± 0.1	15.2 ± 2.2	25.8 ± 4.1	18.2 ± 2.9	10 ± 4	22 ± 4	44.0 ± 6.3
	10%	3.5 ± 0.4	14.6 ± 2.6	24.6 ± 4.3	18.5 ± 3.0	10 ± 4	24 ± 6	73.3 ± 17.5
	15%	3.6 ± 0.2	12.9 ± 1.3	21.7 ± 1.8	17.0 ± 0.8	7 ± 2	23 ± 1	77.0 ± 23.7

Table 6-4: Summary of cyclic fracture tests on mortar beams tested after 28 days

	Dosage (cement repl.)	MOR (MPa)	Elastic Modulus (GPa)	Critical crack length (mm)	Critical SIF (MPa.mm$^{0.5}$)	Critical CTOD (µm)	Critical strain energy release rate (N/m)	Toughness at 0.20 mm (N.mm)
Control	0%	3.1 ± 0.5	18.1 ± 1.2	27.8 ± 1.5	18.6 ± 2.9	11 ± 2	19 ± 5	34.0 ± 8.9
C2000	5%	3.7 ± 0.3	19.1 ± 2.1	27.8 ± 1.7	22.1 ± 3.0	12 ± 2	26 ± 5	33.6 ± 5.7
	10%	3.8 ± 0.5	18.3 ± 1.9	25.7 ± 2.2	20.9 ± 4.2	10 ± 3	24 ± 7	39.5 ± 4.5
	15%	3.5 ± 0.2	18.7 ± 1.2	27.5 ± 1.6	20.3 ± 1.8	11 ± 1	22 ± 3	47.8 ± 2.0
C850	5%	4.3 ± 0.5	20.0 ± 3.3	28.9 ± 3.5	26.6 ± 5.8	15 ± 4	35 ± 10	56.6 ± 7.2
	10%	3.7 ± 0.3	15.7 ± 2.4	26.6 ± 4.0	21.4 ± 4.0	13 ± 5	29 ± 7	51.1 ± 5.5
	15%	3.9 ± 0.2	18.1 ± 1.2	27.0 ± 2.7	22.3 ± 1.4	12 ± 3	27 ± 2	57.9 ± 7.5
F55	5%	4.1 ± 0.3	15.5 ± 3.8	57.4 ± 47.0	14.8 ± 11.0	12 ± 5	83 ± 0.157	79.5 ± 15.7
	10%	4.9 ± 0.4	17.5 ± 1.2	23.3 ± 2.0	25.1 ± 3.0	10± 3	36 ± 7	81.3 ± 19.8
	15%	5.2 ± 0.3	16.8 ± 0.9	23.4 ± 1.9	26.1 ± 0.7	10± 2	40 ± 1	84.1 ± 16.6
F33	5%	3.9 ± 0.5	16.5 ± 1.4	26.7 ± 1.8	22.2 ± 3.3	13 ± 2	30 ± 7	54.0 ± 2.2
	10%	4.1 ± 0.1	14.1 ± 0.9	22.1 ± 1.2	19.9 ± 0.7	1 ± 2	28 ± 1	68.8 ± 11.6
	15%	4.2 ± 0.4	15.1 ± 1.3	22.9 ± 1.5	21.1 ± 2.3	9 ± 2	29 ± 4	64.3 ± 8.6

6.2.2.3. Effect of hydration period

The effect of hydration length for specimens cured for 7 and 28 days were studied for all grades. Testing parameters such as MOR, flexural toughness, critical energy release rate, and critical crack length are summarized in Figure 6-10. Effect of micro- and sub-micron fiber types at different dosages compared to control mixes and effect of curing periods are also reported. Similar to the studies conducted by Lou and Beaudoin [167,168], the wollastonite fibers show an optimum dosage level beyond which the effectiveness of the fiber diminishes. For instance coarser micro-fibers (C2000/C850) were more effective at dosages between 5-10 %, and finer sub-micron fibers (F55/F33) are much more effective at higher dosages of 10-15 % of cement content.

Quantitative comparisons with control beams suggest that flexural strength and total toughness increased by as much as 30% and 60% for F55 and F33 sub-micron fiber types at 15% replacement after 7 days of curing. The 28 day test results follow a similar trend in terms of improvements in strength and toughness. Comparison between 7 and 28 day tests on mortar specimens with C850 at 15% dosage reveal that there is almost a 30% increase in the maximum load carrying capacity (from 3 MPa to 3.9 MPa) and 50% increase in total toughness (from 39 to 58 N.mm) with increase in curing duration. F55 fibers show an increase in maximum load capacity of 27% (from 4.1 MPa to 5.2 MPa) and toughness of 9% (from 77 N.mm to 84 N.mm) at 15% dosage after 28 days of curing. For F33 fibers an interesting trend can be seen that even though flexural strength increased moderately by

184

about 15% after 28 days of curing for all three, there was a reduction in total toughness for 10% and 15% dosages indicating increased strength resulting in brittleness.

Flexural strength of control beams increased by only 7% when hydration period was increased from 7 to 28 days. However the strength of specimens with micro and sub-micron fibers increased by as much as 30% and 20%, respectively after 28 days of curing. These results are similar to the compression tests, however the fibers as evident are far more effective in tension especially when cured for longer durations. Effect of increase in hydration period on flexural toughness measured at test limit of span/1500, is less obvious. The flexural toughness of C850 and F55 increased by 30% and 10%, respectively with curing. Beams with C2000 and F33 fibers have inconsistent growth/decay in toughness. Toughness of control beams reduces by 28 % after 28 days as well.
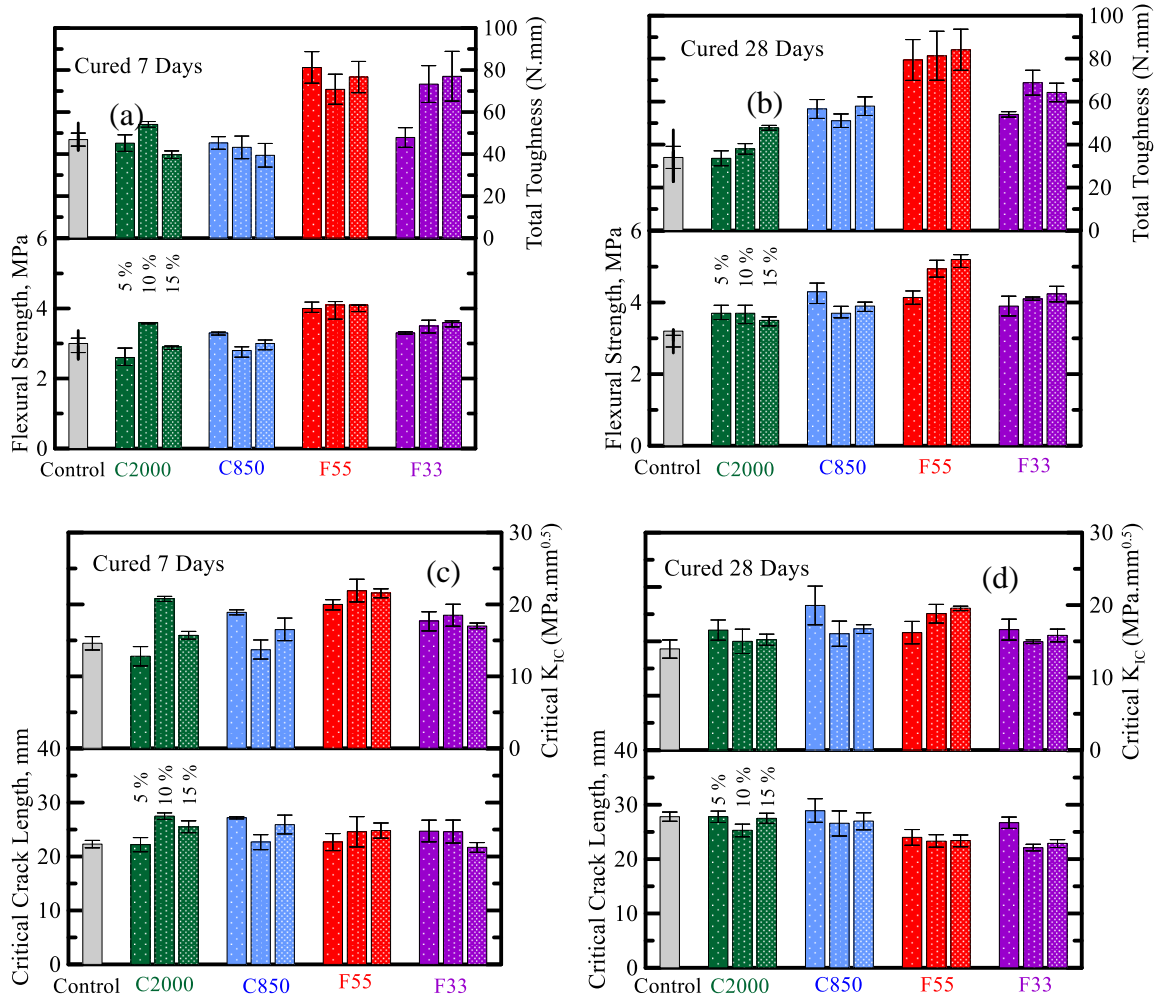
Figure 6-10: Effect of hydration period on performance of wollastonite fiber reinfored

composites

Critical SIF for mode I fracture (K_{IC}) measured q of control beams is about 19 MPa.mm$^{0.5}$. Beams reinforced with wollastonite fibers have K_{IC} values ranging from 20-27 MPa.mm$^{0.5}$. Again K_{IC} values of beams with wollastonite fibers are higher after 28 days, compared to 7 days of curing, suggesting improvement in fracture resistance of the matrix.

6.2.3. Shrinkage Cracking of Wollastonite Blended Matrices

6.2.3.1. Time history of cumulative moisture loss and rate of evaporation

Figure 6-11 shows the reproducibility of the moisture loss experiments for the control cement paste and pastes containing 15% of C850 and F55 fibers at an OPC replacement level of 15% by mass. A typical set of cumulative moisture loss and evaporation-time responses obtained from the experiments performed for up to 24 hours are shown. The overall moisture lass and evaporation rate response of both the control and Wollastonite fiber reinforced specimens are found to be quite similar. Parameters that characterize the initial evaporation rates, transition time between Stages I and II, their diffusivities, and the cumulative moisture loss are determined as described earlier and reported in Table 6-5.
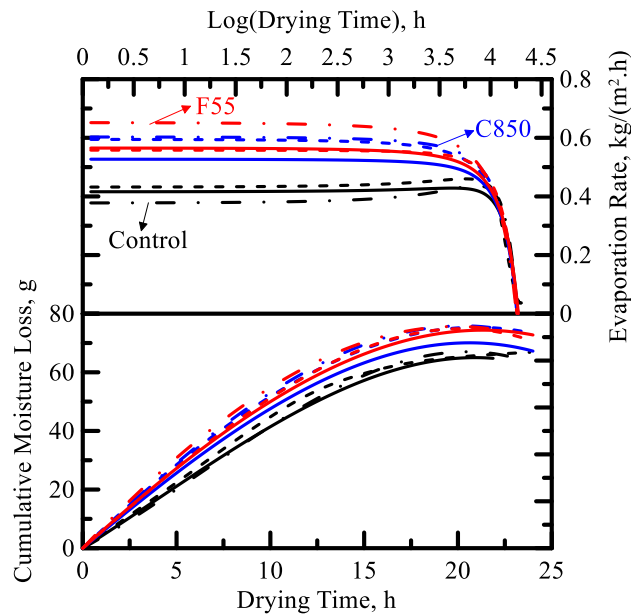
Figure 6-11: Cumulative moisture loss and evaporation rate curve of replicates at 15% dosage

Table 6-5: Summary of Moisture Transport Parameters

Specimen Type	Initial Evap. Rate (kg/(m²h))	Cumulative Moisture Loss at 24 h (g)	Transition Time (h)	Diffusivity Stage II (m²/s) x 10⁻²
Control	0.40 ± 0.08	64.7 ± 0.9	11.4 ± 1.5	1.48 ± 0.22
C2000	0.49 ± 0.10	67.5 ± 3.1	9.0 ± 1.2	1.57 ± 0.08
C850	0.55 ± 0.08	70.1 ± 3.0	8.4 ± 1.7	1.65 ± 0.08
F55	0.56 ± 0.07	71.4 ± 2.4	8.6 ± 2.4	1.69 ± 0.16
F33	0.54 ± 0.05	69.2 ± 2.0	9.6 ± 0.5	1.61 ± 0.08

Diffusivity of the constant drying rate phase, i.e. stage I, was determined as 1.85 m2/hr by fitting the experimental response to the simulated moisture loss curve. Cumulative moisture loss of control specimens are found to be 5-10% lower, and evaporation rates 22-40% lower than those of the specimens reinforced with different grades of wollastonite fibers.

6.2.3.2. Effect of w/s ratio

The estimated normalized cumulative moisture loss for the control paste and the pastes incorporating 15% of C2000, C850, F55 and F33 grades of wollastonite were found to be 0.188, 0.232, 0.239, 0.242 and 0.235 g/g of the initial mass of the paste. It is well known that the cumulative moisture loss will be higher for higher w/s systems. Cement replacement by wollastonite allowed for a higher effective w/s ratio (since the fibers can be considered to be relatively inert during the early ages) as compared to control paste resulting in a 29% increase in the cumulative moisture loss. Higher cumulative moisture loss can be also inferred from the Stage I and Stage II diffusivities as shown in Table 3. During Stage I or the constant drying phase, most of the mass loss occurs at the paste-air

interface through vapor diffusion into the air and is independent of the internal capillary transport processes in the material. Hence, Stage I diffusivities are observed to be similar for all the specimens irrespective of the material constitution. Beyond the transition time, as the external interface gets saturated, the rate of evaporation declines. Phase transition then takes place within the capillary pores and mass transfer occurs in the micro-structure [203]. It is postulated here that, in this secondary drying phase, the rate of diffusivity is influenced by the pore structure features and the presence of inclusions. For the Wollastonite fiber reinforced pastes, the Stage II diffusivity is thus observed to be higher by up to 14%. The combined effect of increased initial evaporation rates for the Wollastonite fiber reinforced specimens and the variability in diffusivity between Stages I and II contributes to an increase in the cumulative moisture loss when compared to the control paste.

6.2.3.3. Effect of fiber type

A significant influence of cement replacement with wollastonite can be observed in the reduction of Stage I to Stage II transition times and the drying modes. This can be attributed to the contribution of these fibers in controlling early-age cracking. Addition of wollastonite decreased the transition time from 11 to 8 hours as shown in Table 6-5, which indicates a faster initial evaporation rate that could be attributed to higher number of micro-cracks as observed in surface of the fiber reinforced specimens. Comparison of the initial evaporation rate and diffusivities based on the type of wollastonite fiber indicates an interesting trend. According to Figure 6-12, average diffusivity of Stage II increased

189

moderately by 6%, 11%, 14% and 9% for the specimens containing C2000, C850, F55 and F33 fibers respectively, as compared to the control specimen.
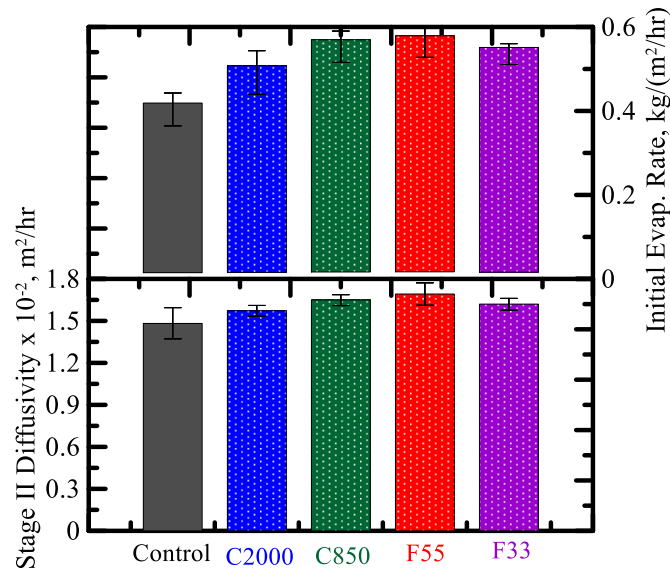
Figure 6-12: Effect of wollastonite addition on Stage II diffusivities and initial evaporation rate

Similar to diffusivity, initial evaporation rate is also influenced by the size of wollastonite fibers. Finer wollastonite particles result in up to 40% higher evaporation rates when compared to the control specimen as shown in Figure 6-12. The parameters influencing the evaporation include both the higher effective w/c ratio as well as the size of the wollastonite inclusions. Since during stage II, diffusivity is controlled by internal mass transfer, the microstructure plays a significant role in the drying process. Specimens reinforced with wollastonite fibers exhibit a higher diffusivity as the microstructure allows for the moisture to travel easily through the cracked surface area. The uniform distribution of acicular wollastonite inclusions within the paste arrests the cracks at a micro-scale level, thereby

limiting cracking at the macro level. Such a mechanism produces more distributed internal micro-cracks, thus enabling shorter and possibly less tortuous path for moisture diffusion, resulting in enhanced diffusivity, evaporation rate, and moisture loss.

6.2.4. Surface Crack Morphology under Shrinkage Cracking

Representative images from the surface crack morphology study are shown in Figures 6-13 (a-e). It is evident that the wollastonite fibers are effective in restraining the surface crack growth as the reduction of plastic shrinkage cracks due to addition of finer sub-micron wollastonite fibers can be attributed to their smaller size and the ability of arresting cracks at the micro level. The crack morphology results are summarized in Figure 6-14. Total area of cracks, crack length and width have been considered to compare different groups of specimen. Wollastonite fibers are observed to reduce the magnitude/extent of cracking, especially when finer fibers are used. Among all four grades of wollastonite fibers, the finest variety, F55 is most effective in improving resistance to early age shrinkage cracks.
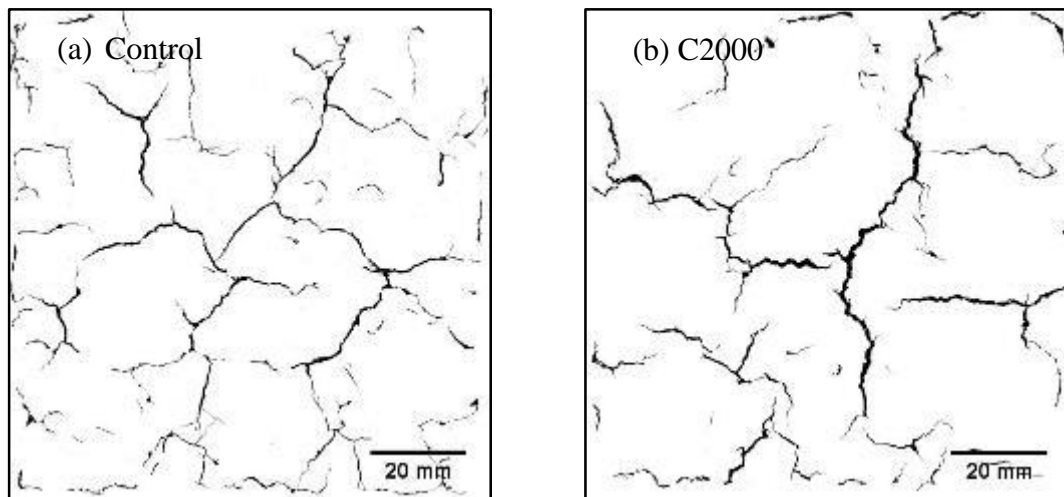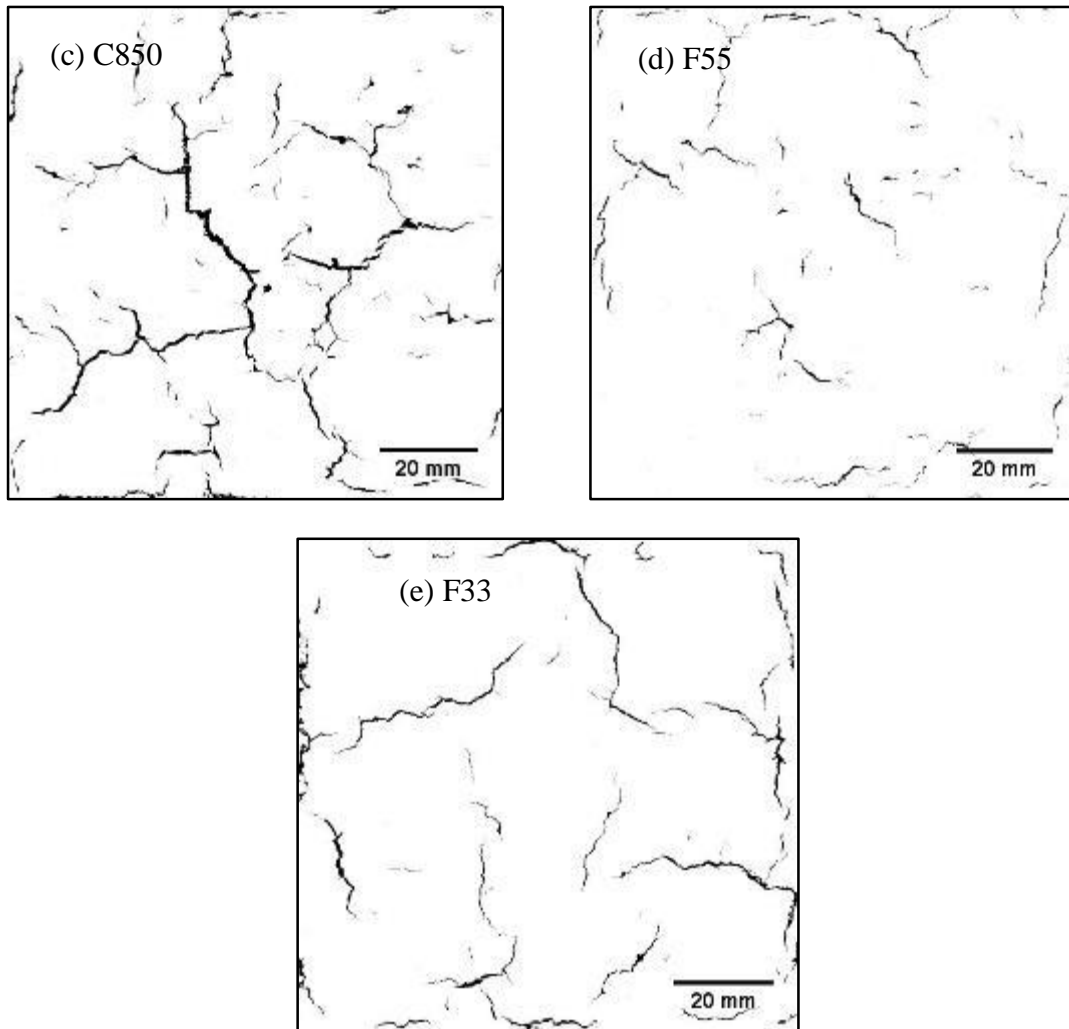
Figure 6-13: Processed binary images of surface cracks observed representative test coupons [199]

Total length of cracks and their width is reduced by a factor of two, and cracked area is reduced by as much a factor of three for specimens reinforced with F55 fibers as compared to the control paste. F33 fibers are far more effective in arresting early age shrinkage cracks by reducing the crack width and total cracked area by 17 and 41 %, respectively.

Finer wollastonite fibers with higher aspect ratios have more acicular features and contribute more to the traditional toughening mechanisms through crack bridging, fiber pullout and rupture, when compared to the coarser fibers. The remaining forms of wollastonite fibers are also effective in limiting shrinkage crack growth, albeit not as effective as F55 fibers. For instance, C2000 fibers can reduce the total crack length and area by about 30 %. C850 fiber reduces the length of cracks by 40 % and cracked area by about 9 %. The overall effect of crack length reduction is comparable among all the fiber types tested as shown in Figure 6-14(b). The contribution of wollastonite fibers in controlling early age shrinkage cracks is more evident in terms of the crack width. This attribute has tremendous impact in terms of long-term mechanical and durability properties of concretes.
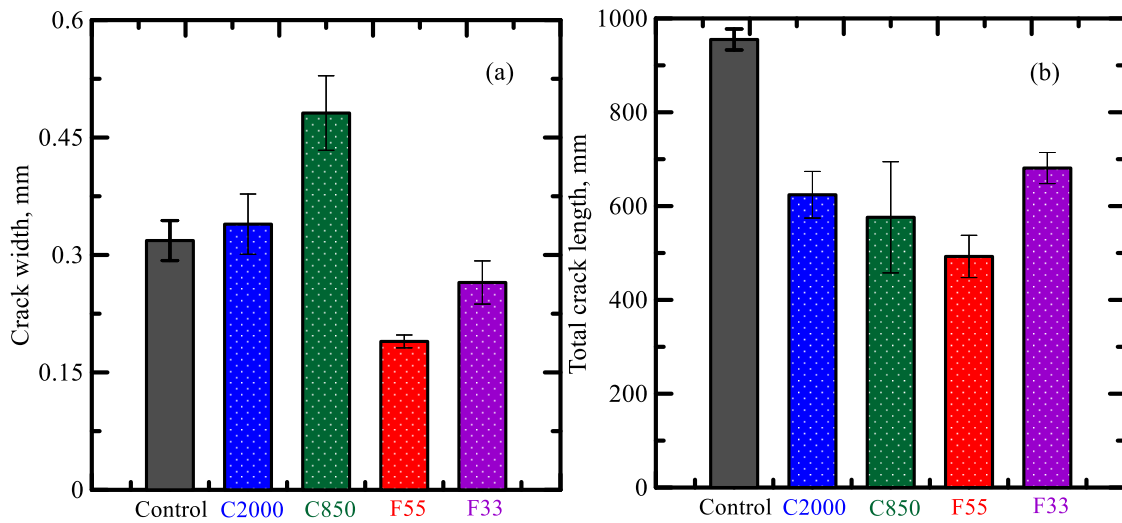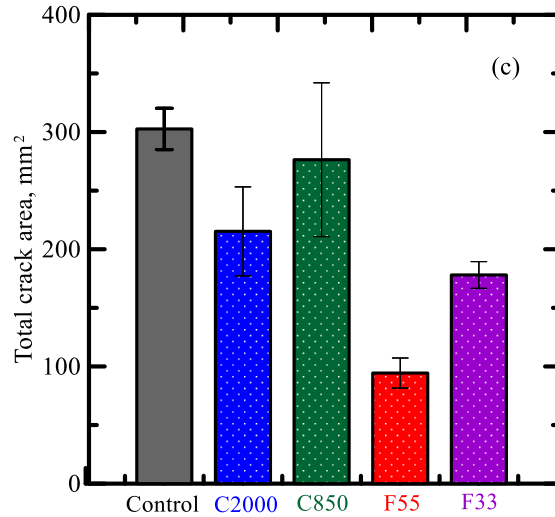
Figure 6-14: Effect of Wollastonite fibers in altering early age shrinkage in cement based

paste specimens: a) crack width; b) total crack length; c) total track area

Sequential crack formation was studied using a crack quantification technique on planar

images obtained at different time intervals during the test. Figure 6-15 shows the

development of crack area with respect to time during the drying experiment. It is evident

that the visible crack initiation for the all of the specimens happens at around 2 hours after

the beginning of the test. The crack area does not seem to grow after about 5 hours into the

test. As can be noticed in this figure, the progression of crack area is much faster in the

control specimen and asymptotes at about 3 hours into the testing. Addition of wollastonite

fibers to the cement paste limits both the rate of development and the overall extent of the

total crack area. Similar to the trends reported earlier for diffusion and evaporation, the

improvement in performance is linked to the size of the fibers. The use of F55 fibers result

in the lowest crack formation rate (defined as crack area change per unit time), which is an

order of magnitude lower rate than that of the control paste. The differences in the observed

194

trends can be also explained in terms of the microstructure of these fibers. Again, the finer wollastonite fibers, are more acicular (needle like) in shape and have higher aspect ratio than the coarser fiber (see Figure 1). Combination of these features and the fact that particle size of the finer wollastonite grades are more in the range of cement particles, finer fibers are more effective in bridging cracks at micro level, and have better contribution to the overall toughening mechanism.
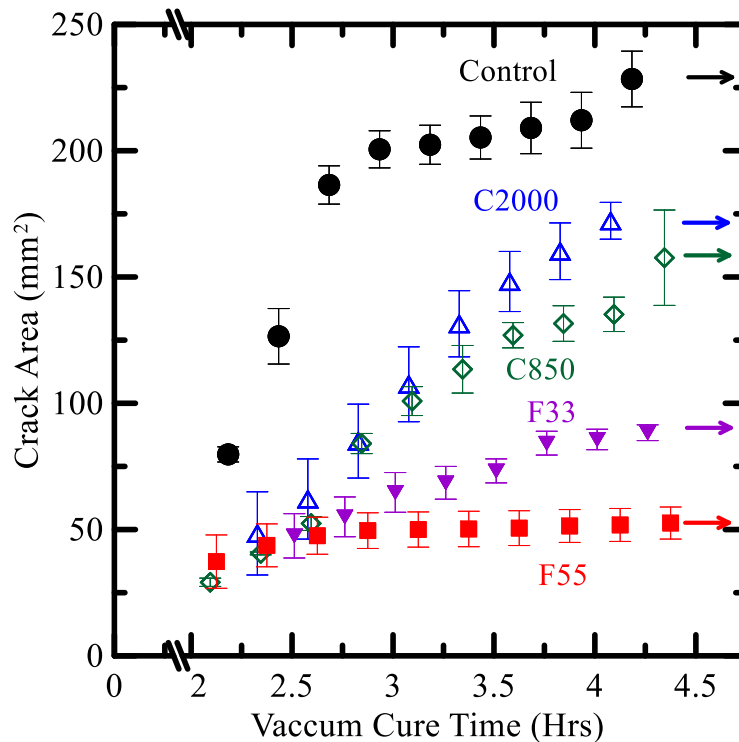
Figure 6-15: Effect of wollastonite in sequential crack formation

The relationship between crack area and normalized cumulative moisture loss is shown in Figure 6-16. A higher surface crack area does not correlate with higher cumulative moisture loss magnitudes. This is attributed to the higher number of cracks of smaller width allowing a higher amount of water evaporation than fewer wider cracks. A network

195

of small, distributed, internal micro-cracks contributes to a much higher evaporation rates, diffusivities, and cumulative moisture loss at the end result in a lower cracked area as shown in Figure 11.
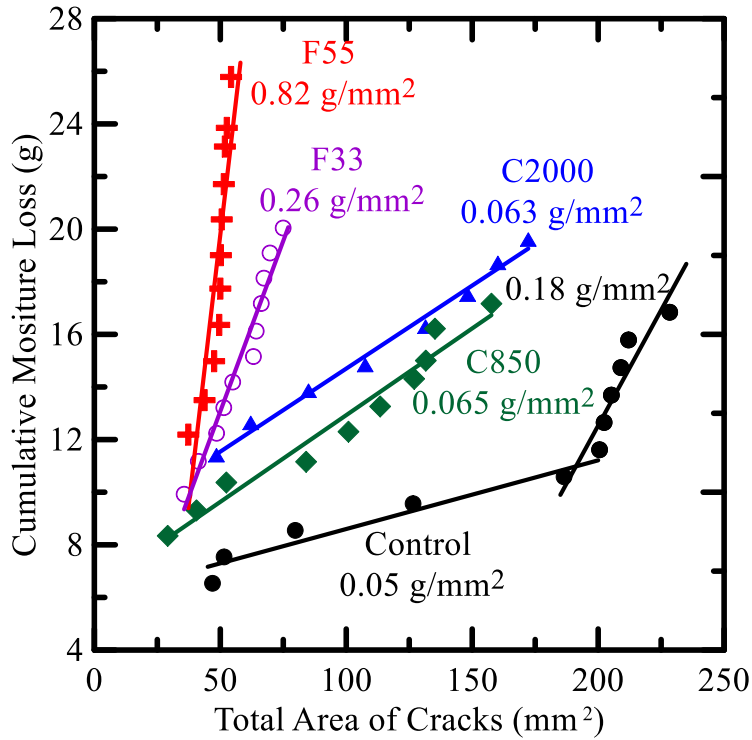
Figure 6-16: Correlation between cumulative moisture loss and crack morphology [199]

6.3. Microstructural observations

Fractured surfaces were observed under an environmental Scanning Electron Microscope with a high brightness Schottky Field Emission Source. Key features observed in test coupons with different wollastonite fibers are shown in Figure 8. Bundled coarser micro-fibers (C2000/C850) can be seen at isolated locations in Figure 8 (a-b).

As discussed earlier, the coarser fibers (C2000, C850) have lower aspect ratios have less acicular features than the finer fibers, as evident in the micrographs presented in Figure 6-

17. In line with the available literature, it could be speculated that the wollastonite micro-fibers with larger particle sizes have limited contribution to the overall toughening mechanism of the cementitious composite. Finer wollastonite fibers (F55 and F33) with particle sizes similar to cement particles, have more acicular features and are far more effective in bridging the micro-cracks. Numerous wollastonite fibers embedded in cementitious matrix can be seen in Figure 6-17(c-d) suggesting uniform distribution of finer sub-micron fibers along the failure surfaces. At some locations fiber-matrix de-bonding, fiber pullout and rupture mechanisms which are dominant toughening mechanisms can also be seen for F55 fibers. Marginal length of these micro-fibers results in limited enhancement of toughening, but a significant increase in the load carrying capacity and first cracking strength. Deflection in crack path shows the effectiveness of fibers and corroborates the findings from the mechanical tests.
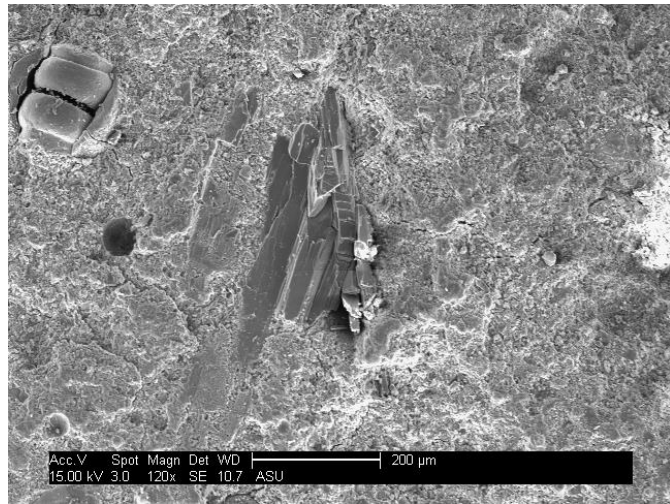
(a)
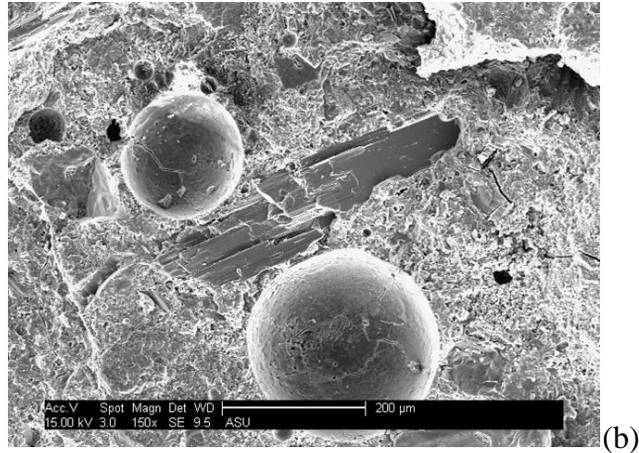
(b)
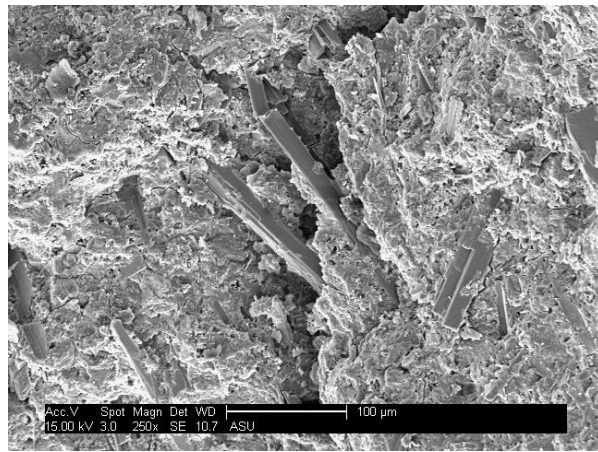
(c)

(d)

Figure 6-17: SEM micrographs of wollastonite fibers: (a) C2000, (b) C850, (c) F55, (d)

F33 inside cementitious matrix

198

6.4. Conclusions

Effectiveness of naturally occurring mineral wollastonite micro-fibers of four different grades with average particle sizes varying from 33 to 2000 microns on restricting drying shrinkage cracks in fresh cementitious paste and improvement of fracture properties of hardened specimens was evaluated. Analytical techniques to solve diffusivity based boundary value problem, quantification of crack intensity using image analysis were employed to evaluate the effectiveness of wollastonite fibers in reinforcing brittle cementitious matrix in early age conditions. However acicular wollastonite micro-fibers are efficient in arresting crack growth by reducing width of surface cracks by a factor of 2, and restricting total cracked area by as much a factor of 3. Fracture mechanics parameters were used for characterization of the toughening effects. Results suggest that wollastonite fibers moderately increase compressive strength, and significantly increase fracture strength and toughness resulting in enhanced ductility and improved resistance to crack growth. Comparison with control mix shows a compressive strength increase of up to 30% after 28 days of curing; flexural strength increase of up to 41% and toughness up to 147% after 28 days of curing. Owing to the limited length of the fibers, the toughening effects are restricted, however their role in bridging cracks at the micro-level could be used to develop an efficient reinforcing material. The reinforcement ability of these wollastonite fibers have been found to be dependent on the volume fraction, particle size distribution and shape.

7. DEVELOPMENT AND CHARACTERIZATION OF LIGHT-WEIGHT SANDWICH COMPOSITE SYSTEMS

An application area of previously discussed strain hardening cementitious composites (SHCC) systems in structural systems is discussed in this chapter. SHCC systems such as Textile Reinforced Concrete (TRC) can be used as a stress skin layer along with a lightweight cellular core material in the form of a sandwich composite. While the stress skin is intended to provide tensile capacity and enhance the mechanical properties of the composite, core element is intended to provide thickness and work as a thermal barrier. In this chapter, the choice of stress skin and core elements, their individual properties and comparison between plain core and sandwich composite is evaluated in static and low-velocity dynamic conditions. Bending strength and stiffness depend on the properties of skin and core as well as the interface bond strength [205]. The core material influences the flexural rigidity of the composite section by providing depth to the flexural member and transferring of shear loads between the facings [206]. Shear strength, modulus, and ductility of the core affects the failure mode and energy absorption capacity of sandwich composites under impact [207, 208]. The core material is also know to serve as a thermal barrier with optimal thermal conductivity and heat capacity. Sandwich elements produced with ferrocement and aerated concrete showed improvements in compressive strength, flexural strength, and ductility [209]. Considerable improvement in flexural properties was also observed with autoclaved aerated concrete and Carbon Fiber Reinforced Polymer (CFRP) facings [210]. Flexural response of TRC with AR-glass and rigid polyurethane foam core has also been investigated analytically [208].

200

Sandwich composites have been made with two types of aerated concrete core (AAC and FRAC) and ARG textile-reinforced skin layers [211]. The light-weight aerated concrete core offers good thermal insulation, and the TRC skin offers tensile strength, stiffness, and ductility. The proposed sandwich structure is a viable alternative to Structural Insulated Panels (SIP) manufactured by laminating expanded polystyrene panels (ESP) and Oriented Strand Board (OSB) facings [212]. Conventional sandwich material with polystyrene foam as core do not offer complete composite action and demonstrate drastically lower stiffness and ductility compared to aerated concrete core [213]. Also compressive strength of aerated concrete is about 4-8 times greater than polystyrene and unlike SIP panels, it is not susceptible to fire, mildew, rot, fungus, and water damage. Therefore the proposed sandwich system is expected to outperform ESP or SIP in terms of long term durability.

Alkali-Resistant glass (ARG) textiles with a perpendicular set of warp and weft yarns bonded at the junction points were used. Density of the textile in both warp and weft directions was four yarns/cm with 400 filaments of 13.5 μm diameter per yarn. Mechanical properties included a tensile strength in the range of 1270–2450 MPa and modulus of elasticity of 70-78 GPa [2,214]. The textile layers used as top and bottom stress skins were manufactured with a cement-based binder using hand lay-up process with Portland cement (Type I/II) at a dosage of 3150 kg/m3 along with fly ash (Class F) as 20 % partial substitution. Water-cementitious solid (cement and fly ash) ratio of 0.3, and high-rate water reducer at 0.2 % of cementitious solids were used. Static tensile and flexural properties of similar TRC composites with ARG textile structure were addressed extensively in previous work [2, ,214]. The elastic modulus, ultimate tensile strength, tensile strain capacity, and

flexural strength depend on the number of textile layers and matrix formulation and are in the range of 2.23-3.55 GPa, 7-21 MPa, and 3.1–5.9%, 13.4–20.6 MPa, respectively. Low-velocity flexural impact tests conducted only on TRC skin elements with 6-8 layers of ARG textiles indicated dynamic flexural strength and energy absorption capacity in the range of 11–30 MPa, and 1.68–4.90 J for impact energies in the range of 7–35 J [2]. Typical experimental responses of ARG-TRC under static tension, flexure and impact are summarized in Figure 7-1.
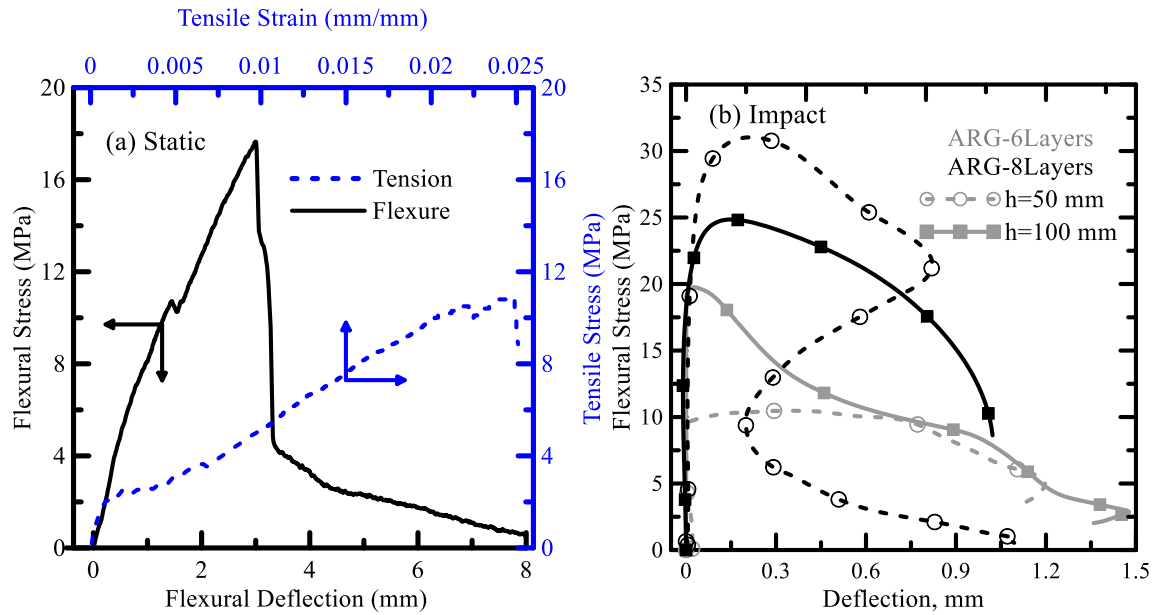
Figure 7-1: Comparison of mechanical properties of TRC skin composites with ARG textiles [2]

Aerated concrete (AC) is a lightweight, noncombustible, low cement-content material with good thermal characteristics. Aerated concrete is manufactured from a mixture of Portland cement, fly ash (or other sources of silica), water, and aluminum powder or paste [215].Typical mixture proportions used for producing these blocks are listed in Table 7-1.

After mixing, hydrogen gas is generated in accordance with Equation 7-1, resulting in a highly porous structure. Approximately 80% of the volume of the hardened material is made up of pores with a general ratio of 2.5:1.0 air-pores to micro-pores [216]. This results in lower density and compressive strength when compared to normal-weight concrete. Dry density of 400-800 kg/m3 and compressive strength values of 2-6 MPa are common for aerated concrete products [217]. Thermal conductivity is reported to be 0.07-0.11 W/m.°C which is several times less than normal weight concrete [218].

$$2Al + 3Ca(OH)_2 + 6H_2O \rightarrow 3CaO.Al_2O_3.6H_2O + 3H_2 \uparrow$$ Equation 7-1
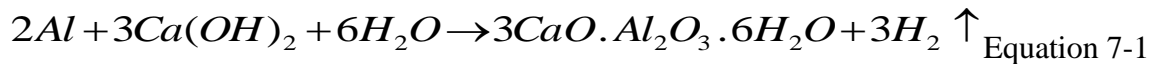
Table 7-1: Mix proportions of Aerated Concrete (percentage by weight)

	FRAC	AAC
Cement	28	18
Fly ash	42	0
Silica	0	27
Lime Stone + Gypsum	0	8
Recycled Material	0	9
Water ~ 38 °C (100 °F)	28	38
Polypropylene Fiber	0.2 – 0.4	0
Aluminum Paste	<0.1	<0.1
Other additives (classified)	0.3	0

This mixture is typically autoclaved for accelerated strength gain and reduction of shrinkage cracking and is referred to as Autoclaved Aerated Concrete (AAC). A more recent class of aerated concrete is Fiber-Reinforced Aerated Concrete (FRAC) wherein short polymeric fibers are used for internal reinforcement. The autoclaving process is eliminated to prevent the damage to fibers at high temperatures and curing is performed at room temperature. FRAC can be considered as a pseudo-ductile composite characterized by a ductile elasto–plastic behavior [219]. Elimination of the autoclaving process reduces

the strength and introduces inhomogeneity in the material, though, it lowers the production costs associated with the energy required for this process. Figure 7-2(a) shows the micro graph of the pore-structure of FRAC.

It has been shown that adding short polypropylene fibers to lightweight cementitious panels improves the mechanical properties such as modulus of rupture and resistance to crack propagation [220]. Similar to many other cellular solids, aerated concrete can exhibit a considerable amount of post-peak residual strength under compression after cracking as shown in Figure 7-2(b). Post-peak response under compression is predominantly characterized by sequential crushing of pores and collapse of cellular walls [221]. Under tensile/flexural loads, plain AAC shows brittle response while FRAC shows a ductile behavior, schematically illustrated in Figure 7-2©. Flexural ductility of FRAC can be attributed to the presence of short fibers that bridge the cracks and enable carrying residual load in the post-peak region.
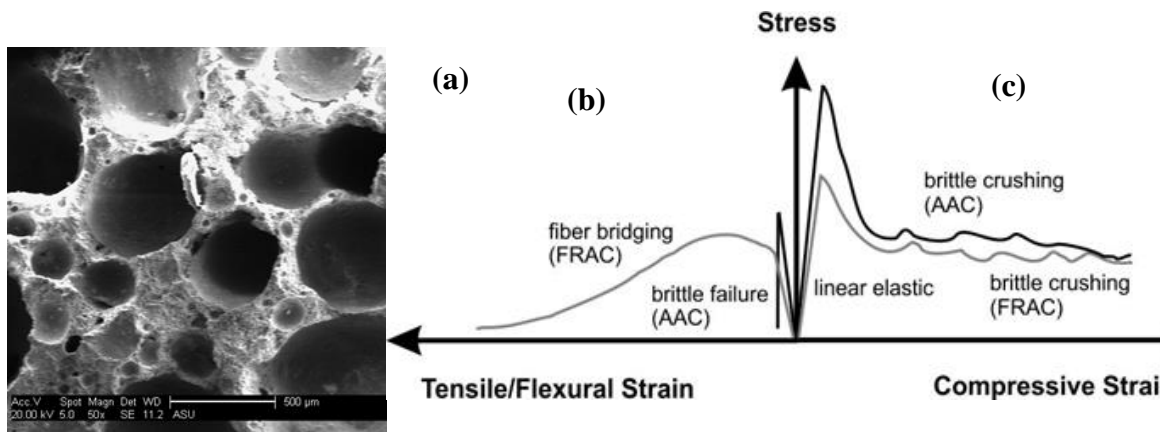
Figure 7-2: (a) Pore-structure of aerated concrete, (b-c) schematics of strain-stress response for AAC (black) and FRAC (gray) [222]

204

A comprehensive set of physical and mechanical tests (static) were performed on AAC and FRAC materials and the results have been presented earlier [222]. These included density, compressive response, flexural response, and tensile response and thermal conductivity. Table 7-2 summarizes some of the properties determined based on the above experiments. The compressive strength values for the AAC and FRAC under study are 5.6 and about 3.1 MPa, respectively. The difference in strength and modulus can be related to the autoclave process in the production of AAC. However the deflection capacity and toughness in FRAC are much higher, due to the bridging action of short polymeric fibers under bending.

Table 7-2: Selected material properties for aerated concrete [222]

	FRAC	AAC
Compressive Strength: Fc: MPa	3.05-3.22	5.61
Residual Compressive Strength: MPa	1.71-1.76	1.52
Elastic Modulus: GPa	4.51-5.02	7.50
Poisson's Ratio	0.26-0.27	0.26
Flexural Strength: MPa	0.27-0.56	0.66
Flexural stiffness: N/m	4.20-4.58	4.06
Toughness at 15.2 mm displacement: N.m	13.16-24.27	0.30
Tensile Strength, Ft: MPa	0.10-0.13	-

7.1. Flexural Impact Response of Aerated Concrete

Impact behavior of cement-based materials has been the topic for several studies based on low-velocity impact. Various impact tests include: Charpy, Izod, drop-weight, split Hopkinson bar (SHB), explosive, and ballistic tests. These tests can be either instrumented or heuristically based and the resistance can be measured based on fracture energy, damage accumulation, and measurement of the number of drops to achieve a desired damage or stress level [2]. Bindiganavile and Banthia [223,224] showed that flexural strength is higher under impact loading in comparison to quasi-static loading for fiber-reinforced

concrete. Polymeric fiber-reinforced concrete showed an improvement in energy absorption under impact loading. Manolis et al.[225] also showed that fibrillated polypropylene fibers significantly improve the impact resistance of concrete slabs.

Impact test set-up used in this study is shown in Figure 7-3(a) includes an instrumented hammer that is dropped freely on a specimen placed in a three-point bending system. The drop heights can be adjusted within a range from 1 to 2000mm which can be controlled by means of an electronic hoist and release mechanism. The hammer is released from a predetermined drop height by means of a triggering switch which is backed by an electronic brake release mechanism. The data acquisition system consists of a PC based National Instruments PCI acquisition card and a Lab view program. The impact force induced by the falling hammer is measured by a strain-gage based load-cell with a range of 90 kN mounted on the hammer behind the blunt shaped impact head. A linear variable differential transformer (LVDT) with a range of +10 mm was connected to the bottom of specimen (tension zone) by means of a lever arm. A MATLAB code was developed for processing and interpretation of load, acceleration and deflection. This code smoothens, reduces, and filters the data for the impact test period and calculates experimental parameters such as stress, stiffness, toughness, velocity, etc. Figure 7-3(b) shows the typical time history for the impact load, deflection of mid-span, and acceleration of a representative FRAC specimen.
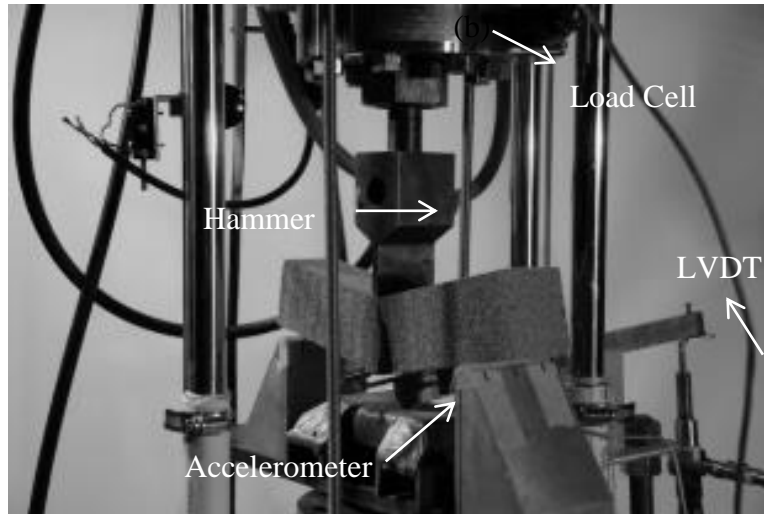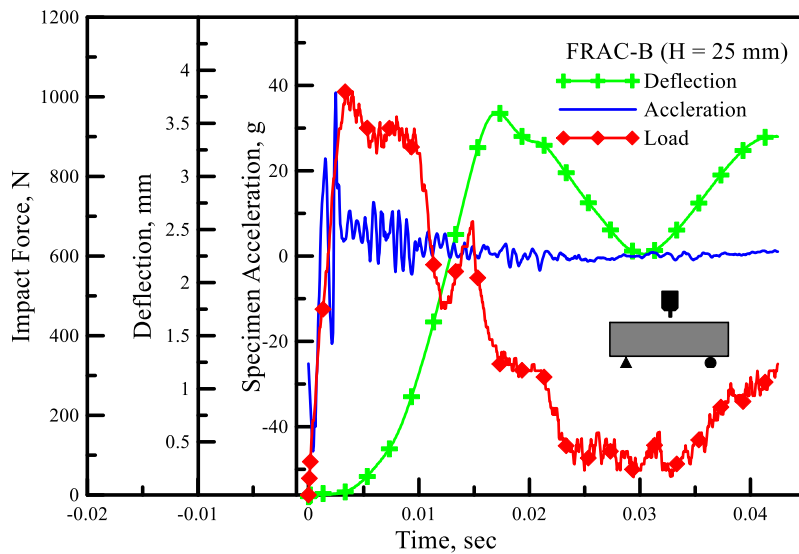
Figure 7-3: a) Impact test set up, b) typical time-history for impact event [226]

Flexural stress vs. deflection of the same specimen is shown in Figure 7-4(a). The latter

can be categorized in five distinct zones: zone 1 is the linear elastic range that ends with

the formation of the first crack. The stress corresponding to this point is defined as the limit

of proportionality (LOP). This is followed by Zone 2 and 3 which is characterized by

multiple cracks associated with strain softening where fibers are bridging the crack. Zone

4 can be attributed to the fiber pull-out and failure, followed by zone 5 in which rebound takes place. Zone 4 and 5 can only be observed under special cases where the combination of specimen size and drop height allows for such behaviors. If there is sufficient ductility in the specimen to absorb the applied energy, some of the stored energy released causes a rebound that is characterized by a reduction in deflection of the specimen as the load is decreased. Five (or more) replicate specimens were tested for each condition. Figure 3(b) shows typical results for all the replicate tests, showing good reproducibility.
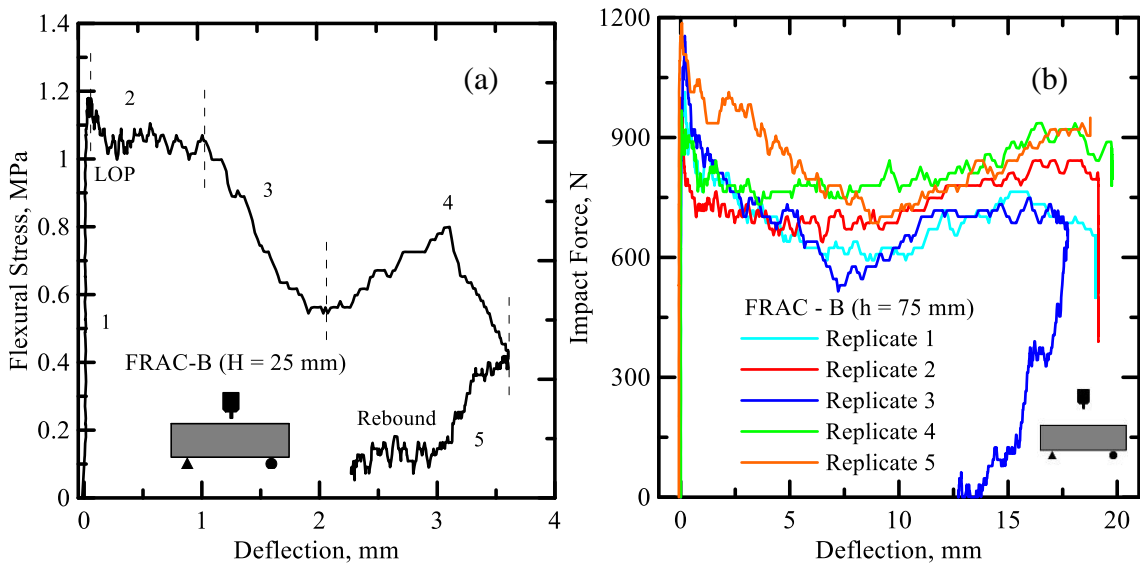
Figure 7-4: (a) typical flexural stress vs. deflection, (b) typical test results for replicate tests

AAC and FRAC materials were studied for their impact response using three different cross-sections: A (50x50 mm), B (50x100 mm), and C (100x100 mm), all with a span of 250 mm. The impact test was performed on aerated concrete at three different drop heights: 25, 75, and 150mm and the correspondingly potential energy of the impact ranged between

3 to 21 J. As the drop height increased, the input energy (potential energy) and drop velocity of the hammer increased, as a result, the strain rates increased.

Figure 7-5(a) shows the summary of time-history of impact force for the representative AAC-C and FRAC-C specimens. The peak impact force is somewhat independent of the drop height for the specimens with smaller cross-section, due to their limited damage tolerance and strain capacity. However as evident, effect of the drop height is more pronounced for larger specimens of AAC-C and FRAC-C. Impulse of the applied force during the impact event can be measured as the area enclosed within the force-time response, and can be used as a measure to compare the performance of these systems under different conditions. Impulse measure which is related to the load-capacity for AAC-C increases from 12.18 N.s to 17.22 N.s with increase in average strain rate from less than 0.1 s-1 to 7.7 s-1, which corresponds to drop heights of 25 and 75 mm, respectively. However in the absence of fiber reinforcement, AAC has limited strain and energy absorption capacity especially at higher strain rates, as under drop height of 150 mm, corresponding to an average strain rate of 17.8 s-1, the impulse measure drops down to 5.12 N.s. The maximum impact force increase proportionally with the drop height for FRAC-C, as evident in Figure 7-5(b). The maximum impact force for FRAC-C increases from 1620 to 2400 N with increase in average strain rate from 0.8 - 20.9 s-1. The main difference in these systems is because of the energy absorption capacity of FRAC due to the presence of short fibers. Energy absorption capacity or toughness measured by the area enclosed within the load-deformation curve is a measure of the ductility of different systems. For AAC-C, the average toughness values decrease proportionally from 2.2 to

0.46 J, with increase in drop height from 25 to 150 mm. The average toughness of FRAC-C however increases from 4.0 to 4.4 J, with increase in drop heights from 25 to 75 mm. At drop height of 150 mm, however toughness of FRAC-C decreases to 2.4 J, which is still greater than the maximum toughness of AAC-C.
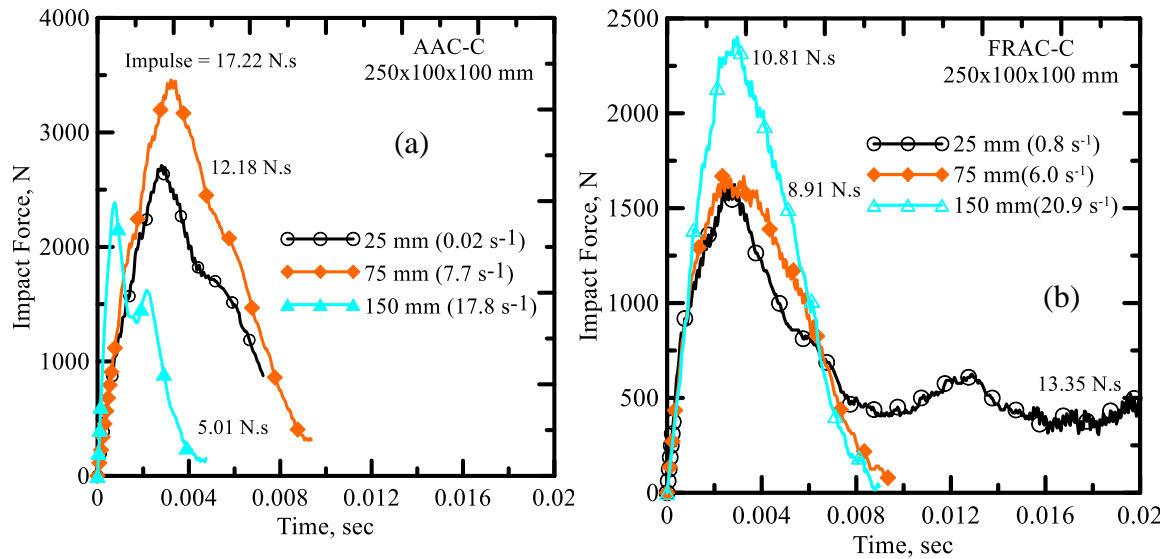
Figure 7-5: Effect of drop height on force-time response for: (a) AAC and (b) FRAC

[226]

The size effect can be studied by comparing A and C groups, while the comparison between A and B groups discloses the beam depth effect. Figure 7-6 shows the comparison among A, B, and C for representative AAC and FRAC specimens tested at various drop heights. As evident, the flexural strength decreases and toughness increases, with increase in cross-section. Also, in line with the static results, flexural strength or MOR of AAC specimens is moderately greater than FRAC. However toughness of FRAC specimens is significantly higher than AAC, due to the bridging action of fibers at high deflection levels.
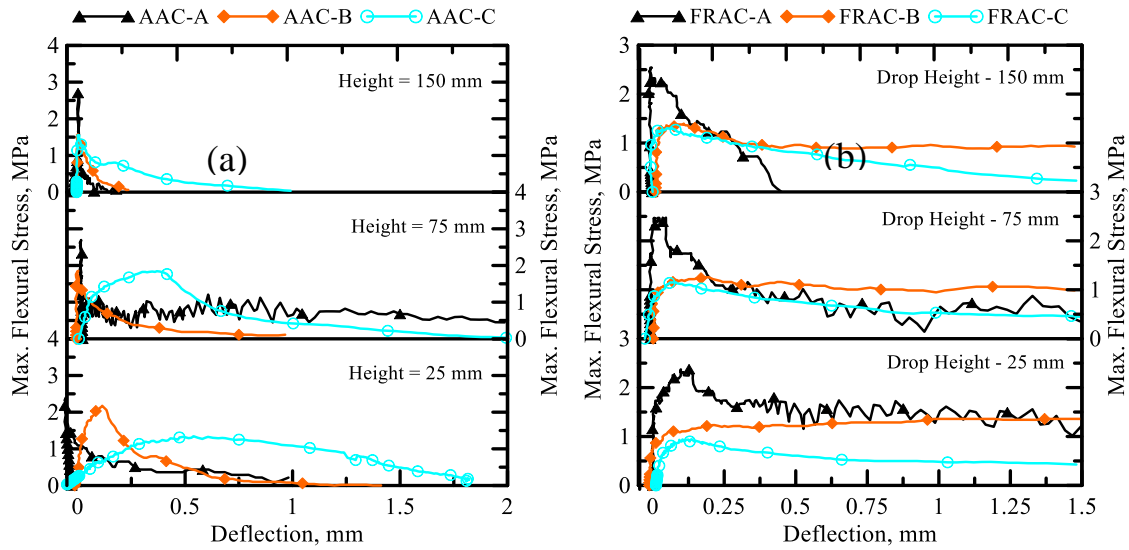
Figure 7-6: Size effect on AAC subjected to impact: a) AAC and b) FRAC

Crack growth under flexural impact loading was studied using a high-speed Phantom camera at a speed of 4000 fps. Image-J software was used for converting the video to individual frames. Figure 7-7 shows the time-lapse images of a typical impact response for AAC-C tested at drop height of 75 mm. Stages of crack growth were related to load (P), deflection (δ),stress (σ), and crack width (w) at discrete time steps. Figure 7-8 shows the time-lapse images of a typical impact response for aerated concrete specimens tested at drop height of 75 mm. For AAC, as deflection increases from 0.03-0.96 mm, the average crack width also increases to about 0.3-5.4 mm. For FRAC, the crack width also increases with deflection until the last time step where the crack width and deflection both decreases due to the rebound action of the hammer. As evident cracking is predominantly localized in the form of one major crack under impact conditions. This limits the mechanical performance of aerate concrete, and the effort is to ensure development of multiple cracking in these systems with the use TRC as stress skin layers.

211
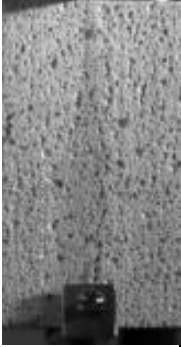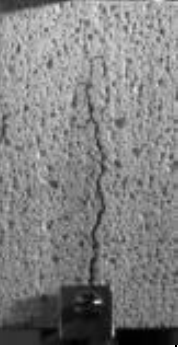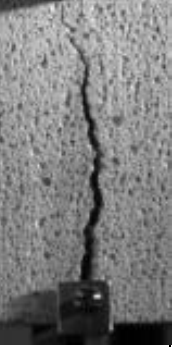
T = 0 ms P = 0 N δ = -0.04 mm w = 0.0mm	T = 1500 ms P = 1716 N δ = 0.03 mm w = 0.3 mm	T = 1840 ms P = 1441 N δ = 0.07 mm w = 0.7 mm	T = 2870 ms P = 515 N δ = 0.24 mm w = 2.0 mm	T = 3680 ms P = 174 N δ = 0.51 mm w = 3.4 mm	T = 4500 ms P = 1 N δ = 0.96 mm w = 5.4 mm

Figure 7-7: Crack propagation of the representative AAC-C specimen
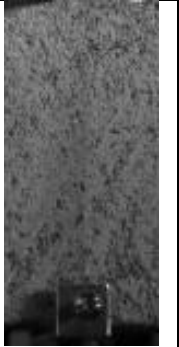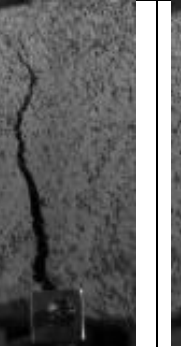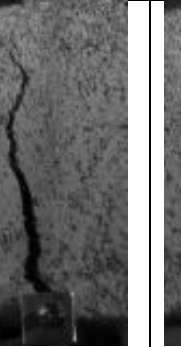
T = 0 μs P = 0 N δ = 0.03 mm w = 0.0 mm	T = 3970 μs P = 1513 N δ = 0.77 mm w = 0.8 mm	T = 6380 μs P = 640 N δ = 2.37 mm w = 2.2 mm	T = 13080 μs P = 468 N δ = 12.80 mm w = 3.9 mm	T = 16270 μs P = 141 N δ = 17.60 mm w = 4.2 mm	T = 19770 μs P = 61 N δ = 15.53 mm w = 4.1 mm

Figure 7-8: Crack propagation of the representative FRAC-C specimen [226]

7.2. Flexural Response of Sandwich Composite System

In the current study, sandwich composites of different geometries have been tested under quasi-static and medium strain rate flexural loading using instrumented static and impact tests [211]. In order to study the beam depth effect, two different geometries are labelled as sections A and B, corresponding to nominal beam cross-sections of 50x50 mm and 50x100mm were developed. The length of these sandwich coupons were kept constant at 250 mm. Figure 7-9 compares the flexural response of aerated concrete and corresponding sandwich composites for nominal specimen depth of 50 mm. Flexural strength of TRC-AAC-A increases under both static and impact loading by a factor of 2 and 4 when compared to the plain AAC-A core. In both quasi-static and impact loading cases the plain AAC undergoes a predominantly brittle failure with a single crack in the mid span. In the absence of fibers, AAC is brittle in nature and loses its structural integrity soon after the peak load. There is hardly any resistance to propagation of tensile cracks and post-peak response for this material. However, in the presence of the skin layer ductile behavior with multiple flexural cracks in the core element and subsequent delamination of the skin element at higher deflection levels and strain rates is observed (Fig. 7a-b). Interfacial delamination is mainly caused at higher strain rates, possibly due to the bending-stiffness mismatch between the layers and is related to the delamination fracture toughness [227, 228]. At the advent of delamination, widening of the major flexural cracks along the depth is restricted which promotes additional flexural cracks further enhancing energy absorption capacity.
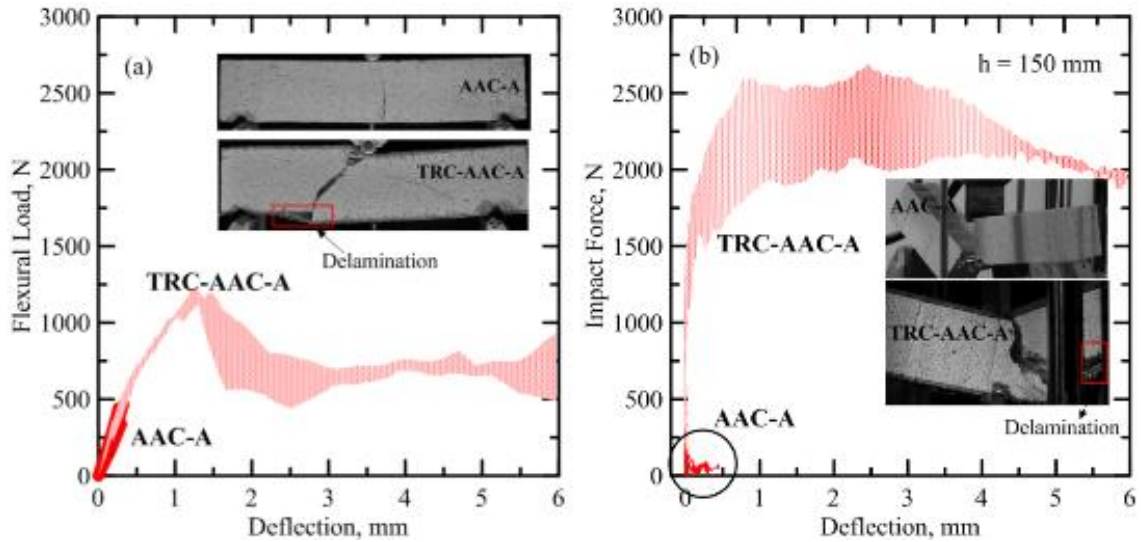
Figure 7-9: Effect of textile reinforcement on AAC under (a) static loading, (b) impact

loading

Similar trends are evident in Figure 7-10 which discusses the response of TRC-FRAC composites against the plain FRAC core. In case of FRAC, a well-defined post-peak response is observed due to the presence of the internal fibers. Fiber reinforcement helps in bridging the cracks under tensile/flexural loading, providing higher energy absorption capacity [2]. Typical damage mechanism involved could be explained to be associated with fiber de-bonding and nucleation of micro-voids [229]. Under static and impact loading, average flexural strength of the sandwich beams, TRC-FRAC-A compared to the plain FRAC-A increases by a factor of 4 and 3 respectively. Presence of a major crack in the mid-span of the core element compared to multiple cracks of the sandwich composite is evident in Figure 36a-37a.

214
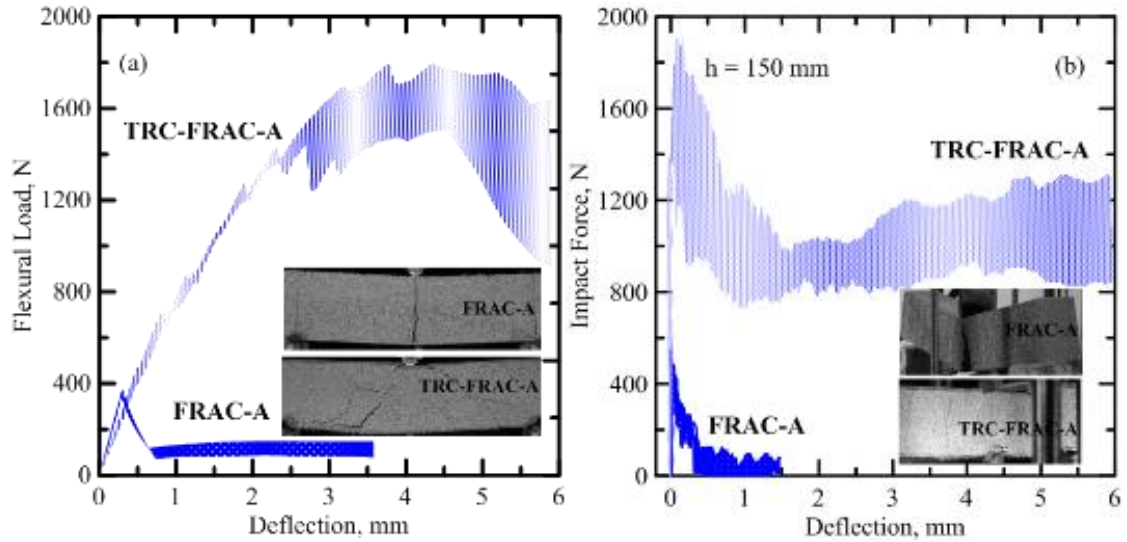
Figure 7-10: Effect of textile reinforcement on FRAC under (a) static, (b) impact loading

Energy response of the sandwich beams were compared based on the core materials as shown in Figure 7-11. The plain AAC core material as discussed earlier is brittle with a very low toughness (< 0.5 J) compared to FRAC with enhanced core and a toughness of 2 J under input potential energy of up to 21 J [230]. TRC layer at the top and bottom of plain core enhances the energy absorption through distributed cracking such that the toughness of TRC-AAC-A beams are as much as 50 times higher than the plain AAC core under drop height of 150 mm. The toughness of the sandwich specimens also increase with the strain rate and cross-sectional area such that for TRC-AAC-A and TRC-AAC-B represent increases by 150% and 50%, respectively for transition from static to impact loading. Delamination of TRC layer from the core restricts the relative improvement of the toughness of the TRC-AAC-B specimens at only about 14 times higher than the plain AAC-B specimens. The improvements in energy absorption capacity of TRC-FRAC-A sandwich beams is less drastic when compared to plain FRAC-A. Average toughness

215

increases by about 20 times due to the skin elements at h= 150 mm. For TRC-FRAC-A beams, change in toughness levels from static to impact loading is relatively insignificant, with maximum toughness of about 4.0 J for drop height of 75 mm. However larger beams, TRC-FRAC-B have considerably higher toughness (6-8 J) and show an increasing trend by about 75% for static to impact loading. The energy absorption capacity of TRC-AAC-B is within the same range of TRC-FRAC-B at different strain rates.
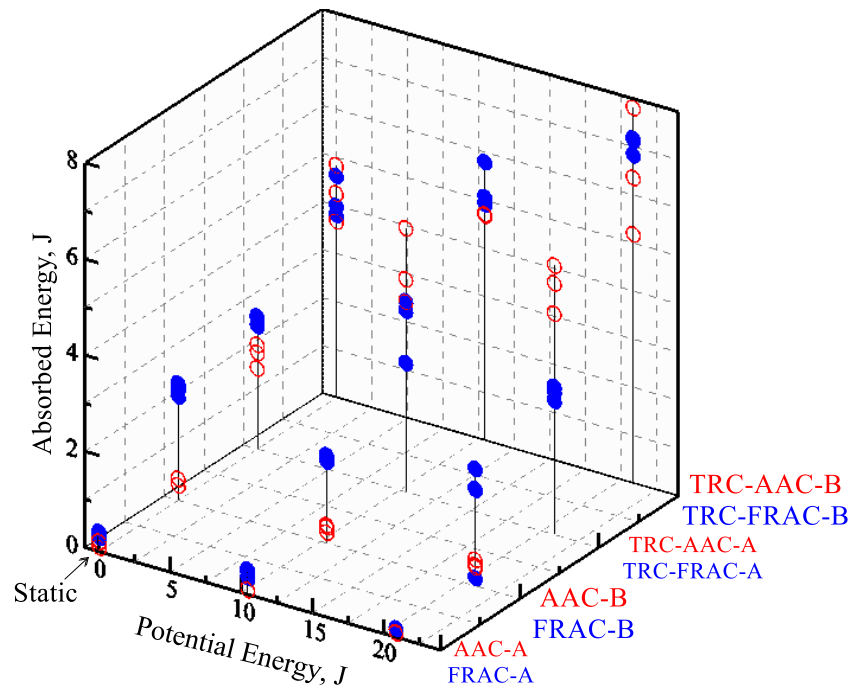
Figure 7-11: Effect of textile reinforcement on energy absorption measure at 2.5 mm of deflection

Sandwich composites in general have superior energy absorption capacity by a range of 3-6 under static loading, and as much as 4-8 times under impact loading, when compared to plain aerated concrete. At a given level of input energy, skin layer improves the energy absorption capacity by as much as 5-10 times. This signifies that as much as 50% of the

216

impact energy applied to the sandwich is absorbed by the composite, and could be considered as the driving factor for preference of sandwich composites over traditional cementitious system especially under impact or ballistic type loadings

7.3. Crack Propagation

Crack propagation was studied using 2-D digital image correlation (DIC) technique with a high resolution digital camera and a Phantom (v.7) high speed camera. A commercial software Vic-2D 2009 developed by Correlated Solutions, Inc. was used for image analysis. Initiation of failure modes depend on the interaction of TRC stress skins and core, sectional dimensions, and strain rates [231]. The unique pore structure of the aerated concrete core material was used as a random, isotropic, and non-periodic speckle pattern, required for DIC. The displacement field is determined by tracking the movement of a pixel subset from the reference image to deformed images. Only the longitudinal strain field (εyy %) along with the progression of cracks at different stages of loading is reported. Time history of deflection (δ), force (P) and flexural strength (σ) of corresponding images are also correlated. Time lapse images of strain fields in representative specimens of TRC-FRAC-B and TRC-AAC-B beams under impact loading at a drop height of 300 mm, respectively are presented in Figures 7-12, 7-13. Under static loading as evident in Figure 11 (frames A2, F2) tensile cracks emanate from the bottom tensile skin near the mid-span of the section and move toward the compression layer at specific crack spacing. The load transfer mechanism continues until the core material form multiple diagonal tension and shear cracks. Ultimately, however crack formation is dominated by widening of major crack (see frames A4, F4) and evidence of delamination of the core-skin layer is shown.

217

Under impact loading however, initial cracks originate from the top skin due to compression failure due to localized indentation of the skin and deformation of the core is evident in Figure 7-12 and 7-13 (frames A2, F2). Core material is subjected to shear loading due to lamina/core stresses, however its internal reinforcement increases the damage tolerance. A combination of failure modes comprising of flexural, delamination, and core shear govern the failure modes as shown in these figures. The specific mode of failure between these two composite systems cannot be discerned and is likely that combinations of events lead to the final failure governed by diagonal tension and shear strength of the core. In case of TRC-FRAC-B, the internal fiber reinforcement restricts the localized high strain bands and increases critical cracking strain by a factor of 2 under static loads and 18 under impact loading (see strain scale in Fig. 7-12 and 7-13). This could be attributed to classical toughening mechanisms such as fiber pullout and crack bridging. The pattern of cracks is similar under both loading modes, however the extent of strain localization bands, and crack opening is visibly much larger under impact as opposed to static loading. The addition of the stress skin layers with TRC clearly result in formation of multiple cracks in the core element. This is a major improvement from the single crack formation, reported earlier for aerate concrete in Figures 7-7 and 7-8. Multiple cracking occurs when there is less energy demand for formation of new cracks as opposed to widening of existing cracks, and the contribution of the core element in improvement of the mechanical properties is significantly enhanced.
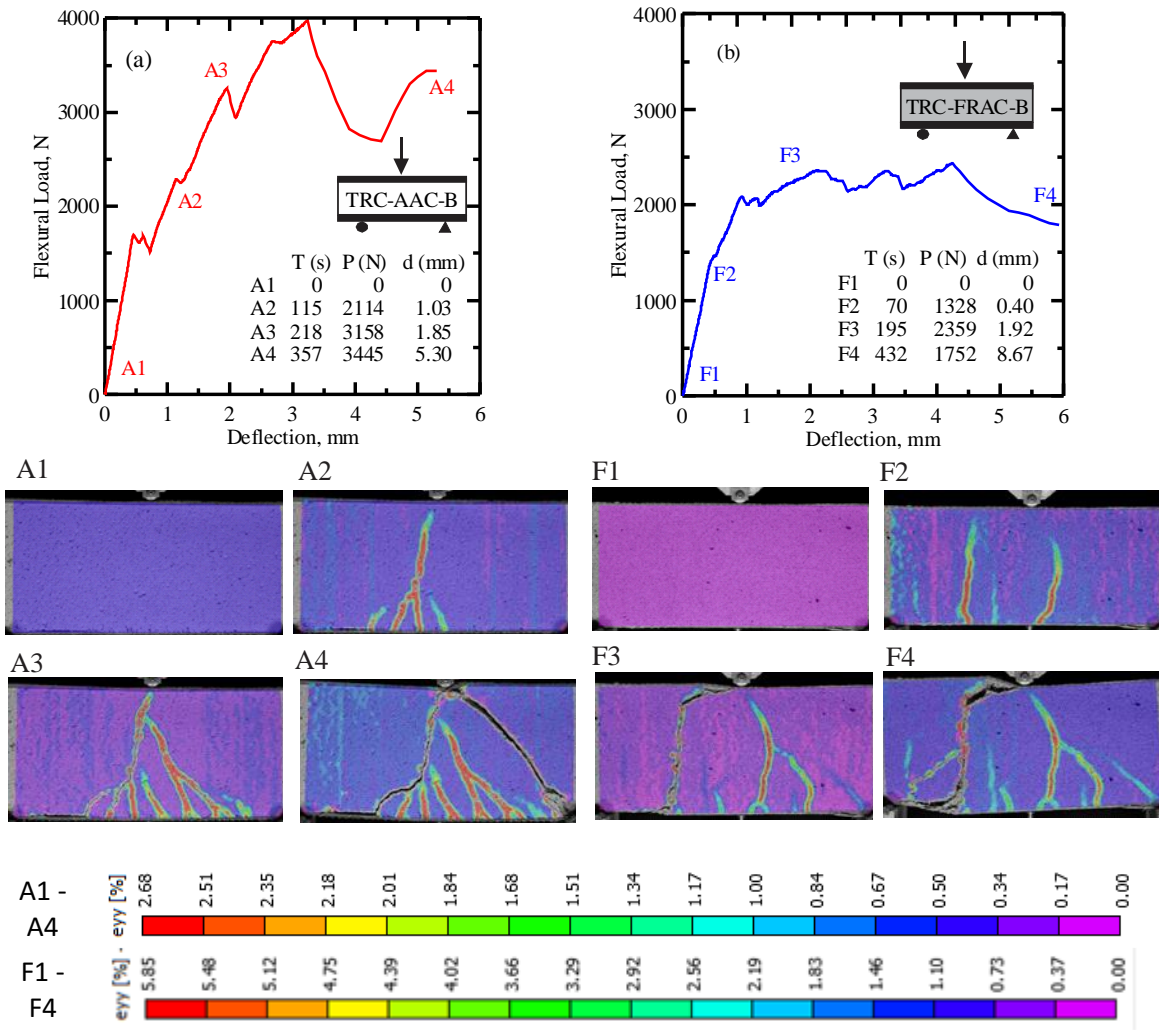
Figure 7-12: Typical time lapse images and longitudinal strain field of (a) TRC-AAC-B

and (b) TRC-FRAC-B under static loading
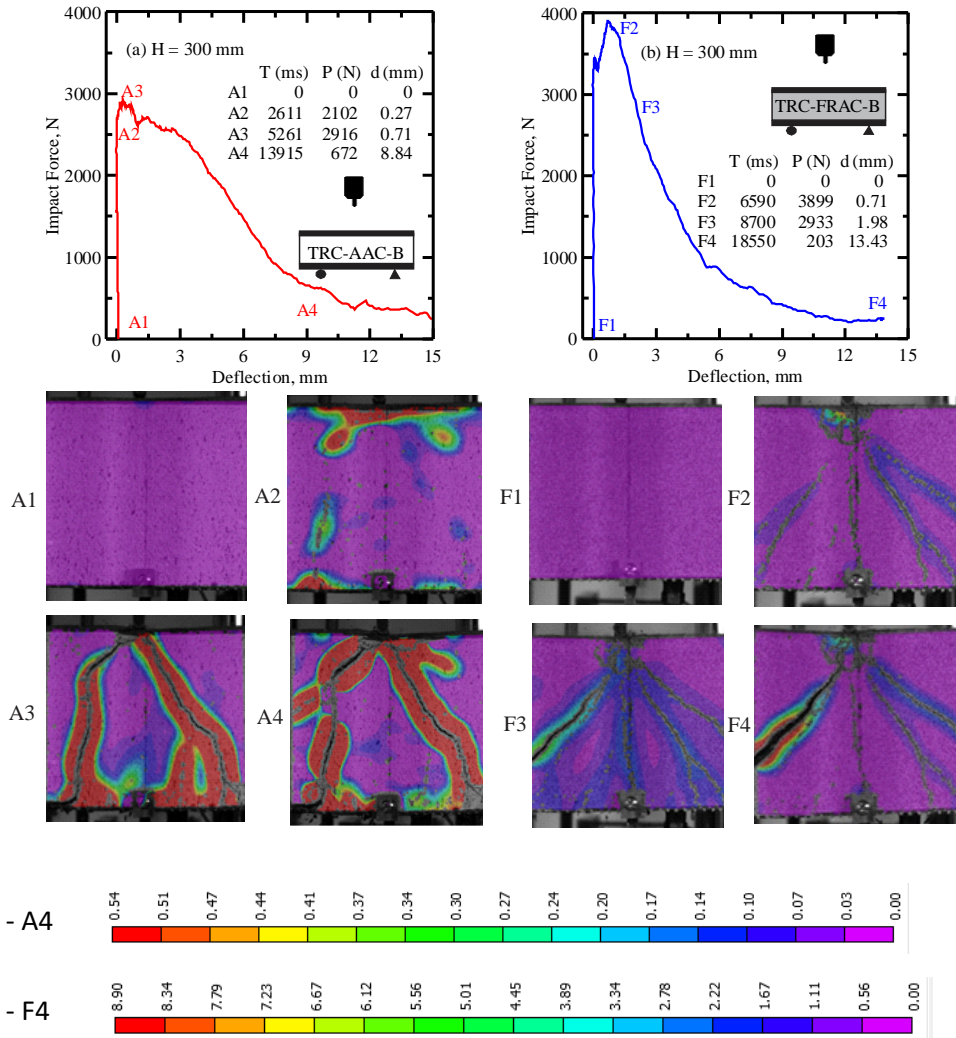
Figure 7-13: Typical time lapse images and longitudinal strain field of (a) TRC-AAC-B

and (b) TRC-FRAC-B under impact loading

In the context of optimizing the composite action and improving long term durability,

critical parameters are the tensile properties of the TRC facing, shear strength of the core

material, and interlaminar bond. Additional layers of textile reinforcement in the tension

skin, or alternate textile systems with carbon, aramid or polypropylene could be considered.

Improving interface characteristics affects ductility, as efficient interlaminar bonding alters

the cracking mechanism [232]. Shear delaminations can be considered reduced with

discrete or continuous stainless steel connectors. Also use of polymer based adhesives [232], adding roughness to contact surface of the core [210], or use of mechanical adhesives are alternate approaches [233]. Proper analytical modelling of the sandwich structure is also essential for optimization of design parameters.

7.4. Conclusions

Behavior of sandwich composite with aerated concrete core and AR-Glass textile-reinforced stress layer was investigated under quasi-static and intermediate strain rate impact loading. Aerated concrete core was chosen for this study due to its unique characteristics of a light-weight, pseudo-ductile material with good thermal properties. It was found that textile reinforcement at the tension and compression faces of the beam element results in formation of multiple flexural cracking in the stress layer, and diagonal tension cracking in the core element. Transition of single major crack in the plain aerated concrete core to distributed multiple cracking in the sandwich composite results in significant improvement in the load carrying, flexural stiffness, and energy absorption capacity, under static and dynamic loads are documented. Overall behavior of the composite is highly dependent on the behavior of the individual components of sandwich unit and interfacial bonding. Effects of material properties of the core material, cross-sectional area, drop height of impactor and cracking mechanisms were studied in detail. Unique attributes of these construction materials include manufacturing efficiency, moderate weight-strength ratio, and thermal efficiency. Sandwich composite with aerated concrete can therefore be a potential building material in low-cost sustainable construction especially in seismic zones.

8. OTHER AREAS OF APPLICATION OF STRAIN HARDENING CEMENTITIOUS COMPOSITES (SHCC)

This chapter addresses two new areas of application of SHCC systems in structural application. Use of SHCC systems as composite shapes in the form of structural components such as C, hat, T, and L sections, as well as rectangular closed sections with optimized cross sections. These textile reinforced composite sections promise a host of new construction products for competing and replacing wood and light gage steel based elements for lightweight construction and panel application. The several aspects of manufacturing textile-cement laminates using a series of dies to accommodate different structural shapes and geometries. The design and manufacturing of a continuous tractor feed system as well as the dies are important steps in the development of the project in order to move towards a continuous line of production. Such developments may then be transferred to an industrial production phase using continuous manufacturing lines. The objectives of this project is to address four main aspects of manufacturing, testing of textile reinforced cement composites. The other area of application of SHCC that is being currently looked at is the area of repair and retrofitting by using SHCC laminates with pre-cracked or virgin masonry units and evaluating their bond strength through a unique testing setup. Several SHCC-masonry bond assemblies with different geometries and layers of textile were manufactured, and tested under direct tension and fatigue tension up to 100,000 cycles. Failure strength to break the bond between the SHCC laminate and masonry unit were evaluated and compared the different systems.

8.1. Production of Structural Sections

8.1.1 Overview

Through the use of the automated pultrusion system, several types of SHCC systems can be manufactured efficiently and with adequate precision and quality control. Preparation for production includes the establishment of a workable mix design and the calculation of the required number of textile layers for the desired textile volume fraction. Manual tasks for manufacturing these systems include handling of the textile layers before and after the pultrusion process, stacking of the layers of textile and finishing of the matrix layers to ensure a smooth surface finish.

8.1.2. Mix Design

For production of textile reinforced concrete (TRC) laminates, an optimized blended mortar mix design from the previous chapter was adopted. A water to cement ratio of 0.32 and cement to sand ratio of 2:1 were used for all samples. 15% of the total cement content was replaced by silica fume at about 5% and wollastonite at about 10%. Addition of supplementary cementitious materials such as silica fume and wollastonite offers multitude of benefits such as improvement in packing density, shrinkage control due to lower cement content, improvement in density and strength. Addition of wollastonite as discussed in the previous chapter, leads to micro-reinforcement of the matrix due to its acicular structure and aids in crack-bridging mechanisms. The contribution of these supplementary cementitious materials, and the influence of different parameters such as aspect ratio and dosage, have been discussed extensively in the previous chapters. Superplasticizer was used to increase the workability of the mix, specifically for the paste bath to allow for better

coating of the textile. Standard laboratory mixing procedures were followed as a fixed, 5L Hobart mixer was used to dry mix materials for one minute, followed by four minutes of wet mixing. Superplasticizer was added to the mix after two minutes of wet mixing. The mix proportions for all mixes are shown below in Table 8-1.

Table 8-1: Mix Design of TRC Laminates

Material	Weight Percentage
Portland Cement (Type III/IV)	46.75%
Silica Fume	2.75%
Fine Silica Sand (Grit #60)	27.5%
Water	17.5%
Wollastonite (F-55)	5.5%
High range water reducer	0.01%

8.1.3. Production of Structural Shapes

The number of layers required is dependent upon specimen thickness and the textile properties such as weave pattern and yarn diameter. A standard calculation was performed for every sample casting to ensure consistency between samples of different shape and volume. Flat rectangular plates are the simplest samples to produce using the pultrusion system. After deciding on the desired textile volume fraction and batching the matrix, the system was prepared by filling the water and paste baths, greasing the pulling mechanism and rollers, and turning on the building air pressure. When casting structural shapes with the automated pultrusion system, such as the angle and channel cross-sections shown in Figure 8-1, the procedure was similar to that used when casting flat plates.

The computer controlled pultrusion equipment developed at the Composite Materials Laboratory at ASU, discussed in the earlier chapter was used. The matrix was batched and mixed using standard mixing protocol with a portion used for the top and bottom matrix layers and finishing and the rest used in the paste bath for coating textile. The system can operate with the same VI inputs and run continuously at the same speed. Matrix coated textiles were stacked layer by layer as a flat plate with intermediate layers of matrix placed in between the textile layers to ensure adequate thickness of the composite.
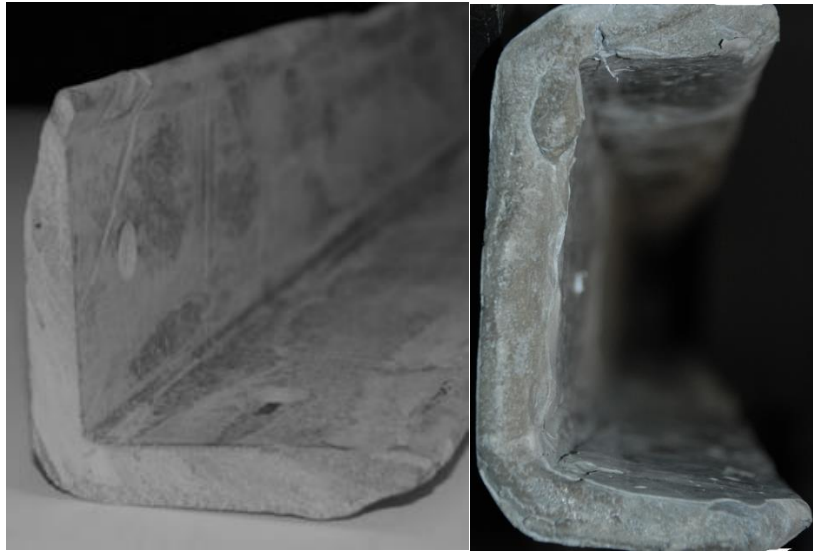
Figure 8-1: Cross section of pultruded shapes with TRC laminates

The difference in casting process is in the way the freshly cast laminates are shaped in the mold inside the in-situ pressing station as shown in Figure 8-2(a). Once all layers were stacked and the specimen is finished, the freshly cast flat plate was pressed initially at 10 psi with the pneumatic press to improve the impregnation of the matrix inside the openings of the fabric structure, and give specimen its desired shape. The wet sample was wrapped in plastic cloth and laid on the mold. As shown in Figure 8-2(b), buffer boards were used

225

to ensure contact between the mold and the press. During the consolidation process, the pneumatic press was used to apply maximum pressure of 20 psi for about 4 hours, which created a uniform and smooth surface finish. When casting the L- sections, a series of steel L-sections were be used as molds to create several structural sections with TRC systems. C-sections can also be produced using a similar technique with an outer jig made of two angles connected to cement board and a wooden board as the inner mold as shown in Figure 8-2(b). Figure 8-2(c) shows the mold setup used for casting of L-sections.
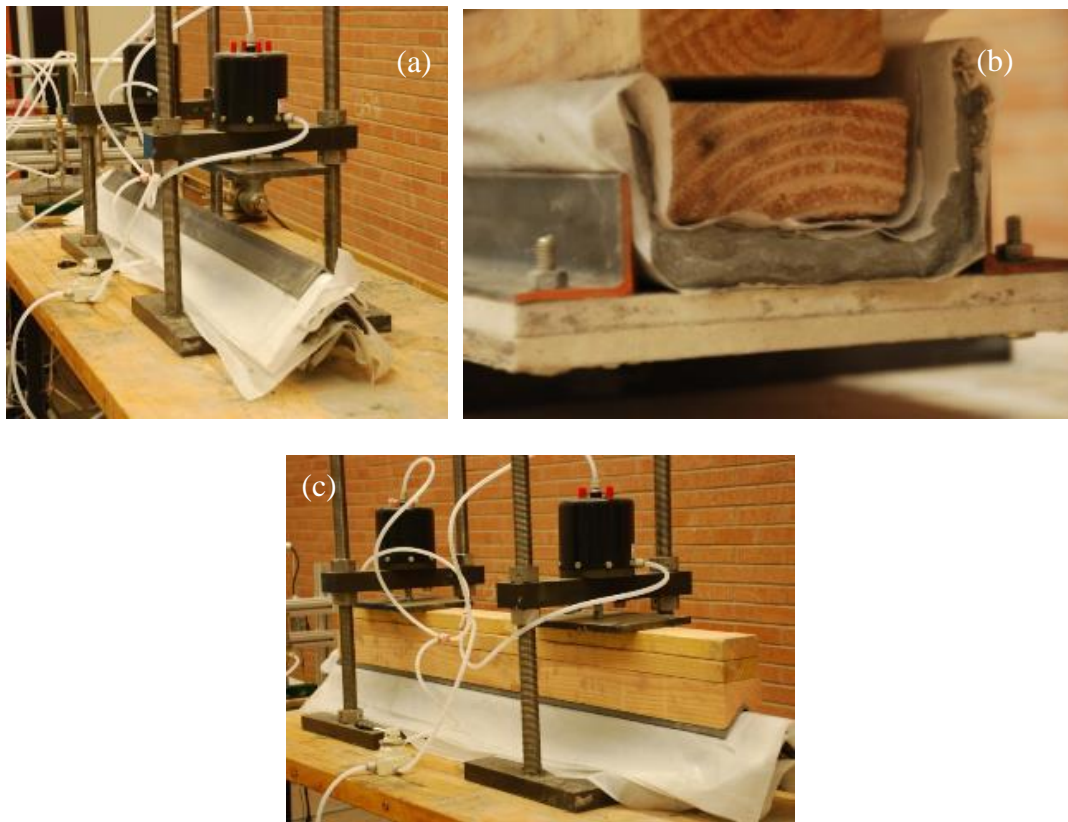
Figure 8-2: (a) casting of angle shapes using steel angles as molds; (b) casting of channel sections with wooden buffer boards and steel angles; (c) pressing station being used for forming angles

226

8.2. Experimental Setup

The material properties were characterized using uniaxial tension, and compression using closed loop tests as well as digital image correlation analysis to characterize the mode of failure. Figure 8-3 shows the experimental setup for testing of alkali-resistant glass (ARG) textile reinforced specimen 4ft (1.2 m) long, L3x3x0.5 in. (75x75x12 mm) manufactured at ASU.
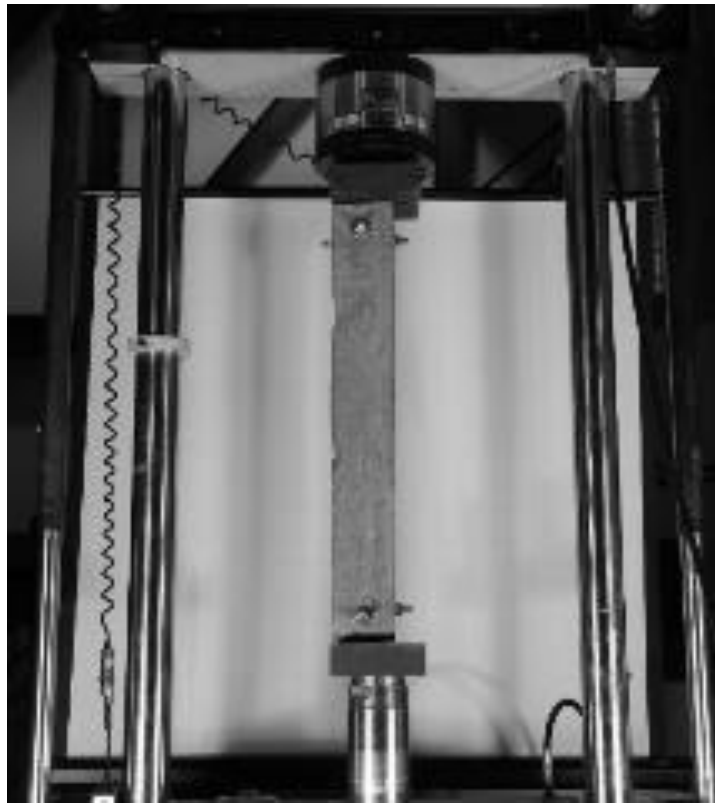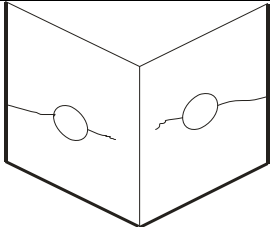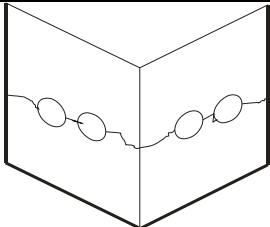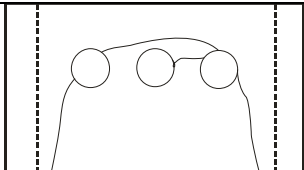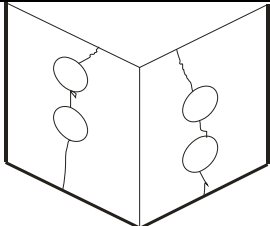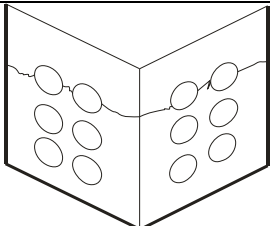
Figure 8-3: Experimental setup developed at ASU for large scale testing of structural shapes

Three different gripping systems were fabricated and evaluated to find the variation in mechanical response of TRC structural shapes in regards to connection type. The gripping

systems varied from one another based on the number and diameter of holes and spacing
in between the holes. The different gripping systems and modes of failure are summarized
in Table 8-2.

Table 8-2: Gripping systems used for testing structural shapes (C and L) and modes of
failure

Gripping Style	Schematic View	Hole Specification	Failure Pattern Observed
I		$d = 0.5$ in $n = 1$ hole/leg	Tensile bearing failure near across the hole
II		$d = 0.38$ in $n = 2$ hole/leg	Tensile bearing failure near across the hole. Through crack.
III		$d = 0.38$ in $n = 2$ hole/leg	Shear block failure observed under tension.
IV		$d = 0.5$ in $n = 2$ holes/leg	Compression failure.
V		$d = 0.25$ in $n = 6$ holes/leg	Tensile bearing failure near across the hole. Through crack.

Amongst the different gripping styles, Grip V produced the best results under tension and compression and was selected for further testing. Schematics of grip V are shown in Figure 8-4. Figure 8-5, shows the failure patterns observed with grip V when used for testing C-sections. It is to be noted that the specimen used here was a 2 ft long section and hence due to comparatively less gage length, distributed cracking was limited to only near the grips.
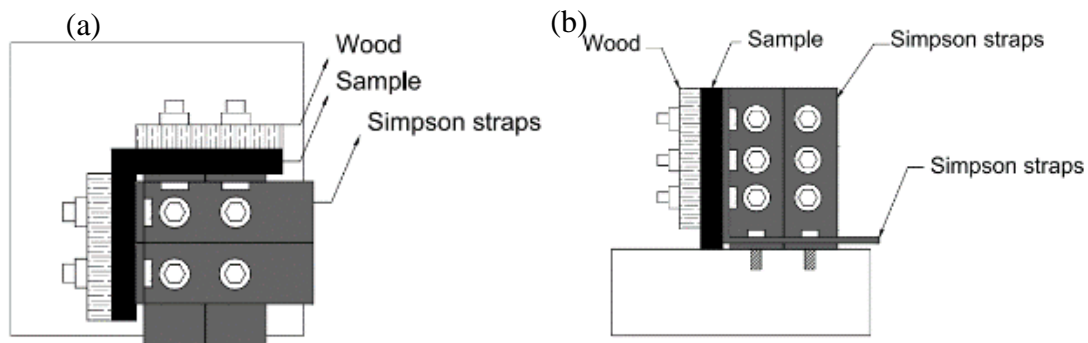
Figure 8-4: (a) plan and (b) elevation view of grip V used for mechanical testing of structural shapes

Amongst the different structural shapes tested in this study, gripping of the C-sections was most challenging due to it higher contact area as opposed to L-sections. The tensile response of C-sections and mode of failure observed were considered as a basis for selecting a suitable gripping system. A comparison between the different gripping types used to test C-sections are shown in Figure 8-6. As evident the type V grips, showed multiple cracking and also showed the best results for tension testing of C-sections. The difference between the type II and III grips are in the arrangement of #2-0.38 in holes as shown in Table 8-2, where type V gripping system have as many as #6-0.25 in holes.

(a)
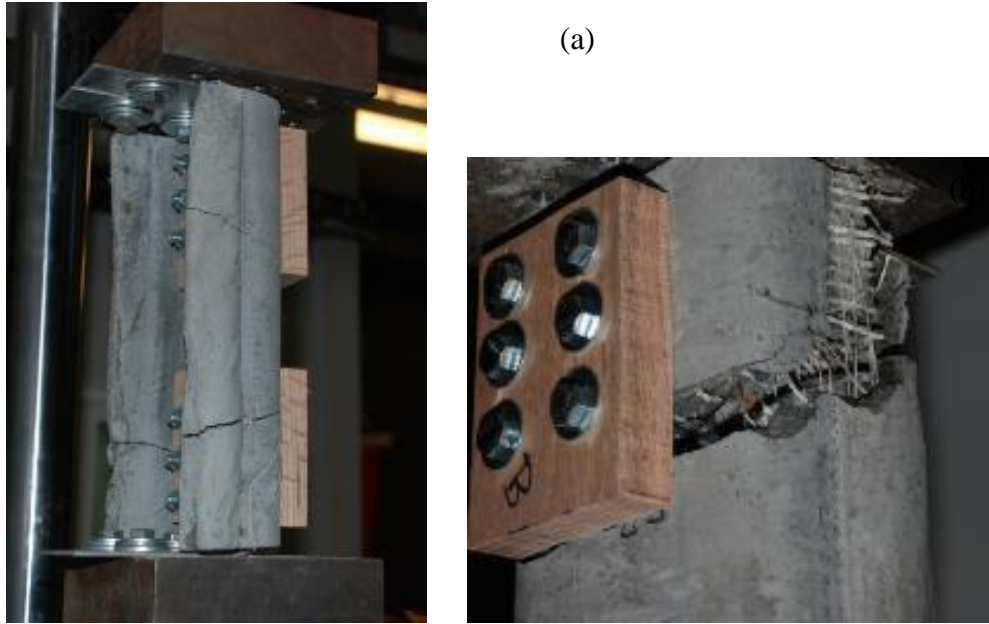
Figure 8-5: Cracking patterns observed with grip V when used for testing channel
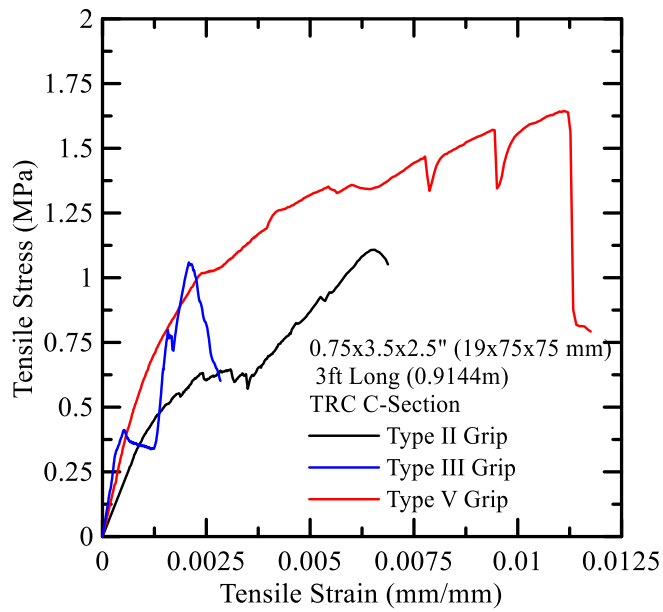
sections

Figure 8-6: Comparison between tensile test results obtained from different gripping

types used for testing C-sections

A comparison between the different gripping types used to test L-sections are shown in Figure 8-7. As shown in Figure 8-7(a), type V grips showed the best results when used for testing channel sections in terms of formation of distributed cracks and accurate measurement of initial stiffness. Although both type II and V grips showed distributed cracking, however the extent of distributed cracking was more evident with Type V grips. This could be attributed to the increase in count of holes, and reduced hole diameter; thus enabling a more uniform gripping pressure to be applied to the specimen. Figure 8-7(b), shows the type I and IV grips used for compression testing of L-sections. It is to be noted that the tensile strength of a standard 2"x4" structural lumber wood member is about 2-11 and compressive strength is about 7-16 MPa, depending upon type or density of the wood used [234]. Thus the current TRC systems, are comparable to lumber members in terms of the tensile and compressive properties. In the addition from durability, fire and water resistance, energy absorption and long term performance viewpoints; TRC shape significantly outperform traditional wood sections.
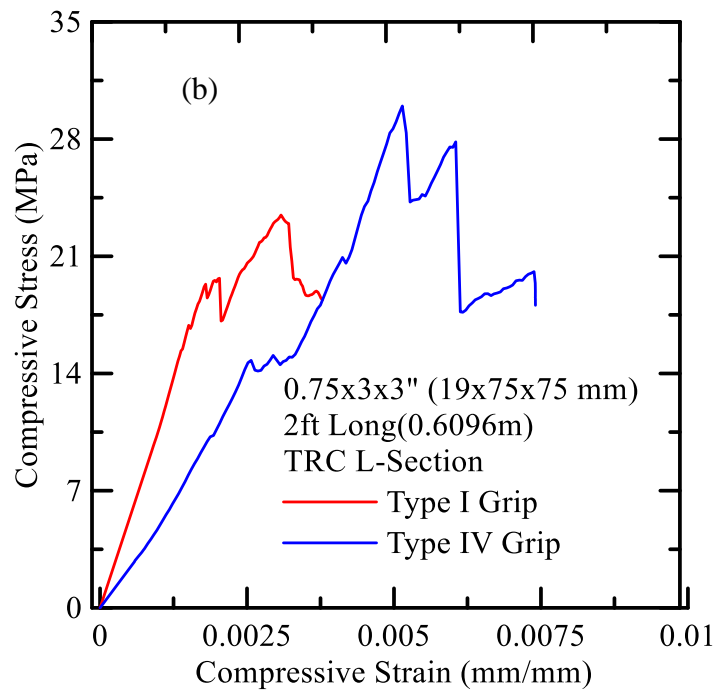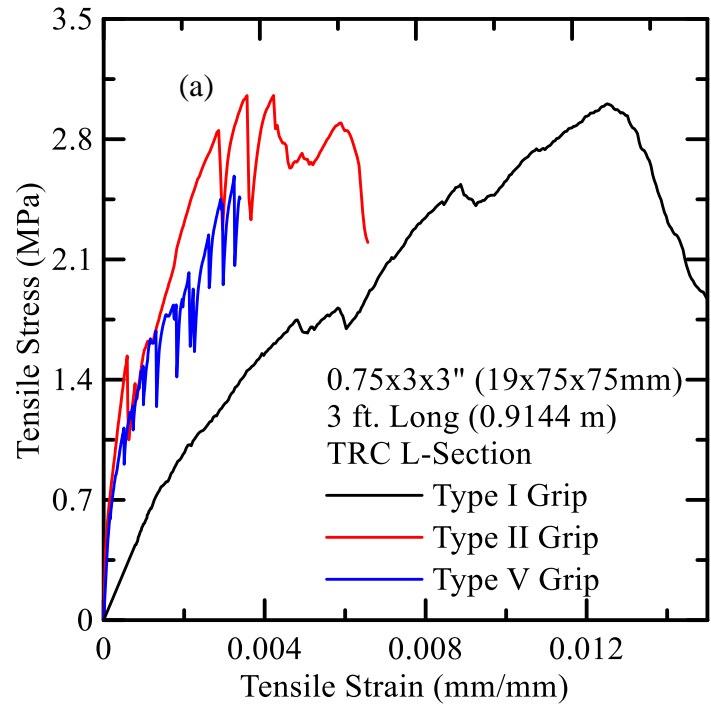
Figure 8-6: Comparison between tensile and compression test results obtained from

different gripping types used for testing L-sections made with TRC

Distributed cracking could be documented using the DIC technique discussed extensively in the previous chapters. The strain development and growth of cracks of a representative 1 m long L-TRC specimen under tension is shown in Figure 8-8 at different strain levels. Figure 8-9 shows the lateral strains that develop in a representative 0.6m long L-TRC specimen under compression.

| 105 sec | 145 s | 150 s | 165 s | 180 s | 200 s |
| 0.1% ε | 0.18% | 0.19% | 0.22% | 0.27% | 0.32% |
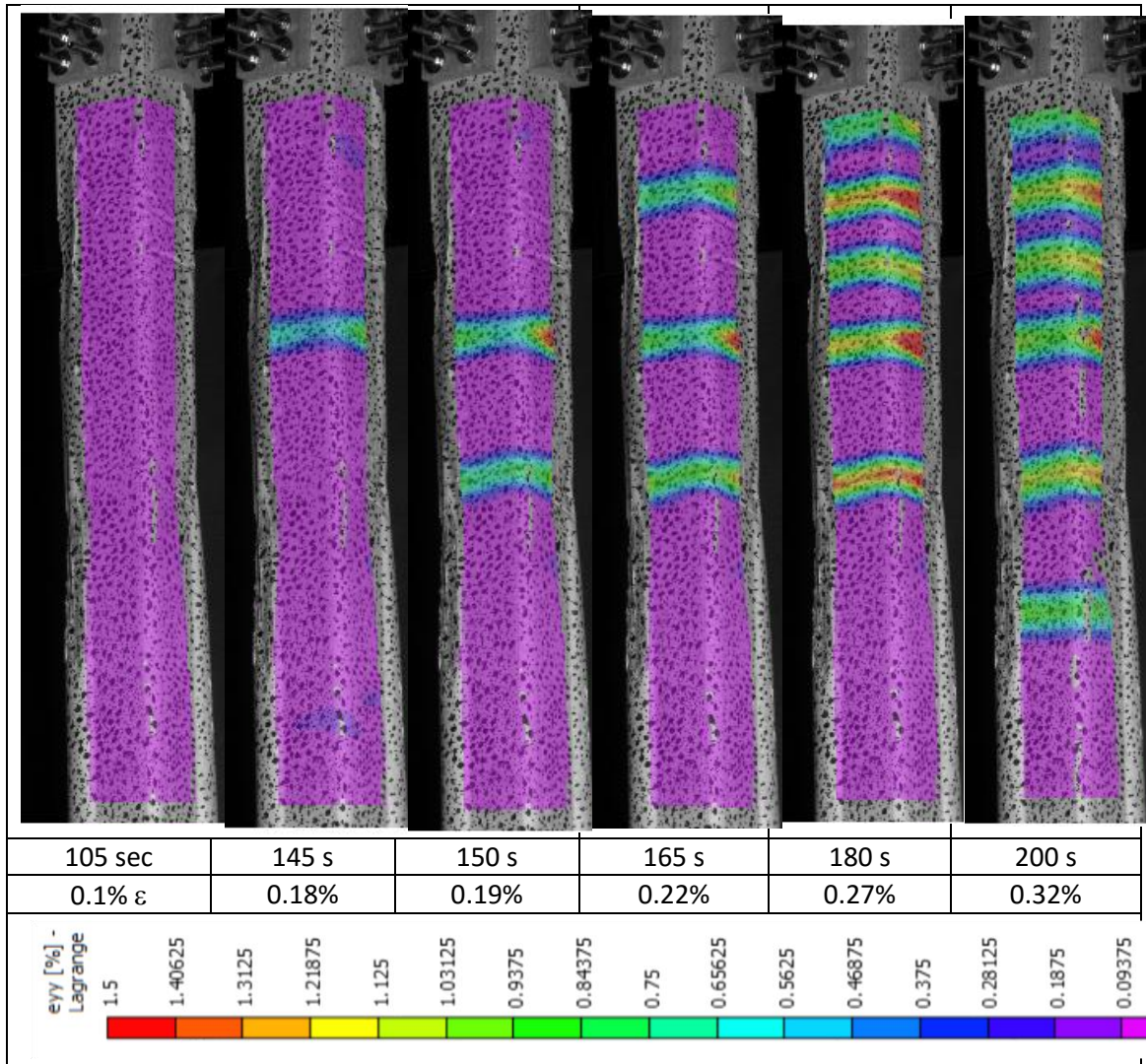
Figure 8-7: Distributed cracking observed in a 1 m long L-TRC specimen under tension
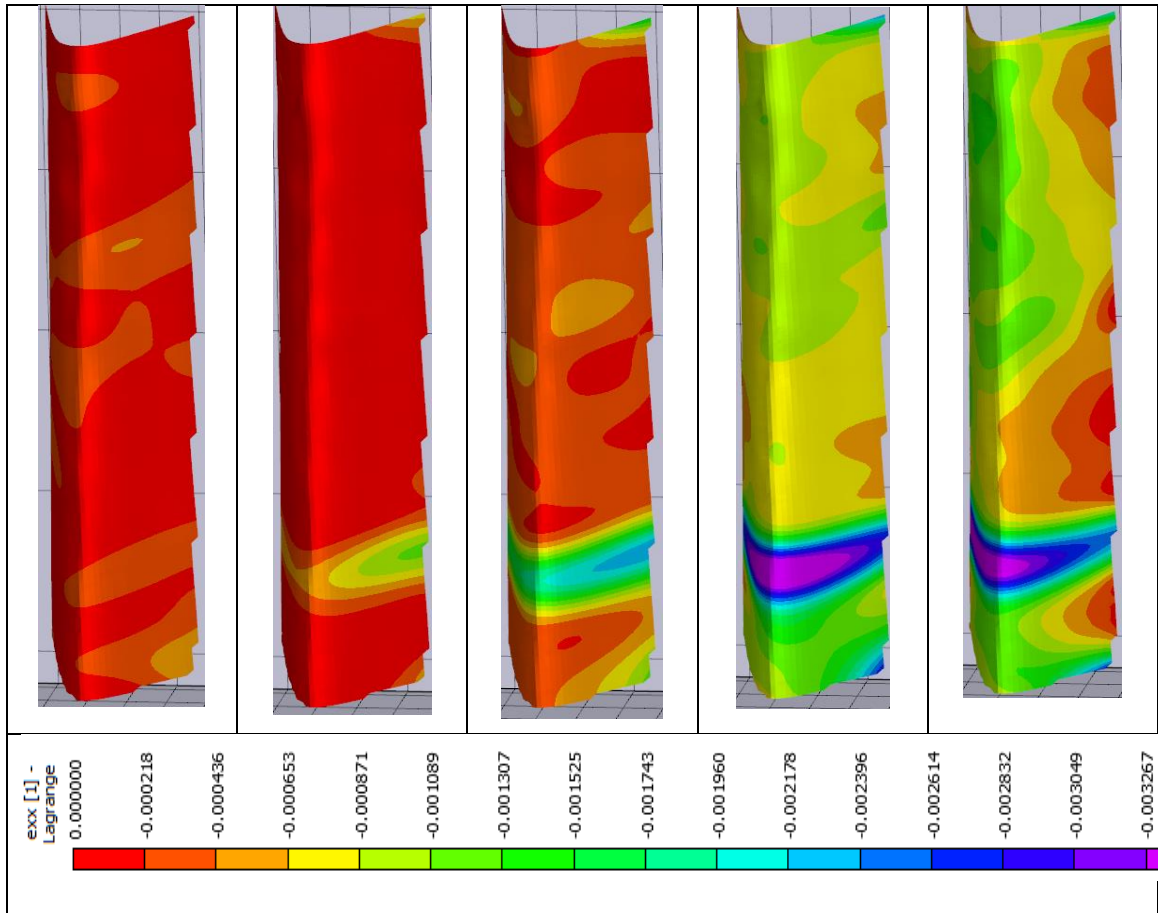
Figure 8-8: Lateral strains (x-dir) observed in a 1.2m long L-TRC specimen under

compression

8.3. Future Work

Further testing would be conducted on these TRC sections with different geometries, textile

materials, thicknesses, and effective length; to get a better understanding of these systems

Structural mechanics will be used to test and verify the analysis and design equations for

these sections. Modelling will be multi-tiered starting with the material level, using

interface, textile, and matrix by employing models based on finite difference approach.

234

Second level modelling will use tension, shear and compression response and build a parametric flexural model to obtain the bending moment-curvature relationship of the sections and define the modes of failure under various curvature conditions. Finally, design level modeling will utilize a plastic analysis approach based on the yield-line limit analysis. By developing methods to utilize, design, and construct cement based composites in structures, we pursue sustainable new materials and design approaches. The direction of work addresses a serviceability based design and promises to deliver a robust design methodology for new composite sections that integrates materials ductility with serviceability, strength and long term durability.

8.4. Use of SHCC systems for repair and rehabilitation

Crack formation in concrete structures is quite common due to the intrinsic brittle nature and its limited tensile capacity. Moreover, the cracks are a path for the access of deleterious substances, which may reduce the useful life of structures. The theme of this project is on implementation of advanced cementitious composite materials for applications on cracks in structural elements such as hydraulic structures, bridge decks and elevated slab or slabs on ground. The research focuses on addressing the main challenges of using cement based composite materials to seal existing cracks, their compatibility and adhesion to old concrete, deformation, and their use as an indicator of the state of deformation during the time of application.

Recently an experimental method was developed at ASU to measure interfacial bond strength within TRC skin and masonry block [235]. The test setup designed by the group is used perform a direct tension on the bond assembly as shown in Figure 8-10. The block

component which is 200x100x50 mm in dimension, is held within a specially designed gripping system shown in Figure 8-11. The TRC laminate which is 300x75x12 mm in dimension, is held within a hydraulic grip at low pressure to avoid localized crushing. The test arrangement is designed so as the bond between the block and TRC is line with the line of applied load. These tests were performed on conventional concrete with multiple layers of ARG textile layers. Both quasi-static and fatigue tensile procedures were developed and conducted on these assemblies. This study was extended to light-weight aerated concrete discussed extensively earlier. Effect of blended matrices, multiple textile layers were evaluated under monotonic tensile and cyclic loading-unloading tests.
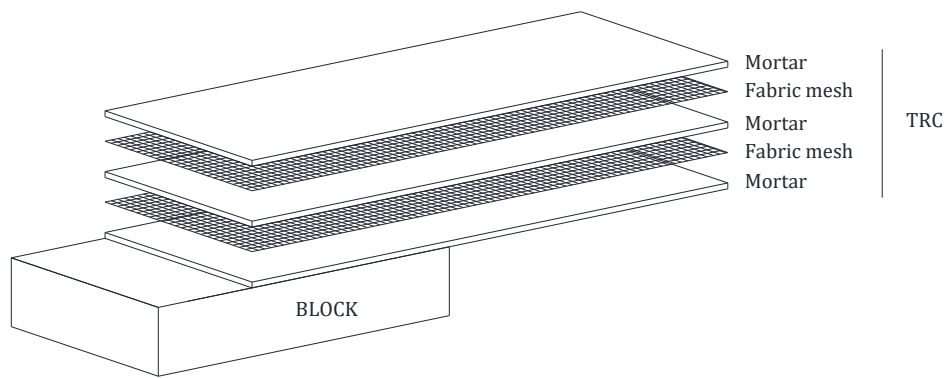
Figure 8-9: Schematics of the masonry block–TRC bond assembly

Figure 8-10: Experimental setup for performing bond tests

8.4.1. Preparation of Masonry Block-TRC Skin Bond Assembly

A standard mortar mix design was used which included 850g of type I/II cement, 150g of fly ash, and 500g of sand. Water to solid ratio of 0.35 was used. Standard laboratory mixing procedure was used. Figure 8-12 shows the molding sequence of the bond assemblies, wherein fabric and matrix layers are stacked layer wise above the masonry blocks. The bond assemblies were covered with polyethylene and moist cured until the day of testing. Monotonic and fatigue tension tests were conducted on these specimens.
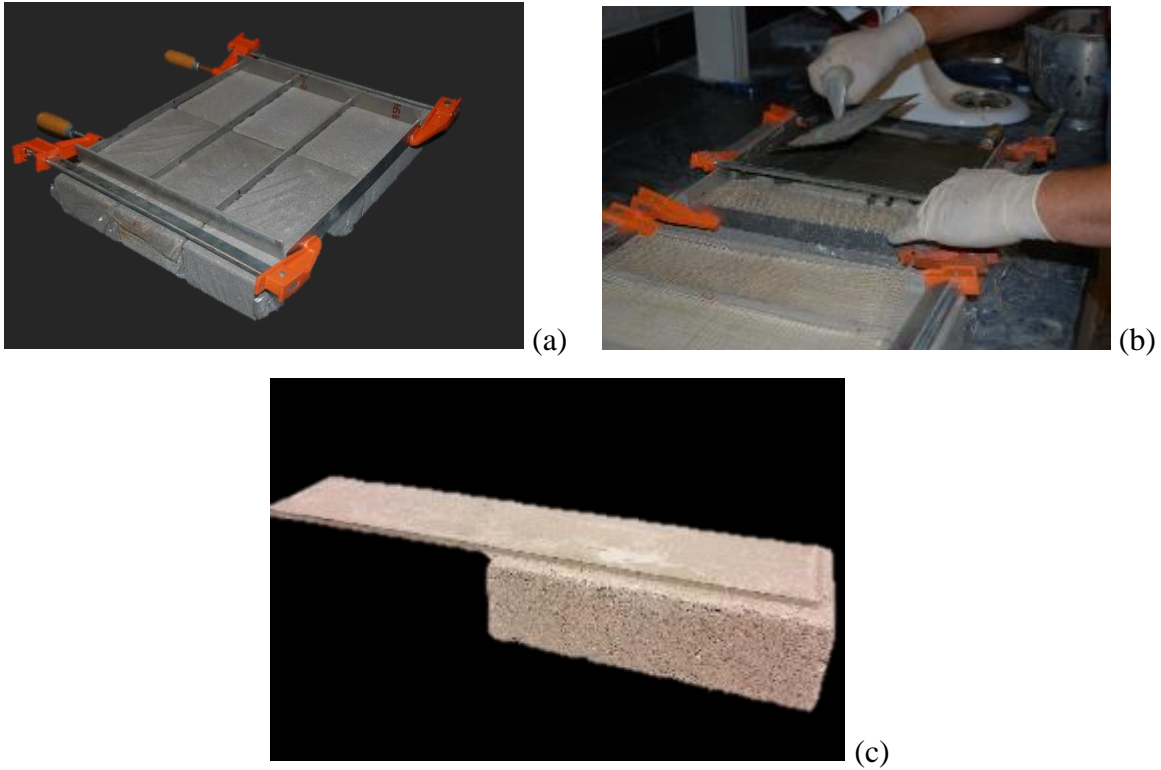
Figure 8-11: (a) Arrangement of masonry blocks, (b) stacking of fabric and matrix for

TRC layer, (c) Finished TRC-masonry bond assembly

8.4.2. Monotonic Bond Tests

Monotonic tension on these bond assemblies were conducted under displacement control,

and the loading rate was fixed at 0.4 mm/min until 1 mm of displacement and 2.54 mm/min

until the end of the test. Fatigue tests up to 100000 cycles were performed, and cycles to

failure were reported.

Figure 8-13 shows the stress-strain responses of three representative bond specimens with

differing textile volume fractions. As expected, ultimate tensile strength and toughness

increases with textile volume fraction. All three curves follow the same general elastic

portion. Each specimen reaches its first crack at higher strains relative to their textile

volume fractions. The specimen with the highest textile volume fraction of 2.7% had a much higher strain capacity than that of the other lower levels of fabric volume fractions.
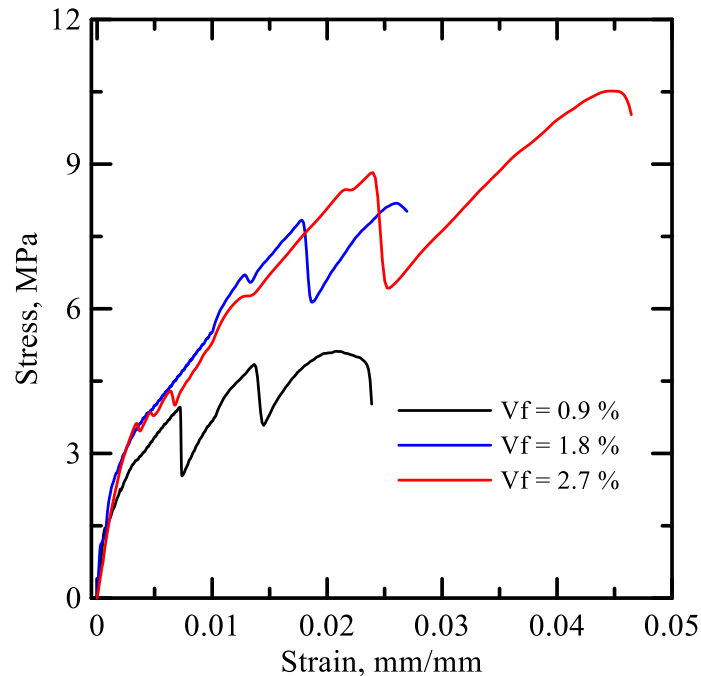
Figure 8-12: Effect of volume fraction on tension stress strain response of

TRC-masonry assemblies

Digital image correlation technique was employed to measure the non-uniform strain distribution along the bond surface and distributed parallel cracks on the TRC surface. The DIC strain contours shown in Figures 8-13 of representative specimens with different textile volume fractions. It is evident that with increasing textile volume fraction, there is reduction in crack spacing and increase in extent of distributed cracking. Specimens with a volume fraction of 0.9% show very large crack spacing with large strain values of nearly 4%. The midrange volume fraction of 1.8% shows higher extent of distributed cracking across the TRC face with strains of about 2%. Finally, the high volume fraction specimens

of 2.7% show many distributed cracks with low strains of about 1.3%. As shown in Figure 12(c), the mortar block actually fails before the TRC laminate specimen.
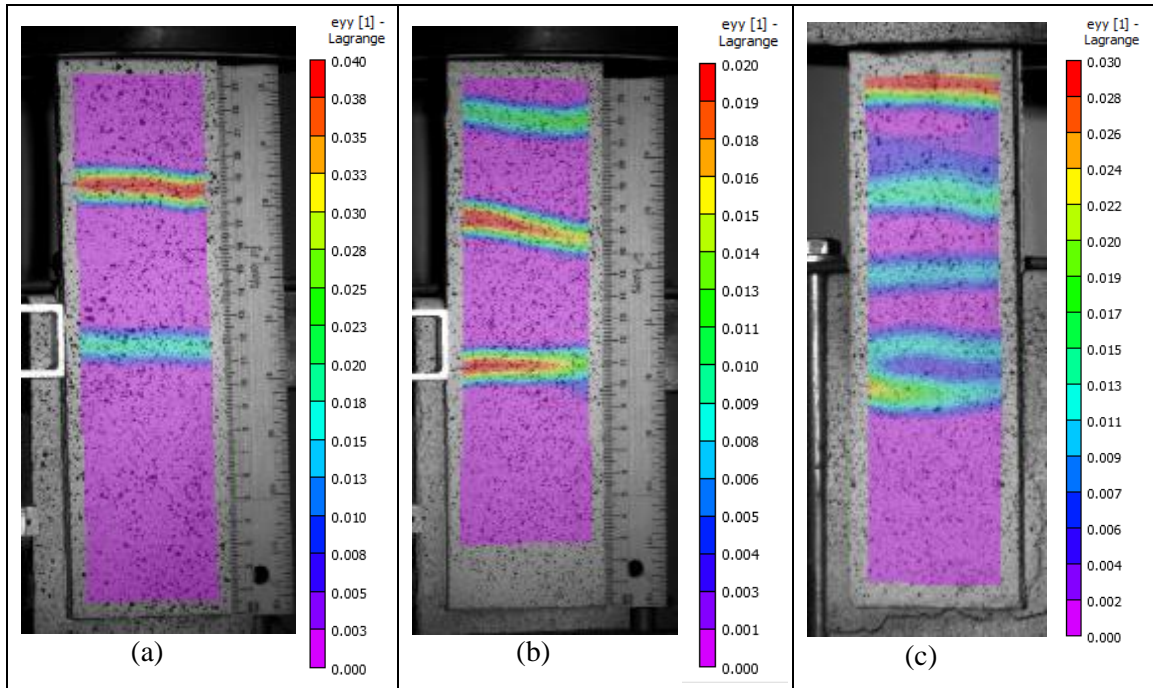
Figure 8-13: DIC strain contour of bond specimen under static tension with textile volume fraction of: (a) 0.9%, (b) 1.8%, (c) 2.7%

Figure 8-14 shows the comparison between two different block assemblies: normal weight concrete and fiber reinforced aerated concrete, with same volume fraction of 1.8%. As evident, this test could be easily employed to measure the delamination stress between the aerated concrete core element and TRC skin layer, which is a dominant failure mechanism in the sandwich composites as discussed in the previous chapter. Regular concrete blocks as apparent have significant higher interlaminar bond strength as compared to aerate concrete blocks. This could be related to the better compressive strength of the concrete block.
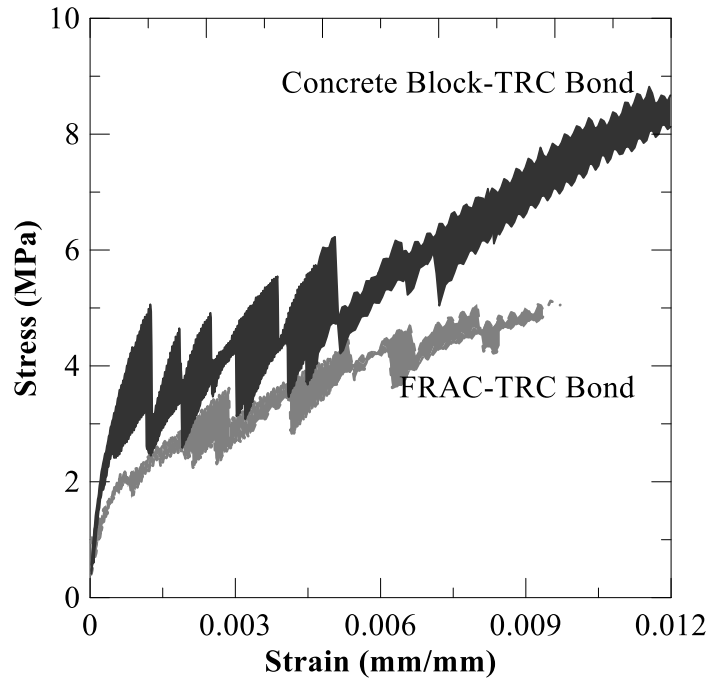
Figure 8-14: Tensile response of concrete block and FRAC bond assemblies with 1.8% ARG

8.4.3. Fatigue Bond Tests

Fatigue test was a cyclic loading-unloading test under displacement control was developed for this study, load-deformation of a representative specimen is shown in Figure 8-15. The test is based on a fatigue-style of loading, and includes an initial monotonic state of loading up to 0.5 mm (0.02 in), followed by 100,000 cycles at the frequency of 5 Hz between 0.5 to 1 mm (0.02 – 0.04 in) of deformation, followed by another monotonic loading stage up to failure. The deflection limits were decided after conducting several monotonic tests on the bond assembly.
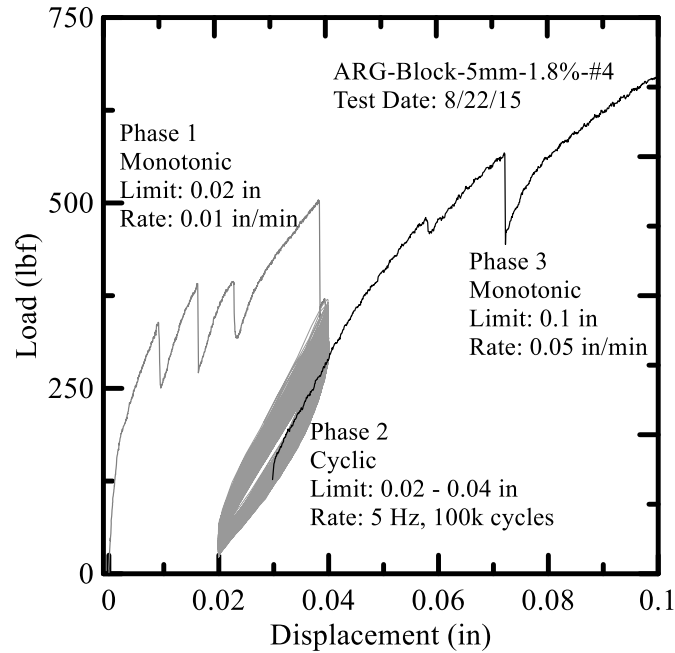
Figure 8-15: Test response obtained from fatigue test on TRC-Masonry bond assembly

Figure 8-16 shows the fatigue and static tension superimposed load-displacement curves of bond specimens with a textile volume fraction of 1.8%. The fatigue response shows a higher initial tensile response followed by a lower strain capacity and generally lower ultimate tensile strength than that of the static tension responses. The reduced strain and strength capacity is expected as the fatigue specimens have undergone at up to 100,000 before being pulled until failure. The cyclic fatigue reduces the tensile strength and strain capacity of the specimens.

242
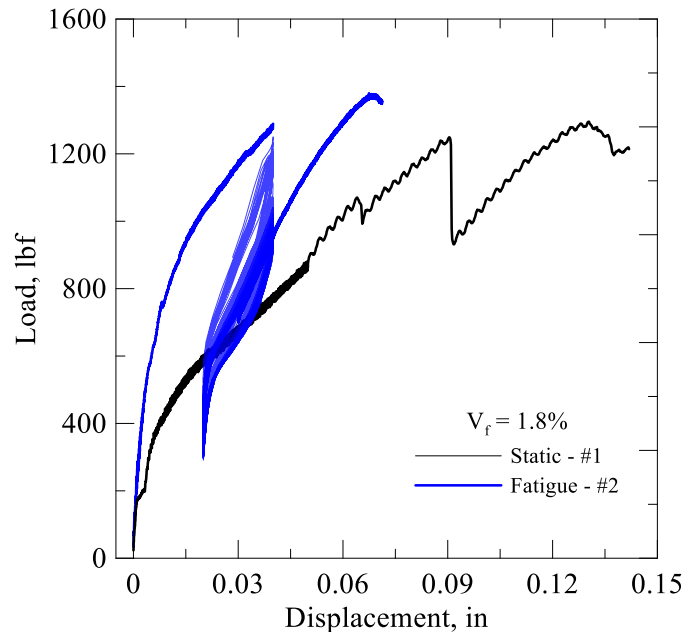
Figure 8-17 shows the cyclic load-displacement curves for three different volume fractions. Bond specimens with a volume fraction of 1.8% and 2.7% showed much higher fatigue life than those with a lower volume fraction of 0.9%. The higher volume fractions also allowed the specimens to endure the entire 100,000 cycles of the test. Highest volume fraction of 2.7% allowed an increase in the peak strength in the phase 3. However the stress levels recorded during the fatigue cycles are lower than vol. fraction of 1.8%.

The loading-unloading modulus was measure from each of the fatigue cycles as shown in Figure 8-17. As evident the modulus measured during the loading stage is same as the unloading stage in the initial cycles up to about 5000 cycles. Consequently the loading modulus moderately higher than the unloading modulus, suggesting yielding of the bond and tensile cracking in the TRC layer. The loading modulus was used to study the effect of volume fraction as shown in Figure 8-18. As evident at low volume fraction of 0.9%

specimens failure prematurely whereas at higher volume fractions, the loss in modulus is much less with increasing fatigue life.
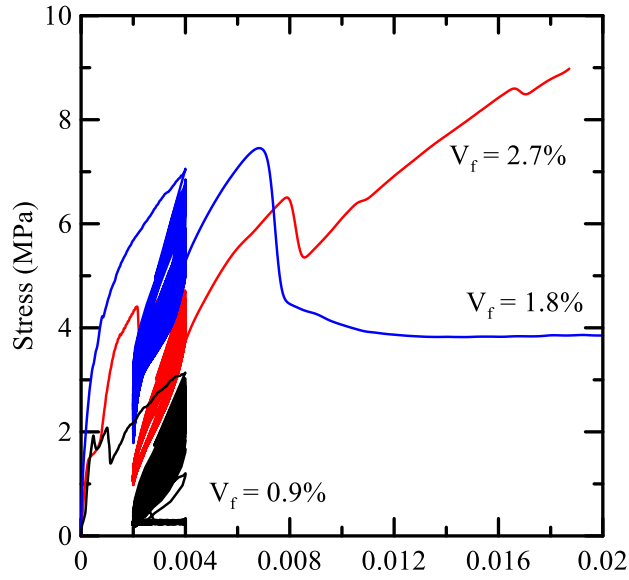
Figure 8-16: Effect of volume fraction on cyclic tensile fatigue load displacement response
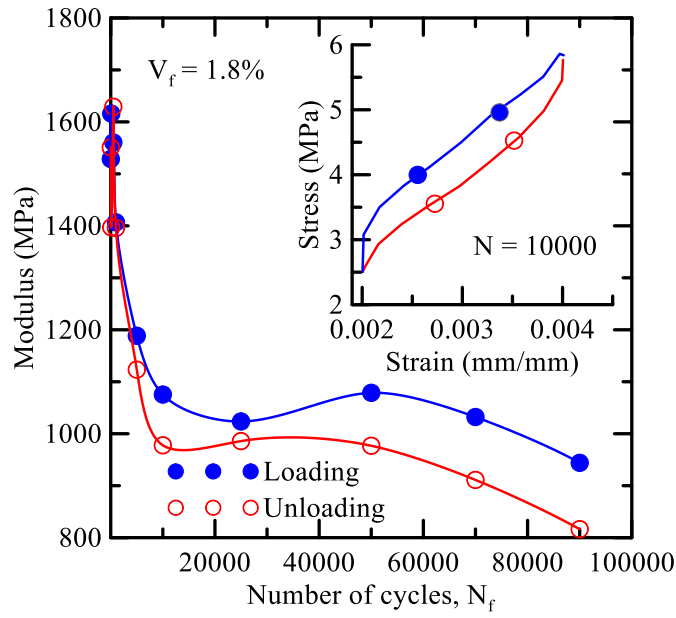
Figure 8-17: Comparison between loading and unloading modulus

The maximum stress measured in 10 selected cycles were plotted in Figure 8-19. As evident, with increasing fatigue cycles, strength reduction is significantly higher at lower volume fractions of TRC. The fatigue life significantly improves with higher dosages of fabric layers.
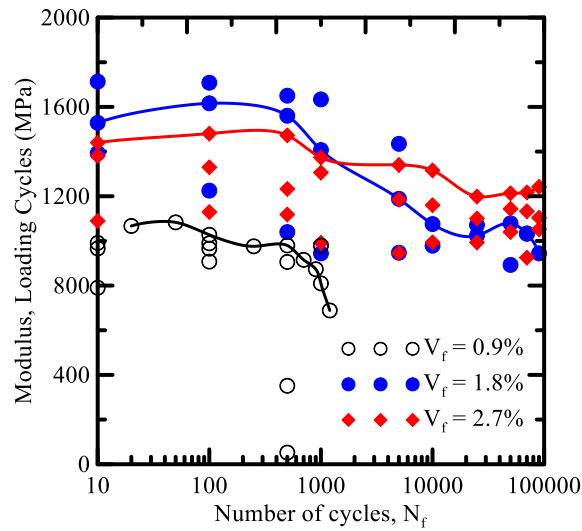
Figure 8-18: Degradation of compliance with fatigue cycles
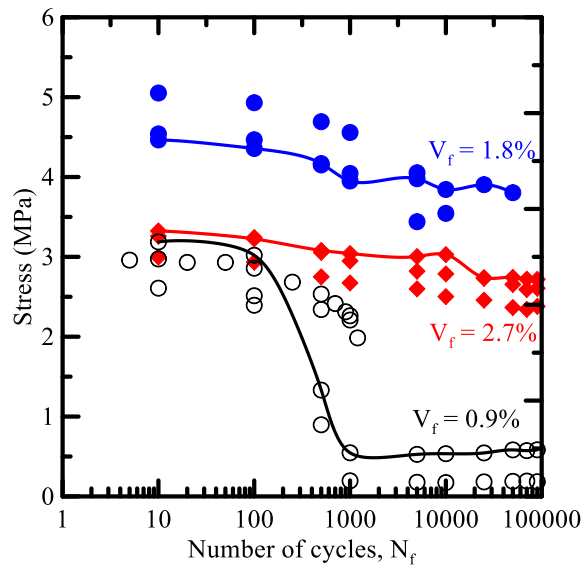
Figure 8-19: Stress vs fatigue life (S-N) at different volume fractions of TRC layer

245

8.5. Conclusions

Two new areas of application of SHCC systems were evaluated in this chapter. Structural sections with customized cross-sections and length were developed using the automated pultrusion section. Viability of using these sections as tension and compression elements were evaluated using a series of instrumented tests. Connection of these structural members were discussed and several parameters such as diameter, number, and spacing of holes were evaluated. The failure mode observed under tension and compression with different connection styles were discussed. It was found that these structural section made with several layers of TRC composites could easily replace existing lumber based construction. Another application of SHCC systems for retrofitting works was also evaluated. A unique test setup to measure delamination stress between the TRC layers and existing masonry units was developed. Series of monotonic tension and fatigue tests were conducted on these bond assemblies with different layers of textiles. It was observed that higher dosage of fabric layers, improves the fatigue life of these bond assemblies. Such SHCC systems could be easily extended to crack mitigation of existing structural systems which are subjected to dynamic loadings such as bridge decks, and hydraulic structures.

REFERENCES

1   Naaman AE, Reinhardt HW,"Setting the stage: toward performance based classification of FRC composites", In: Proc of 4th Int workshop on High Performance Fiber Reinforced Cement Composites (HPFRCC-4), Ann Arbor, USA, June 15-18, 2003, pp. 1–4.

2   Mobasher, B., "Mechanics of fiber and textile reinforced cement composites", CRC Press - Taylor and Francis Group, 2012, pp. 451.

3   Mobasher, B. Pivacek, A., and Haupt, G. J., "Cement based cross-ply laminates", Journal of Advanced Cement Based Materials, 1997, Vols. 6, pp. 144-152.

4   Swamy, R., N., Hussin, M. W., "Continuous woven polypropylene mat reinforced cement composites for applications in building construction", In Textile Composites in Building Construction, P. Hamelin and G. Verchery (Eds.), Part 1, 1990, pp. 57-67.

5   Kruger, M. Ozbolt, J., and Reinhardt, H.W., "A New 3D Discrete Bond Model to Study The Influence of Bond on Structural Performance of Thin Reinforced and Prestressed Concrete Plates", Proc., 4th Int. RILEM Workshop on High Performance Fiber Reinforced Cement Composites (HPFRCC4), Eds. A.E., Naaman and H.W., Reindhart, Ann Arbor, 2003, pp. 49-63.

6   Peled A, Bentur A. Geometrical characteristics and efficiency of textile fabrics for reinforcing composites. Cement and Concrete Research 2000; 30: 781-790.

7   Meyer C., and Vilkner G., "Glass Concrete Thin Sheets Prestressed with Aramid Fiber Mesh" Proceeding of the Fourth International RILEM Workshop on High Performance Fiber Reinforced Cement Composites (HPFRCC4), Eds. A.E., Naaman and H.W., Reindhart, Ann Arbor, 2003, pp. 325-336.

8   Häußler-Combe, U.; Jesse, F.; Curbach, M.: Textile reinforced concrete - overview, experimental and theoretical investigations. In: Li, V. C. et al. (Eds): Fracture Mechanics of Concrete Structures. Proceedings of the fifth International Conference on Fracture Mechanics of Concrete and Concrete Structures/Vail, Colorado/USA/12-16 April, 2004. Ia-FraMCos, 204, pp. 749-756.

9   Peled A., Cohen Z., Mobasher, B., "Mechanical properties of hybrid fabrics in pultruded cement composites", Cement and Concrete Composites, 2009, Vols. 31 (9), pp. 647-57.

10   Soranakom, C., Mobasher, B., "Geometrical and mechanical aspects of fabric bonding and pullout in cement composites", Materials and Structures, 2009, Vol. 42, pp. 765 – 777.

11   Narayanan, N., and Ramamurthy, K.,"Structure and properties of aerated concrete: a review", Cement and Concrete Composites, 2000, Vols. 20, 321 - 329.

12   Roels, S., Sermijn, J., Carmeliet, J., "Modelling unsaturated moisture transport in autoclaved   aerated concrete: A microstructural approach," Building Physics 2002 – 6th Nordic Symposium, Trondheim, Norway, pp. 167-174.

13   Pacheco-Torgal, F., et. al., "Eco-efficient Masonry Bricks and Blocks: Design, Properties and Durability". Woodhead Publishing, 2015, ISBN: 978-1-78242-318-8, pp. 548.

14   Mobasher, B., Peled, A., Pahilajani, J., Distributed cracking and stiffness degradation in fabric-cement composites, 2006, Materials and Structures, Vol. 39, 317-331.

15   Mobasher, B., Mechanics of fiber and textile reinforced concrete, 2011, CRC Press, ISBN 9781439806609, pp. 473.

16   Pivacek, A., Haupt, G.J., Mobasher, B., Cement Based Cross-Ply Laminates, 1997, Advanced Cement Based Materials, Vol. 6, pp. 144-152.

17   Mobasher, B., Pivacek, A., A Filament Winding Technique for Cement Based Cross-ply Laminates, Cement and Concrete Composites, 1998, Vol. 20, pp. 405-415.

18   BASF–Master Builders Solutions, Technical Document, Master MAC 2200 CB Macrosynthetic Fiber with Chemical Bond, http://www.master-builders-solutions.basf.us/en-us/products/masterfiber/2514.

19   Mobasher, B., Li, C.Y., Modeling of stiffness degradation of the interfacial zone during fiber debonding, Composites Engineering 5 (1995) 1349-1365.

20   S. Igarashi, A., Bentur, S. Mindess, The effect of processing on the bond and interfaces in steel fiber reinforced cement composites, CemConcr Compos, 18 (1996) 313-322.

21   Sueki, S., Soranakom, C., Peled, A., and Mobasher, B., "Pullout-Slip Response of Fabrics Embedded in a Cement Paste Matrix, ASCE Journal of Materials Engineering, Vol. 19, 9, 2007.

22   Flávio de Andrade Silva, Mobasher, B., Soranakom, C. and Toledo Filho, R., "Effect of Fiber Shape and Morphology on the Interface Mechanical Characteristics in Sisal Fiber Cement Based Composites," Journal of Cement and Concrete Composites Volume 33, Issue 8, September 2011, Pages 814-823

23   Yao, Y., Silva, F.A., Butler, M., Mechtcherine, V., Mobasher, B., Tension stiffening in textile-reinforced concrete under high speed tensile loads, Cement and Concrete Composites, 2015, 64, pp. 49-61.

24   Sutton, M. A., Wolters, W. J., Peters, W. H., Ranson, W. F., McNeil, S. R. Determination of Displacements Using an Improved Digital Correlation Method. Image Vision Comput 1983; 1(3): 133-139. doi:10.1016/0262-8856(83)90064-1.

25   Bruck, H. A., McNeil, S. R., Sutton, M. A., Peters, W. H. Digital Image Correlation Using Newton-Raphson Method of Partial Differential Correction. ExpMech 1989; 29(3): 261-267. doi: 10.1007/BF02321405.

26   Destrebecq, J-F., E. Toussaint, E. Ferrier. Analysis of cracks and deformations in a full scale reinforced concrete beam using a digital image correlation technique. ExpMech 2011; 51(6): 879-890.

27   Koerber, H., Xavier, J., Camanho, P. P. High strain rate characterisation of unidirectional carbon-epoxy IM7-8552 in transverse compression and in-plane shear using digital image correlation. Mech Mater 2010; 42: 1004-1019. doi:10.1016/j.mechmat.2010.09.003.

28   Gao, G., Huang, S., Xia, K. Li, Z. Application of Digital Image Correlation (DIC) in Dynamic Notched Semi-Circular Bend (NSCB) Tests. ExpMech 2015; 55: 95–104. doi: 10.1007/s11340-014-9863-5.

29   Technical data sheet of MAC 2200 CB fibers,Link: https://www.master-builders-solutions.basf.us/en-us/products/masterfiber/2514

30   Technical data sheet of Dramix fibers, Link: data sheet dramix - bekaert.com

31   Weblink   of   source   of   synthetic   polypropylene   Cofisa   fibers: http://fibramix.en.ec21.com/

32   Silva, F., Butler, M., Mechtcherine, V., Zhu, D., Mobasher, B. Strain rate effect on the tensile behavior of textile-reinforced concrete under static and dynamic loading, Materials Science and Engineering A, 2011, 528, 1727-34.

33   Dey, V., Kachala, R., Bonakdar, A., Mobasher, B., Mechanical properties of micro and sub-micron wollastonite fibers in cementitious composites, Construction and Building Materials, 2015, 82, pp. 351-359.

34   Brameshuber, W., Koster, M., Hegger, J., Voss. S., Gries, T. , Barle, M., Reinhardt, H.-W., Krüger, M., : Textile Reinforced Concrete (TRC) for Integrated Formworks. In: 12. Internationale Techtextil-Symposium für technische Textilien, Vliesstoffe und textilarmierte Werkstoffe. . Messe Frankfurt GmbH, 07.04.03-10.04.03, Frankfurt. Frankfurt: 2003, 4.23. - CD-Rom

35   Kruger, M. Ozbolt, J., and Reinhardt, H.W., "A New 3D Discrete Bond Model to Study The Influence of Bond on Structural Performance of Thin Reinforced and Prestressed Concrete Plates", Proceeding of the Fourth International RILEM Workshop on High Performance Fiber Reinforced Cement Composites (HPFRCC4), Eds. A.E., Naaman and H.W., Reindhart, Ann Arbor, 2003, pp. 49-63.

36   Häußler-Combe, U.; Jesse, F.; Curbach, M.: Textile reinforced concrete - overview, experimental and theoretical investigations. In: Li, V. C. et al. (Eds): Fracture Mechanics of Concrete Structures. Proceedings of the Fifth International Conference on Fracture Mechanics of Concrete and Concrete Structures/Vail, Colorado/USA/12-16 April, 2004. Ia-FraMCos, 204, pp. 749-756.

37.   Meyer C., and Vilkner G., "Glass Concrete Thin Sheets Prestressed with Aramid Fiber Mesh" Proceeding of the Fourth International RILEM Workshop on High Performance Fiber Reinforced Cement Composites (HPFRCC4), Eds. A.E., Naaman and H.W., Reindhart, Ann Arbor, 2003, pp. 325-336.

38   Brameshuber, W., Brockmann, T., Hegger, J., Molter, M., Textilbeton - Betontechnologie und Tragverhalten, Untersuchungen zum Textilbewehrten Beton, Beton 09/2002, Seiten 424-429, (2002).

39   Jesse, F.; Curbach, M.: A new approach for determining geometrical properties of glass fibre reinforcement in grc composites. In: di Prisco, M.; Felicetti, R.,; Plizzari, G. A.. (Hrsg.): Fibre-Reinforced Concretes: Proceedings of the "Sixth International RILEM-Symposium - BEFIB 2004", Varenna, 20.-22.9.2004. Bagneux : RILEM, 2004, S. 267-278.

40   Peled, A. and Mobasher, B.,"Pultruded Fabric-Cement Composites," ACI Materials Journal, Vol. 102 , No. 1, pp. 15-23, 2005.

41   Reinhardt, H.-W., Krüger, M., Grosse, C.U.: Concrete Prestressed with Textile Fabric. In: Journal of Advanced Concrete Technology Vol. 1(2003), No. 3, pp. 231-239.

42   Weblinks: http://warpknits.vrtxinc.com/product/all-categories/tricot-knit-fabric;
http://www.norcostco.com/sharkstooth-scrim-material-20-flame-retardant-
white.aspx; http://en.texsite.info/Tricot_weave

43   Peled, A. and Mobasher, B., "Pultruded Fabric-Cement Composites," ACI
Materials Journal, Vol. 102 , No. 1, pp. 15-23, 2005.

44   Kazuhisa, S., Noayoshi, K., Yasuo, K., "Development of carbon fiber reinforced
cement", Advanced Materials: The big Payoff National SAMPE Technical
Conference, Publ. by SAMPE, Covina, CA, USA, Vol. 21, 1998, pp. 789-802.

45   Nishigaki, T., Suzuki, K., Matuhashi, T., and Sasaki, H., "High strength continuous
carbon fiber reinforced cement composite (CFRC)", Proceeding of the third
international symposium on brittle matrix composites, Brandt, A. M. and Marshall,
I H. (Eds.), Warsaw, Poland, Elsevier Applied Science, 1991, pp. 344-355.

46   Mobasher, B. Pivacek, A., and Haupt, G. J., "Cement based cross-ply laminates",
Journal of Advanced Cement Based Materials, No. 6, 1997, pp. 144-152.

47.   Bauchamoyer, J., "Development of an Automated Pultrusion System for
Manufacturing of Textile Reinforced Cementitious Composites", 2015, Arizona
State University, Honors Thesis, pp. 29.

48   Häußler-Combe, U.; Jesse, F.; Curbach, M.: Textile reinforced concrete - overview,
experimental and theoretical investigations. In: Li, V. C. et al. (Eds): Fracture
Mechanics of Concrete Structures. Proceedings of the Fifth International
Conference on Fracture Mechanics of Concrete and Concrete Structures/Vail,
Colorado/USA/12-16 April, 2004. Ia-FraMCos, 204, pp. 749-756.

49   Talreja, R.,"Stiffness Properties of Composite Laminates With Matrix Cracking and
Interior Delamination," Eng. Fracture Mechanics, Vol 25. No. 5/6, pp. 751-762,
1986.

50   Mobasher, B., Stang, H., and Shah, S. P., "Microcracking in Fiber Reinforced
Concrete," J. of Cem. & Conc. Res., Vol. 20, 1990, pp. 665-676.

51   B. Mobasher, "Micromechanical Modeling of Filament Wound Cement-Based
Composites," ASCE, Journal of Engineering Mechanics, Volume 129, No. 4, pp.
373-382, 2003.

52   A. Peled, and B. Mobasher, "Cement Based Pultruded Composites with Fabrics,"
Proceedings of the 7th International Symposium on Brittle Matrix Composites
(BMC7), Warsaw, Poland, pp. 505-514, 2003.

53   Agarwal, B. D., and Broutman, L. J.(1990) ,Analysis and Performance of Fiber Composites, 2nd edition, Wiley.

54   Karihaloo, Bhushan L. (1995)" <u>Fracture mechanics and structural concrete</u>" Harlow, Essex, England : Longman Scientific & Technical.

55   Mobasher, B., Pahilajani, J., Peled, A., (2006), "Analytical simulation of tensile response of fabric reinforced cement based composites", Cement and Concrete Composites, Vol. 28, pp. 77-89.

56   Horii, H; Hasegawa, A; and Nishino, F., (1987) "Process Zone Model and Influencing Factors in Fracture of Concrete," in G-28, 1987, pp. 205-219.

57   Nemat-Nasser, S., and Hori, M. (1993) Micromechanics: overall properties of Heterogeneous Materials.

58   Aveston, J., G. A. Cooper, and A. Kelly. "The Properties of Fiber Composites." Conference Proceedings, National Physical Laboratory (IPC Science and Technology Press Ltd). Paper 1 (1971) p. 15.

59   Mobasher, B., and Shah, S. P., "Interaction Between Fibers and the Cement Matrix in Glass Fiber Reinforced Concrete", American Concrete Institute, ACI SP-124, pp. 137-156, 1990

60   Peled, A., Mobasher, B., Sueki, S. "Technology Methods In Textile Cement-Based Composites" Concrete Science and Engineering, A Tribute to Arnon Bentur, Edited By: K. Kovelr, J. Marchand, S. Mindess, and J. Weiss, RILEM Proceedings PRO 36, March 2004. pp. 187-202.

61   Sueki, S., Peled, A., Mobasher, B., "Pullout-Slip Response of Fabrics Embedded in a Cement Paste Matrix", Journal of Cement and Concrete Research, manuscript in review, 2004.

62   Stang, H. and Shah, S.P. (1986). Failure Of Fiber-Reinforced Composites By Pull-Out Fracture Journal of Materials Science, 21: 953-957

63   Hetényi, M. 1946. Beams on Elastic Foundation. University of Michigan Press, Ann Arbor. 255pp.

64   Jones, R.M. (1975) Mechanics of Composites Materials, McGraw Hill Book Co.

65   Mobasher B, Peled A, Pahilajani J., "Distributed cracking and stiffness degradation in fabric-cement composites", Materials and Structures 2006; Vols. 39(287), pp. 317–331.

66   Mobasher B. and Li, C.Y., "Mechanical properties of hybrid cement-based composites" ACI Materials J., 1996, Vols. 93(3), pp. 284-292.

67   Mobasher, B. Pivacek, A., and Haupt, G. J., "Cement based cross-ply laminates", Journal of Advanced Cement Based Materials, 1997, Vols. 6, pp. 144-152.

68   Soranakom C, Mobasher B, Bansal S., "Effect of material non-linearity on the flexural response of fiber reinforced concrete", Proceeding of the Eighth International Symposium on Brittle Matrix Composites BMC8, Warsaw, Poland, 2006, pp. 85-98.

69   Mobasher, B., "Mechanics of Fiber and Textile Reinforced Cement Composites", CRC press, 2011, ISBN: 9781439806609, pp. 480.

70   Peled A, Mobasher, B., "Pultruded fabric-cement composites", ACI Materials Journal, 2005; Vol. 102(1), pp. 15-23.

71   de Oliveira e Sousa JLA, Gettu R., "Determining the tensile stress-crack opening curve of concrete by inverse analysis", Journal of engineering mechanics. 2006; Vol. 132(2), pp. 141-148.

72   Olesen, J. F. (2001), "Fictitious crack propagation in fiber-reinforced concrete beams", Journal of Engineering Mechanics, Vol. 127(3), pp. 272-280.

73   Zhang J, Stang H., "Applications of stress crack width relationship in predicting the flexural behavior of fibre-reinforced concrete", Cement and Concrete research 1998; Vol. 28(3),pp. 439-452.

74   Kitsutaka Y., "Fracture parameters by polylinear tension-softening analysis", Journal of engineering mechanics, 1997; Vol. 123(5) ,pp. 444-450.

75   Mobasher, B., and, Li, C. Y., "Effect of Interfacial Properties on the Crack Propagation in Cementitious Composites," Journal of Advanced Cement Based Materials, 1996, Vol. 4 (3), pp. 93-106.

76   Li, C. Y., and Mobasher, B., "Finite Element Simulations of Toughening in Cement Based Composites," Journal of Advanced Cement Based Materials, 1998, Vols. 7, pp. 123-132.

77   Soranakom C, Mobasher B. "Closed form solutions for flexural response of fiber reinforced concrete beams", Journal of Engineering Mechanics 2007; Vols. 133(8), pp. 933-41.

78   Taheri M, Barros JA, Salehian H., "Design-oriented approach for strain-softening and strain-hardening fibre hybrid reinforced concrete elements failing in bending", Fibre Concrete 2011, ONCRETE 2011, Prague, Czech Republic, 8th – 9th September 2011.

79   Taheri M, Barros JA, Salehian H., "Parametric Study of the Use of Strain Softening/Hardening FRC for RC Elements Failing in Bending", Journal of Materials in Civil Engineering, 2012;Vols. 24(3), pp. 259-274.

80   Varma RK, Barros JA, Sena-Cruz J., "Design-curves of strain softening and strain hardening fibre reinforced concrete elements subjected to axial load and bending moments", BEFIB 2012– Fibre_reinforced Concrete. Edited by J. Barros et al. Guimarães, Prtugal, 2012.

81   Ferrara L, Ozyurt N, di Prisco M., "High mechanical performance of fibre reinforced cementitious composites: the role of "casting-flow induced" fibre orientation", Materials and structures, 2011;Vols. 44(1), pp. 109-128.

82   Buratti N, Mazzotti C, Savoia M., "Post-cracking behaviour of steel and macro-synthetic fibre-reinforced concretes", Construction and Building Materials, 2011, Vols. 25(5), pp. 2713-2722.

83   Soranakom C, Mobasher B., "Closed-form moment-curvature expressions for homogenized fiber-reinforced concrete", ACI Material Journal 2007; Vols. 104(4), pp. 351-9.

84   Soranakom C, Mobasher B., "Correlation of tensile and flexural response of strain softening and strain hardening cement composites", Cement Concrete Composites, 2008;Vols. 30, pp. 465-477.

85   Soranakom C, Mobasher B., "Flexural Analysis and Design of Textile Reinforced Concrete", 4th Colloquium on Textile Reinforced Structures (CTRS4), Dresden, Germany, June 3-5 2009, pp. 273-288.

86   Naaman AE, Duane O, Husamuddin N, "Elastic modulus of SIFCON in tension and compression", ACI Materials Journal, 1992, Vols. 88(6), pp. 603-613.

87   Soranakom C, Mobasher B. Closed-form moment-curvature expressions for momogenized fiber reinforced concrete. ACI Material Journal 2007; 104(4):351-9.

88   Soranakom C, Mobasher B. Closed form solutions for flexural response of fiber reinforced concrete beams. Journal of Engineering Mechanics 2007;133(8):933-41.

89   Peled, A., Sueki, S., Mobasher, B. (2006), "Bonding in fabric-cement systems: Effects of fabrication methods", Cement and Concrete Research, Vol. 36, pp. 1661-71.

90   Krauss, S., Mobasher, B., "Tensile Testing of Textile Reinforced Concrete – A Round Robin Program", 2011, A report to RILEM Committee, Arizona State University.

91   Wille, K., Kim, J.D., Naaman, A.E., "Strain-hardening UHP-FRC with low fiber contents", Materials and Structures, RILEM 2010, DOI 10.1617/s11527-010-9650-4

92   Zhu, D., Peled, A., Mobasher, B., "Dynamic Tensile Testing of Fabric-Cement Composites, Construction and Building Materials, 2011, Vols. 25, pp. 385-395.

93   Weil, N. A., and Daniel, I. M. D. "Analysis of Fracture Probabilities in Nonuniformly Stressed Brittle Materials," Journal of American Ceramic Society, 1964, Vols. 47 (6), pp. 268-274

94   V. Calard, J. Lamon , "A probabilistic-statistical approach to the ultimate failure of ceramic-matrix composites—part I: experimental investigation of 2D woven SiC/SiC composites," Composites Science and Technology, 2002, Vols. 62, pp. 385–393.

95   PCI Recommended Practice for Glass Fiber reinforced Concrete Panels-MNL128-01, fourth edition

96   G. Ramakrishna, T. Sundararajan, Studies on the durability of natural fibres and the effect of corroded fibres on the strength of mortar, Cem. Concr. Compos. 27 (2005), pp. 575–582.

97   A. Belaadi, A. Bezazi, M. Bourchak, F. Scarpa, Tensile static and fatigue behaviour of sisal fibres, Mater. Des. 46 (2013) 76–83.

98   Filho, R.D.T., Scrivener, K., England, G.L., Ghavani, K., "Durability of alkali-sensitive sisal and coconut fibres in cement mortar composites", Cement and Composites, Vol. 22, 2000, pp. 127-143.

99   Y. Li, Y.-W. Mai, L. Ye, Sisal fibre and its composites: a review of recent developments, Compos. Sci. Technol. 60 (2000) 2037–2055.

100   Majumdar, A.J and Laws, V. (1991), "Glass fibre reinforced cement." Oxford BSP Professional Books, 197.

101   Mobasher, B., and Shah, S. P.(1989). "Test Parameters for Evaluating Toughness of Glass-Fiber Reinforced Concrete Panels." ACI Materials Journal, 86 (5), 448-458.

102   Shah, S.P., Ludirdja, D., Daniel, J.I., and Mobasher, B. (1988). "Toughness – Durability of Glass Fiber Reinforced Concrete Systems." ACI Materials Journal, 85(5), 352-360.

103   Soroushian, P., Tlili, A., Yohena, M., and Tilsen, B.L. (1993). "Durability Characteristics of Polymer-Modified Glass Fiber Reinforced Concrete." ACI Material Journal, 90(1), 40-49

104   Orlowsky, J., Raupach, M., Cuypers, H and Wastiels, J.(2005). "Durability modelling of glass fiber reinforcement in cementitious environment", Materials and Structures, 38,155-162.

105   Bentur, A., Diamond, S. (1984)."Fracture of glass fiber reinforced cement."Cement and Concrete Research, 14, 31-34.

106   Bentur, A.(1985)" Mechanisms of potential embrittlement and strength loss of glass fiber reinforced cement composites."Proc., Durability of Glass Fiber Reinforced Concrete Symposium,PCI, Chicago,ed. S. Diamond,109-123.

107   Stucke, M.S., Majumdar, A.J., (1976). "Microstructure of glass fibre-reinforced cement composites", Cement and Concrete Research 11(6) 1019-1030

108   Hegger, J., Will, N., Bruckermann, O., and Voss, S., (2006)"Load-bearing behavior and simulation of textile reinforced concrete", Materials and Structures, 39, 765-776.

109   Banholzer, B., Brockmann, T., and Brameshuber, W., (2006), Material and bonding characteristics for dimensioning and modeling of textile reinforced concrete (TRC) elements, Materials and Structures, 39, 749-763

110   Bentur, A., Diamond, S. (1984)."Fracture of glass fiber reinforced cement."Cement and Concrete Research, 14, 31-34.

111   Bentur, A.(1985)" Mechanisms of potential embrittlement and strength loss of glass fiber reinforced cement composites."Proc., Durability of Glass Fiber Reinforced Concrete Symposium,PCI, Chicago,ed. S. Diamond,109-123.

112   R.M. de Gutiérrez, L.N. Díaz, S. Delvasto, Effect of pozzolans on the performance of fiber-reinforced mortars, Cem. Concr. Compos. 27 (2005) 593–598.

113   Marikunte, S., Aldea, C. and Shah, S. (1997). "Durability of glass fiber reinforced cement composites: effect of silica fume and metakaolin.", Journal of Advanced Cement Based Composites, 5, 100-108.

114   A.B.L. Pimentel, H. Savastano, Durability of cellulose–cement composites modified by polymer, Eng. Agr. 26 (2006) 344–353.

115   Qi, C., Tianyou, B. (2003)."A review of the development of the GRC industry in China.", Proc., GRCA, 12th Congress, Barcelona, Spain, eds. J.N. Clarke and R. Ferry, 37.

116   Ambroise, J. and Péra, J. (2005). "Durability of glass-fibre cement composites: comparison between normal, Portland and calcium sulphoaluminate cements.", Proc., Composites in Construction - Third International Conference, Lyon, 1197-1204.

117   Gartshore, G.C., Kempster, E. and Tallentire, A.G. (1991)."A new high durability cement for GRC products." Proc.,Glassfibre Reinforced Cement Association 6th Biennial Congress, Maastricht, Netherlands, 3-12.

118   Cuypers, H., Wastiels, J., Orlowsky, J.,and Raupach, M. (2003). "Measurement of the durability of glass fibre reinforced concrete and influence of matrix alkalinity.", Proc., Brittle Matrix Composites 7, eds.A.M. Brandt, V.V. Li and I.H. Marshall, Warsaw, 163-172.

119   Cuypers, H., Van Itterbeeck, P., De Bolster, E., Wastiels, J. (2005) "Durability of cementitious composites.", Proc., Composites in Construction- Third International Conference, Lyon, France, 1205-1212.

120   Cuypers, H., Gu, J., Croes, K, Dumortier, S., Wastiels, J. (2000). "Evaluation of fatigue and durability properties of E-glass fibre reinforced phosphate cementitious composite.", Proc., Brittle Matrix Composites 6, eds. A.M. Brandt, V.C. Li, I.H. Marshall, Warshaw, 127-136.

121   Cuypers, H., Wastiels, J., Van Itterbeeck, P., De Bolster, E., Orlowsky, J. and Raupach, M. (2006)."Durability of glass fibre reinforced composites experimental methods and results.", Composites Part A, 37, 207-215.

122   Brameshuber, W. and Brockmann, T. (2001). "Calcium aluminate cement as binder for textile reinforced concrete." Proc., International Conference on Calcium Aluminate Cements (CAC), Edinburgh, Scotland, 659-666.

123 Brameshuber, W., Brockmann. (2001). "Development and optimization of cementitious matrices for textile reinforced concrete.", Proc., 12th International Congress of the International Glassfibre Reinforced Concrete Association, Dublin, Ireland, eds. N. Clarke and R. Ferry, 237-249.

124 Ambroise, J. and Péra, J. (2005). "Durability of glass-fibre cement composites: comparison between normal, Portland and calcium sulphoaluminate cements.", Proc., Composites in Construction - Third International Conference, Lyon, 1197-1204.

125 G.H.D. Tonoli, S.F. Santos, A.P. Joaquim, H. Savastano Jr, Effect of accelerated carbonation on cementitious roofing tiles reinforced with lignocellulosic fibre, Constr. Build. Mater. 24 (2010) 193–201.

126 P. Soroushian, J.-P. Won, M. Hassan, Durability characteristics of CO2-cured cellulose fiber reinforced cement composites, Constr. Build. Mater. 34 (2012), 44–53.

127 K. Bilba, M.A. Arsene, Silane treatment of bagasse fiber for reinforcement of cementitious composites,Compos. Part A:Appl. Sci.Manuf. 39 (2008) 1488–1495.

128 J. Claramunt, M. Ardanuy, J.A. García-Hortal, R.D.T. Filho, The hornification of vegetable fibers to improve the durability of cement mortar composites, Cem. Concr. Compos. 33 (2011) 586–595.

129 Litherland, K.L., Oakley, D.R., and Proctor, B.A. (1981). "The Use of Accelerated Aging Procedures to Predict the Long Term Strength of GRC Composites." Cement and Concrete Research, 11(3), 455-466.

130 Cockram, D.R., Litherland, K.L., Proctor, B.A., and Yale, B. (1983)."Assessing the Durability of Glass Compositions." Research and Development Laboratories of Pikington Brothers PLC, Lancashire, Glastech, 56, 644-649.

131 Proctor, B.A., Oakley, D.R., and Litherland, K.L. (1982)."Developments in the Assessment and Performance of GRC Over 10 Years." Composites (Guildgord),173-180.

132 Proctor, B.A., (1981)."Past Development and Future Prospect for GRC Materials." Proceedings, International Congress on Glass Fibre Reinforced Cement ,The Glass Fibre Reinforced Cement Association, Gerrards Cross, 50-67.

133   Aindow, A.J., Oakley, D.R. and Proctor, B.A. (1984)."Comparison of the weathering behaviour of GRC with predictions made from accelerated aging tests." Cement and Concrete Research, 14, 271-274.

134   Litherland, K.L.(1986)."Test methods for evaluating the long term behaviour of GFRC." Proc., Durability of Glass Fiber Reinforced Concrete Symposium, PCI, Chicago, 210-221.

135   Proctor, B.A., Oakley, D.R. and Litherland, K.L.(1982)."Developments in the assessment and performance of GRC over 10 years, Composites, 13, 173-179.

136   Soranakom, C., and Mobasher, B. (2008), "Correlation of Tensile and Flexural Responses of Strain Softening and Strain Hardening Cement Composites." Cement and Concrete Composites, 30, 465 – 477.

137   Soranakom, C., and Mobasher, B. (2007)."Flexural Modeling of Strain Softening and Strain Hardening Fiber Reinforced Concrete." Proc., Fifth International RILEM Workshop, High Performance Fiber Reinforced Cement Composites, HPFRCC5, Mainz, Germany, 155-164.

138   Naaman, A. E., and Reinhardt H. W.(2006)."Proposed Classification of HPFRC Composites Based on Their Tensile Response." Materials and Structures, 39, 547–555.

139   Bartos, J.M., Peter, and Zhu, W. (1996). " Effect of Microsilica and Acrylic Polymer Treatment on the Aging of GRC.", Cement and Concrete Compositions, 18, 31 - 3

140   Soranakom C, Mobasher B.. (2008). "Correlation of tensile and flexural response of strain softening and Strain Hardening Cement Composites. Cement and Concrete Compos, 30:465–77.

141   Mobasher, B., Dey, V., Cohen, Z., Peled, A. (2014). , "Correlation of constitutive response of hybrid textile reinforced concrete from tensile and flexural tests", 2014, vol. 53, pp. 148-161.

142   Dey V., Mobasher, B., "Quantitative Characterization of Accelerated Aging in Cement Composites using Flexural Inverse Analysis", 2016, Cement and Concrete Composites,   Manuscript in Review.

143   ASTM C947-03, "Standard test method for flexural properties of thin-section glass-fiber   reinforced concrete (using simple beam with third-point loading), 2009.

144   Mohr B.J., Nanko, H., Kurtis, K.E. (2005) "Durability of kraft pulp fiber–cement composites to wet/dry cycling", Cement Concrete Composites, 27,435–448.

145   Singh, SM. (1985) "Alkali resistance of some vegetable fiber and their adhesion with Portland Cement", Res Indust, 15, pp. 121-126.

146   Gram, HE.,(1983)"Durability of natural fibers in concrete", Swedish Cement and Concrete Research Institute, Research Fo. 1:83, Stockholm, pp. 255.

147   Bentur, A., Akers, SAS., (1989). "The microstructure and aging of cellulose fiber reinforced autoclaved cement composites", International Journal of Cement Composites Lightweight Concrete, 11 (2), 111-115.

148.   Mehta PK, Monteiro PJM. Concrete: Microstructure, Properties and Materials. Boston: McGraw-Hill, 2006.

149.   Lura P, Pease B, Mazzotta GB, Rajabipour F, Weiss J. Influence of shrinkage-reducing admixtures on development of plastic shrinkage cracks. ACI Mater J 2007; 104(2):187-94.

150.   Banthia N, Gupta R. Plastic shrinkage cracking in cementitious repairs and overlays. Mater Struct 2009; 42(5):567-79.

151.   Mora-Ruacho J, Gettu R, Aguado A. Influence of shrinkage-reducing admixtures on the reduction of plastic shrinkage cracking in concrete. Cem Concr Res 2009; 39(3):141-6.

152.   Cohen MD, Olek J, Dolch WL. Mechanism of plastic cracking in portland cement and portland cement-silica fume paste and mortar. Cem Concr Res 1990; 20(1):103-19.

153.   Kwon SJ, Na UJ, Park SS, Jung SH. Service life prediction of concrete wharves with early-aged crack: Probabilistic approach for chloride diffusion. Struct Saf 2009; 31(1):75-83.

154.   Huang XM, Yang CY. Early-age concrete cover crack and its effects on concrete cover. Key Eng Mater 2006; 302-303:630-6.

155.   Yoon IS, Schlangen E, de Rooij MR, van Breugel K. The effect of cracks on chloride penetration into concrete. Key Eng Mater 2007; 348-349:769-72.

156   Grzybowski M, Shah S. Shrinkage Cracking of Fiber Reinforced Concrete. ACI 1990; 81(2):138-148.

157   Qi C, Weiss J, Olek J. Characterization of plastic shrinkage cracking in fiber reinforced concrete using image analysis and a modified Weibull function. Materials and Structures 2003; 36(260):386-395

158   Banthia N, Azzabi M, Pigeon M, Restrained shrinkage cracking in fiber reinforced cementitious composites, Materials and Structures Rilem 1993; 26(161): 405-413.

159.   Soroushian P, Ravanbakhsh S. Control of plastic shrinkage cracking with specialty cellulose fibers, ACI Mater J 1998; 95(4):429-35.

160   Naaman A, Wongtanakitcharoen T, Hauser G. Influence of different fibers on plastic cracking of concrete. ACI 2005; 102:49-58.

161   Soroushian P, Ravanbakhsh S. Control of plastic shrinkage cracking with specialty cellulose fibers. Materials Journal 1998; 95:429-435

162   Banthia N, Yan C. Shrinkage crackingin polyolefin fiber-reinforced concrete. ACI 2000; 97:432-437.

163.   Hannant, D. J.,"Fibre cements and fibre concretes", John Wiley & Sons, Chicester, 1978, pp. 219.

164.   Li, Z., Mobasher, B., and Shah, S. P., "Characterization of interfacial properties in platelet-reinforced cementitious composites", Journal of the American Ceramic Society, 1991, Vol. 74 (9), pp. 2156-64.

165.   Ransinchung, G.D., Kumar, B., Kumar, V., "Assessment of water absorption and chloride ion penetration of pavement quality concrete admixed with wollastonite and microsilica", Construction and Building Materials, 2009, Vols. 23, pp.1168 – 1177.

166.   Nikonova, N.S., Tikhomirova, I.N., Belyakov, A.V., Zakharov, A.I., "Wollastonite in Silicate Matrices", Glass and Ceramics, 2003, Vol. 60, Nos. 9-10, pp. 342-346.

167.   Beaudoin, J. J., Low, N., M., P.,"The flexural toughness and ductility of Portland cement-based Binders reinforced with wollastonite micro-fibres", Cement and Concrete Research, 1994, Vol. 24, No. 2, pp. 250-258.

168.   Beaudoin, J. J., Low, N., M., P.,"Flexural strength and microstructure of cement binders reinforced with wollastonite micro-fibres", Cement and Concrete Research, 1993,   Vol. 23, pp. 905-916.

169.   NYCO, Brand of S&B Group, Technical Document, "Physical Properties of Wollastonite", Internet Source: http://www.sandb.com/wp-content/uploads/Physical-Properties-Overview.pdf

170. Beaudoin, J. J., Low, N., M., P.,"Mechanical properties of high performance cement binders reinforced with wollastonite micro-fibres", Cement and Concrete Research, 1992, Vol. 22, pp. 981-989.

171. Beaudoin, J. J., Low, N., M., P.,"The effect of wollastonite micro-fibre aspect ratio on reinforcement of Portland cement-based matrices", Cement and Concrete Research, 1993,   Vol. 23, pp. 981-989.

172. Mathur, R., Misra, A,K., Goel, P., "Influence of wollastonite on mechanical properties of concrete", Journal of Scientific and Industrial Research, 2007,66, pp. 1029-1034.

173. Kalla, P., Misra, A., Gupta, R.C., Csetenyi, L., Gahlot, V., "Mechanical and durability studies on concrete containing wollastonite-fly ash combination", Construction and Building Materials, 2013, Vols. 40, pp. 1142-1150.

174. Solliman, A.M., Nehdi, M.L., "Effects of shrinkage reducing admixture and wollastonite microplatelet on early-age behavior of ultra-high performance concrete", Cement & Concrete Composites, Vol. 46, 2014, pp. 81-89.

175. Ransinchung, G.D.R.N., Kumar, B., "Investigations on pastes and mortars of ordinary Portland cement admixed with wollastonite and microsilica", Journal of Materials in Civil Engineering, ASCE, 2010, Vol. 22, pp. 305-313.

176. Ransinchung G.D., Singh B.N., Kumar B, Kumar V., "Micro structural behavior of wollastonite and microsilica admixture concrete for rigid pavements", Highway Resources Journal, 2008;Vol. 1(1), pp. 13–20.

177. RILEM Technical Committee 89-FMT, 'Determination of Fracture Parameters (K_{IC} and $CTOD_c$) of Plain Concrete Using Three-Point Bend Tests', RILEM Draft Recommendations, Materials and Structures, 23 (No. 6) (1990) 457–460.

178. Jenq, S.M.Y., Shah, S.P., "Two parameter fracture model for concrete", Journal of Engineering Mechanics, ASCE, 1985, Vol. 111 (19), pp. 1227 – 1241.

179. Mobasher, B., Peled, A., "Use of r-curves for characterization of toughening in platelet reinforced concrete," Proceedings, International Conferences on Fracture Mechanics of Concrete and Concrete Structures (FraMCoS V) Vail Colorado, 2004. pp.1137-1143

180. Arino, A., Mobasher, B., "Effect of ground copper slag on strength and toughness of cementitious mixes", ACI Materials Journal, 1999, Title no. 96-M10, pp. 68-73

181. RILEM Technical Committee 89-FMT, "Determination of fracture parameters (k_{ic} and $ctod_c$) of plain concrete using three-point bend tests", RILEM Draft Recommendations, Materials and Structures, 1990, Vol. 23 (6), pp. 457–460.

182. Mobasher, B., Mehdi, B., Bonakdar, A., "Back calculation procedure for cyclic flexural fracture tests in Platelet Reinforced Concrete", ACI Special Publication, Manuscript in Review.

183 Lura P, Pease B, Mazzotta GB, Rajabipour F, Weiss J. Influence of shrinkage-reducing admixtures on development of plastic shrinkage cracks. ACI Mater J 2007; 104(2):187-94.

184 Banthia N, Gupta R. Plastic shrinkage cracking in cementitious repairs and overlays. Mater Struct 2009; 42(5):567-79.

185 Mora-Ruacho J, Gettu R, Aguado A. Influence of shrinkage-reducing admixtures on the reduction of plastic shrinkage cracking in concrete. Cem Concr Res 2009; 39(3):141-6.

186. Sanjuan MA, Moragues A. A testing method for measuring plastic shrinkage in polypropylene fibre reinforced mortars. Mater Lett 1994; 21:239-46.

187. Nanni A, Ludwig DA, Mcgillis MT. Plastic shrinkage cracking of restrained fiber-reinforced concrete. Transp Res Rec 1993; 1382:69-72.

188. Banthia N, Gupta R. Test method for evaluation of plastic shrinkage cracking in fiber-reinforced cementitious materials. Exp Tech 2007; 31(6):44-8.

189. Naaman AE, Wongtanakitcharoen T, Hauser G. Influence of different fibers on plastic shrinkage cracking of concrete. ACI Mater J 2005; 102(1):49-58.

190. Ma Y, Zhu B, Tan M, Wu K. Effect of Y type polypropylene fiber on plastic shrinkage cracking of cement mortar. Mater Struct 2004; 37:92-5.

191. Jacobsen S, Aarseth LI. Effect of wind on drying from wet porous building materials surfaces-A simple model in steady state. Mater Struct 1999; 32:38-44.

192. Shimomura T, Maekawa K. Analysis of the drying shrinkage behavior of concrete using a micromechanical model based on micropore structure of concrete. Mag Concr Res 1997; 49(181):303-322.

193. Dey, V., Kachala, R., Bonakdar, A., and Mobasher, B. (2015). "Mechanical properties of micro and sub-micron properties of wollastonite fibers in cementitious composites." Construction Building Material, 82, 351–359.

194. Xu, S. L, and Reinhardt, H. W., "Crack extension resistance and fracture properties of quasi-brittle softening materials like concrete based on the complete process offracture" International Journal of Fracture, 1998, Vol. 92 (1), pp. 71-99.

195. C Ouyang, B Mobasher, SP Shah, "An R-curve approach for fracture of quasi-brittle materials", Engineering fracture mechanics, 1990, Vol. 37 (4), pp. 901-913.

196. Sanford, R. J., "Principles of fracture mechanics", Prentice Hall, NJ, 2003, pp. 404.

197 Bakhshi M., Mobasher B., "Experimental observations of vacuum drying of early-age Portland cement paste", Cement and Concrete Composites 2011; 31:474-484.

198 Bakhshi M, Mobasher B, Soranakom C. Moisture Loss Characteristics of Cement-Based Materials under Early-Age Drying and Shrinkage Conditions. Construction and Building Materials 2012; 30:413–425.

199 Dey, V., Kachala, R., Bonakdar, A., Neithalath, N., Mobasher, B., "Quantitative 2D Restrained Shrinkage Cracking of Cement Paste with Wollastonite Microfibers", Journal of Materials in Civil Engineering, ASCE, 2016, DOI: 10.1061/(ASCE)MT.1943-5533.0001592.

200 Copeland, L.E., Hayes, J.C., "Determination of non-evaporable water in hardened Portland-cement paste", ASTM Bulletin 1953; 194:70-4.

201 Dey, V., Dakhane, A., Neithalath, N., Mobasher, B. Digital Image Correlation on a 2D Restrained Slab to Quantify the Early-Age Shrinkage Cracking Characteristics of Binder Systems. 2015, ACI Fall Convention, Denver, CO.

202 Crank J. The mathematics of diffusion. New York: Oxford Science Publications, 1989.

203. Bakhshi, M., Characterization and Modeling of Moisture Flow through hydrating cement-based materials under early-age drying and shrinkage conditions, Arizona State University, PhD dissertation, 2011, pp. 289.

204 Mathwork file exchange, Matlab Central (2003), Skeleton Intersection Detection, [Online], Available: http://www.mathworks.com/matlabcentral/fileexchange/4252-skeleton-intersection-detection

205. Tekalur, S.A., et.al. "Shock loading response of sandwich panels with 3-D woven E-glass composite skins and stitched foam core", Composites and Technology, 2009, Vols. 69, pp. 736 - 753

206.   Manalo, A.C., Aravinthan, T., Karunasena, W., "Mechanical properties characterization of the skin and core of a novel composite sandwich structure", Journal of composite Materials, 2012, Vols. 47 (14), pp. 1785-1800.

207.   Zhao, H., Elnasri, I., Girard, Y., "Perforation of aluminum foam core sandwich panels under impact loading – An experimental study", International Journal of Impact Engineering, 2007, Vols, pp. 1246-1257

208.   Shams, A., Hegger, J., Horstmann, M., "An analytical model for sandwich panels made of textile reinforced concrete", Construction and Building Materials, 2014, Vols. 64, pp. 451-459.

209.   Memon, N.,A., Sumadi, S.,R., Ramli, M., "Ferrocement encased lightweight aerated concrete: A novel approach to produce sandwich composite", Materials Letters, 2007, Vols. 61, pp. 4035 - 4038.

210.   Uddin, N., Fouad, F., Vaidya, U.K, Khotpal, Am., Perez, J.C.S., "Structural characterization of hybrid fiber reinforced polymer (FRP) – autoclaved aerated concrete (AAC) panels", Journal of Reinforced Plastics and Composites, 2006, Vols. 25, pp. 981-999.

211.   Dey, V., Zani, G., Colombo, M., Di Prisco, M., Mobasher, B., "Flexural Impact Response of Textile-Reinforced Aerated Concrete Sandwich Panels", Journal of Materials and Design, 2015, doi: 10.1016/j.matdes.2015.07.004

212.   Kermani, A., "Performance of structural insulated panels", Proceedings of the Institution of Civil Engineers, Structures and Buildings, 2006, Vols. 159, pp. 13 - 19

213.   ElKashef, M., AbdelMooty, M., "Investigating the use of autoclaved aerated concrete as an infill in reinforced concrete sandwich panels", Materials and Structures, 2015, Vol. 48, Issue 7, pp. 2133-46.

214.   Mobasher, B., Dey, V., Cohen, Z., Peled, A., "Correlation of constitutive response of hybrid textile reinforced concrete from tensile and flexural tests", 2014, Vols. 53, pp. 148-161.

215.   523.2R, ACI., "Guide for Precast Cellular Concrete Floor, Roof and Wall Units", American Concrete Institute. Farminton Hills. 1996.

216.   Narayanan, N and Ramamurthy, K.,"Structure and properties of aerated concrete: a review": Cement and Concrete Composites, 2000, Vols. 20, 321 - 329.

217.   ASTM C-1693, "Standard Specification for Precast Autoclaved Aerated Concrete (AAC) Wall Construction Units". ASTM International, PA. 2009.

218.   Holt, E and Raivio, P.,"Use of gasification residues in aerated autoclaved concrete": Cement and Concrete Research, 2005, Vols. 35, 796 - 802.

219.   Zollo, F. Ronald, and Hays, D.Carol., "Engineering Material Properties of a Fiber Reinforced Cellular Concrete": ACI Materials Journal. Title no. 95- M61.

220.   Perez-Pena, M and Mobasher, B.,"Mechanical properties of fiber reinforced lightweight concrete composites": Cement and Concrete Research, 1994, Vols. 24, pp. 1121 - 1132.

221.   Gibson, L.J and Ashby, M.F.,"Cellular Solids, Structure and Properties". Cambridge : Cambridge University Press, 1997.

222.   Bonakdar, A, Mobasher, B and Babbit, F. ,"Physical and mechanical characterization of fiber-reinforced Aerated Concrete (FRAC)", ACI Spring Convention. Chicago, IL : American Concrete Institute, March 21 - 25, 2010.

223.   Bindiganavile, V and Banthia, N.,"Polymer and steel fiber-reinforced cementitious composites under impact loading. Part 1: bond - slip response": ACI Materials Journal, Vols. 98(1), 17 - 24.

224.   Bindiganavile, V and Banthia, N., "Polymer and steel fiber-reinforced cementitious composites under impact loading. Part 2: flexural toughness": ACI Materials Journal, Vols. 98 (1), 17 - 24.

225.   Manolis, G.D, et al., et al.,"Dynamic properties of polypropylene fiber-reinforced concrete slabs": Cement and Concrete Composites, 1997, Vols. 19, 341 - 349.

226.   Dey,V., Bonakdar,A., Mobasher,B., Low-velocity flexural impact response of fiber reinforced aerated concrete, Cem. Concr. Compos. 49 (2013) 100–110.

227.   Hong, S., Liu, D., "On the Relationship between Impact Energy and Delamination Area",   Experimental Mechanics, 1988 Vols. 29, pp. 115-120.

228.   Pozuelo, M., Carreno, F., Ruano, O.,A., "Delamination effect on the impact toughness of an ultrahigh carbon-mild steel laminate composite", Composites Science and Technology, 2006, Vols. 66, pp. 2671-76.

266

229.   Lee, H.K., Liang, Z., "Computational modeling of the response and damage behavior of fiber reinforced cellular concrete": Computers & Structures, 2004, Vols. 82, 581 – 592.

230.   Dey,V., Bonakdar,A., Mobasher,B., Low-velocity flexural impact response of fiber reinforced aerated concrete, Cem. Concr. Compos. 49 (2013) 100–110.

231.   Daniel, I.,M., et. al., "Failure modes of composite sandwich beams", International Journal of Damage Mechanics, 2002, Vols. 11, pp. 309-334.

232.   Keller, T., Schaumann, E., Vallee, T., "Flexural behavior of a hybrid FRP and lightweight concrete sandwich bridge deck", Composite Part A: applied science and manufacturing, Vols. 38, 2007, pp. 879-889.

233.   Mosallam, A., et. al., "Structural evaluation of reinforced concrete beams strengthened with innovative bolted/bonded advanced frp composites sandwich panels, Composite Structures, 2015, pp. 421-440.

234.   Machinery Handbook, 29th Edition, Large Print and Toolbox Edition, Weblink: http://www.engineersedge.com/lumber.htm

235.   Faria de F.E., Mobasher, B., "Advanced cementitious composite materials for application on cracks in concrete dams", Technical Report, Arizona State University, 2015, pp.43.